Electromagnetic radiation from matter under extreme conditions

Simon Turbide
Department of Physics
McGill University
Montréal, Québec
Canada

A Thesis submitted to
McGill University
in partial fulfillment of the requirements for the degree of
Doctor of Philosophy

Your file Votre référence
ISBN: 978-0-494-25272-7
Our file Notre référence
ISBN: 978-0-494-25272-7

Contents

LIST OF FIGURES

List of Tables

Abstract

The subject of this thesis is the production of electromagnetic radiations during relativistic heavy ions collisions. Since they constitute one of the major ways to probe the presence of a quark-gluon plasma (QGP), their evaluation through theoretical models is very important. The photon production at low-to intermediate transverse momentum (p_T) is first studied. The photon production rate in a mesonic gas is evaluated within a massive Yang-Mills (MYM) approach. Earlier calculations are reexamined with additional constraints, including new production channels and with the inclusion of form-factors. Adding primordial N-N contribution and existing baryonic and QGP production rates, we can reproduce the photon spectra observed at the Super Proton Synchrotron (SPS). The intermediate to high-p_T region is dominated by the physics of jets. A treatment, complete to leading-order in the strong coupling, is used to calculate energy loss in the strongly interacting medium. This approach is convolved with a physical description of the initial spatial distribution of jets and with an expansion of the emission zone. The role played by jet-plasma interactions is highlighted, showing that they dominate in the range $2 < p_T < 4$ GeV, at the Relativistic Heavy Ion Collider (RHIC). This mechanism has an important impact on both the total photon yield and the photon azimuthal asymmetry, turning the coefficient v_2 negative. Finally, the dilepton production at high p_T is calcultated with hard-thermal loops (HTL) effects, showing, that in perfect analogy with real photons, jet-plasma interactions also dominate the dilepton yield around $p_T = 4$ GeV.

Résumé

Le sujet de cette thèse est la production de radiations electromagnétiques produites durant une collision d'ions lourds aux energies relativistiques. Comme les photons constituent l'un des principaux outils pour sonder la formation d'un plasma quark-gluon (QGP), leur evaluation à travers des modèles théoriques est fondamentale. La production de photons ayant un momentum transverse (p_T) de faible à intermédiaire, est d'abord étudiée. La contribution provenant du secteur mésonique est évaluée dans une approche Yang-Mills massive (MYM). D'anciens calculs sont réexaminés avec des contraintes additionnelles, incluant des canaux de production et des facteurs de forme. Ajoutés aux collisions N-N primordiales ainsi qu'à des taux de production disponibles pour la contribution des baryons et du QGP, les résultats expérimentaux observés au Super Proton Synchrotron (SPS) sont reproduits avec succès. La région d'intermédiaire à haut p_T est dominée par la physique des jets. Un traitement, complet au premier ordre en la constante de couplage α_s, est utilisé afin de calculer la perte d'énergie dans un milieu régit par l'interaction forte. Cette approche est convoluée avec une description physique de la distribution initiale de jets et avec une expansion de la zone d'émission. Le rôle joué par l'interaction jet-plasma est mis en lumière, montrant que celle-ci domine dans le domaine $2 < p_T < 4$ GeV, au Relativistic Heavy Ion Collider (RHIC). Ce mécanisme a un impact important sur la production totale de photons, mais aussi sur sa distribution elliptique, rendant le coefficient v_2 négatif. Finalement, la production de dileptons à haut p_T est calculée avec l'effet des boucles thermales dures (HTL), montrant, dans une parfaite analogie avec les photons réels, que l'interaction jet-plasma domine aussi le spectre de dileptons autour de $p_T = 4$ GeV.

Acknowledgments

I would like to express my sincere thanks to my supervisor, Professor Charles Gale, for accepting me as his student, and for all the help necessary for the completion of this degree. His precious advises, based on his important knowledge on nuclear physics, guided me during my work. He gave me the opportunity to participate to conferences and summer school, and to collaborate with other researchers in the field. His availability for students and his personality make him a person with whom it is pleasant to work.

I would like to thank also Profs. Sangyong Jeon and Guy Moore for their help through numerous discussions. I have also appreciate to collaborate with Prof. Ralf Rapp. His rapidity to answer at my emails often amazed me. Special thanks also go out to Profs. Dinesh Srivastava, Brian Cole, and Dr. Rainer Fries.

J'aimerais également remercier mes compagnons de doctorat et amis, Jean-Sébastien Gagnon et François Fillion-Gourdeau, pour leur aide en physique, et aussi pour leur jovialité. Leur bonne humeur auront animé les journeées, surtout les heures de dinner, durant ces dernières années.

J'adresse aussi des remerciements aux autres étudiants que j'ai côtoyés, Pierre-Hugues Beauchemin, Alex Bourque et Guangyou Qin, et qui m'ont apporté leur aide au cours de mes recherches.

Finalement, je tiens à remercier, ma famille pour son support, mais surtout celle qui partage ma vie depuis mon arrivée à McGill, qui me soutient et m'encourage inconditionnellement, ma copine Andréanne.

1

INTRODUCTION

The quest of understanding the behaviour of nuclear matter under extremely high density and temperature has been one of the main goals of nuclear physicists for decades. We define ordinary nuclear matter by an infinite ensemble of strongly interacting hadrons and mesons, without surface effects. This field of research is important for two reasons. First, from a fundamental point of view, it is interesting to know what happens when ordinary matter is submitted to very high temperatures and/or densities, and secondly, this knowledge is essential to explain the behaviour and characteristics of astrophysical bodies, like neutron stars and supernovae, since their insides are expected to be made of such matter.

In order to reach a deeper understanding of the physics involved in those phenomena, elaboration of theoretical models and their confirmation by experimental measurements is needed. As the astrophysical bodies are not at hand, being too distant and too rare, one has to find a substitute on earth, for those phenomena. The only known candidate is heavy-ions collisions.

1.1 Heavy-Ion Collisions and phase of nuclear matter

A important wealth of information can be obtained by colliding heavy ions at high energy. During a very short period (less than 100 fm/c $\sim 3 \times 10^{-22}$s), depending on the beam energy, we expect the overlapping zone to reach states of high temperature/density. However, as the nuclei have finite extension, we cannot talk about infinite nuclear matter : surface effect might become important and would have to be taken into account. Figure 1.1 indicates some trajectories which relativistic heavy-ion collisions may follow. The collision starts with cold matter and follow a pre-equilibrium stage (dashed lines) which cannot be mapped on the phase diagram. The energy deposited is redistributed among the strongly interacting particles, leading to thermalization at high temperature. Drived by internal pressure, the system expands and cools, tracing a path (solid lines) in the phase diagram, until a freeze-out temperature. At this point the distance between the particles is large enough, and they cease to interact.

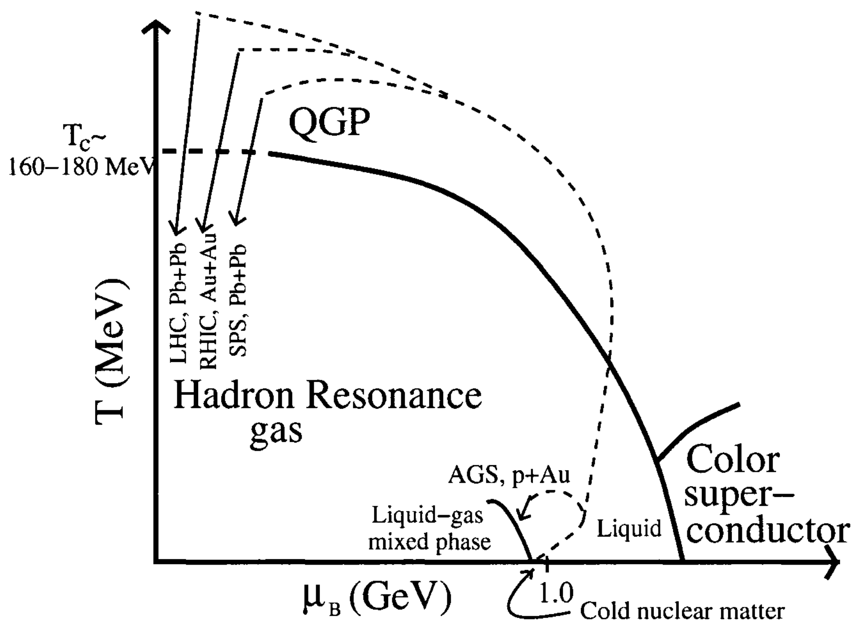

Figure 1.1: Nuclear matter phase diagram.

The trajectory in the phase diagram depends on the size of the ions and on the beam energy. Symmetric A+A reactions in the Fermi-energy regime (E/A $\sim$ 50 MeV/nucleon) and asymmetric hadron(h)+A reactions at some GeV are the best candidates for observing a nuclear liquid-gas phase transition [1]. Calculations by myself [2], based on the Boltzmann transport equation [3] have shown that for such reactions, the system takes about 60-65 fm/c to thermalize, leaving a state of depleted average density, ρ/ρ_0 $\sim$1/4-1/3 for central collisions, and low-to-moderate excitation energy $E^*/A < 9$ GeV. The approximate energy density at thermalization would be $\epsilon \sim$0.05 GeV/fm^3. Analysis of 6.2-14.6 GeV proton on Au [4] collisions at the Brookhaven Alternating Gradient Synchrotron (AGS) accelerator, suggest that above $E^*/A \sim 5$ GeV, the desexcitation mechanism change abruptly from a sequential emission of fragments (characteristic of a liquid phase), to simultaneous emission. This simultaneous emission of fragments, the multifragmentation, would be a signature that the system has entered into the spinodal region, which is an unstable region in the liquid-gas coexistence zone. The nuclear liquid-phase transition would have a critical endpoint at a temperature of about 7.5 MeV [5]. At larger baryon density, lies the color superconductor (CSC) phase [6], induced by quark pairing at the Fermi surface, and separated from the QGP by a first order phase transition at a temperature estimated to $T = 30 - 50$ MeV. Compact astrophysical bodies like neutron stars, may be the systems of relevance for the CSC phase [7].

The hadrons are not fundamental particles : they are made of quarks, which interact through gluon exchange. The fundamental theory describing those interactions is Quantum Chromodynamics (QCD) [8], which predicts the confinement of quarks inside hadrons at zero temperature. At non-zero temperature, from lattice QCD calculations, there is strong evidence that around a temperature of 170 MeV, or equivalently an energy density of about ϵ=1 GeV/fm^3 [9], there should be a phase transition between an ordinary confined hadronic gas phase and a quark-gluon plasma (QGP), with an associate change in the relevant degrees of freedom. From Pb-Pb collision at center of mass energy $\sqrt{s} = 17.3A$ GeV, at the CERN Super Proton Synchrotron (SPS), results suggest an energy density $\epsilon \sim 3.5$ GeV/fm^3 and thermalization time as small as 1 fm/c. Energy densities as large as 15 GeV/fm^3 have been achieved at the Relativistic Heavy Ion Collider (RHIC) [10], in Au-Au collisions at $\sqrt{s} = 200A$ GeV, and energy densities in the order of 100 GeV/fm^3 [5] are expected for the future Large Hadron Collider (LHC) which should begin to run at CERN in 2008. For the LHC, the system will be Pb-Pb at $\sqrt{s} = 5.5A$ TeV.

Though large energy densities have been claimed to be observed at SPS and RHIC, it is not enough to conclude on the formation of a QGP. Indeed, this confirmation will need much more than just one observable. The quest for the QGP, which is also the goal of this thesis, is a real challenge, since the QGP is not a final state. Its evaluated life-time is some fm/c, and its experimental detection involves not directly the partons (quarks and gluons), but the hadrons produced during and after the phase transition, when quarks convert to hadrons. However, as we will discuss in the next section, even if we cannot see directly the QGP, there still exists detectable particles, which can probe this early phase : the photons.

1.2 *Photons as probe of the Quark-Gluon Plasma*

The photons, real and virtual, interact only electromagnetically with the surrounding matter. The coupling constant α which gives the strength of the electromagnetic interaction is much smaller than the coupling constant for strong interaction : $\alpha \sim 1/137$ while $\alpha_s \sim 0.3$ for QGP at temperature $T \sim 0.4$ GeV [11]. Evidences for an early thermalization of the strongly interacting medium created during relativistic heavy-ions collisions appear from ratio of final particles and from their elliptic flow (see for example Ref. [10] for such discussion at RHIC). No thermalization is however expected for photons. With α that small, the mean free path λ of the photon is much larger that the lifetime of the QGP, such that the photons produced during a QGP phase would leave the medium without rescattering. The smallness of α has two important consequences: first, it allows application of ordinary perturbation theory for the calculation of the photon production rates, and second, in the absence of rescattering, the photons spectral emissivity will reflect directly the property of the medium. This is why the photon is probably the most important tool for probing the QGP.

We have to be aware, however, that photons experimentally detected come from each phase of the collision. First of all, photons may be produced during the early phase: during the overlap of the two nuclei and during a pre-equilibrium phase, i.e. after collisions of nuclei but before thermalization is reached. Thereafter, in a scenario with formation of QGP at thermalization, photons will be produce by collisions at the partonic level, such as $q+g \to q+\gamma$, for example. In the subsequent hadronic phase, photons are produced by inelastic collisions of surrounding hadrons, like $\pi+\rho \to \pi+\gamma$ and $\pi+N \to N+\gamma$. Finally, after freeze-out, decay of neutral mesons like π^0 and η will also contribute to the photon yield. We will see later in this thesis that each contributing phase has its own features : some phase will be dominant at low-p_T, and another at intermediate or high-p_T, where p_T is the photon momentum transverse to the beam axis. Thus, the shape of the total photon yield measured in heavy-ions collisions can gives priceless clues about the QGP existence.

1.3 High p_T suppression

At present, one of the most striking measurements in support of the creation of hot and dense matter at RHIC is the discovery of high p_T suppression in central Au-Au collisions. This phenomenon is observed in single hadron spectra [12, 13] and in the disappearance of back-to-back correlations of high p_T hadrons [14].

There are a number of factors that can potentially influence the spectrum of high p_T partons in heavy ion collisions, compared to that in hadron-hadron collisions:

(i) A difference between the parton distribution functions of a proton and a heavy nucleus. This can be both depletion (shadowing) or excess (anti-shadowing) depending on the value of momentum fraction x.

(ii) The initial state multiple-scattering effect. This is the well known Cronin effect caused by multiple soft scatterings a parton may suffer before it makes a hard collision. This can, of course, only be significant in interactions involving at least one nucleus.

(iii) Final state energy loss. This is due to the interaction between the produced hard parton and the hot and dense environment.

Our kinematical range of application in this work is mainly mid-rapidity. There, initial state effects cannot explain high p_T suppression, as otherwise such suppression should also be observed in d-Au collisions, which is not the case [15]. High p_T suppression has to arise from a final state effect: jet energy loss[16]. On top of experimental evidence for the suppression cited above, it has also been proposed [17, 18] that azimuthal anisotropy at high p_T could also be explained by jet energy loss. Induced gluon bremsstrahlung, rather than elastic parton scattering, has been identified to be the dominant mechanism for jet energy loss [19, 20]. In the thermal medium, a coherence effect, the Landau-Pomeranchuk-Migdal (LPM) [21] effect, controls the strength of the bremsstrahlung emission. Several models of jet quenching through gluon bremsstrahlung have been elaborated by many different authors: Baier-Dokshitzer-Mueller-Peigné-Schiff (BDMPS) [22, 23], Gyulassy-Levai-Vitev (GLV) [24], Kovner-Wiedemann (KW) [25] and Zakharov [26]. There have also been phenomenological studies where different energy loss mechanisms were added onto Monte Carlo jet models [27, 28, 29] (see also [30] for a recent review).

We will see later that jets do not only support QGP creation by their suppression, but also by the photons they produce when they scatter in the QGP.

1.4 Structure and Originality of the Thesis

The following work is divided into 6 chapters. It starts with chapter 2, which discuss the production of real photons at low to intermediate p_T ($p_T < 4$ GeV). Low p_T photons are emitted principally during the latter phase of the reaction, when the temperature is lower, while hotter phase of the reaction shift photons toward higher p_T. In this chapter, we are mostly concerned with hadron gas emission, improving previous analysis in several respects. $\pi\rho a_1$-meson gas rates are revisited and extended, including strangeness reactions. The physics involved in hadron interactions can not be complete without the inclusion of form-factors, which takes care of finite-size effects. Adjusting consistently the coupling constants and form-factors with measured values of meson masses and widths, we highlight for the first time the importance of t-channel exchange of the $\omega(782)$, which constitutes the major contribution in the hadronic sector for $p_T > 2$ GeV. Those new hadronic photon production rate calculations, done by myself, have been added to existing baryonic and QGP contributions, and evolved in space-time through a fireball model, by one of our collaborators, Ralf Rapp. Our results have been published in Physical Review C **69** 014903 (2004). Our results also appeared in the proceedings of the Montreal-Rochester-Syracuse-Toronto meeting (MRST04) : Int. J. Mod. Phys. A **19**, 5351 (2004).

In chapter 3, we present the formalism developed by Arnold, Moore and Yaffe (AMY) [31], which correctly treats the induced gluon bremsstrahlung, with the LPM effect (up to $O(g_s)$ corrections). Though this doesn't constitute my own work, this section is important since this model for the parton energy loss will be used in all following chapters. It also constitutes one of the first practical applications of this formalism.

In chapter 4, we confront for the first time, the AMY formalism to high-p_T suppression data, such as π^0 momentum distribution. In has been proposed in Ref. [32] that jets crossing the QGP can also produce photons by its Compton scattering or annihilation with a thermal parton from the medium. In this process, the photon takes all the momentum of the incoming jet, so that we can talk of a jet-photon conversion. We calculate for the first time the impact of the energy loss of jets, in the jet-photon production, and find that while the effect of energy loss is non-negligible, reducing the yield by a factor ~ 1.4, the jet-photon conversion is still the single most important source of photons around p_T=4 GeV at RHIC. To this, we add the photon bremsstrahlung induced by the jets in the medium, mechanism that was absent in Ref. [32], and all other major sources of photons, in order to have a complete picture of the total photon yield. This work has been published in Physical Review C **72** 014906 (2005).

Chapter 5 discuss the production of photons and pions in peripherical collisions. At non-zero impact parameter, the zone formed by the hot matter is asymmetric in the transverse plane of the collision. Since the strength of the suppression depends of the amount of matter crossed by the jet, the number of pions and photons produced will depends on their azimuthal angle. It is generally observe that high-p_T pions are produced in smaller quantities in the direction where the medium is thicker. One observable which describe this feature is $v2$, the second coefficient in the Fourier decomposition of particles angular distribution. For pions, $v2$ is observed to be positive. We have calculated for the first time, the coefficient $v2$ for high-p_T photons. We find that due to the dominant jet-photon conversion around p_T-4 GeV, photons produced in the direction where the medium is thicker are more important, i.e. $v2$ is negative. Those new results have been published in Physical Review Letter **96** 032303 (2006).

While the previous chapters were related to real photon production, chapter 6 calculates the high-p_T production of virtual photons, which produce leptons pairs (e^+e^- or $\mu^+\mu^-$). The leading order interaction of a jet with QGP ($q + \bar{q} \to \gamma^*$) is revisited, including this time the effect of jet energy-loss. Hard thermal loop (HTL) corrections are also included for the first time in dilepton production from incoming jets. We find that HTL corrections turn out to be even more important for incoming jet than usual incoming thermal parton. With this inclusion, the jet production of dileptons is as important as Drell-Yan at RHIC, for low value of invariant mass M. This work has been submitted to Physical Review C (hep-ph/0601042). Finally, chapter 7 contains the thesis summary and related discussion.

All chapters in this thesis include complicated multi-dimensional integrals, which we have carried out using computers. The convergence of all numerical calculations has been verified by varying the number of iterations and the number of calls to the integrated functions.

1.5 *Useful definitions*

Before studying photon production, it is important to define a quantity that is often used, the rapidity:

$$y = \frac{1}{2}\ln\left(\frac{E+p_z}{E-p_z}\right) = \frac{1}{2}\ln\left(\frac{1+v_z}{1-v_z}\right) . \tag{1.1}$$

With this definition, the particle energy E and its projection momentum p_z, along the beam direction, can be written as

$$E = \sqrt{p_T^2 + M^2}\cosh y\,, \quad p_z = \sqrt{p_T^2 + M^2}\sinh y\,. \tag{1.2}$$

where p_T is the transverse momentum, and M the particle mass. Under a boost β in the z-direction, the rapidity changes according to

$$y \to y' = \frac{1}{2}\ln\left(\frac{E - \beta p_z + p_z - \beta E}{E - \beta p_z - p_z + \beta E}\right) = y - \frac{1}{2}\ln\left(\frac{1+\beta}{1-\beta}\right) \tag{1.3}$$

This is why the rapidity is useful, since it follows an addition rule under a Lorentz transformation. Also, for a massless particle ($v = 1$), the speed projection is given by $v_z = \cos\theta$, where θ is the angle between $\vec{p}$ and the beam direction $\hat{z}$. It follows that

$$y \sim \frac{1}{2}\ln\left(\frac{1+\cos\theta}{1-\cos\theta}\right) = -\ln\left(\tan\frac{\theta}{2}\right)\,. \tag{1.4}$$

In the present study, photons and pions will be calculated at midrapidity, $y = 0$, which corresponds to particles emitted in the transverse direction ($\theta = \pi/2$). Finally, the particle production is often written with the differential element d^3p/E, where $d^3p = p_T dp_T d\phi dp_z$. We can write this differential element as a function of the rapidity:

$$dp_T d\phi dp_z = \mathcal{J}\, dp_T d\phi dy\,. \tag{1.5}$$

The Jacobian for the relation is simply

$$\mathcal{J} = \left|\frac{\partial p_z}{\partial y}\right| = \sqrt{p_T^2 + M^2}\cosh y = E\,. \tag{1.6}$$

This gives

$$\frac{d^3p}{E} = p_T dp_T d\phi dy = d^2p_T dy\,. \tag{1.7}$$

2

Production of low and intermediate p_T photons

In this chapter, we study the thermal emission of photons from hot and dense hadronic matter at temperatures close to the expected phase transition to the Quark-Gluon Plasma (QGP). Earlier calculations of photon radiation from ensembles of interacting mesons are re-examined with additional constraints, including new production channels as well as an assessment of hadronic form factor effects. Whereas strangeness-induced photon yields turn out to be moderate, the hitherto not considered t-channel exchange of ω-mesons is found to contribute appreciably for photon energies above $\sim$ 1.5 GeV. The role of baryonic effects is assessed using existing many-body calculations of lepton pair production. We argue that our combined results constitute a rather realistic emission rate, appropriate for applications in relativistic heavy-ion collisions. Supplemented with recent evaluations of QGP emission, and an estimate for primordial (hard) production, we compute p_T photon spectra at SPS energy.

2.1 Thermal photons emission

Within the thermal field theory framework, the differential photon emission rate from an equilibrated system can be written as [33]

$$p_0 \frac{dR}{d^3p} = \frac{\mathrm{Im}\Pi^R_{\mu\nu} g^{\mu\nu}}{(2\pi)^3(1 - e^{p_0/T})} \tag{2.1}$$

where $\mathrm{Im}\Pi^R_{\mu\nu}$ is the retarded photon self-energy at finite temperature. An equivalent formula exist for the production rate of dileptons through the production of a virtual photon:

$$E_+E_-\frac{dR^{e^+e^-}}{d^3p_+d^3p_-}=\frac{2e^2}{(2\pi)^6(p_++p_-)^4}(p_+^\mu p_-^\nu+p_-^\mu p_+^\nu-g^{\mu\nu}p_+\cdot p_-)\frac{\mathrm{Im}\Pi^R_{\mu\nu}}{e^{(p_++p_-)/T}-1} \tag{2.2}$$

$p=p_++p_-, p_0=\sqrt{|\overrightarrow{p}|^2+M^2}, M$ are respectively the dilepton momentum, energy and invariant mass. For real photon, we have simply $p_0=|\overrightarrow{p}|$. The derivation of Eq. 2.2 will be done in Chap. 6. In this formalism, in-medium effects and higher topologies are included in $\mathrm{Im}\Pi^R_{\mu\nu}$. It has been shown in Ref. [34] that taking the imaginary part of the photon self-energy corresponds to integrating the square of the scattering amplitudes $\mathcal{M}$ over the phase-space of the reaction. This is illustrated in Fig. 2.1, where the scattering $\pi+\rho\to\pi+\gamma$ can be extracted from cutting a two-loops photon self-energy with π and ρ mesons.

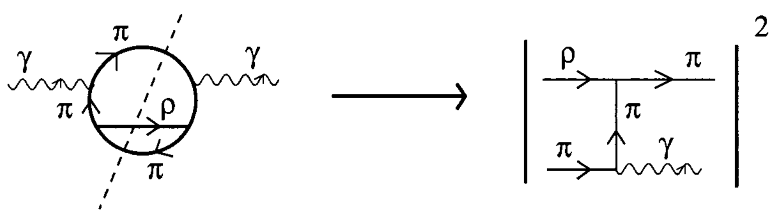

Figure 2.1: Picture of the $\pi+\rho\to\pi+\gamma$ coming from cutting a two-loops photon self-energy.

So, an alternative to using Eq. 2.1, one may use relativistic kinetic theory. For a given reaction $1+2\to3+\gamma$, the pertinent rate becomes (see appendix B)

$$\begin{aligned}p_0\frac{dR}{d^3p}=\int&\frac{d^3p_1}{2E_1(2\pi)^3}\frac{d^3p_2}{2E_2(2\pi)^3}\frac{d^3p_3}{2E_3(2\pi)^3}\frac{2\pi}{2}|\mathcal{M}|^2\\&\delta^4(p_1+p_2-p_3-p)f(E_1)f(E_2)(1\mp f(E_3))\end{aligned} \tag{2.3}$$

where the f's are the Fermi-Dirac (Bose-Einstein) distribution functions for fermions (bosons), and $1\mp f(E_3)$ is the suppression (enhancement) factor for the particle 3 in the final state. There is no such factor for the photon as we assume the hot matter's volume small enough so that electromagnetic radiations leave the medium without rescatterings. It also corresponds to assuming that the phase-space distribution of photons is low. Then $(1 + f(p_0)) = (1 + (2\pi)^3 dN^\gamma / d^3x d^3p) \sim 1$. After some time, the photons could come to equilibrium under the electromagnetic interactions with the plasma: then the photons yield should be given by a black body spectrum at temperature T. But the photon equilibration time is far much greater than the QGP and the hadron gas phase together. The evaluation of the equilibration time and mean free path of photons can be found in appendix A.

As the scattering amplitude is usually expressed in term of the Mandelstam variables s, t, u, it is natural to integrate over those variables. After some algebric manipulations, the photon production rate can be written as

$$p_0 \frac{dR}{d^3p} = \frac{1}{16(2\pi)^7 p_0} \int_{s^{min}}^{\infty} ds \int_{t^{min}}^{t^{max}} dt \int_{E_1^{min}}^{\infty} dE_1 \int_{E_2^{min}}^{E_2^{max}} dE_2 \; |\mathcal{M}|^2$$
$$f(E_1) f(E_2)(1 \mp f(E_1 + E_2 - p_0)) \frac{1}{\sqrt{aE_2^2 + 2bE_2 + c}} \tag{2.4}$$

The derivation of this equation, with the coefficients a, b, c, can be found in appendix B.

In quantum field theory, the scattering amplitude is obtained by evolving an initial state $|p_1, p_2\rangle$ up to a final state $|p_3, p\rangle$, through the time ordered operator T [8]:

$$i\mathcal{M}(2\pi)^2 \delta^4(p_1 + p_2 - p_3 - p) = \lim_{T \to \infty} \left({}_0\langle p_3, p | T(exp[i \int_{-T}^{T} dt\, \mathcal{L}_{int}]) | p_1, p_2 \rangle_0 \right) \tag{2.5}$$

where all diagrams retained have to be connected and amputated. The external states in 2.5 are eigenstates of the Hamiltonian in unperturbed theory. This is however more difficult to justify for finite temperature interacting systems, since there is no properly defined asymptotic states. The term inside the exponential, is the interacting part of the Lagrangian : this is the function from which all scatterings will be derived.

2.2 Mesonic contribution

2.2.1 Effective Chiral Lagrangians

In this section, we consider $1 + 2 \to 3 + \gamma$ scattering with mesons in the initial and final state, using the relativistic kinetic theory framework (Eq. 2.4). We don't include $1+2 \to 3+4+\gamma$ processes as the phase-space for the emitted photon is considerably reduced. Such processes usually contribute only in the limit $p_0 \to 0$ [35]. Reactions like $1 + 2 + 3 \to 4 + \gamma$ are also disfavoured because the particles density is not high enough to allow in large quantity, reactions with more that two particles in the initial state.

The interaction of mesons is not perturbative in a QCD context, such that $\mathcal{M}$ cannot be obtained from a finite number of Feynman diagrams involving quarks and gluons. Effective theory is rather used, with mesons as degrees of freedom. It is essential that such a theory respects the symmetries of QCD. The Chiral Symmetry (see Ref. [36] for a review) is perfectly respected in QCD with massless quarks. We know however that quarks are not massless (light quarks are about 5-10 MeV), but since the relevant energy scale is given by $\Lambda_{QCD} \sim 200$ MeV, we expect the chiral currents to be approximately conserved.

At low temperature, hadronic matter can be approximated by a pion gas and its chiral partner, the σ meson. The potential, which generates the vacuum expectation value $< \sigma >_0$ of the σ field , has to be chirally invariant. The simplest choice is $V \propto (\pi^2 + \sigma^2 - f_\pi^2)^2$, where $f_\pi =< \sigma >_0$.

In the non-linear sigma model (NLSM), the σ degree of freedom is eliminated by sending its mass to infinity. This confines the dynamics to the chiral circle, defined by the minimum of the potential : $\pi^2 + \sigma^2 = f_\pi^2$. The usual parametrization is given by

$$U_2 = e^{i\frac{\vec{\tau}\cdot\vec{\pi}}{f_\pi}} \tag{2.6}$$

with τ_i being the Pauli matrices, such that

$$\frac{1}{2}tr[U_2^\dagger U_2] = \frac{1}{f_\pi^2}(\pi^2 + \sigma^2) \tag{2.7}$$

The kinetic term for the pseudoscalar mesons is given by

$$\frac{1}{2}\partial_\mu\sigma\partial^\mu\sigma + \frac{1}{2}\partial_\mu\overrightarrow{\pi}\partial^\mu\overrightarrow{\pi} = \frac{f_\pi^2}{4}tr[\partial_\mu U_2^\dagger\partial^\mu U_2] \tag{2.8}$$

At this point, we have a chirally global $SU(2)_L \times SU(2)_R$ symmetry. This can be generalized to higher flavor number N_f, such that for $SU(3)_L \times SU(3)_R$, we have

$$U_3 = U = \exp\left[\frac{2i}{F_\pi}\sum_a \frac{\lambda_a\psi_a}{\sqrt{2}}\right] = \exp\left[\frac{2i}{F_\pi}\psi\right] \tag{2.9}$$

with $F_\pi = \sqrt{2}f_\pi$, and λ_a are the Gell-Mann matrices. ψ is the pseudoscalar octet:

$$\psi = \begin{pmatrix} \frac{\pi^0}{\sqrt{2}} + \frac{\eta_8}{\sqrt{6}} & \pi^+ & K^+ \\ \pi^- & -\frac{\pi^0}{\sqrt{2}} + \frac{\eta_8}{\sqrt{6}} & K^0 \\ K^- & \bar{K}^0 & -\frac{2\eta_8}{\sqrt{6}} \end{pmatrix} \tag{2.10}$$

To describe photon production in a gas consisting of light pseudo-scalar, vector and axial vector mesons (π, K, ρ, K^*, a_1) we employ the massive Yang-Mills (MYM) approach [37], which is capable of yielding adequate hadronic phenomenology at tree level with a rather limited set of adjustable parameters. Vector and axial vector fields are implemented as massive gauge fields into the covariant derivative:

$$\begin{aligned} \partial_\mu U \to D_\mu U &= \partial_\mu U - ig_0 A_\mu^L U + ig_0 U A_\mu^R \\ A_\mu^L &= 1/2(V_\mu + A_\mu) \\ A_\mu^R &= 1/2(V_\mu - A_\mu) \end{aligned} \tag{2.11}$$

where $V_\mu = \frac{1}{\sqrt{2}}\lambda^a V_\mu^a$ and $A_\mu = \frac{1}{\sqrt{2}}\lambda^a A_\mu^a$ are the vector and axial vector meson matrices respectively. Under global $SU(3)_L \times SU(3)_R$ transformation, U and $A_\mu^{L(R)}$ transform like

$$U \to L\,U\,R^\dagger\,, \quad A_\mu^L \to L\,A_\mu^L\,L^\dagger\,, \quad A_\mu^R \to R\,A_\mu^R\,R^\dagger \tag{2.12}$$

with $L^\dagger L = 1$ and $R^\dagger R = 1$. The complete chiral Lagrangian can be written as [37, 38]:

$$\begin{aligned}\mathcal{L} = &\tfrac{1}{8}F_\pi^2 \mathrm{Tr} D_\mu U D^\mu U^\dagger + \tfrac{1}{8}F_\pi^2 \mathrm{Tr} M(U + U^\dagger - 2) \\ &-\tfrac{1}{2}\mathrm{Tr}\left(F_{\mu\nu}^L F^{L\mu\nu} + F_{\mu\nu}^R F^{R\mu\nu}\right) + m_0^2 \mathrm{Tr}\left(A_\mu^L A^{L\mu} + A_\mu^R A^{R\mu}\right) + \gamma \mathrm{Tr} F_{\mu\nu}^L U F^{R\mu\nu} U^\dagger \\ &-i\xi \mathrm{Tr}\left(D_\mu U D_\nu U^\dagger F^{L\mu\nu} + D_\mu U^\dagger D_\nu U F^{R\mu\nu}\right) \ . \end{aligned} \tag{2.13}$$

In the above,

$$\begin{aligned} F_{\mu\nu}^{L,R} &= \partial_\mu A_\nu^{L,R} - \partial_\nu A_\mu^{L,R} - ig_0\left[A_\mu^{L,R}, A_\nu^{L,R}\right] \ , \\ M &= \frac{2}{3}\left[m_K^2 + \frac{1}{2}m_\pi^2\right] - \frac{2}{\sqrt{3}}(m_K^2 - m_\pi^2)\lambda_8 \ . \end{aligned} \tag{2.14}$$

In Eq. 2.13, the second term is introduced to explicitly break chiral symmetry by giving mass to pseudoscalar mesons. The third and fourth terms represent respectively the kinetic and mass terms of the massive gauge fields. Finally, the last two terms are added for phenomenological considerations. It can be verified that each term in Eq. 2.13, except the second one , are invariant under the chiral transformations 2.12.

Electromagnetism is introduced through a $U(1)$ transformation [38, 39]

$$\begin{aligned} \delta U &= i\epsilon[Q, U] \\ \delta A_\mu^{L(R)} &= i\epsilon[Q, A_\mu^{L(R)}] + \frac{1}{g_0}Q\partial_\mu\epsilon \end{aligned} \tag{2.15}$$

where $Q = \lambda_3/2 + \lambda_8/\sqrt{12}$=diag$(\frac{2}{3}, -\frac{1}{3}, -\frac{1}{3})$ is the quark charge matrix. When we apply this transformation on $\mathcal{L}$, they are all invariant except the mass term of the left- and right- handed vector fields, such that

$$\delta\mathcal{L} = m_0^2 \mathrm{Tr}[Q(A_\mu^L + A_\mu^R)]\frac{2}{g_0}\partial_\mu\epsilon\,. \tag{2.16}$$

We then add three additional terms

$$\mathcal{L}_1 + \mathcal{L}_2 + \mathcal{L}_3 = \frac{-2em_0^2}{g_0}\mathrm{Tr}[Q(A_\mu^L + A_\mu^R)] - \frac{1}{4}(\partial_\mu B^\nu - \partial_\nu B^\mu)^2 + \frac{2e^2 m_0^2}{g_0^2}B_\mu B^\mu \mathrm{Tr}[Q^2] \tag{2.17}$$

where e is the electric charge. The electromagnetic field B_μ transform under $U(1)$ like

$$\delta B_\mu = \frac{1}{e}\partial_\mu\epsilon \tag{2.18}$$

making the total Lagrangian $\mathcal{L} + \mathcal{L}_1 + \mathcal{L}_2 + \mathcal{L}_3$ invariant under $U(1)$. This imply that the electric charge and current density have to be conserved. But the final shape of the Lagrangian is not yet fixed. Indeed, when we expand $\mathcal{L}$ in terms of pseudoscalar, vector and axial vector fields, we find a mixing term $\sim \partial_\mu \psi A^\mu$ coming from $\mathrm{Tr} D_\mu U D^\mu U^\dagger$. We can get rid of this term with the redefinitions:

$$\begin{aligned}
V_\mu &\to \frac{\tilde{V}_\mu}{\sqrt{1-\gamma}} \\
A_\mu &\to \frac{\tilde{A}_\mu}{\sqrt{1+\gamma}} + \frac{g_0 \tilde{F}_\pi}{2m_0^2}\left[\partial_\mu \tilde{\psi} - \frac{i\tilde{g}}{2}[\tilde{V}_\mu, \tilde{\psi}]\right] \\
\psi &\to \frac{\tilde{\psi}}{Z} \\
\tilde{g} &= \frac{g_0}{\sqrt{1-\gamma}} \\
Z &= \sqrt{1 - \frac{\tilde{g}^2 \tilde{F}_\pi^2}{4m_V^2}}, \quad \tilde{F}_\pi = \frac{F_\pi}{Z} = 135\mathrm{MeV} \\
m_V &= \frac{m_0}{\sqrt{1-\gamma}}, \quad m_A = \frac{m_0}{Z\sqrt{1+\gamma}}
\end{aligned} \tag{2.19}$$

$\tilde{\psi}$,$\tilde{V}_\mu$ and $\tilde{A}_\mu$ are the physical fields, while m_V and m_A are the physical vector and axial vector mass. With this diagonalization, the new term $\mathcal{L}_1$ becomes

$$\mathcal{L}_1 = \frac{-2e\, m_V^2}{\tilde{g}} B_\mu \mathrm{Tr}[Q\, \tilde{V}^\mu] = \frac{-2e\, m_V^2}{\tilde{g}} B_\mu \left[\frac{\rho_0}{\sqrt{2}} + \frac{\omega_8}{\sqrt{6}}\right] \tag{2.20}$$

In the ideal mixing [40], we have $\omega_8 = \frac{\sqrt{2}\omega + \phi}{\sqrt{3}}$, and the electromagnetic Lagrangian

$$\begin{aligned}
\mathcal{L}_{EM} = \mathcal{L}_1 &= \frac{-\sqrt{2}\, e}{\tilde{g}} B_\mu \left[m_\rho^2 \rho_0^\mu + \frac{m_\omega^2}{3}\omega^\mu - \frac{\sqrt{2} m_\phi^2}{3}\phi^\mu\right] \\
&= -B_\mu \left[C_\rho\, m_\rho^2 \rho_0^\mu + C_\omega\, m_\omega^2 \omega^\mu + C_\phi\, m_\phi^2 \phi^\mu\right]
\end{aligned} \tag{2.21}$$

has the same form that the Vector Meson Dominance (VMD) model [41]. In principle, the C's coefficients are determined from $e\sqrt{2}/\tilde{g}$, but we can rather take advantage of available experimental data to fix them and constrain the theory. As we will show latter in this chapter, C_ω and C_ϕ are much smaller than C_ρ, so that for our study, we consider only the $\rho - \gamma$ coupling. Coming back to Eq. 2.17, $\mathcal{L}_2$ is the usual kinetic term for photons and $\mathcal{L}_3$ prevents the photons from getting a mass [41]. Indeed, from the terms $\mathcal{L}_{EM}$, $\mathcal{L}_2$ and $\mathcal{L}_3$, the propagator for a photon of momentum p is:

$$D(p) = \frac{1}{p^2 - \frac{C_\rho^2 m_\rho^2 p^2}{p^2 - m_\rho^2}} \sim \frac{1}{p^2(1+C_\rho^2)} \sim \frac{1-C_\rho^2}{p^2} \tag{2.22}$$

for $p^2, C_\rho \to 0$. This leads to a charge renormalization $\tilde{e}^2 = e^2(1-C_\rho^2)$. At this point, we have all the ingredients to find the parts of the Lagrangian responsible for the $1+2 \to 3+\gamma$ scatterings. By expanding $\mathcal{L}$, we can find the cubic and quartic interacting terms:

$$\begin{aligned}
\mathcal{L}_{VA\psi} &= \frac{i\eta_2\tilde{g}}{2}\mathrm{Tr}\left[(\partial_\mu\tilde{A}_\nu - \partial_\nu\tilde{A}_\mu)[\partial^\mu\tilde{V}^\nu, \tilde{\psi}]\right] + \frac{i\eta_1\tilde{g}}{2}\mathrm{Tr}\left[(\partial_\mu\tilde{V}_\nu - \partial_\nu\tilde{V}_\mu)[\tilde{A}^\mu, \partial^\nu\tilde{\psi}]\right] ; \\
\mathcal{L}_{V\psi\psi} &= \frac{i\tilde{g}}{2}\mathrm{Tr}\left[\tilde{V}_\mu[\partial^\mu\tilde{\psi}, \tilde{\psi}]\right] + \frac{i\tilde{g}\delta}{2m_V^2}\mathrm{Tr}\left[(\partial_\mu\tilde{V}_\nu - \partial_\nu\tilde{V}_\mu)\partial^\mu\tilde{\psi}\partial^\nu\tilde{\psi}\right] ; \\
\mathcal{L}_{VVV} &= \frac{i\tilde{g}}{2}\mathrm{Tr}\left[(\partial_\mu\tilde{V}_\nu - \partial_\nu\tilde{V}_\mu)\tilde{V}^\mu\tilde{V}^\nu\right] ; \\
\mathcal{L}_{VV\psi\psi} &= -\frac{\tilde{g}^2}{8}\mathrm{Tr}\left[[\tilde{V}_\mu, \tilde{\psi}]^2\right] + \frac{\tilde{g}^2\delta}{4m_V^2}\mathrm{Tr}\left[[\tilde{V}_\mu, \tilde{V}_\nu]\partial^\mu\tilde{\psi}\partial^\nu\tilde{\psi}\right] \\
&\quad + \frac{\tilde{g}^2\delta}{4m_V^2}\mathrm{Tr}\left[(\partial_\mu\tilde{V}_\nu - \partial_\nu\tilde{V}_\mu)\left([\tilde{V}^\mu, \tilde{\psi}]\partial^\nu\tilde{\psi} + \partial^\mu\tilde{\psi}[\tilde{V}^\nu, \tilde{\psi}]\right)\right] \\
&\quad + \frac{\tilde{g}^2 C_4}{2}\mathrm{Tr}\left[(\partial_\mu\tilde{V}_\nu - \partial_\nu\tilde{V}_\mu)\tilde{\psi}(\partial^\mu\tilde{V}^\nu - \partial^\nu\tilde{V}^\mu)\tilde{\psi} - (\partial_\mu\tilde{V}_\nu - \partial_\nu\tilde{V}_\mu)^2\tilde{\psi}^2\right] ,
\end{aligned} \tag{2.23}$$

where

$$\begin{aligned}
\eta_1 &= \frac{\tilde{g}\tilde{F}_\pi}{2m_V^2}\sqrt{\frac{1-\gamma}{1+\gamma}} + \frac{4\xi Z^2}{\tilde{F}_\pi\sqrt{1+\gamma}} , \\
\eta_2 &= \frac{\tilde{g}\tilde{F}_\pi}{2m_V^2}\sqrt{\frac{1+\gamma}{1-\gamma}} - \frac{4\gamma}{\tilde{F}_\pi\tilde{g}\sqrt{1-\gamma^2}} , \\
\delta &= 1 - Z^2 - \frac{2Z^4\xi\tilde{g}}{(1-Z^2)\sqrt{1-\gamma}} , \\
C_4 &= \frac{\tilde{g}^2\tilde{F}_\pi^2}{16m_V^4}\left(\frac{1+\gamma}{1-\gamma}\right) - \frac{\gamma}{m_V^2(1-\gamma)} + \frac{2\gamma}{\tilde{g}^2\tilde{F}_\pi^2(1-\gamma)} .
\end{aligned} \tag{2.24}$$

The Lagrangians described above contain only processes involving conservation of intrinsic parity [42, 43]. For example, only reactions with $(-1)^{N_i^\psi} = (-1)^{N_f^\psi}$, are included, where N_i^ψ and N_f^ψ are the number of pseudoscalar mesons in the initial and final state respectively. Anomalous reactions can by included via Wess-Zumino terms [42]. For our purpose, we need only terms connecting two vector mesons and one pseudoscalar meson :

$$\mathcal{L}_{VV\psi} = g_{VV\psi}\epsilon_{\mu\nu\alpha\beta}\mathrm{Tr}[\partial^\mu V^\nu \partial^\alpha V^\beta \psi]\,, \tag{2.25}$$

where $\epsilon_{\mu\nu\alpha\beta}$ is the Levi-Civita tensor.

2.2.2 *Symmetries and conservation laws*

The construction of Feynman diagrams, describing the different processes producing photons, is now possible. Eq. 2.5 is thus needed as well as the Lagrangians we have seen. However, each process must fulfil certain symmetries and conservation laws: conservation of electromagnetic current, G-parity, conservation of isospin and strangeness.

Electromagnetic current conservation

By definition, the interacting term of a photon with surrounding matter is writing by [8, 41]

$$\mathcal{L}_\gamma = B_\mu j^\mu_{EM} \tag{2.26}$$

where j_{EM} is the electromagnetic current density. The scattering amplitude for a process $i \to f + \gamma$ is:

$$\mathcal{M}^\mu = \langle f|j^\mu_{EM}(p)|i\rangle \tag{2.27}$$

for any initial and final states i and f. After contracting with the external photon of momentum p, we get

$$p_\mu\mathcal{M}^\mu = p_\mu\langle f|j^\mu_{EM}(p)|i\rangle = \langle f|p_\mu j^\mu_{EM}(p)|i\rangle = i\int d^4x e^{ip\cdot x}\langle f|\partial_\mu j^\mu_{EM}(x)|i\rangle = 0 \tag{2.28}$$

for conserved current ($\partial_\mu j^\mu_{EM} = 0$). The relation $p_\mu\mathcal{M}^\mu = 0$ is also known as Ward identity. The conservation of the electromagnetic current also implies the conservation of charge at each vertex. Examples of Ward identity verifications can be seen in appendix C.

G-parity

The quantum number G is defined for hadrons made of up and down quarks only. Its quantum operator is given by [44]

$$G = C \cdot e^{i\pi I_2} \tag{2.29}$$

where C is the electric charge conjugation operator, changing up to a phase factor, a particle to its antiparticle state. I_2 is the second component of the isospin operator $\overrightarrow{I}$, and π is the angle by which we rotate the state. Since the strong interaction is assumed to be isospin and C invariant, it means that the G quantum number is conserved for strong interactions. The importance of G lies in its commutativity with $\overrightarrow{I}$, $[G, \overrightarrow{I}] = 0$, because it has for consequence that all members of an isospin multiplet have the same G-quantum number. For instance, the G-parities of the π, ρ, ω and a_1 mesons are respectively $-1, +1, -1$ and -1. That means for example, that the process $a_1 \to \rho + \pi$ is allowed because $G_{in} = G_{a_1} = G_{out} = G_\rho \times G_\pi = -1$.

Isospin and strangeness conservation

The π, ρ, ω and a_1 mesons all have three charges state of approximately the same mass. Then they all have isospin $I = 1$, with the positive, negative and neutral charge states associated to $I_3 = 1, -1, 0$ respectively. The ω meson has only a neutral charge state, so that $I = 0$. Since the strong interaction is isospin invariant, isospin must be conserved at each vertex involving mesons. Usually, taking care of charge conservation already involve isospin conservation. However, there is a particular case where charge can be conserved but not the isospin : $a_1^0 \to \rho^0 + \pi^0$. All the mesons here have $I = 1$ and $I_3 = 0$. While the charge is conserved, the Clebsh-Gordan coefficient $(I_3^\rho\, I_3^\pi | I_3^{a_1}\, I^{a_1})_{1\times 1}$ for this process is zero.

Strangeness is another conserved quantum number during strong interactions. The K^+, K^0, K^{*+}, K^{*0} mesons have $S = 1$ while the $K^-, \bar{K}^0, \bar{K}^{*0}, K^{*-}$ mesons have $S = -1$. All mesons made of up and down quarks have $S = 0$. Strangeness is an additive quantum number.

2.2.3 *Adjustment of coupling constants and hadronic form factor*

The chiral Lagrangian model that we have shown contains six unknown parameters: m_0, ξ, γ, $\tilde{g}$, C_ρ and $g_{VV\psi}$. The constants C_ρ can immediately be fixed with the electromagnetic decay of the ρ: $\rho \to \gamma$ followed by $\gamma \to e^+e^-$, where the Quantum Electrodynamic (QED) Lagrangian will be used for the latter transition. The theoretical definition of the width for a decay process $1 \to 2+3+...+f$, in the frame of particle 1, is [8]

$$\Gamma_{1\to 2+3+...+f} = \frac{1}{2m_1}\int \frac{d^3p_2}{2E_2(2\pi)^3}\frac{d^3p_3}{2E_3(2\pi)^3}\cdots\frac{d^3p_f}{2E_f(2\pi)^3}(2\pi)^4 \left|\bar{\mathcal{M}}\right|^2_{1\to 2+3+...+f}\delta^4(p_1-p_2-p_3-...p_f) \tag{2.30}$$

For the $\rho \to e^+e^-$ transition, this gives

$$\Gamma_{\rho\to e^+e^-} = \frac{\alpha\, C_\rho^2\, m_\rho}{3}\,. \tag{2.31}$$

From the experimental value for the decay width, $\Gamma_{\rho\to e^+e^-} = 6.85 \pm 0.11$ keV, we get $C_\rho = 0.059$. With the experimental values $\Gamma_{\omega\to e^+e^-} = 0.6 \pm 0.02$ keV and $\Gamma_{\phi\to e^+e^-} = 1.2 \pm 0.1$ keV, it implies that C_ω^2 and C_ϕ^2 are respectively smaller than C_ρ^2 by a factor ~ 11 and ~ 7, and this is why we keep only the $\rho - \gamma$ coupling in Eq 2.21. The parameters m_0, ξ, γ, $\tilde{g}$ can be adjusted from the masses and widths of the $\rho\,(m_\rho, \Gamma_{\rho\to\pi\pi})$ and $a_1(m_{a_1}, \Gamma_{a_1\to\pi\rho})$, allowing for two possible solutions:

$$\begin{aligned}(\mathrm{I}):&\quad \tilde{g} = 10.3063,\ \gamma = 0.3405,\ \xi = 0.4473,\ m_0 = 0.6253\ \mathrm{GeV}\ ;\\ (\mathrm{II}):&\quad \tilde{g} = 6.4483,\ \gamma = -0.2913,\ \xi = 0.0585,\ m_0 = 0.875\ \mathrm{GeV}\ .\end{aligned} \tag{2.32}$$

In the absence of additional empirical constraints, the use of one set over another is difficult to justify. However, in Ref. [45] it has been suggested to invoke the experimental determination of D- to S-wave content in the final state of the $a_1 \to \rho\pi$ decay.

D-to S-wave content

The decay width for the transition $a_1 \to \pi\rho$ is related to

$$\Gamma \propto \sum_{m_s^a, m_s^\rho} \int d\Omega \left|\mathcal{M}_{m_s^a, m_s^\rho}\right|^2 \propto \sum_{m_s^a} \left|\left\langle \phi_{\rho\pi} | e^{-iHt} | \phi_{a_1} \right\rangle\right|^2 \tag{2.33}$$

where m_s's are the spin projections in the third axis, H is the Hamiltonian and $d\Omega = d\sin\theta\, d\phi$. The wave functions for a_1 in the initial state and $\rho\pi$ in the final state are

$$\begin{aligned} |\phi_{a_1}\rangle &= |J=1, m_s^a, S=1, l=0\rangle \;, \\ |\phi_{\rho\pi}\rangle &= \alpha \Big[f_S \, |J=1, m_s^a, S=1, l=0\rangle + f_D \, |J=1, m_s^a, S=1, l=2\rangle \Big] \;, \end{aligned} \tag{2.34}$$

with l the orbital angular momentum which has to be even from parity conservation, and α some common factor. This gives

$$\sum_{m_s^a} \left|\left\langle \phi_{\rho\pi} | e^{-iHt} | \phi_{a_1} \right\rangle\right|^2 = \sum_{m_s^a, m_s^\rho} \int d\Omega \left| i\, f_S\, \delta_{m_s^a}^{m_s^\rho}\, Y_0^0(\Omega) + i\, f_D \sum_{m_l} (1, 2, m_s^\rho, m_l | 1, m_s^a) Y_{m_l}^2(\Omega) \right|^2 \tag{2.35}$$

where Y are spherical harmonics. In the a_1 center of mass, we fixe the ρ momentum along the z axis, giving $\theta = 0$, so that $Y_{m_l}^2(\theta = 0) = 0$ unless $m_l = 0$. We thus have:

$$\mathcal{M}_{m_s^a, m_s^\rho}^{m_l=0} = i\, \frac{f_S}{\sqrt{4\pi}} \delta_{m_s^a}^{m_s^\rho} + i\, f_D \sqrt{\frac{5}{4\pi}} (1, 2, m_s^\rho, 0 | 1, m_s^a) \delta_{m_s^a}^{m_s^\rho} \,. \tag{2.36}$$

The more general shape the vertex for the $a_1^\mu(q) \to \rho^\nu(p) + \pi(r)$ decay can have is

$$V_{\mu\nu} = -i\, W\, g_{\mu\nu} - i\, X\, p_\mu q_\nu \tag{2.37}$$

where W and X are functions of p and q. Then the decay amplitude can also be expressed as

$$\begin{aligned} \mathcal{M}_{m_s^a, m_s^\rho}^{m_l=0} &= -i\, W \epsilon_{m_s^a} \cdot \epsilon_{m_s^\rho} - i\, X\, p \cdot \epsilon_{m_s^a}\, q \cdot \epsilon_{m_s^\rho} \\ &= -i\, \delta_{m_s^a}^{m_s^\rho} \left[W \left(-\frac{E_\rho}{m_\rho} \delta_{m_s^a}^0 - \delta_{m_s^a}^1 - \delta_{m_s^a}^{-1} \right) - X \frac{m_{a_1}}{m_\rho} |\overrightarrow{p}|^2 \delta_{m_s^a}^0 \right] \,. \end{aligned} \tag{2.38}$$

ϵ represents the polarization vector for an external particles. Comparing Eqs. 2.36 and 2.38, we find that

$$\frac{D}{S} = \frac{f_D}{f_S} = \sqrt{2}\frac{(W(m_\rho - E_\rho) - X\, m_{a_1}|\vec{p}|^2)}{(W(2m_\rho + E_\rho) + X\, m_{a_1}|\vec{p}|^2)}\,. \tag{2.39}$$

For the two parameter sets given above, Eq. 2.32, one finds

$$\text{(I)} : D/S = 0.36\,, \quad \text{(II)} : D/S = -0.099\,. \tag{2.40}$$

The result with set II agrees well with the experimental value $-0.107\pm$ 0.016 [46]. Finally, the last coupling constant, $g_{VV\psi}$ can be fixed by the decay $\omega \to \pi + \gamma$. In our model, this process goes via the $\omega\rho\pi$ vertex, and the ρ^0 couples to the photon via 2.21. As the ρ here is off-shell, by convention, a form-factor should be introduced.

Form-factors

Form-factors (FF) are introduced to reflect the finite-extent of the fields that appear in the effective vertex. The FF is obtained by the Fourier-transform of the distribution of charges inside hadrons

$$\hat{F}(q) = \int d^3x\, e^{-i\mathbf{q}\cdot\mathbf{x}}\rho(x)\,. \tag{2.41}$$

If the charge distribution was narrow, $\rho(x) = \delta^3(\mathbf{x})$, we would get $\hat{F}(q) = 1$. However, since hadrons are made of quarks, their finite extension may be probed when the exchanged momentum is large. Form-factors are usually parameterized as $\hat{F}(q) = \hat{F}(0)/(1 - q^2/\Lambda^2)^n$ in the spacelike region ($q^2 < 0$), where the powers $n = 1, 2$ correspond to monopole and dipole respectively, and Λ is the pole mass, which is in the order of the heavier hadrons ($\Lambda \sim 1-2$ GeV). Since hadron interactions depend on $\hat{F}$, their dynamics are sensitive to the q^2 behaviour of $\hat{F}$. In principle, the strong interaction of the constituents quarks and gluons should fix this q^2 dependence. However, in the low-energy QCD regime, a nonperturbative treatment of QCD is necessary, and such method like QCD sum rules or lattice gauge theory are at present still inconclusive.

Here, we assume a dipole parametrization for the FF, in order to be consistent with the dilepton yield calculations using the in-medium $\rho(770)$ spectral function [47, 48], discussed latter in Sec. 2.3. In the timelike region, for a process $R \to X+Y$, we have

$$\hat{F} = \left(\frac{2\Lambda^2 + m_R^2}{2\Lambda^2 + \left(\sqrt{m_X^2 + q_{CM}^2} + \sqrt{m_Y^2 + q_{CM}^2}\right)^2} \right)^2 \tag{2.42}$$

where q_{CM} is the particle momentum in the center of mass of R. $\hat{F}$ is normalized to 1 when the particles go on-shell, and $\Lambda = 1$ GeV. This FF has been used in Ref. [48] to successfully describe the decay of many ρ induced mesonic resonances R with masses $m_R \leq 1300$ MeV. The form-factor is introduced in an effective vertex V_{eff} simply by:

$$V_{eff}(q) = V(q) \times \hat{F}(q)\,, \tag{2.43}$$

where $V(q)$ is the bare vertex. The width for the $\omega \to \pi\gamma$ decay is then

$$\Gamma_{\omega\to\pi\gamma} = \frac{|\bar{\mathcal{M}}|^2 q_{CM} \hat{F}^2}{8\pi m_\omega^2}\,. \tag{2.44}$$

The experimental value for the width is 0.7174 MeV, giving $g_{\omega\pi\rho} = \sqrt{2} g_{VV\psi} = 22.6$ GeV^{-1}. If one rather set $\hat{F} = 1$, we would get $g_{\omega\pi\rho} = 11.93$ GeV^{-1}. The a_1 radiative decay $\Gamma_{a_1\to\pi+\gamma}$ contains also an off-shell strong vertex. Using $\hat{F}$, we get

$$(\mathrm{I}) : \Gamma_{a_1\to\pi+\gamma} = 2.2 \text{ MeV}\,, \quad (\mathrm{II}) : \Gamma_{a_1\to\pi+\gamma} = 0.033 \text{ MeV}\,. \tag{2.45}$$

Neither set I nor set II reproduce the experimental value 0.64± 0.246 MeV. For the sake of quantitative analyse, another set is defined as

$$(\mathrm{III}) : \quad \tilde{g} = 5.834,\ \gamma = -0.464,\ \xi = 0.1157,\ m_0 = 0.847 \text{ GeV}\,, \tag{2.46}$$

leading to

$$m_{a_1} = 1.4 \text{ GeV},\ m_\rho = 0.7 \text{ GeV},\ \Gamma_\rho = 0.17 \text{ GeV} \tag{2.47}$$

$$\Gamma_{a_1} = 0.3 \text{ GeV},\ D/S = -0.49,\ \Gamma_{a_1\to\pi+\gamma} = 0.44 \text{ MeV} \tag{2.48}$$

All features of the three sets are summarized in table 2.1

Observables	set I	set II	set III	exp. values
m_ρ	0.77 GeV	0.77 GeV	0.7 GeV	0.7758± 0.0005 GeV
m_{a_1}	1.26 GeV	1.26 GeV	1.4 GeV	1.23± 0.04 GeV
$\Gamma_{\rho\to\pi\pi}$	150.7 MeV	150.7 MeV	170 MeV	150.3± 1.6 MeV
$\Gamma_{a_1\to\pi\rho}$	400 MeV	400 MeV	300 MeV	400±175 MeV
$\Gamma_{a_1\to\pi\gamma}$	2.2 MeV	0.033 MeV	0.44 MeV	0.64± 0.25 MeV
D/S	0.36	-0.099	-0.49	-0.107± 0.016

Table 2.1: Fixing parameters and predictions for three sets of parameters.

To be consistent with this procedure, all our processes in the mesonic sector should now include form-factors. It's important to include FF in a way which doesn't violate the Ward identity. For this reason, and because photon produced in the range $p_0 > 1.5$ GeV are dominated by t-channel exchange, we will assume the same dipole form for each hadronic vertex appearing in the amplitudes. Thus, for a t-channel exchange (spacelike region), we take the FF to be

$$F = \left(\frac{2\Lambda^2}{2\Lambda^2 - t}\right)^2 \tag{2.49}$$

where in the limit of low exchange momentum, the finite extension of the hadrons cannot be probed, and $F \to 1$. We then approximate the four-momentum transfer in a given t-channel exchange of meson X by its average $\bar{t}$ according to

$$\left(\frac{1}{m_X^2 - \bar{t}}\right)^2 \left(\frac{2\Lambda^2}{2\Lambda^2 - \bar{t}}\right)^8 = \frac{1}{4p_0^2}\int_0^{4p_0^2} \frac{dt(2\Lambda^2)^8}{(m_X^2 - t)^2(2\Lambda^2 - t)^8} \,. \tag{2.50}$$

The averaging procedure allows to factorize form factors and amplitudes which much facilitates the task of rendering the final expression gauge-invariant, since we can then simply multiply the rate parametrizations with $F(\bar{t})^4$. We get the 4^{th}-power because in a $2 \to 2$ scattering amplitudes, there is two vertices, so that each vertex bring a FF, and since the production is related to the square the scattering amplitudes, the production rate including vertex will be given

$$p_0 \frac{dR_{with\,FF}}{d^3p} = p_0 \frac{dR_{no\,FF}}{d^3p} \times F(\bar{t})^4 \tag{2.51}$$

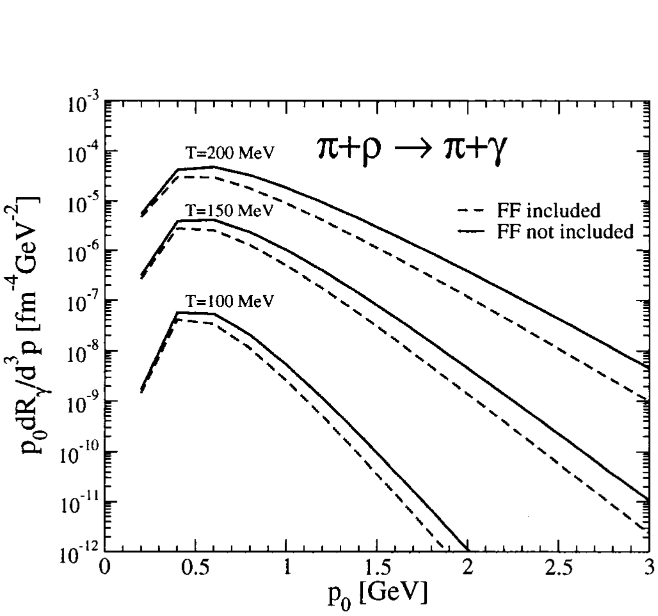

Figure 2.2: The effect of hadronic form factors on a typical photon-producing reaction in a nonstrange meson gas, $\pi\rho \rightarrow_{a_1\pi\rho} \rightarrow \pi\gamma$ (set II), for 3 different temperatures. Solid and dashed lines are without and with the inclusion of $F(\bar{t}_\pi)^4$, respectively.

The range of the strong interaction between mesons is determined by the lightest exchanged particle X. Eq. 2.50 is solved numerically; for $X = \pi, \omega, K$, we get respectively

$$\begin{aligned}
\bar{t}_\pi &= 34.5096 p_0^{0.737} - 67.557 p_0^{0.7584} + 32.858 p_0^{0.7806}\,, \\
\bar{t}_\omega &= -61.595 p_0^{0.9979} + 28.592 p_0^{1.1579} + 37.738 p_0^{0.9317} - 5.282 p_0^{1.3686}\,, \\
\bar{t}_K &= -76.424 p_0^{0.6236} + 36.944 p_0^{0.6604} + 39.0448 p_0^{0.5873}\,. \qquad (2.52)
\end{aligned}$$

where p_0 is the photon energy. The impact of the form factors is indicated by the difference of solid and dashed curves in Fig. 2.2, which should still be considered as a conservative estimate of the suppression effect. The reduction of the rate in the 2-3 GeV region amounts to a factor of $\sim$4, which is quite in line with the earlier estimates of Ref. [49].

2.2.4 Production rates

The role of the a_1 pseudovector

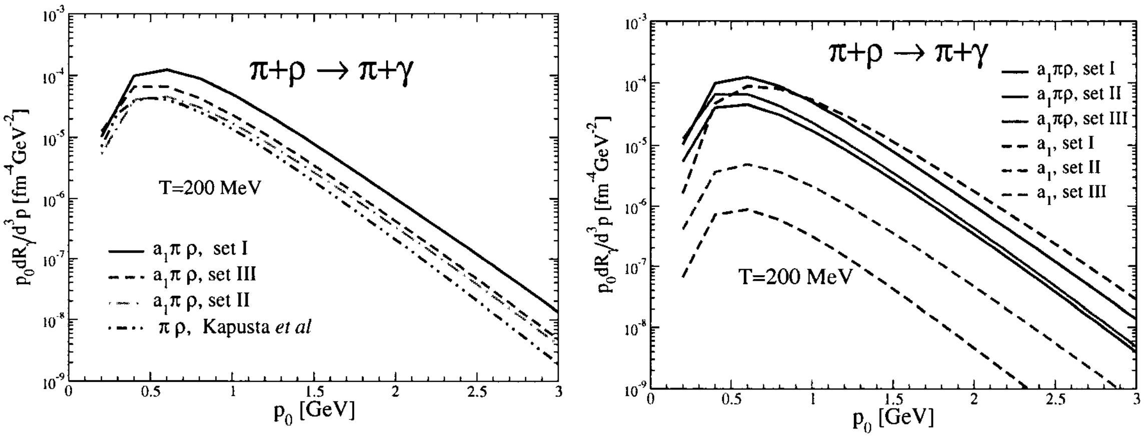

Figure 2.3: Left panel: $\pi + \rho \to \pi + \gamma$ from $\pi\rho a_1$ intermediate states added coherently, at a temperature T=200 MeV for the three sets discussed in section I. The dashed-double dot curve represents the result from Ref. [49]. Right panel: a_1 and $a_1\pi\rho$ contribution to $\pi + \rho \to \pi + \gamma$. No form factors are included here.

Figure 2.3 shows the reaction $\pi + \rho \to \pi + \gamma$ for the three sets of parameters. The ordering of those rates is the same as the ordering of a_1 radiative decays : larger radiative decay gives larger results for $\pi + \rho \to \pi + \gamma$. Importantly, we point-out that getting a radiative decay n-time bigger does **not** imply a $\pi + \rho \to \pi + \gamma$ rate bigger by the same factor. This statement is accurate for the pure a_1 contribution to $\pi + \rho \to \pi + \gamma$ (right panel of Fig. 2.3), but the total $\pi + \rho \to \pi + \gamma$ rate is given by a coherent sum of diagrams containing virtual a_1 and other meson species. Therefore, even if the photon yield from the a_1 diagrams with set I is considerably larger than the corresponding contribution of set II (right panel Fig. 2.3), once we coherently add the other contributions, the result for set I becomes about four times the result of set II. Still considering $\pi + \rho \to \pi + \gamma$, note that set II, which reproduces well the hadronic phenomenology of the a_1, could perhaps be interpreted as a slightly conservative estimate, as it under-predicts the radiative decay. To quantify this further, when parameters are adjusted to reproduce the a_1 electromagnetic width, (set III), the new photon rate for $\pi + \rho \to \pi + \gamma$ is bigger than that of set II by a factor less than two.

To have a rough estimate of the error associated with those rates, one can simply consider the range spanned by the results with II (good D/S, wrong $\Gamma_{a_1 \to \pi+\gamma}$) and those with set III (wrong D/S, good $\Gamma_{a_1 \to \pi+\gamma}$). The consequence of this exercise is that set II is used here, and that we regard the uncertainty relative to its use to be within a factor of two. For the sake of comparison, around p_0=3 GeV, the result from set II is a factor 2 larger than those Ref. [49], where the a_1 was not included.

The role of the ω vector

The Feynman diagrams with ω exchanges, in the process $\pi + \rho \to \pi + \gamma$, are shown in Figs. C.1.4, C.1.5 and C.1.6 in Appendix C. However, as we will discuss in section 2.3, the s-channel exchanges are already included in the in-medium ρ calculations. In order to avoid double counting, we include here only the t-channel contributions. This procedure is correct when coherence effects between s and t channels can be neglected. We can see in Fig. 2.4 that this is indeed the case: adding the pertinent amplitudes coherently (long-dashed line) or incoherently (dotted line) gives essentially identical results. Then, it is possible to absorb the ω s channel in the in-medium ρ spectral function, and add the t channel separately. The Ward identity is also preserved, since the s and t channels respect gauge invariance individually, as shown in Appendix C.

The left panel of Fig. 2.4 furthermore shows that when $g_{\omega\pi\rho}$ is fixed without FF (short-dashed line), ω t-channel exchange is not the prevalent contribution at high energy. When the larger value of $g_{\omega\pi\rho}$ is employed (solid line), ω t-channel exchange (without FF) is substantially enhanced. However, as argued above, a complete calculation requires a consistent treatment of FFs, not only in the fits for coupling constants. The pertinent results are summarized in the right panel of Fig. 2.4: both ω exchange and other $\pi\rho a_1$ contributions are reduced, but the former (solid line) becomes dominant at high energy. After the publication of our results in PRC **69**, 014903 (2005), the importance of the ω t-channel exchange has been challenged in Ref. [53]. However, these authors intentionally omit the insertion of FFs to "understand the relative importance of ω and a_1 exchange processes". In view of the discussion above, in the scenario with no FF, it is right that the ω t-channel exchange is not the single most important contribution, but this conclusion changes when FFs are introduced (and they have to be) to take care of the finite extent of the mesons.

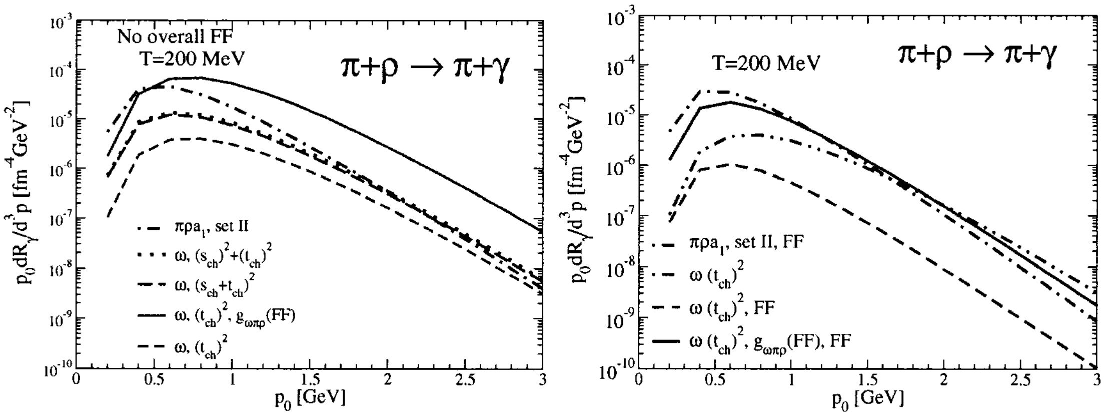

Figure 2.4: Left panel: $\pi + \rho \to \pi + \gamma$ at T=200 MeV for $a_1\pi\rho$ (dot-dashed line), ω t-ch with $g_{\omega\pi\rho}$ fixed without FF (short dashed line), ω t-ch with $g_{\omega\pi\rho}$ fixed with FF (solid line), ω diagrams added coherently (long dashed) and incoherently (dotted line). No overall form-factor. Right panel: Effect of an overal FF.

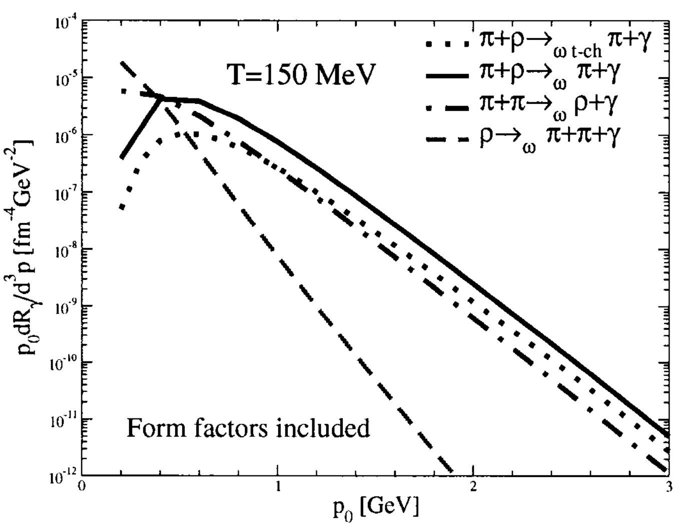

Figure 2.5: Effect of the ω as exchange particle at a temperature T=150 MeV. The solid, dot-dashed and dashed lines show respectively $\pi+\rho \to \pi+\gamma, \pi+\pi \to \rho+\gamma$ and $\rho \to \pi+\pi+\gamma$ with ω exchanged. The dotted line show $\pi + \rho \to \pi\gamma$ with ω exchanged in the t-channel only.

We can also study the effect of the ω exchange in $\pi+\pi \to \rho+\gamma$ and $\rho \to \pi+\pi+\gamma$ processes, obtained from $\pi + \rho \to \pi + \gamma$ by crossing symmetry [8]. Fig. 2.5 shows the

ω contribution in the $\pi - \rho$ collision, with the s and t channels added coherently (solid line), and also the reactions obtained from crossing symmetry : $\pi - \pi$ (dot-dashed line) and ρ decay (dashed line). Surprisingly, the $\pi - \pi$ contribution is not much smaller than $\pi - \rho$, as one would have expected. Usually, the total energy is shared between the photon and the mesons in the final state. The mass difference between the final state of $\pi + \pi \to \rho + \gamma$ and $\pi + \rho \to \pi + \gamma$ is $(m_\rho - m_\pi)$ ~0.63 GeV, so that we expect the photon distribution in the latter process, to be shifted up by $\sim$ 0.63 GeV relatively to the former process. We can see that this is indeed the case in the left panel of Fig. 2.6. This reasoning is correct when s channels are included, which is not the case for $\pi - \pi$ collisions with ω exchange : only t and u channels are present. At high energy, the $t \to 0$ limit dominates and there is some direct exchange between one incoming π and the emitted photon, reducing the effect of the large ρ mass in the final state.

Strange and non-strange sectors

From here on, we employ parameter set II. We proceed with a systematic evaluation of all processes generating photons based on the interaction vertices contained in Eq. (2.13). The explicit reactions considered include all possible s-, t- and u-channel (Born-) graphs for the reactions: $X + Y \to Z + \gamma$, $\rho \to Y + Z + \gamma$ and $K^* \to Y + Z + \gamma$. For X, Y, Z we have each combination of ρ, π, K^*, K mesons which respect the conservation of charge, isospin, strangeness and G-parity defined for non-strange mesons. The axial a_1 meson has been considered as exchange particle only (the $a_1 \to \pi\gamma$ decay is automatically incorporated via s-channel $\pi\rho$ scattering). The Feynman diagrams for the processes and their corresponding scattering amplitudes are in Appendix C. Using Eq. 2.4, the thermal photon production rates are readily obtained from the coherently-summed matrix elements in each channel. For practical purposes, we quote below parametrizations of our resulting photon production rates. In the following, the photon energy p_0 and the temperature T are both in GeV. The units of the production rates are ($\mathrm{fm}^{-4}\mathrm{GeV}^{-2}$). Parametrization for $K^* \to K + \pi + \gamma$

and $K+K \to \rho+\gamma$ do not appear because their rates have been found to be negligible.

$$\begin{aligned}
p_0\frac{dR_{\pi+\rho\to a_1\pi\rho\to\pi+\gamma}}{d^3p} &= \frac{F^4(\bar{t}_\pi)}{T^{-2.8}}exp\left(\frac{-(1.461T^{2.3094}+0.727)}{(2Tp_0)^{0.86}} + (0.566T^{1.4094}-0.9957)\frac{p_0}{T}\right)\\
p_0\frac{dR_{\pi+\rho\to\omega\, t-ch\to\pi+\gamma}}{d^3p} &= \frac{F^4(\bar{t}_\omega)}{T^{-1}}exp\left(\frac{(1.865T^{1.02}-2.6)}{(2Tp_0)^{0.62}} + (3.053T^{1.8}-1.038)\frac{p_0}{T}\right)\\
p_0\frac{dR_{\pi+\pi\to a_1\pi\rho\to\rho+\gamma}}{d^3p} &= \frac{F^4(\bar{t}_\pi)}{T^{5}}exp\left(-\frac{(9.314T^{-0.584}-5.328)}{(2Tp_0)^{-0.088}} + (0.3189T^{0.721}-0.8998)\frac{p_0}{T}\right)\\
p_0\frac{dR_{\rho\to a_1\pi\rho\to\pi+\pi+\gamma}}{d^3p} &= \frac{F^4(\bar{t}_\pi)}{T^{2}}exp\left(-\frac{(-35.459T^{1.126}+18.827)}{(2Tp_0)^{(-1.44T^{0.142}+0.9996)}} - 1.21\frac{p_0}{T}\right)\\
p_0\frac{dR_{\pi+K^*\to K+\gamma}}{d^3p} &= \frac{F^4(\bar{t}_\pi)}{T^{-3.75}}exp\left(-\frac{0.35}{(2Tp_0)^{1.05}} + (2.3894T^{0.03435}-3.222)\frac{p_0}{T}\right)\\
p_0\frac{dR_{\pi+K\to K^*+\gamma}}{d^3p} &= \frac{F^4(\bar{t}_\pi)}{T^{3}}exp\left(-(5.4018T^{-0.6864}-1.51)(2Tp_0)^{0.07} - 0.91\frac{p_0}{T}\right)\\
p_0\frac{dR_{\rho+K\to K+\gamma}}{d^3p} &= \frac{F^4(\bar{t}_K)}{T^{-3.5}}exp\left(-\frac{(0.9386T^{1.551}+0.634)}{(2Tp_0)^{1.01}} + (0.568T^{0.5397}-1.164)\frac{p_0}{T}\right)\\
p_0\frac{dR_{K^*+K\to\pi+\gamma}}{d^3p} &= \frac{F^4(\bar{t}_K)}{T^{-3.7}}exp\left(\frac{-(6.096T^{1.889}+1.0299)}{(2Tp_0)^{(-1.613T^{2.162}+0.975)}} - 0.96\frac{p_0}{T}\right)
\end{aligned} \tag{2.53}$$

The parametrizations for the nonstrange reaction channels in the present work differ from the ones quoted in Ref. [51], which are based on Ref. [38], in two respects. First, in the latter article the amplitudes in two channels, as written, violate the Ward identity [52]. Second, the choice of parameters underlying Ref. [51] yields an D/S ratio which is at variance with the experimental value. This is corrected here, together with amplitudes which have been verified for current conservation. As in Ref. [38], parameter set (II) yields smaller emission rates than set (I) for the (leading) $\pi\rho \to \pi\gamma$ process at high energies. In addition, our results using set II are another ~40% smaller than the corresponding ones in Ref. [38].

Rather little attention has been paid in the literature so far to the calculation of photon emission rates involving strange particles, mostly because existing analyses have found them to be quantitatively suppressed. In Ref. [50], the channel $K_1 \to K\gamma$ was investigated and shown to be appreciable relative to non-strange sources only in a limited kinematical domain. Here, we seek to quantify the latter relative to the $\pi\rho a_1$ emissivities within the same effective Lagrangian framework as encoded in the $SU(3)$ extension implicit in Eq. (2.13). To optimally reproduce the (measured) hadronic phenomenology, we are, however, lead to decouple the non-strange axial vector meson (a_1) from the strangeness sector. This allows to simultaneously satisfy the (electromagnetic) Ward identities and fix both the strange vector mass, m_{K^*}=895 MeV, independent of the ρ mass, and the universal coupling constant as to match the empirical value [46] of the K^* width, $\Gamma(K^* \to K\pi)\simeq$50 MeV, giving $g_K = 9.2$.

The results for the strange and non-strange sectors, with form-factors, are summarized in Fig. 2.6 for a temperature T=200 MeV. Above p_0=1 GeV, production rates are dominated by $\pi + \rho \to \pi + \gamma$ reactions, especially by the ω t-channel exchange. Below 1 GeV, $\pi + \pi \to \rho + \gamma$ and $\rho \to \pi + \pi + \gamma$ are the dominant mechanisms. In the strange sector, the main emission source is $\pi + K^* \to K + \gamma$, in complete analogy to the $\pi + \rho \to \pi + \gamma$ reaction in the non-strange sector. Overall, the total strange contribution accounts for $\sim$ 25% of the net contribution around p_0 = 1 GeV, while this reduces to $\sim$ 15% at p_0=3 GeV (right panel of Fig. 2.6).

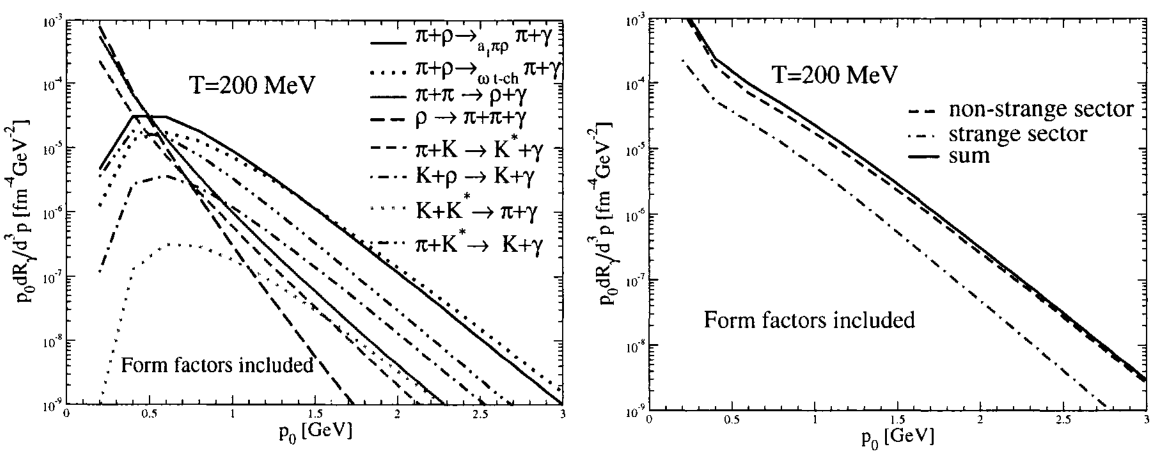

Figure 2.6: Strange and non-strange meson contributions to the production rate of photons at T=200 MeV.

2.3 Baryonic contributions

It is important to realize that thermal emission rates of dileptons and photons are intimately connected, both being based on the e.m. current-current correlator, albeit evaluated in distinct kinematical domains, i.e. timelike ($M^2 = p_0^2 - p^2 > 0$) vs. lightlike ($M^2 = 0$), respectively. We recall that baryonic sources are very important [54, 55] for understanding the observed excess in low-mass ($M \leq 1$ GeV) dilepton production in (semi-) central *Pb-Au* collisions at both full (160 AGeV) [56] and lower (40 AGeV) [57] SPS energies. It is therefore mandatory to scrutinize the role of baryons in photon production, especially since most investigations have thus far not revealed substantial contributions [58, 59, 60].

We here make use of the hadronic many-body calculations of the in-medium $\rho(770)$ spectral function [47, 61, 62, 63, 48], which, when evaluated for $M^2 \to 0$, directly yield pertinent photon emission rates via Eq. (2.1). Within the vector dominance model (VDM), one has (schematically)

$$\mathrm{Im}\Pi_{\mathrm{em}} = \sum_{V=\rho,\omega,\phi} \frac{m_V^4}{g_V^2} \mathrm{Im}D_V \tag{2.54}$$

(m_V, g_V and $\mathrm{Im}D_V$: vector-meson masses, coupling constants and spectral functions, respectively). In the following we focus on contributions arising from the ρ-meson, which are dominant since $g_\rho^2/g_\omega^2 \simeq 10$. Three different contributions to the ρ self-energy are shown in Fig. 2.7. Diagram (a) shows the decay of the ρ meson into two thermal pions, $\Sigma_{\rho\pi\pi}$, surrounded by hot nuclear matter. This contribution has been calculated by Urban *et al.* in Ref. [63]. Diagrams (b) and (c) show the medium modifications through resonant ρ-meson scattering off baryons ($\Sigma_{\rho B}$), calculated by Rapp, Chanfray and Wambach, in Ref. [47], and mesons ($\Sigma_{\rho M}$), calculated by Rapp and Gale in Ref. [48]. The ρ-h (h=π, K, ρ, N, Δ,...) interactions are incorporated through self-energy expressions of type [64]

$$\Sigma_{\rho h}^{\mu\nu}(p_0, \vec{p}; T) = \int \frac{d^3q}{(2\pi)^3} \frac{1}{2\omega_h(q)} [f^h(\omega_h(q)) - f^{\rho h}(\omega_h(q) + p_0)] \; \mathcal{M}_{\rho h}^{\mu\nu}(p, q) \; , \tag{2.55}$$

where the isospin averaged ρ scattering amplitude $\mathcal{M}_{\rho h}$ is integrated over the thermal distribution $f^h(\omega_h(q)) = [\exp(\omega_h(q))/T \pm 1]^{-1}$ of the corresponding hadron species h with $\omega_h(q) = \sqrt{m_h^2 + \vec{q}^2}$. The advantage of writing the self-energy in terms of the forward scattering amplitude (s-channel) is that in-medium resonance widths, accounting for higher order effects in temperature and density, are readily implemented without facing problems of double-counting. All of the resonances used in constructing the ρ self-energy are enumerated in Refs. [62, 48], along with the details on how the interactions are constrained by hadronic phenomenology.

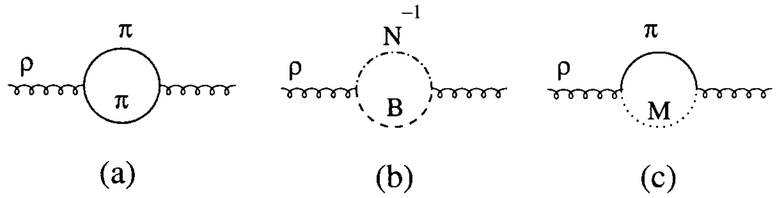

Figure 2.7: Different contributions to ρ self-energy. (a) Decay into two pions; (b) excitation of baryonic resonances; (c) excitation of mesonic resonances in $\pi\rho$ scattering.

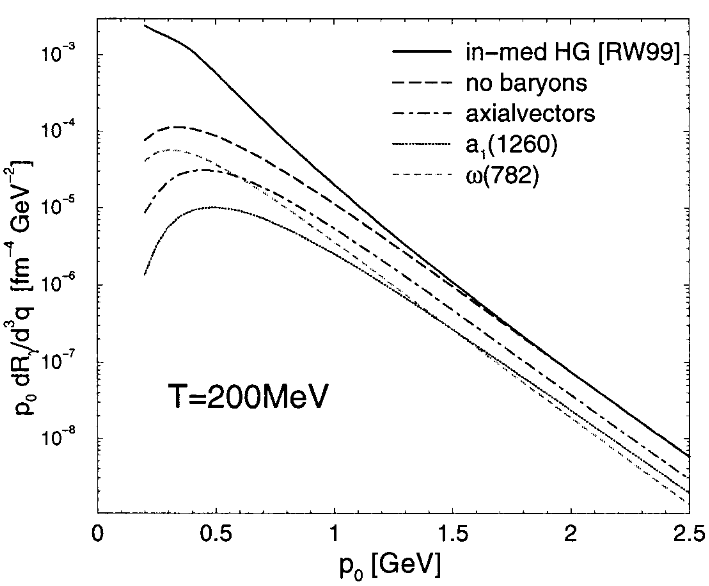

Figure 2.8: Thermal photon production rate in the hadronic many-body approach of Refs. [63, 47, 48] based of an in-medium ρ spectral function. The temperature and the baryon chemical potential are T = 200 Mev and μ_B=220 MeV.

The results from the hadronic many-body approach are compiled in Fig. 2.8 for a temperature-density value characteristic for meson-to-baryon ratios at full CERN-SPS energy (160 AGeV). The solid curve is the net photon spectrum obtained by taking the full (ρ-meson) spectral density to the photon point, whereas the long-dashed curve represents the non-baryonic (sub-) component. One observes that the low-energy regime, $p_0 \lesssim 1$ GeV, of the photon emissivity is dominated by baryonic effects (quite reminiscent to what has been found for low-mass dileptons). These are mostly due to direct ρN resonances such as $\Delta(1232)$, $N(1520)$, as well as $\Delta(1232)N^{-1}$ and NN^{-1} excitations in the two-pion cloud of the ρ (which, to leading order in density, correspond to t-channel one-pion exchange (OPE) in processes of type $\pi N \to \gamma N$). These contributions should be rather reliable for baryon densities up to at least normal nuclear matter density, $\rho_0 = 0.16$ fm^{-3}, being constrained by photo-absorption spectra on nucleons and nuclei [61].

Beyond ~ 1 GeV, mesonic (resonance) states become the dominant source of photons in the many-body approach, which includes radiative decays of $\omega(782)$, $h_1(1170)$, $a_1(1260)$, $f_1(1285)$, $\pi(1300)$, $a_2(1320)$, $\omega(1420)$, $\omega(1650)$, $K^*(892)$ and $K_1(1270)$. In particular, the $\omega \to \pi\gamma$ decay exhibits an appreciable low-energy strength, consistent with the early results of Ref. [49]. Note that all hadronic vertices carry (dipole) form factors with typical cutoff parameters of around 1 GeV, as extracted from an optimal fit to measured hadronic and radiative branching ratios within VDM [48]; t-channel exchange processes between mesons as discussed in Sec. 2.2.4 (e.g., a_1-exchange in $\pi\rho \to \pi\gamma$) are not implicit in the spectral densities leading to the the results of Fig. 2.8. They are mostly relevant at photon energies beyond 1 GeV and therefore do not significantly figure into bulk (low-mass) dilepton production, the latter being dominated by (transverse) momenta $p_T \lesssim M$.

We finally have to address the question of how to combine the various hadronic sources, computed in two different frameworks, into the total emission rate. Two issues arise when simply adding all of the emission rates shown in Figs. 2.6 and 2.8: double-counting and coherence. The a_1 s-channel graph is present in both ρ spectral function and the MYM framework. We remove it from the former, where it plays a minor role, whereas it induces significant interference effects in the $\pi\rho a_1$ complex. If coherence is unimportant, t-channel contributions can be evaluated separately. It was verified that this was the case for the ω exchange (see Fig. 2.4), so that the incoherent addition of the t-channel contribution is justified. We believe that it is fair to say that the enumeration of hadronic photons sources given in the mesonic and baryonic sections, together with form factor inclusions, currently represents the most realistic evaluation of the full hadron gas emissivity.

2.4 QGP contribution

The in-medium annihilation of a quark with an antiquark ($q + \bar{q} \to g + \gamma$) and the Compton scattering of a quark with a gluon ($q + g \to q + \gamma, \bar{q} + g \to \bar{q} + \gamma$) have already been calculated by Kapusta *et al.* in Ref. [49]. We show here the approach followed by Wong, in Ref. [65]. The cross-section for the $q + \bar{q} \to g + \gamma$ process is [8]

$$\frac{d\sigma_{q\bar{q}\to g\gamma}}{dt} = \left(\frac{e_f}{e}\right)^2 \frac{8\pi\alpha_s\alpha}{s(s-4m^2)}(T^a_{i,j})^2 \left\{ \left(\frac{m^2}{t-m^2} + \frac{m^2}{u-m^2}\right)^2 + \frac{m^2}{t-m^2} + \frac{m^2}{u-m^2} \right.$$
$$\left. - \frac{1}{4}\left(\frac{t-m^2}{u-m^2} + \frac{u-m^2}{t-m^2}\right)\right\}, \tag{2.56}$$

where m, e_f are the mass and charge of the quarks, and $T^a_{i,j}$ is the generator of the strong interaction ($\sum_{i,j,a} T^a_{i,j} = 4$). For $p_0 \gg m$ and $p_0 \gg T$, we have that $s \gg m^2$. The cross-section is then dominated by the terms with $t \to m^2$ and $u \to m^2$. We have that $t - m^2 = -2p_0(E_q - |\vec{p_q}|\cos\theta_{\gamma q})$, where $E_q, \vec{p_q}$ are the energy and momentum of the incoming quark. From a Taylor expansion around $\theta_{\gamma q} = 0$, we get

$$\frac{1}{t-m^2} \sim \frac{1}{2p_0(E_q - |\vec{p_q}|)} - \frac{\theta_{\gamma q}|\vec{p_q}|}{2p_0(E_q - |\vec{p_q}|)^2} \sim \frac{1}{p_0|\vec{p_q}|\left(\frac{m^2}{|\vec{p_q}|^2} + \theta^2_{\gamma q}\right)}. \tag{2.57}$$

Thus, for $|\vec{p_q}| \gg m$, the angular distribution of $1/(t-m^2)$ is very narrow around $\theta_{\gamma q} = 0$, which implies that $\vec{p} \propto \vec{p_q}$. So, the differential cross-section can be approximated by

$$p_0 \frac{d\sigma_{q\bar{q}\to g\gamma}}{d^3p} = p_0 \frac{\sigma(s)_{q\bar{q}\to g\gamma}}{2}\left[\delta^3\left(\vec{p} - \vec{p_q}\right) + \delta^3\left(\vec{p} - \vec{p_{\bar{q}}}\right)\right] \tag{2.58}$$

where $\sigma(s)_{q\bar{q}\to g\gamma}$ is given by

$$\sigma_{q\bar{q}\to g\gamma}(s) = \int dt \frac{d\sigma_{q\bar{q}\to g\gamma}}{dt} \sim \left(\frac{e_f}{e}\right)^2 (T^a_{i,j})^2 \frac{4\pi\alpha_s\alpha}{s}\left[\ln\left(\frac{s}{m^2}\right) - 1\right]. \qquad (2.59)$$

In this approximation, as the emitted photon get the direction and the momentum of the incoming quark, we can speak of quark-photon conversion. A similar result is obtained for Compton scattering:

$$p_0 \frac{d\sigma_{qg\to q\gamma}}{d^3p} = p_0 \sigma(s)_{qg\to q\gamma}\delta^3(\vec{p} - \vec{p_q}) \qquad (2.60)$$

with

$$\sigma(s)_{qg\to q\gamma} \sim \left(\frac{e_f}{e}\right)^2 (T^a_{i,j})^2 \frac{2\pi\alpha_s\alpha}{s}\left[\ln\left(\frac{s}{m^2}\right) + \frac{1}{2}\right]. \qquad (2.61)$$

In the relativistic kinetic theory framework, the photon production rate will be given by

$$\begin{aligned} p_0 \frac{dR}{d^3p} = & \int \frac{d^3p_q}{(2\pi)^3}\frac{d^3p_{\bar{q}}}{(2\pi)^3} f_F(E_q) f_F(E_{\bar{q}})(1 + f_B(E_q + E_{\bar{q}} - p_0)) \\ & |v_q - v_{\bar{q}}|(2N_s+1)^2 \sum_{f,i,j,a} p_0 \frac{d\sigma_{q\bar{q}\to g\gamma}}{d^3p} \\ & + 2\int \frac{d^3p_q}{(2\pi)^3}\frac{d^3p_g}{(2\pi)^3} f_F(E_q) f_B(E_g)(1 - f_F(E_q + E_g - p_0)) \\ & |v_q - v_g|(2N_s+1)^2 \sum_{f,i,j,a} p_0 \frac{d\sigma_{qg\to q\gamma}}{d^3p} \end{aligned} \qquad (2.62)$$

where f_F, f_B are respectively the Fermi-Dirac and Bose-Einstein distribution function, and the factor $(2N_s + 1)$ is the spin degeneracy. The factor 2 in the second term takes care of both $qg \to q\gamma$ and $\bar{q}g \to \bar{q}\gamma$. After some algebric manipulations, the photon production rate is finally expressed as

$$p_0 \frac{dR}{d^3p} = \sum_f \left(\frac{e_f}{e}\right)^2 \frac{T^2\alpha_s\alpha}{4\pi^2} f_F(p_0)\left[2\ln\left(\frac{4p_0 T}{m^2}\right) - C_{ann} - C_{Com}\right] \qquad (2.63)$$

with $C_{ann} = 1.91613$ and $C_{Com} = 0.41613$. In the massless quarks limit, we get a singularity. However, it has been shown in Ref. [49] that when one accounts for hard-thermal loops resummation (HTL), defined latter in Chapter 6, it corresponds to substitute the vacuum mass by the effective thermal mass : $m \to \sqrt{2}m_F = T\sqrt{4\pi\alpha_s/3}$.

In order to verify the validity of the quark-photon conversion, we have to substitute in 2.62 the exact definition of the differential cross-section:

$$p_0 \frac{d\sigma^{1+2\to 3+\gamma}}{d^3p} = \frac{1}{E_1\, E_2 |v_1 - v_2| (2\pi)^2} \int \frac{d^3p_3}{E_3} \delta^4(p_1 + p_2 - p_3 - p) \frac{d\sigma}{dt} \pi s^2 \quad (2.64)$$

For massless quarks, the cross-sections have singularities at $t = 0$ and $u = 0$. Following Kapusta *et al.* [49], we can delete the region of phase space causing the divergence by introducing a regulator k_c, such that

$$-s + k_c^2 \leq t \leq -k_c^2\,, \quad 2\,k_c^2 \leq s < \infty \quad (2.65)$$

while for $t > -k_c^2$, we add the HTL photon self-energy, that will be calculated in Chapter 6. Then, the exact result for the photon production rate in the QGP from $2 \to 2$ processes becomes

$$p_0 \frac{dR_{\text{exact}}}{d^3p} = \int_{1,2,3} p_0 \frac{d\sigma^{1+2\to 3+\gamma}}{d^3p} \Bigg|_{t \leq -k_c^2} + \lim_{M\to 0} \left(\frac{3\pi M^2}{2\alpha} \frac{dR^{e^+e^-}}{d^4p} \right) \Bigg|_{t > -k_c^2} \quad (2.66)$$

where the integral in the first term corresponds to the phase-space of the incoming and outgoing partons, while the HTL dilepton production rate $dR^{e^+e^-}/d^4p$ is from Eq. 6.38. The exact results, for $k_c = \sqrt{2} m_F$, are shown by the solid lines in Fig. 2.9, while the quark-photon conversion are shown by the dashed lines. Then, above $p_0 = 1$ GeV, i.e. in the region where $p_0 \gg T$, we can observe the validity of the quark-photon conversion approximation.

The bremsstrahlung ($q + g \to q + g + \gamma$) and annihilation ($q + \bar{q} + g \to g + \gamma$) photon production rate have been calculated by Arnold, Moore and Yaffe in Ref. [31]. Their model, which include the Landau-Pomeranchuk-Migdal (LPM) effect, will be presented in Chapter 3. Here, we take advantage of an available parametrization of their result [66], which, after added to the quark-photon conversion 2.63, is illustrated by the dashed-dotted line in Fig. 2.10. The observation that this QGP contribution is similar to the full hadronic result (sum of solid and dashed curves) within a factor ~2 over essentially all energy below 3 GeV might not be a mere coincidence. A similar behaviour has been found for dilepton production rates [62], perhaps suggesting a type

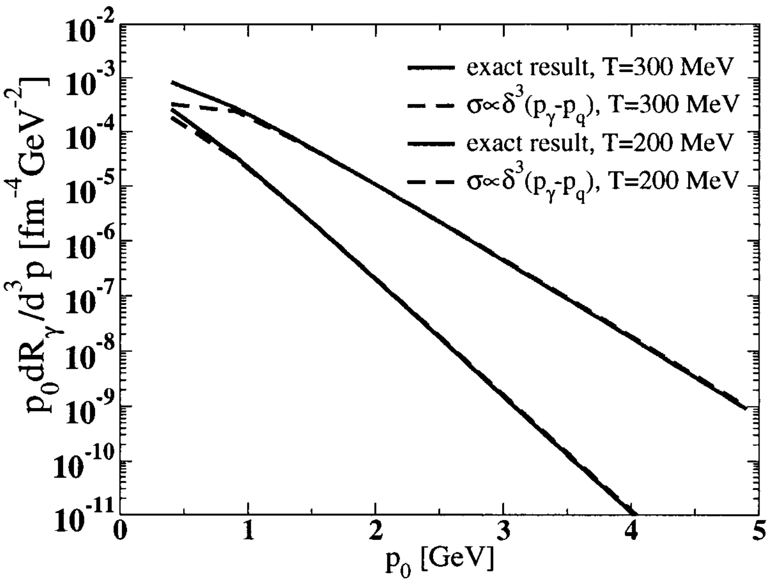

Figure 2.9: Production rate of photon in the QGP by leading annihilation and Compton scattering, using the exact differential cross-section (solid lines) and the quark-photon conversion (dashed lines) for two different temperatures.

of "quark-hadron duality" for e.m. emission close to the expected phase boundary. Finally, our result for the mesonic sector, including $a_1\pi\rho\omega$ exchange and the strange sector, with consistent form-factors, are an overall factor ~ 2 higher that the results shown in Ref. [49], for $\pi\rho$ exchange without FF.

2.5 Space-time evolution

For a realistic comparison with direct photon spectra as extracted in heavy-ion collisions, the thermal rates of the previous sections have to be convoluted over the space-time history of the reaction. Assuming that thermal equilibrium can be established and maintained, hydrodynamic simulations are the method of choice (see Ref. [67]). Here we employ a more simple fireball model [62, 68, 69], which incorporates essential elements of hydrodynamic calculations. The fireball evolution is started at a "formation" (or thermalization) time $t_0 \leq 1$ fm/c, which relates to the initial longitudinal extent of the firecylinder as $\Delta z \simeq \Delta y\, t_0$ with $\Delta y \simeq 1.8$ corresponding to the approximate rapidity coverage of a thermal distribution. The fireball

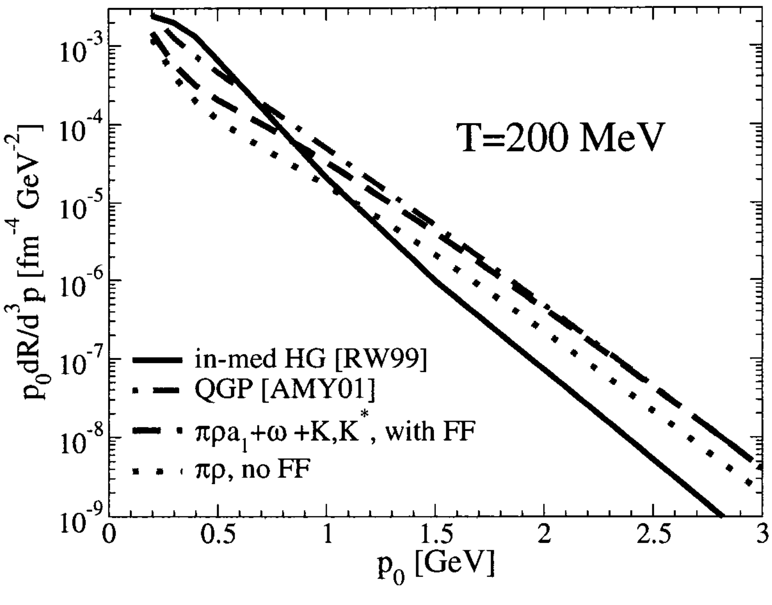

Figure 2.10: Comparison of HG and QGP photon production rates at T=200 MeV. Solid line: hadronic many-body approach of Refs. [47, 62, 48], dashed line: mesonic contribution including hadronic form factors, dotted line: result from Kapusta *et al.* [49] for $\pi\rho$ exchanges without form factors, dashed-dotted line: complete leading-order QGP emission [66].

is placed at a rapidity y_0, adjusted to the rapidity window of the observed particles. The subsequent volume expansion, $V_{FB}(t)$, is carried through QGP, mixed and hadronic phases until "thermal" freezeout at T_{fo}=100-120 MeV, where hadrons cease to interact. Cylindrical volume expansion is assumed:

$$V_{FB}(t) = 2(z_0 + v_z + \frac{1}{2}a_z\, t^2)\pi(r_0 + \frac{1}{2}a_\perp\, t^2)^2 \tag{2.67}$$

with $r_0 = 1.2A^{1/3}$ for central collisions. The parameters v_z, a_z and $a_\perp$ are adjusted to the finally observed flow velocities.

The equations of state (EoS) for QGP and HG are modelled via thermal quasiparticles and a resonance gas (including about 50 species), respectively. Based on the conservation of net baryon-number, N_B, and total entropy, S, one is able to extract the temperature and baryon chemical potential at any given (proper) time, thereby defining a trajectory in the μ_B-T plane. The transition from the QGP to HG phase is placed at "chemical freezeout" points extracted from hadron ratios in experiment [70]. Consequently, in the HG evolution from chemical to thermal freezeout, hadrons stable under strong interactions (pions, kaons, etc.) have to be conserved explicitly by introducing associate chemical potentials (μ_π, μ_K, etc.). This has not been done in previous calculations of thermal photon production [67, 71, 72], and induces a significantly faster cooling in the hadronic phases [73]. In addition, at collider energies (RHIC and LHC), the conservation of the observed antibaryon-to-baryon ratio (which at midrapidities is no longer small) in the hadronic evolution becomes important [74]. An accordingly introduced (effective) chemical potential for antibaryons has been shown to impact the chemistry at later stages appreciably [74]. For each collision energy, the value of the specific entropy, S/N_B, is fixed to reproduce observed hadron abundances. The total yield of thermal photons in an A-A collision then follows as

$$p_0 \frac{dN_\gamma^{thermal}}{d^3p}(p_T) = \frac{1}{\Delta y} \int\limits_{y_{min}}^{y_{max}} dy \int dt\, V_{FB}(t) \left(p_0 \frac{dR}{d^3p}(p_0 = p_T \cosh(y - y_0)) \right) , \tag{2.68}$$

averaged over a rapidity interval, $[y_{min}, y_{max}]$ according to the experimental coverage ($\Delta y = y_{max} - y_{min}$). To incorporate transverse expansion in the spectra, in the thermal rest frame isotropic photon momentum distributions are boosted into the laboratory (lab) frame using an average of about 70% of the time-dependent transverse (surface) expansion velocity at each moment in the fireball evolution. The mesons chemical potentials are introduced as multiplicative fugacity factors, so that each initial mesons x receive a $\exp[\mu_x/T]$ factor. For example, the production rate for $\pi + \pi \to \rho + \gamma$ will be multiplied by $\exp[2\mu_\pi/T]$ while the production rate for $\pi + \rho \to \pi + \gamma$ will received a $\exp[3\mu_\pi/T]$ factor, since the $\rho \to \pi\pi$ decay gives $\mu_\rho = 2\mu_\pi$.

2.6 *Non-thermal photons*

Second, an additional contribution to direct photon spectra arises from prompt photons in primordial N-N collisions. The minimal baseline for a heavy-ion reaction constitutes the collision-number scaled expectation from proton-nucleon collisions. An accurate description at SPS is still a matter of debate [75], so that we here employ empirical scaling relations in $x_t = 2p_T/\sqrt{s_{NN}}$, extracted from fits to data in Ref. [76]. For $x_t \gtrsim 0.1$, corresponding to center of mass energy in the nucleon-nucleon system $\sqrt{s_{NN}} \lesssim 50$ GeV and photon transverse momenta p_T above 2 GeV, the cross section fit (at midrapidity, y=0) reads

$$p_0 \frac{d^3\sigma_\gamma^{pp}}{d^3p} = 575 \; \frac{(\sqrt{s_{NN}})^{3.3}}{(p_T)^{9.14}} \; \frac{\text{pb}}{\text{GeV}^2} \,, \tag{2.69}$$

We supplement this with a smooth cutoff for $p_0 \leq 2$GeV, where the parametrization (2.69) is no longer reliable. We assume the following cutoff function

$$F = \left(\frac{1.25}{1+\frac{1}{p_T^2}}\right)^5 \text{ for } p_T < 2 \text{ GeV}\,, \quad F = 1 \text{ for } p_T \geq 2 \text{ GeV} \tag{2.70}$$

The "regulated" p-p cross-section is now

$$p_0 \frac{d^3\hat{\sigma}_\gamma^{pp}}{d^3p} = F \times \left[575 \; \frac{(\sqrt{s_{NN}})^{3.3}}{(p_T)^{9.14}}\right] \frac{\text{pb}}{\text{GeV}^2} \,, \tag{2.71}$$

The naive extrapolation to a collision of two nuclei A and B at impact parameter b predicts the prompt photon spectrum to be

$$\begin{aligned} p_0 \frac{dN_\gamma^{prompt}}{d^3p}(b; p_T, y=0; \sqrt{s}) &= p_0 \frac{d^3\hat{\sigma}_\gamma^{pp}}{d^3p} \; ABT_{AB}(b) \\ &= p_0 \frac{d^3\hat{\sigma}_\gamma^{pp}}{d^3p} \; \frac{N_{coll}}{\sigma_{pp}^{in}} \end{aligned} \tag{2.72}$$

with T_{AB} as the nuclear overlap function, N_{coll} as the number of primordial N-N collisions, and σ_{pp}^{in} as the inelastic N-N cross section. The lack of a consistent microscopic description of photon production in p-p complicates the task to assess nuclear corrections, such as shadowing or intrinsic k_T broadening (Cronin effect), see *e.g.* Ref. [77] for a recent discussion. As a substitute for a more rigorous calculation, we here adopt the following strategy: since the intrinsic k_T effects at the N-N level are in principle contained in the parametrization, Eq.(2.69), the nuclear effect is approximated by fitting an additional (nuclear) k_T-smearing to p-A data. The latter is modelled by folding the parameterized spectrum over a Gaussian distribution

$$f_1(k_T) = \frac{1}{\pi\langle\Delta k_T^2\rangle} \; \mathrm{e}^{-k_T^2/\langle\Delta k_T^2\rangle} \,. \tag{2.73}$$

Here, f_1 represents the transverse momentum distribution of an incoming partons, and is normalized to

$$\int d^2k_T f_1(k_T) = 1\,. \tag{2.74}$$

The total transverse momentum distribution of a system of two incoming partons would be

$$f_2(k_T) = \int d^2k_T^1 f_1(|\vec{k}_T^1|) f_1(|\vec{k}_T^1 - \vec{k}_T|) = \frac{1}{2\pi\langle\Delta k_T^2\rangle} e^{\frac{-k_T^2}{2\langle\Delta k_T^2\rangle}}\,. \tag{2.75}$$

Within this model, the prompt photon in A-B collision will be given by

$$p_0\frac{dN_\gamma^{prompt}}{d^3p}(b; p_T, y=0; \sqrt{s}) = \frac{N_{coll}}{\sigma_{pp}^{in}}\int d^2k_T f_2(k_T) p_0 \frac{d^3\hat{\sigma}_\gamma^{pp}}{d^3p}(|\vec{k}_T - \vec{p}_T|) \tag{2.76}$$

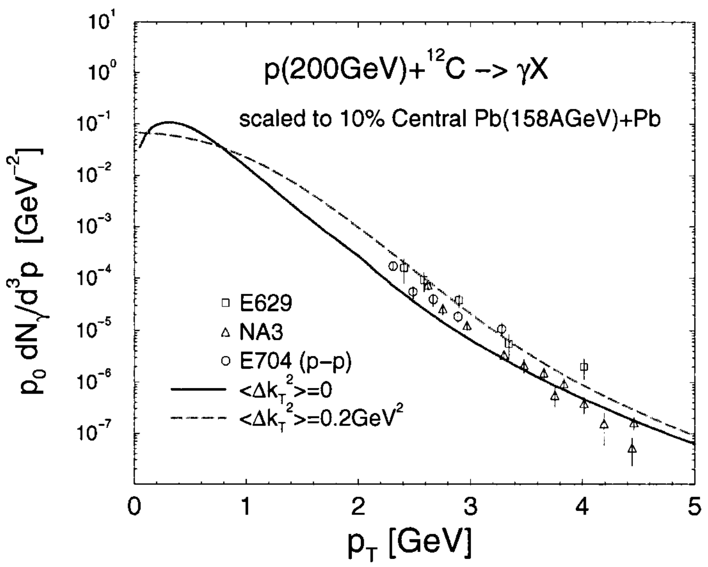

Figure 2.11: Direct photon data in proton-Carbon collisions, scaled to central *Pb-Pb* collisions at SPS energies (see text for details). The curves show the effect of the broadening of the primordial photon spectrum generated by the nuclear medium. The data are from Refs. [79] (E629) and [80] (NA3).

The result, together with proton-nucleus data on photon production is shown in Fig. 2.11. The data have been scaled to the 10% central *Pb-Pb* cross section at 158 AGeV according to the procedure used in Ref. [78]. Fitting the *p-A* single photon data in this fashion, an adequate reproduction of the experimental measurements emerges with $\langle \Delta k_T^2 \rangle \simeq 0.1$-$0.2$ GeV^2.

In principle, there is a third source of photons corresponding to emission after initial nuclear impact, but before the formation time τ_0 (the "pre-equilibrium" contribution). It is difficult to assess both theoretically and experimentally; a rough (but uncontrolled) estimate might be had by choosing a somewhat smaller formation time. Note that, in principle, the modelling of those contributions is accessible to *ab-initio* simulations [81].

2.7 Results

2.7.1 SPS

In this section we compute transverse momentum spectra at midrapidities from 10% central Pb(158AGeV)+Pb collisions for which photon spectra have been measured by WA98 [78]. Let us first focus on thermal emission; QGP radiation is always calculated with the complete leading-order result [31], and hadronic radiation as the sum of the hadronic many-body [62, 48], $\pi\rho K^* K$ gas (within MYM) and ω t-channel exchange contributions with form factors as discussed in Sec. 2.2.

In Fig. 2.12 we display results for a rather standard fireball evolution with initial z_0=1.8 fm (corresponding to $\tau_0 \simeq 1$ fm/c and initial temperature $T_i = 205$ MeV) and final temperature $T_{fo} \simeq$ 110 MeV reached after a total lifetime of $\sim$ 13 fm/c. Due to transverse expansion, the total hadron gas yield outshines QGP emission at all momenta. This is in close reminiscence to the calculations of intermediate dilepton spectra within the same framework [68], where QGP radiation was found to constitute about 30% of the thermal component that was able to reproduce the excess observed by the NA50 collaboration [82] (see also Ref. [83]). As expected, photons of baryonic origin prevail in the spectrum for $p_T \lesssim 1$ GeV; this region is thus intimately related to the low-mass (and low-transverse momentum) dilepton enhancement observed by CERES/NA45 [56]. The same feature has been found [84] when comparing the hadronic many-body contributions to the upper limits in $S(200\text{AGeV})+Au$ by WA80 [85]. In the right panel of Fig. 2.12 we illustrate the sensitivity of the hadronic thermal emission to properties of the fireball evolution. When increasing the thermal freezeout time from our (SPS) default value of 106 MeV to 135 MeV, the yield at $p_T \leq 1$GeV is reduced by up to 30%, whereas it is essentially unchanged beyond $p_T \simeq 2$ GeV, thus reflecting emission close to T_c. On the contrary, if the additional boost on the photons due to the transverse expansion is neglected, the high-momentum spectrum is reduced appreciably (by a factor of ~ 3 already at $p_T = 2$ GeV), whereas the low-momentum region is only mildly affected. The critical temperature has been set to $T_c = 175$ MeV, but the total thermal contribution (HG + QGP) should not really depends on this value, as we have seen from Fig. 2.10 that the hadronic and QGP production rates were close to each other around $T = T_c$.

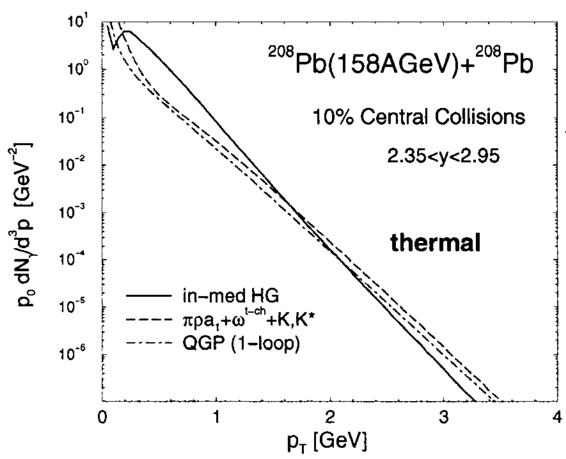

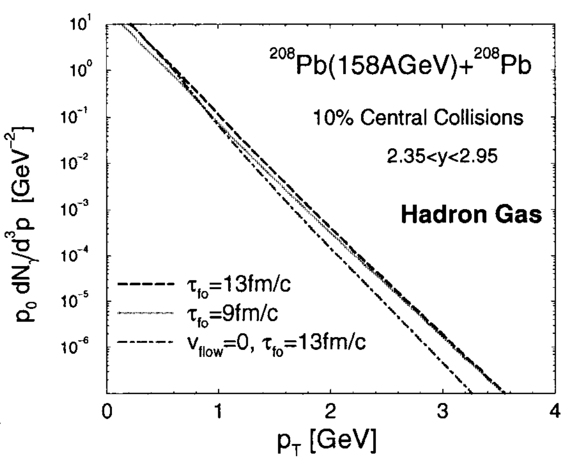

Figure 2.12: Integrated photon emission from various thermal sources in an expanding fireball model for central $Pb+Pb$ collisions at SPS. Left panel: hadronic emission ($T \leq T_c$=175 MeV) from the meson gas component (dashed line) and the in-medium ρ spectral function (solid line) compared to QGP emission ($T_c \leq T \leq T_i$=205 MeV) (dashed-dotted line). Right panel: Sensitivity of the total HG yield to thermal freezeout (long-dashed line: τ_{fo}=13 fm/c corresponding to T_{fo}=106 MeV, dotted line: τ_{fo}=9 fm/c corresponding to T_{fo}=135 MeV) and transverse flow (dashed-dotted line: τ_{fo}=13 fm/c with no transverse boost of the emission source).

As is well-known, high-energy (-mass) photon (dilepton) emission is rather sensitive to initial temperatures in heavy-ion reactions, due to the large (negative) exponents in the thermal factors. This is confirmed by our results for the QGP contribution in Fig. 2.13 when decreasing the formation time from 1 to 0.56 fm/c, the latter implying T_i=250 MeV. Another effect that has been ignored in available hydrodynamic

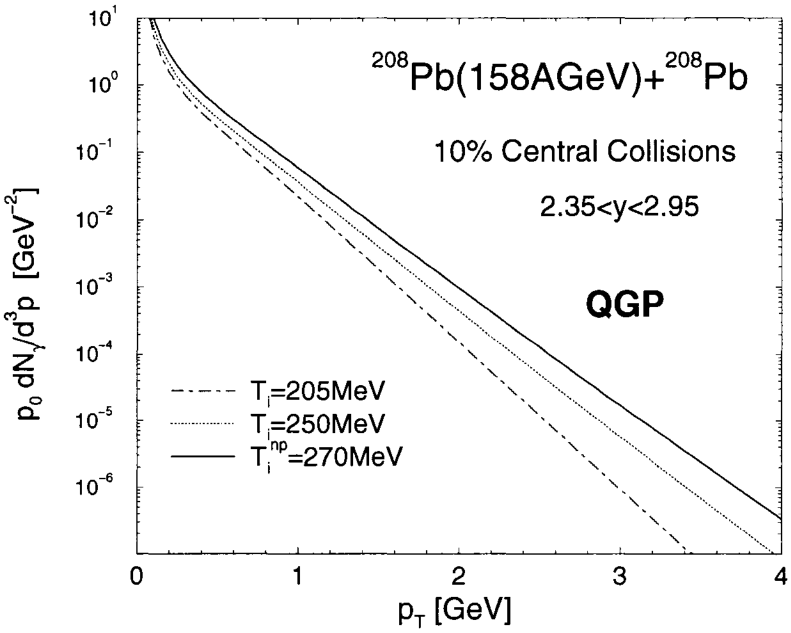

Figure 2.13: Sensitivity of the QGP photon emission yield within an expanding fireball model for central Pb+Pb collisions at SPS.

calculations so far is associated with corrections to the QGP equation of state. The standard assumption is that of an ideal (massless) gas with an effective number of flavours $N_f = 2.5$ corresponding to a total degeneracy d_{QGP}=(10.5N_f+16)=42 (in our default calculations we use d_{QGP}=40). However, lattice gauge theory results [86] indicate ~20% smaller values than the ideal gas for the thermodynamic state variables in the for SPS energies relevant temperature region T=1-2 T_c. Implementing such a reduction into the entropy density (which is the relevant quantity for the fireball evolution) by using d_{QGP}=32 yields an increase of the initial temperature from 250 MeV to 270 MeV without decrease in initial volume [73, 87]. The resulting thermal photon spectrum from QGP radiation shows appreciable sensitivity to this modification at high energies, cf. solid vs. dotted curve in Fig. 2.13. This sensitivity does not persist into the low-energy region $p_T \leq 1$ GeV, and thus does not affect low-mass dilepton production [55].

Let us now turn to a comparison with the recent measurements of WA98 [78]. Our baseline scenario consists of thermal emission (hadronic and QGP) from the ex-

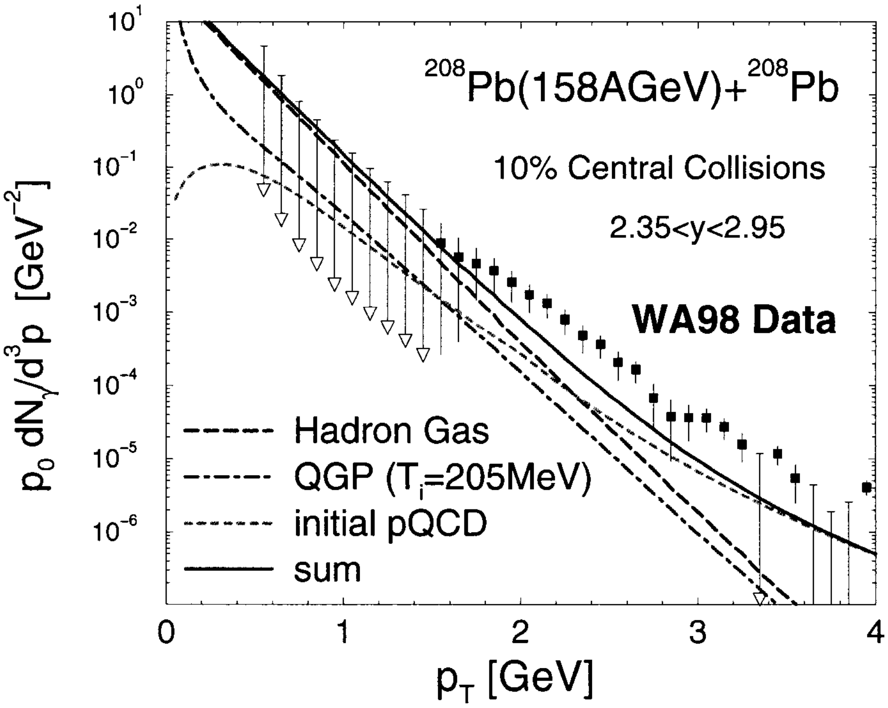

Figure 2.14: Thermal plus prompt photon spectra compared to data from WA98 [78] for central $Pb+Pb$ collisions at SPS .

panding fireball with T_i=205 MeV, supplemented by prompt (pQCD) photons from primordial N-N collisions without any nuclear effects, cf. Fig. 2.14. Up to transverse momenta of about 1.5 GeV the data (upper limits) are essentially saturated by thermal radiation from the hadronic phase. This is important to note since this regime, as discussed above, is directly related to the low-mass dilepton excess observed by CERES/NA45 [56, 57], which can be successfully described within the same approach [62]. Beyond 3 GeV, prompt photons dominate, but do not seem to provide enough yield to account for the data. Since the hadron gas emission is essentially fixed and describes well the low-energy regime, three possibilities are left for the origin of discrepancies above $p_T \simeq 2$ GeV: (i) modifications of the prompt yield, (ii) pre-equilibrium emission, (iii) larger QGP radiation. In the following, cases (i) and (iii) (or a combination thereof) will be investigated.

First, we study the effects of the initial temperature on the photon spectrum. The exercise in the right panel of Fig. 2.12 is repeated adding all sources discussed here, cf. Fig. 2.15. Clearly, when going to (for SPS conditions) rather short formation times of $\tau_0 \simeq 0.5$ fm/c, coupled with non-perturbative (suppression) effects in the QGP EoS, a rather good reproduction of the entire spectrum can be achieved. This statement agrees with the hydrodynamic analyses of Refs. [72, 67].

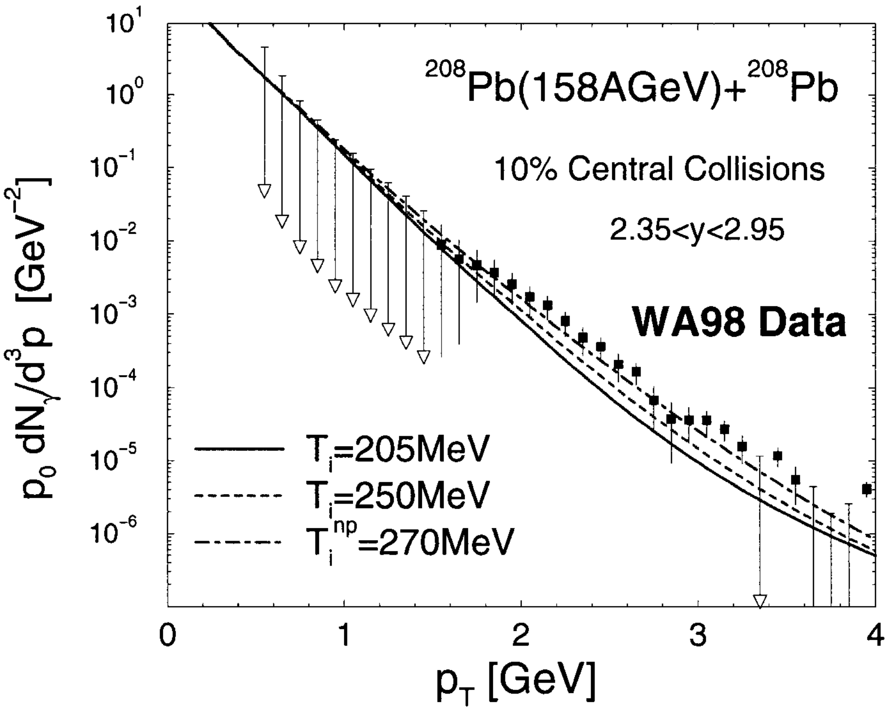

Figure 2.15: Effects of various initial temperatures on the total photon spectra in *Pb+Pb* collisions at SPS, compared to data from WA98 [78].

The second possibility relates to the nuclear Cronin enhancement, which we implement as outlined in the previous Section. The usual assumption to extrapolate nuclear broadening effects on *e.g.* π^0 or γ spectra is that

$$\langle \Delta k_T^2 \rangle_{AA} = N \langle \Delta k_T^2 \rangle_{pA} \ , \tag{2.77}$$

with N=2 [88]. Alternatively, based on a careful analysis of the target (A) dependence in p-A collisions, it has been suggested in Ref. [89] that the Cronin effect is due to no more than one *semi*-hard collision prior to the hard scattering, and therefore saturating as a function of the N-N collision number. In this eventuality, $N \leq 2$. Recalling that, from Fig. 2.11, $\langle \Delta k_T^2 \rangle$=0.1-0.2 GeV^2 gives a reasonable description of the γ spectra in p-C, $\langle \Delta k_T^2 \rangle$-values between 0.2 and 0.3 GeV^2 seem appropriate for central Pb-Pb collisions. One should also note that the pertinent spectral enhancement in the $p_T \simeq 3$ GeV region amounts to a factor of around 3, which is quite consistent with the nuclear enhancement in π^0 production observed in the same experiment [90]. In Fig. 2.16 we have combined the baseline thermal yield (τ_0=1 fm/c, i.e. T_i=205 MeV) with 3 values for the nuclear k_T-broadening, i.e. $\langle \Delta k_T^2 \rangle$=0, 0.2 and 0.3 GeV^2. The thermal plus Cronin-enhanced pQCD spectra provide good description of the WA98 data, even with an initial temperature as low as T_i=205 MeV. This constitutes one of the main results of our work: the photon spectrum in nucleus-nucleus collisions at SPS energies is perfectly compatible with "moderate" initial temperatures. It also complements, within a common thermal framework, earlier descriptions of low- and intermediate-mass dilepton spectra [62, 68].

It is also of interest to quote the values of the transverse momentum where the pQCD yield exceeds the total thermal one; these are p_T=2.55, 1.7 and 1.55 GeV, corresponding to $\langle \Delta k_T^2 \rangle$=0, 0.2 and 0.3 GeV^2, respectively. Again, this compares well with the calculation of intermediate-mass dileptons in Ref. [68], where the Drell-Yan contribution was found to exceed the thermal one at $M_{\mu\mu} \simeq 2$ GeV.

2.7.2 *RHIC and LHC*

At collider energies the space-time evolution of the expanding QGP and hadronic fireball is expected to change in several respects. First, higher energies entail larger charged particle multiplicities per unit rapidity, dN_{ch}/dy. In central Au+Au collisions at full RHIC energy ($\sqrt{s}$ = 200 AGeV) experiments have found [91, 92] about a factor of 2 increase as compared to maximum SPS energy ($\sqrt{s}$ = 17.3 AGeV). Extrapolations into the LHC regime ($\sqrt{s}$ = 5500 AGeV) suggest another factor of up to $\sim$4 enhancement over the RHIC results.

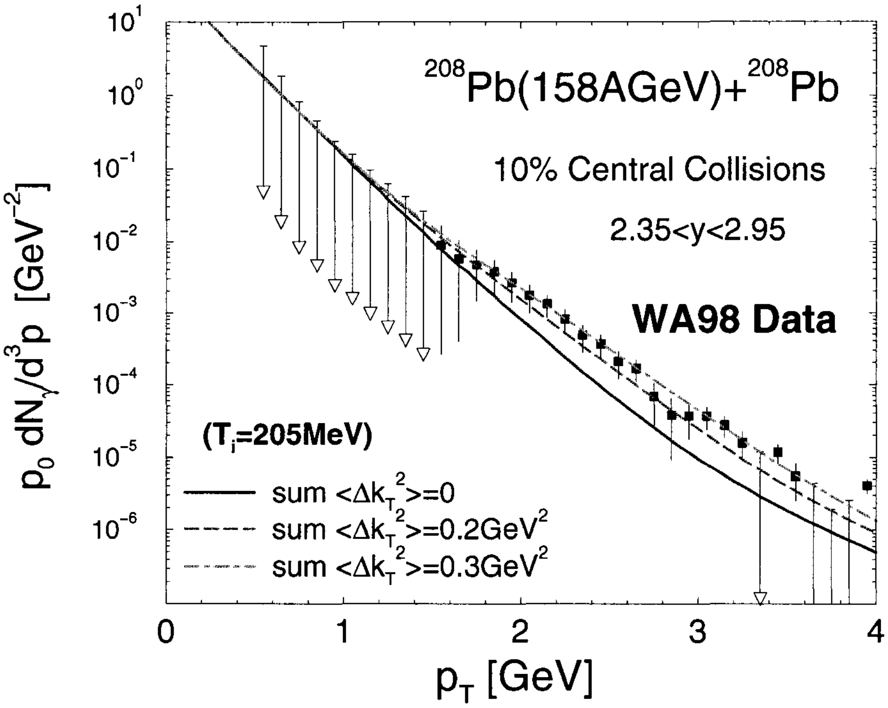

Figure 2.16: Effects of the nuclear broadening of the primordial photon spectrum on the measured spectrum. All the sources discussed in this paper are included in the space-time evolution.

Second, the *net* baryon content at midrapidity decreases, implying small baryon chemical potentials at chemical freezeout, *e.g.* $\mu_B \simeq 25$ MeV at RHIC-200. At the same time, the observed production of baryon-antibaryon pairs strongly rises, resulting in *total* rapidity densities for baryons at RHIC that are quite reminiscent of the situation at SPS energies [93]. This observation not only necessitates the explicit conservation of antibaryon-number between chemical and thermal freezeout [74] (see above), but also requires to evaluate baryonic photon sources with the *sum* of the baryon and antibaryon density.

Third, the transverse expansion (i.e. flow velocity) increases by about 20% from SPS to RHIC (presumably further at LHC), whereas the total fireball lifetime does not appear to change much. The latter, however, is likely to increase at LHC, due the significantly larger system sizes towards thermal freezeout.

All these features are readily implemented [69, 74] into the thermal fireball description employed for SPS energies above. Our thermal photon predictions for full RHIC energy are summarized in Fig. 2.17. The thermal component has been evaluated with

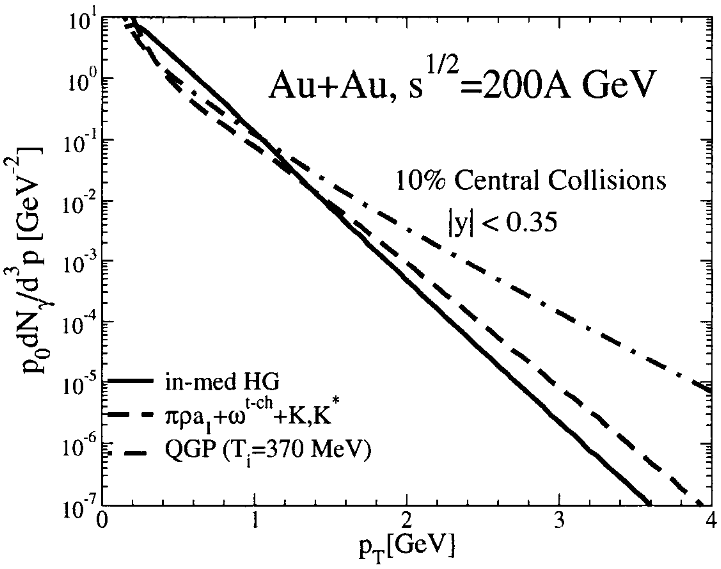

Figure 2.17: Integrated photon emission spectra from central Au+Au collisions at RHIC. Dashed-dotted line: thermal QGP radiation; dashed line: thermal meson gas emission; solid line: in-medium ρ spectral function contribution.

a typical formation time, $\tau_0 = 1/3$ fm/c, as used before in dilepton [69] application (it is also consistent with hydrodynamic approaches that correctly reproduce the elliptic flow measurements which are particularly sensitive to the early phases, see Ref. [94] for a recent review). Again, at low energies, $p_0 \leq 1$ GeV, the major source are still thermal hadrons included in the in-medium ρ spectral function, whereas the range $p_0 \geq 1$GeV appears to be a promising window to be sensitive for thermal QGP radiation. The latter has been calculated assuming chemically equilibrated quark- and gluon-densities throughout. It is conceivable, however, that the early QGP phases are gluon-dominated, i.e. with quark fugacities much smaller than one (even the gluon fugacities could be reduced). In this case, on the one hand, the photon emissivities at given temperature are severely suppressed. On the other hand, if most of the total entropy is produced sufficiently early, smaller fugacities imply larger temperatures, thus increasing the photon yield. The interplay of these effects has been studied for dilepton production in Ref. [69], where it has been found that the net effect consists of a slight hardening of the QGP emission spectrum with a pivot point at $M \simeq 3$ GeV. The prompt photon contribution will be calculated later in Chapter 4, with others high-p_T reactions.

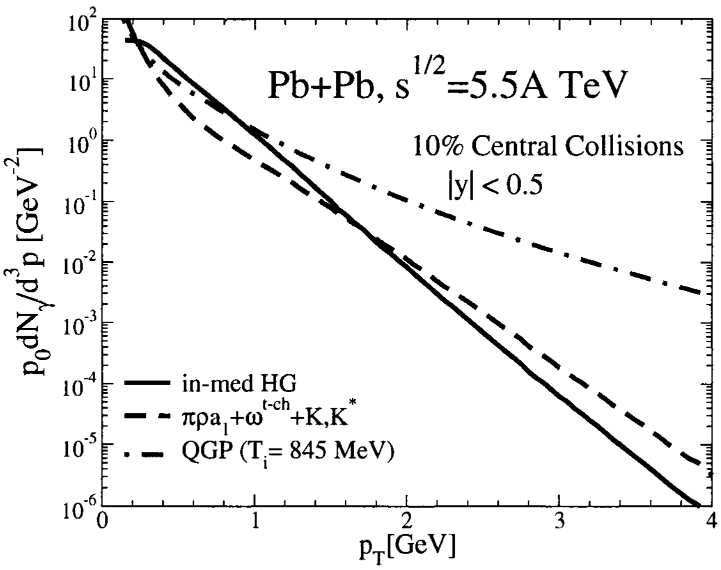

Figure 2.18: Integrated photon emission from various thermal sources in central $Pb+Pb$ collisions at the LHC; line identification as in Fig. 2.17.

We finally turn to the LHC, in Fig. 2.18. According to our estimates, assuming a formation time of 0.11 fm/c (translating into $T_i \simeq 850$ MeV for $dN_{ch}/dy \simeq 3000$), the QGP domination in the window $p_T > 1$ GeV is significantly enhanced relatively to RHIC conditions, although this feature is sensitive to the formation time and a possible chemical undersaturation of the QGP. The transition from HG to QGP dominated emission occurs again close to $p_T = 1$ GeV.

2.8 Summary

In the present chapter we have attempted an improved evaluation of hadronic thermal emission rates for real photons, suitable for realistic applications in relativistic heavy-ion collisions. In the summary below, the aspects that have been done by our collaborator are: the evaluation of photon production in the baryonic sector, and the insertion of the thermal rates into the space-time evolution like fireball model. These were done by Professor Ralf Rapp. In what we think is a more complete treatment than all of the previous ones, our main findings are:

(i) Revisited meson gas emissivities built upon an effective Lagrangian of the massive Yang-Mills type lead to about 40% reduced rates in a $\pi\rho a_1$ gas as compared to previous analyses. An inclusion of strangeness-bearing channels has revealed that the latter contribute at the 20% level. A quantitative evaluation of hadronic form factors has been performed throughout, which is mandatory for applications.

(ii) Photon rates from the baryonic sector have been obtained from a limiting procedure where in-medium ρ spectral densities were carried to the light cone. This procedure makes consistent the real photon analysis with that of low invariant mass dileptons, thereby elucidating the role of baryons in photon emission during nuclear collisions. Their contributions have been shown to be substantial for photon energies $p_0 \leq 1$ GeV.

(iii) As the single most important process at high energies we have identified ω t-channel exchange in the $\pi\rho \to \pi\gamma$ reaction, which had not been considered before.

The total hadronic emissivity has been compared to a recent complete leading-order (in strong and electromagnetic couplings) QCD calculation for the QGP. In the vicinity of the expected phase boundary both rates turned out to be very similar, at all energies of practical relevance. The net rates have been folded over a fireball evolution of nuclear collisions. This approach, albeit schematic, is consistent with observed hadrochemistry and hydrodynamic expansion characteristics, as well as dilepton and charmonium data measured at SPS energies. Using a comprehensive fit of photon cross sections in p-p and p-$\bar{p}$ interactions, an estimate of the Cronin effect (nuclear k_T-broadening) in p-A collisions was first extracted, then generalised to central Pb-Pb collisions to address the WA98 photon measurements at the SPS. Combining the complete set of hadronic rates with QGP emission and our Cronin-effect estimates on the primordial photon component, we are able to reproduce the WA98 data, with moderate values of initial temperature (T_i≃200-240 MeV) and transverse momentum broadening ($\langle \Delta k_T^2 \rangle$≃0.2-0.3 GeV^2).

3

JET ENERGY-LOSS

In this chapter, we present the model for jet energy loss that will be used for pion, photon and dilepton production in the following chapters. In this approach, derived by Peter Arnold, Guy Moore and Laurence Yaffe [31], jets loose their energy by induced gluon bremsstrahlung. We present the basic ingredients for photon emissions through LPM effect, after which the generalization to gluon emission will be done. In this model, the strong coupling constant is **assumed** to be parametrically small, $g_s = \sqrt{4\pi\alpha_s} \ll 1$. Particles with momentum of order T, where T is the temperature, will be called hard, while particles with momentum of order g_sT will be called soft.

3.1 Photon production through bremsstrahlung and annihilation processes

In Sec. 2.4, we have shown the contribution from $2 \to 2$ Compton and annihilation processes. From Eq. 2.63, their production rate, up to a log, is $\mathcal{O}(\alpha\alpha_s)$. The bremsstrahlung ($q + q(g) \to q + \gamma + q(g)$) and annihilation ($q + \bar{q} + q(g) \to \gamma + q(g)$) reactions are shown in Fig. 3.1. Here, the photons and the incoming quarks and antiquarks are hard : $|\vec{k}| \sim |\vec{p}| \sim T$. Naïvely, one expect those processes to contribute at $\mathcal{O}(\alpha\alpha_s^2)$ to the photon production rate. However, when the exchanged gluon is soft, $|\vec{q}| \sim g_sT$, its propagator $1/q^2 \sim 1/g_s^2T^2$ gives a large near on-shell enhancement which causes bremsstrahlung and annihilation processes to be as important than $2 \to 2$ scattering. From energy and momentum conservation, having a soft exchanged gluon imply a collinearity between the photon and the final quark, or between the incoming quark and antiquark for the annihilation process. This collinearity means that the scattering angle is small: $\theta \sim g_s$.

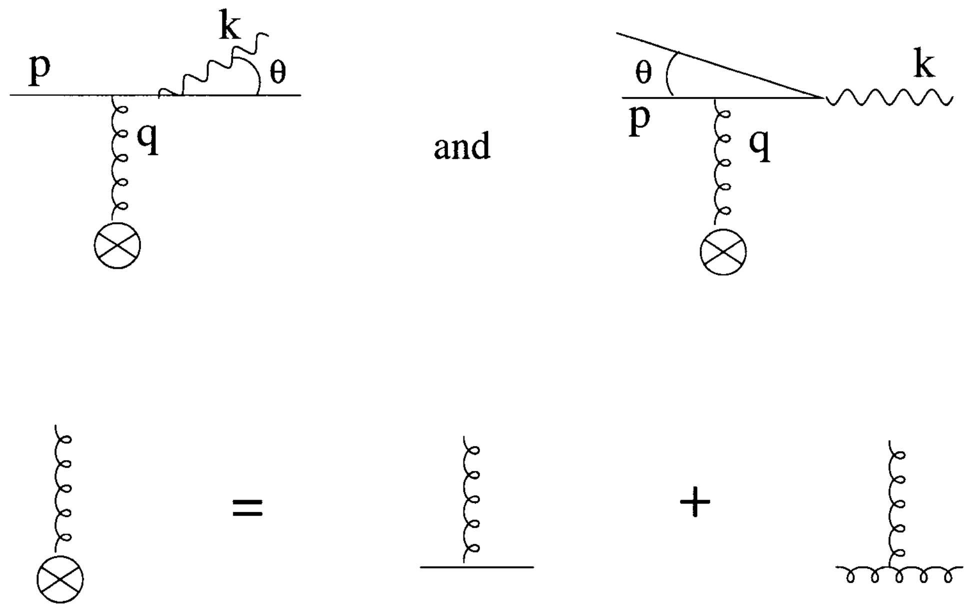

Figure 3.1: Bremsstrahlung and annihilation processes.

The collinearity condition requires that the component of $\overrightarrow{k}$ transverse to the incoming quark is $\mathcal{O}(g_sT)$. In coordinate space, it means that the photon and the quark overlap in space over a time interval $t_F \sim 1/g_s^2T$. This is the formation time of the photon, which turns out to be in the same order that the mean free path for soft scatterings of quarks with surrounding gluons [31]. Therefore, the incoming quarks are likely to have more than one soft scattering with gluons before the photon gets produced. The interference of all those scatterings, known as Laudau-Pomeranchuk-Migdal (LPM) effect [21], can affect the photon production. Then, to evaluate the diagrams in Fig. 3.1 is not enough: we need to take care of all possibles quark scatterings. From Eq. 2.1, the photon production is related to the imaginary part of the photon self-energy, which correspond to considering its cuts. This is shown in Fig. 3.2, where a photon self-energy (ladder diagram), with a given number of soft scatterings, is cut, leading directly to bremsstrahlung and annihilation process with LPM effects.

Considering bremsstrahlung for example, this corresponds to the interference of diagrams with photon emission before and after the soft scatterings. In Fig. 3.2, the curly line indicate the gluons propagator. Since the gluons are soft, $|\vec{q}| \sim g_s T$, their propagator must be resummed, as indicated by the dark circles. This resummation is performed in the hard thermal loops (HTL) approximation [150].

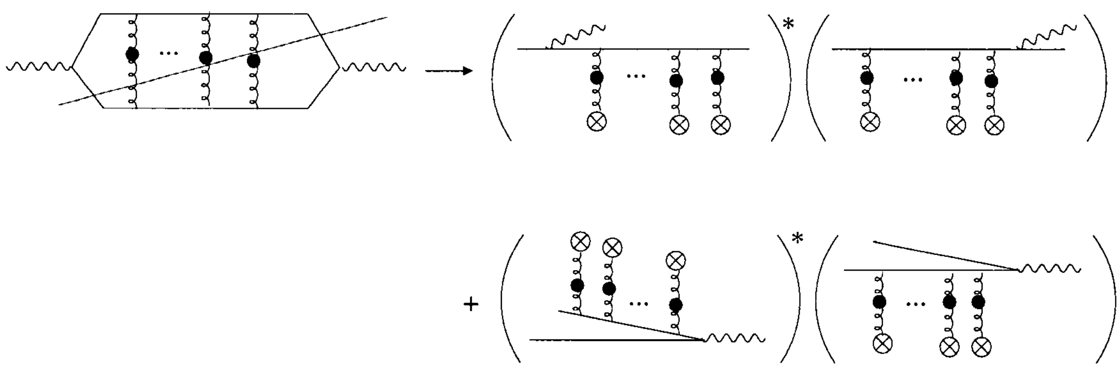

Figure 3.2: Bremsstrahlung and annihilation processes appearing from cutting a photon self-energy diagram with LPM effect.

The total photon self-energy will involve an infinite number of ladder diagrams, each with a different number of gluon rungs. AMY have written this total self-energy in terms of the solution of a linear integral equation, as depicted in Fig. 3.3, which describes the evolution in time of $|p+k\rangle\langle p,k|$ for bremsstrahlung and $|p,(k-p)\rangle\langle k|$ for annihilation. They find [96]

$$k_0 \frac{dR_{brem+anni}}{d^3\mathbf{k}} = \sum_f \left(\frac{e_f}{e}\right)^2 \frac{3\alpha}{4\pi^2} \int_{-\infty}^{\infty} \frac{dp_{||}}{2\pi} \int \frac{d^2p_T}{(2\pi)^2} \frac{f_F(p_{||}+k_0)[1-f_F(p_{||})]}{2[p_{||}(p_{||}+k_0)]^2} \times [p_{||}^2 + (p_{||}+k_0)^2] \mathrm{Re}\left\{2\mathbf{p}_T \cdot \mathbf{f}(\mathbf{p}_T; p_{||}, \mathbf{k})\right\} \tag{3.1}$$

where $p_{||}$ and p_T are the components of $\vec{p}$ respectively parallel and perpendicular to $\vec{k}$. The sections of the $p_{||}$ integral with $p_{||} > 0$, $p_{||} < -k_0$ and $-k_0 < p_{||} < 0$ correspond respectively to bremsstrahlung from quarks, bremsstrahlung from anti-quarks, and pair annihilation. The integral equation is given by

$$2\mathbf{p}_T = i\delta E\, \mathbf{f}(\mathbf{p}_T; p_{||}, k_0) + \frac{2\pi}{3} g_s^2 \int \frac{d^2q_T}{(2\pi)^2} C(\mathbf{q}_T) T \left[\mathbf{f}(\mathbf{p}_T; p_{||}, k_0) - \mathbf{f}(\mathbf{p}_T - \mathbf{q}_T; p_{||}, k_0)\right] , \tag{3.2}$$

and the energy difference between the initial and the final states is

$$\delta E = \frac{p_T^2 + 2m_{\mathbf{F}}^2}{2} \frac{k_0}{p_{||}(k_0 + p_{||})}, \tag{3.3}$$

where $\sqrt{2}m_F = g_s T/\sqrt{3}$ is the effective quark thermal mass. Here $C(\mathbf{q}_\perp)$ is the differential rate to exchange transverse (to the parton) momentum $\mathbf{q}_\perp$. In a hot thermal medium, its value at leading order in α_s is [95]

$$C(\mathbf{q}_\perp) = \frac{m_{\mathrm{D}}^2}{\mathbf{q}_\perp^2(\mathbf{q}_\perp^2 + m_{\mathrm{D}}^2)}, \quad m_{\mathrm{D}}^2 = \frac{g_{\mathrm{s}}^2 T^2}{6}(2N_{\mathrm{c}} + N_{\mathrm{f}}). \tag{3.4}$$

where m_D is the color Debye mass. After solving the integral equation numerically, AMY have expressed their result for the photon production rate by the following parametrization [66] as

$$k_0 \frac{dR_{brem+anni}}{d^3\mathbf{k}} = \sum_f \left(\frac{e_f}{e}\right)^2 \frac{T^2 \alpha \alpha_s}{\pi^2} f_F(k_0) B\left(\frac{k_0}{T}\right) \tag{3.5}$$

with

$$B(x) = \sqrt{\frac{3}{2}} \left[\frac{0.548 \ln(12.28 + 1/x)}{x^{3/2}} + \frac{0.133\,x}{\sqrt{1 + x/16.27}} \right] \tag{3.6}$$

Now, by adding Eq. 3.5 to the quark-photon conversion process, Eq. 2.63, we get a complete leading order α_s result for the photon production rate.

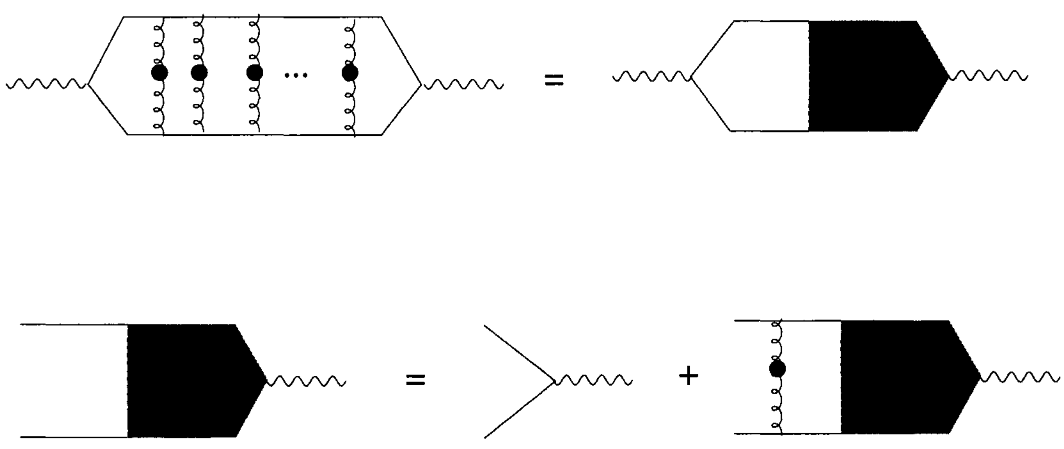

Figure 3.3: Photon self-energy written in terms of the solution to a linear integral equation.

3.2 Gluon production rate

The gluon production can be evaluated within the same formalism. Indeed, it is still possible to resum the diagrams by an integral equation similar to that for photon production rate (see Fig. 3.3). The complication is that gluons, unlike the photons, can scatter during the formation time $t_f \sim 1/g_s^2 T$. This is pictured in Fig. 3.4, for a gluon bremsstrahlung process. The corresponding equation for the gluon production rate, from $q(p+k) \to q(p) + g(k)$ and $q(p) + \bar{q}(k-p) \to g(k)$, is

$$k_0 \frac{dR^g}{d^3\mathbf{k}} = \frac{g_s^2}{16(2\pi)^3 k_0^4} \sum_s N_s d_s C_s \int_{-\infty}^{\infty} \frac{dp}{2\pi} \int \frac{d^2\mathbf{h}}{(2\pi)^2} f_F(p+k_0)[1 - f_F(p)][1 + f_B(k_0)] \times \frac{p^2 + (p+k_0)^2}{p^2(p+k_0)^2} 2\mathbf{h} \cdot \mathrm{Re}\, \mathbf{F}(\mathbf{h}, p, k_0)\,, \tag{3.7}$$

where N_s is the spin-antiparticle degeneracy, and d_s is the color degeneracy.

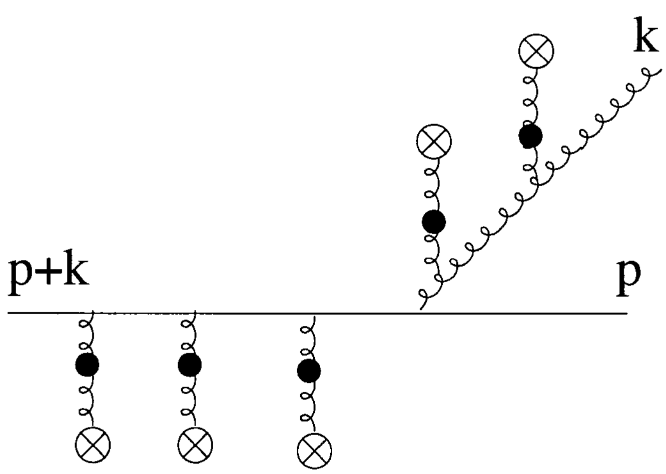

Figure 3.4: A typical bremsstrahlung diagram that needs to be resummed.

However, since we want to find the evolution in time of the jet distribution, it is more convenient to extract the transition rate: $\frac{d\Gamma^q_{qg}(p,k)}{dtdk}$. It represents the probability, per unit of time and gluon momentum k, that an initial quark with momentum p produces a gluon. The gluon production rate can be written in terms of the transition rate by:

$$k_0 \frac{dR^g}{d^3\mathbf{k}} = k_0 \frac{dN^g}{d^3\mathbf{k} d^3x dt} = \sum_p \frac{\text{Number of quark, with mom. } p}{\text{Volume}} \times k_0 \frac{d\Gamma^q_{qg}(p,k)}{dtd^3\mathbf{k}}$$

$$= \sum_s N_s d_s \int \frac{dp\, p^2\, d\Omega}{(2\pi)^3} f_F(p) \frac{d\Gamma^q_{qg}(p,k)}{k_0\, dtdkd\Omega}$$
$$= \sum_s N_s d_s \int \frac{dp}{(2\pi)^3} f_F(p) \frac{p^2}{k_0} \frac{d\Gamma^q_{qg}(p,k)}{dtdk} \tag{3.8}$$

Hence, the transition rate can easily be obtained from Eq. 3.7 (with $p \to p - k_0$) and Eq. 3.8. As the gluon can also scatter into the medium, the other transitions $g \to gg$ and $g \to qq$ have to be evaluated also. The complete expression for all those transition rate turns out to be

$$\frac{d\Gamma(p,k)}{dkdt} = \frac{C_s g_s^2}{16\pi p^7} \frac{1}{1 \pm e^{-k/T}} \frac{1}{1 \pm e^{-(p-k)/T}} \times \left\{ \begin{array}{cc} \frac{1+(1-x)^2}{x^3(1-x)^2} & q \to qg \\ N_{\rm f} \frac{x^2+(1-x)^2}{x^2(1-x)^2} & g \to qq \\ \frac{1+x^4+(1-x)^4}{x^3(1-x)^3} & g \to gg \end{array} \right\} \times$$
$$\times \int \frac{d^2\mathbf{h}}{(2\pi)^2} 2\mathbf{h} \cdot \mathrm{Re}\, \mathbf{F}(\mathbf{h},p,k)\,, \tag{3.9}$$

where the gluon energy has been set to k to simplify the notation. Here C_s is the quadratic Casimir relevant for the process (in QCD, 4/3 for processes involving a quark and 3 for the pure glue process), and $x \equiv k/p$ is the momentum fraction in the gluon (or the quark, for the case $g \to q\bar{q}$). The factors $1/(1 \pm e^{-k/T})$ are Bose stimulation or Pauli blocking factors for the final states, with $-$ for bosons and $+$ for fermions. $\mathbf{h} \equiv \mathbf{p} \times \mathbf{k}$ determines how non-collinear the final state is; it is taken as $\mathcal{O}(gT^2)$ parametrically and therefore small compared to $\mathbf{p} \cdot \mathbf{k}$. Therefore it can be taken as a two-dimensional vector in the transverse space. $\mathbf{F}(\mathbf{h},p,k)$ is the solution of the following integral equation:

$$\begin{aligned} 2\mathbf{h} = i\delta E(\mathbf{h},p,k)\mathbf{F}(\mathbf{h}) + g_s^2 \int \frac{d^2\mathbf{q}_\perp}{(2\pi)^2} C(\mathbf{q}_\perp) \Big\{ & (C_s - C_{\rm A}/2)[\mathbf{F}(\mathbf{h}) - \mathbf{F}(\mathbf{h}-k\,\mathbf{q}_\perp)] \\ & + (C_{\rm A}/2)[\mathbf{F}(\mathbf{h}) - \mathbf{F}(\mathbf{h}+p\,\mathbf{q}_\perp)] \\ & + (C_{\rm A}/2)[\mathbf{F}(\mathbf{h}) - \mathbf{F}(\mathbf{h}-(p-k)\,\mathbf{q}_\perp)] \Big\}\,. \end{aligned} \tag{3.10}$$

The energy difference between the final and the initial states is given by

$$\delta E(\mathbf{h},p,k) = \frac{\mathbf{h}^2}{2pk(p-k)} + \frac{m_k^2}{2k} + \frac{m_{p-k}^2}{2(p-k)} - \frac{m_p^2}{2p}\,, \tag{3.11}$$

where m^2 are the medium induced thermal masses, equal to $m_D^2/2$ for a gluon and $C_f g_s^2 T^2/4 = g_s^2 T^2/3$ for a quark. For the case of $g \to qq$, $(C_s - C_A/2)$ should appear as the prefactor on the term containing $\mathbf{F}(\mathbf{h} - p\,\mathbf{q}_\perp)$ rather than $\mathbf{F}(\mathbf{h} - k\,\mathbf{q}_\perp)$.

One limitation of the current formalism, is that the transition rates are calculated in momentum space assuming the thermodynamic limit. That is, this approach assumes that the incoming parton experiences a uniform medium on the time scale of the formation time of the emitted radiation. Hence, this approach is limited to parton momenta p less than the factorization energy $E_{fact} = \mu^2 L^2/\lambda\hbar$ [97], where μ is the typical size of the soft momentum exchange, λ is the relative size of the mean free path, and L is the size of the hot medium. The factorization limit is reached when the coherence length become as big as L. With $\mu \approx 0.5\,\text{GeV}$, $L \approx 5\,\text{fm}$ and $\lambda \approx 1$ fm, this limits the momenta to the region $p < 30\,\text{GeV}$. This is not a big problem at RHIC energies, where $\sqrt{s_{NN}}$ is only 200 GeV, and it also covers the p_T acceptance of the ALICE detector at the LHC.

3.3 Time evolution of the jet momentum distribution

Next, we use the transition rate expressions to evolve the hard gluon distribution $P_g(p, t=0)$ and the hard quark plus antiquark distribution $P_{q\bar{q}}(p, t=0)$ with time, as they traverse the medium. The joint equations for $P_{q\bar{q}}$ and P_g are

$$\begin{aligned}
\frac{dP_{q\bar{q}}(p)}{dt} &= \int_k P_{q\bar{q}}(p+k)\frac{d\Gamma^q_{qg}(p+k,k)}{dkdt} - P_{q\bar{q}}(p)\frac{d\Gamma^q_{qg}(p,k)}{dkdt} + 2P_g(p+k)\frac{d\Gamma^g_{q\bar{q}}(p+k,k)}{dkdt}\,, \\
\frac{dP_g(p)}{dt} &= \int_k P_{q\bar{q}}(p+k)\frac{d\Gamma^q_{qg}(p+k,p)}{dkdt} + P_g(p+k)\frac{d\Gamma^g_{gg}(p+k,k)}{dkdt} \\
&\quad - P_g(p)\left(\frac{d\Gamma^g_{q\bar{q}}(p,k)}{dkdt} + \frac{d\Gamma^g_{gg}(p,k)}{dkdt}\Theta(2k-p)\right),
\end{aligned} \tag{3.12}$$

where the k integrals run from $-\infty$ to ∞. The integration range with $k < 0$ represents absorption of thermal gluons from the QGP; the range with $k > p$ represents annihilation against an antiquark from the QGP, of energy $(k-p)$. In writing Eq. (3.12), we used $d\Gamma^g_{gg}(p,k) = d\Gamma^g_{gg}(p,p-k)$ and similarly for $g \to qq$; the Θ function in the loss term for $g \to gg$ prevents double counting of final states. Since bremsstrahlung energy loss involves only small $\mathcal{O}(g_s T/p)$ changes to the directions of particles, these equations can be used for the momentum distributions in any particular direction. For a single initial hard particle, $P_{q\bar{q}}(p) = \delta(p - p_0)$, they can be viewed as Fokker-Planck equations for the evolution of the probability distribution of the particle energy and of accompanying gluons. These expressions depend at several points on g_s^2 or α_s. When evaluating them numerically, we have used $\alpha_s = 0.3$, as it is expected for a QGP with temperature $T \sim 400$ MeV [11].

The time evolution of the initial quark+antiquark jet distribution

$$P_{q\bar{q}} = \frac{dN^{q\bar{q}}(p_T)}{dp_T} \propto p_T \frac{dN^{q\bar{q}}}{dy d^2 p_T} \tag{3.13}$$

is shown in Fig. 3.5. The QGP expansion is neglected and the temperature is frozen at $T = 400$ MeV, in order to highlight the effect of energy loss. In the following chapters, the matter expansion and the temperature cooling will be consistently convolved with the jet-suppression formalism shown here.

The initial jet distribution $dN^{q\bar{q}}/dyd^2p_T$ is taken from Eq. 4.48, for RHIC. We observe that the p_T suppression scales with time: the bigger the propagation length, the more important is the energy loss by the jets. The energy loss is less important for small jet momentum, $p_T < 10$ GeV, since there is a compensation between the emission of bremsstrahlung gluons, and the absorption of thermal gluons from the QGP.

The effect of the LPM suppression is also shown in Fig. 3.5, by the double-dot dashed line. This line has been evaluated in a no-LPM scenario, which correspond to solving Eq. 3.10 under the assumption that δE is much greater than the collision term which follow it. While the LPM effect turns out to be small for $p_T \sim$ 5-10 GeV, it becomes important for more energetic partons, reducing the suppression by more than a factor 2.

To conclude, the AMY formalism differs from other energy loss models, like Baier-Dokshitzer-Mueller-Peigné-Schiff (BDMPS) [22, 23], Gyulassy-Levai-Vitev (GLV) [24], Kovner-Wiedemann (KW) [25] and Zakharov [26], in some major ways. The biggest

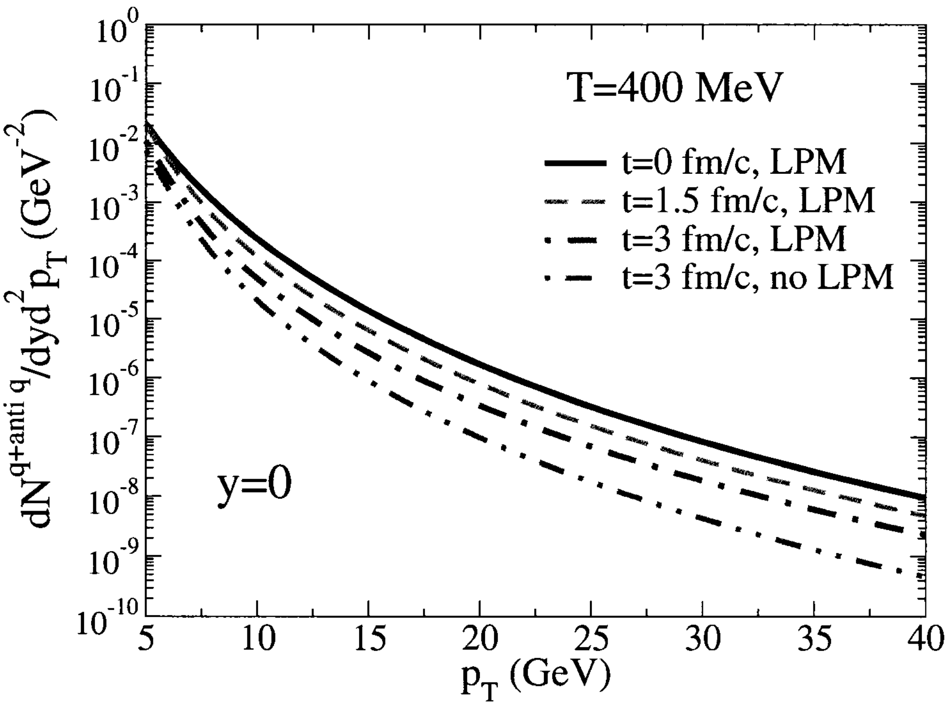

Figure 3.5: Time evolution of the quark+antiquark momentum distribution, in a stationary QGP at constant temperature T =400 MeV.

difference is that the calculation is completely thermal and hence the scatterers are all dynamic. In this calculation, temperature enters through the thermal phase space of the initial and the final particles and there is no assumption of the form of the elementary cross-section. All are calculated completely within the framework of hard thermal loop resummed leading order thermal QCD. Hence, gain or loss due to the absorption of thermal partons as well as the loss process of pair annihilations with the thermal partons are fully included in our calculation. These are missing in the approaches mentioned above. In Ref. [98], thermal absorption and stimulated emission were introduced in the framework of GLV. This was done only up to the first order in the opacity expansion without including the annihilation process with thermal partons. Finally, there are no approximations about whether the Bethe-Heitler or LPM regime is relevant; the transition between these extremes is handled correctly.

4

Production of high-p_T photons.

In this chapter, we use the AMY formalism to calculate the p_T suppression of the jets as they propagate through the QGP. This model is first tested by calculating nuclear modification factor of neutral pions in central Au-Au collisions at RHIC ($\sqrt{s}$ = A$\sqrt{s_{NN}}$=200A GeV) and Pb-Pb collisions at the LHC ($\sqrt{s}$=5.5A TeV). The AMY formalism is convolved with a physical description of the initial spatial distribution of jets and a one dimensional hydrodynamic expansion. We reproduce the nuclear modification factor of pion R_{AA} at RHIC, assuming an initial temperature T_i =370 MeV and a formation time τ_i =0.26 fm/c, corresponding to dN/dy = 1260. The resulting suppression depends on the particle rapidity density dN/dy but weakly on the initial temperature. The jet energy loss treatment is finally included in the calculation of high p_T photons. Photons coming from primordial hard N-N scattering turn out to be the dominant contribution at RHIC for p_T > 5 GeV, while the jet-photon conversion in the plasma dominates for 2 < p_T < 4 GeV, and are thus important for reproducing the new data from RHIC. The range 8 < p_T < 14 GeV is dominated by jet-photon conversion in the plasma at the LHC.

4.1 *Pion production*

The goal of this section is to use the formalism explained in the previous chapter to calculate the neutral pion spectrum in heavy ion collisions. Our approach to this problem relies on the fact that for hard spectra, the AA collision can be regarded as a collection of binary collisions. In this way of formulating the problem, the

AA spectrum is given by the convolution of the elementary nucleon-nucleon (NN) spectrum with geometrical and in-medium factors.

The production of high-p_T particles can by calculated within the factorization theorem [99]. The production of a jet (fast parton having $p_T^{jet} \gg 1$ GeV), at the partonic level, imply a timescale $\sim 1/p_T^{jet}$, which is much smaller than the timescale for the fragmentation of this jet into pions. Thus, we can factorize those two processes and neglect the interference between them. The derivation of the pion production goes as follow. First, the probability to find a parton a, inside the nucleon, with an energy fraction $x_a = E_a/E_N$, is $g(x_a, Q)$, where E_a and E_N are the parton and nucleon energies in the NN center of mass, while Q is the factorization scale. The parton distribution function (PDF) is normalized as

$$\sum_f \int dx_a \, x_a g(x_a) = 1 \,, \tag{4.1}$$

where the sum runs over flavours. The cross-section for the subprocess $a + b \to c + d$ is [99]

$$\begin{aligned} d\sigma_{a+b\to jet+d} = & \frac{1}{4E_a E_b |v_a - v_b|} \left|\mathcal{M}_{a+b\to c+d}\right|^2 \frac{d^4p_c d^4p_d}{(2\pi)^2} \\ & \times \delta^4(p_a + p_b - p_c - p_d)\delta(p_c^2)\delta(p_d^2) \end{aligned} \tag{4.2}$$

In the factorization limit, all external particles are assumed to be on-shell. The c-jet cross-section at the NN level, assuming that the momentum's components of a and b, transverse to the beam direction, are negligibles, will be

$$\begin{aligned} d\sigma^{NN}_{A+B\to c+x} &= \sum_{a,b} \int dx_a \, g(x_a, Q) \int dx_b \, g(x_b, Q) d\sigma_{a+b\to c+d} \\ &= \sum_{a,b} \int dx_a \, g(x_a, Q) \int dx_b \, g(x_b, Q) \\ & \times \frac{\hat{s}}{\pi} K_{jet} \frac{d\sigma^{a+b\to c+d}}{dt} \frac{d^3p_c}{E_c} \delta(\hat{s} + \hat{t} + \hat{u}) \,. \end{aligned} \tag{4.3}$$

The parton-parton cross-section at leading order [8] has been defined by

$$\frac{d\sigma^{a+b\to c+d}}{dt} = \frac{\left|\mathcal{M}_{a+b\to c+d}\right|^2}{16\pi \hat{s}^2} \tag{4.4}$$

with

$$\hat{s} = s_{NN}\, x_a x_b\,, \quad \hat{t} = -\sqrt{s_{NN}}\, x_a p_\perp^c e^{-y_c}\,, \quad \hat{u} = -\sqrt{s_{NN}}\, x_b p_\perp^c e^{y_c} \tag{4.5}$$

The factor K_{jet} accounts for higher order effects. According to [100], K_{jet} is almost p_T^{jet} independent at RHIC energies. We will use $K_{jet} \sim 1.7$ for RHIC and 1.6 for the LHC, based on these results.

Now, we introduce the pion fragmentation function $D_{\pi^0/c}(z, Q^{'})$, which represent the probability for a c-jet to fragments into pions. The fragmentation of a jet into pions involves small momentum exchange: thus $D_{\pi^0/c}$ is not calculable in perturbation theory, and experimental input is needed. The collinearity of the fragmentation imply that the mesons come out $\sim$ parallel to the incoming quark, and $z = |\vec{p}_\pi|/|\vec{p}_c|$ represent the fraction momentum transfered to the pion. The pion cross-section becomes:

$$\begin{aligned} d\sigma_\pi^{NN} &= \sum_{a,b,c,d} \int dx_a\, g(x_a, Q) \int dx_b\, g(x_b, Q) d\sigma_{a+b\to c+d} \int dz D_{\pi^0/c}(z, Q^{'}) \\ &= \sum_{a,b,c,d} \int dx_a dx_b g(x_a, Q) g(x_b, Q) \int dz D_{\pi^0/c}(z, Q^{'}) \\ &\times \int \frac{d^3p_c}{E_c}\frac{\hat{s}}{\pi} K_{jet} \frac{d\sigma^{a+b\to c+d}}{dt} \delta(\hat{s}+\hat{t}+\hat{u}) \end{aligned} \tag{4.6}$$

With the integration elements given by $d^3p_c/E_c = d^3p_\pi/E_\pi/z^2 = d^2p_T\, dy/z^2$, the pion differential cross-section is

$$\frac{d\sigma_\pi^{NN}}{d^2p_T dy} = \sum_{a,b,c,d} \int dx_a dx_b g(x_a, Q) g(x_b, Q) K_{jet} \frac{d\sigma^{a+b\to c+d}}{dt} \frac{1}{\pi z} D_{\pi^0/c}(z, Q^{'})\,. \tag{4.7}$$

For all our calculations, we set the factorization scale (Q) and the fragmentation scale ($Q^{'}$) equal to p_T. We use the CTEQ5 parton distribution function [101], and the π fragmentation function as extracted from e^+e^- collisions [102].

Fig. 4.1 shows our calculation for the spectrum of high p_T neutral pions in pp collisions at RHIC, compared to PHENIX results [103]. One can readily see that our calculation reproduces the data in the region where jet fragmentation is expected to be the dominant mechanism of particle production ($p_T > 5$ GeV/c) [104], while low-p_T

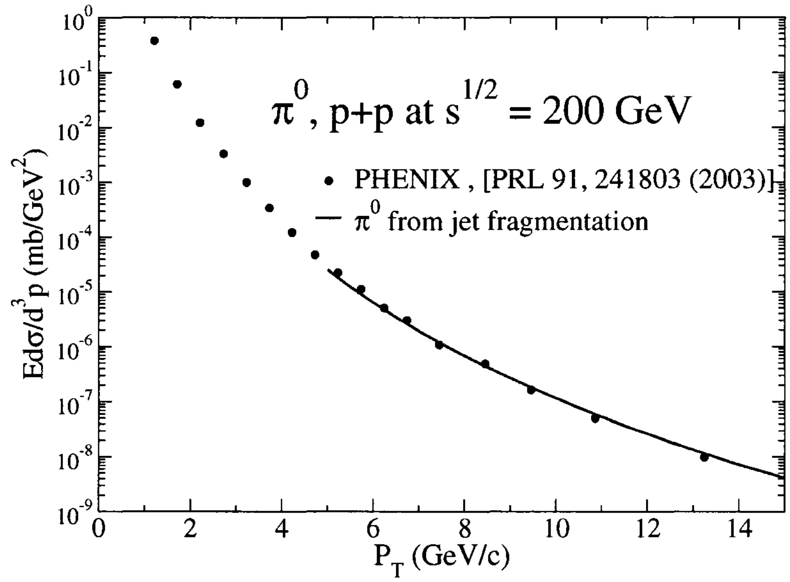

Figure 4.1: Neutral pion spectra in *pp* collisions at RHIC. The data points are from PHENIX and the solid line is the calculated result from jet fragmentation.

pions, which are not under study here, should be created rather by recombination of partons produced during the NN scattering. This represents a solid baseline result.

In AB collisions, in the approximation of superposition of independent NN collisions, the yield of π is given by

$$\frac{dN_\pi^{AB}}{dyd^2p_T} = \frac{\langle N_{\rm coll}\rangle}{\sigma_{in}}\frac{d\sigma_{NN}^{AB}}{dyd^2p_T} \tag{4.8}$$

where $d\sigma_{NN}^{AB}/dyd^2p_T$ is the cross-section at the NN level (including initial and final state effects), $\langle N_{\rm coll}\rangle$ is the average number of NN collisions and σ_{in} is the total inelastic nucleon-nucleon cross-section. The high p_T data in AB collisions can be characterized by the nuclear modification factor:

$$R_{AB} = \frac{dN_\pi^{AB}/dyd^2p_T}{\langle N_{\rm coll}\rangle dN_\pi^{NN}/dyd^2p_T} = \frac{d\sigma_{NN}^{AB}/dyd^2p_T}{d\sigma_\pi^{NN}/dyd^2p_T} \tag{4.9}$$

In the absence of nuclear effect, we get $R_{AB} = 1$. The signature of a Cronin effect would be $R_{AB} > 1$, while high p_T suppression would give $R_{AB} < 1$. To obtain the high p_T π^0 cross-section in AB collisions, we will modify $d\sigma_{NN}^{AB}/dyd^2p_T$ in some ways.

First, the PDF of a nucleus differs from that of a proton;

$$g_A(x_a, Q) = g(x_a, Q) R_A(x_a, Q) \, , \tag{4.10}$$

where the nuclear modification of the structure function R_A takes into account shadowing and anti-shadowing [105]. In this work, we use $R_A(x_a, Q)$ as parametrized by Eskola *et al.* [106].

It's important to verify, before including energy loss effect, if whether or not multiple scattering effects in the initial state must be included in the calculations. This is the well-known Cronin effect caused by multiple soft scatterings a parton may suffer before it makes a hard collision. We have seen in Chapter 2 that it was very important at SPS energies. For RHIC and LHC energies, we expect this effect to be less important, as the elastic cross-section decreases with increasing $\sqrt{s_{NN}}$. A good way to verify at RHIC energies is to take advantage of available data on d-Au collisions, which should not include final state effect. Thus, if important deviation from p-p collisions is seen, it will be an indication of the presence of Cronin effect. Fig. 4.2 shows the neutral pion data in d-Au collisions at RHIC [15] with our calculation for jet-fragmentation with shadowing effect (solid line). Our calculations cover only the high-p_T range of the spectrum, where nucleus-nucleus collisions are expected to scale with the number of nucleon-nucleon collisions. At lower p_T values, the interference between differents NN scatterings cannot be neglected, and the pion production scales rather with the number of participant nucleons. This is why the experimental data in Fig. 4.2 shows $R_{dA} < 1$ in this region. For the high-p_T range, we see that the 1.1-1.2 averaged value of R_{dA} can be reproduced by shadowing effects, so that we will neglect any Cronin effect at RHIC and LHC energies. This represents another step in the establishment of a baseline result. The good fit to R_{dA} also supports the smallness of jet-energy loss in ordinary nuclear matter.

For Au-Au however, as the density reached should be much bigger that for d-Au, we must account for the energy loss of the parton between its production in the hard initial scattering event and its hadronization. We will assume that a jet fragments

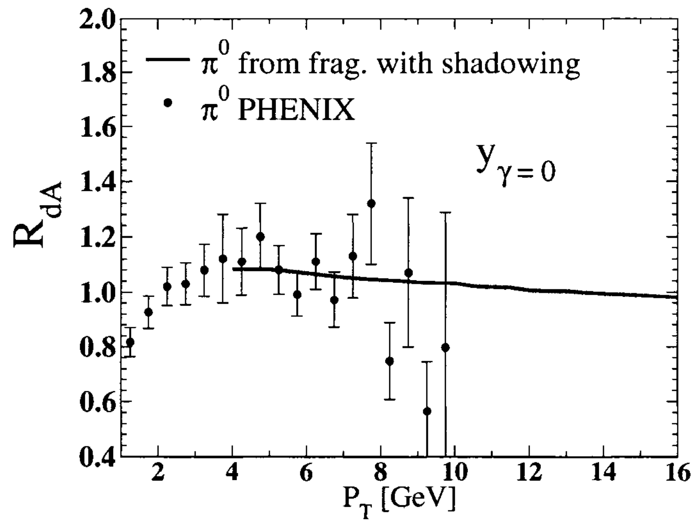

Figure 4.2: Neutral pion spectra in d-Au collisions at RHIC, for $\sqrt{s_{NN}} = 200$ GeV. The data points are from PHENIX and the solid line is the calculated result from jet fragmentation with shadowing effect.

only outside the medium, as may be justified by estimating the formation time of a pion with a typical observed energy. In Ref.[107], the formation time of an emitted pion with energy E_π is estimated to be $\sim R_\pi \frac{E_\pi}{m_\pi}$, where $R_\pi \sim 1$fm is the size of the pion. For a 10 GeV pion, this gives $\tau_f \sim$ 35-70 fm/c. This is much longer than the time spent by a jet in the hot matter created by two colliding nuclei. Therefore, one should consider production, energy loss in medium, and fragmentation to occur sequentially.

We will assume that the fragmentation at the edge of the QGP involves the usual vacuum fragmentation function. The medium effect is then to reduce the parton energy by an amount determined by the Fokker-Planck equations previously presented, Eq. (3.12). As energy loss involve only $O(\sqrt{\alpha_s})$ changes in the direction propagation of the partons, we assume that they keep propagating in the same direction they have been produced. For a final state parton c of momentum p_f, the vacuum fragmentation function is normalized as

$$\sum_h \int_0^{p_f/p_i} dz^0\, z^0\, D_{h/c}(z^0) = 1 - \frac{p_f - p_i}{p_i} = \frac{p_f}{p_i} \tag{4.11}$$

where p_i was the parton's initial momentum, with $p_f < p_i$. As final hadrons fragment from the final momentum p_f rather than from p_i, we can define an effective fragmentation function

$$D_{h/c}^{eff}(z) = \frac{z'}{z} D_{h/c}(z') \tag{4.12}$$

where z'/z is a normalization factor, $z = p_T/p_i$, $z' = p_T/p_f$ and p_T is the momentum (transverse) of the final hadron h. As we calculate only midrapidity hadrons, we have $|\vec{p}| = p_T$. Including now the distribution of possible final states, this is most conveniently written by defining a new medium-inclusive effective fragmentation function,

$$\tilde{D}_{\pi^0/c}(z, Q, \mathbf{r}_\perp, \mathbf{n}) = \int dp_f \frac{z'}{z} \left(P_{q\bar{q}/c}(p_f; p_i|d) D_{\pi^0/q}(z', Q) + P_{g/c}(p_f; p_i|d) D_{\pi^0/g}(z', Q) \right) , \tag{4.13}$$

where $P_{q\bar{q}/c}(p_f; p_i|d)$ and $P_{g/c}(p_f; p_i|d)$ represents the solution to Eq. (3.12), which is the probability to get a given parton with final momentum p_f when the initial condition is a particle of type c and momentum p_i, after a propagation distance d in the hot-medium. This path length is not the same for all jets, because it depends on the location where the jet is produced and on the direction in which the jet propagates. Therefore, one must convolve this expression over all transverse positions $\mathbf{r}_\perp$ and directions $\mathbf{n}$. Since the number of jets at $\mathbf{r}_\perp$ is proportional to the number of binary collisions, the probability is proportional to the the product of the thickness functions of the colliding nuclei at $\mathbf{r}_\perp$. For central collisions where the impact parameter $b \approx 0$, we get

$$\mathcal{P}(\mathbf{r}_\perp) \propto T_A(\mathbf{r}_\perp)\, T_B(\mathbf{r}_\perp) \,. \tag{4.14}$$

For a hard sphere which we use for simplicity, this probability is

$$\mathcal{P}(\mathbf{r}_\perp) = \frac{2}{\pi R_\perp^2} \left(1 - \frac{r_\perp^2}{R_\perp^2} \right) \theta(R_\perp - r_\perp) \,, \tag{4.15}$$

which is normalized to yield $\int d^2 r_\perp\, \mathcal{P}(\mathbf{r}_\perp) = 1$. Since the direction of the jet is fixed by the pion direction ($\mathbf{n} = \frac{\mathbf{p}_\pi}{|\mathbf{p}_\pi|}$), the final in-medium modified fragmentation function is

$$\tilde{D}_{\pi^0/c}(z, Q) = \int d^2 r_\perp\, \mathcal{P}(\mathbf{r}_\perp) \tilde{D}_{\pi^0/c}(z, Q, \mathbf{r}_\perp, \mathbf{n}) \,. \tag{4.16}$$

The AA cross-section is now given by

$$\frac{d\sigma_{NN}^{AA}}{dyd^2p_T} = \sum_{a,b,c,d} \int dx_a dx_b \, g_A(x_a, Q) g_A(x_b, Q) K_{jet} \frac{d\sigma^{a+b\to c+d}}{dt} \frac{\tilde{D}_{\pi^0/c}(z, Q)}{\pi z}, \tag{4.17}$$

Since Eq. (4.17) is expressed in terms of probability distributions, it is straightforward to evaluate it using the Monte-Carlo method. One complication in doing so is that, while the parton traverses the medium, the medium also evolves. Therefore at each time step of solving Eq. (3.12), the temperature must be adjusted to reflect the local environment. In Chapter 2, we used a fireball model [62], in which at a given time, the yield of photons was simply given by the product of the production rates and the volume of the expanding hot matter. Here however, as we have to follow the path of the jets in the matter, such that their exact positions at a given time is really important, we cannot use again the fireball model. We will rather use the 1-D Bjorken expansion model [110] which incorporates the information about the local temperature in a slice of expanding matter.

We assume that the medium expands only in the longitudinal direction, based on the following reasoning. The low p_T neutral pion spectrum at RHIC is well reproduced by a hydrodynamical model incorporating transverse expansion, while the model fails for $p_T > 3$ GeV, suggesting that high-p_T pions mainly come from jet fragmentation [108]. The transverse expansion will have two effects on jet energy loss. First, the expanding geometry will increase the duration of parton propagation. However, the same expansion will make for a falling parton density along the path. Those two effects partially compensate each other and the energy loss is just about the same as in the case without transverse expansion [109].

4.1.1 The Bjorken model

In the absence of viscosity, the evolution of a fluid is governed by

$$\partial_\mu T^{\mu\nu} = 0 \tag{4.18}$$

The energy-momentum tensor is

$$T^{\mu\nu} = (\epsilon + p)u_\mu u_\nu - g_{\mu\nu}P\,, \tag{4.19}$$

ϵ is the energy density and P is the pressure. For a thermal medium expanding only in the z direction, its four-velocity has non-zero components in the t and z direction only:

$$u_\mu = \frac{\partial x_\mu}{\partial \tau} = \left(\frac{\partial t}{\partial \tau}, 0, 0, \frac{\partial z}{\partial \tau}\right) \tag{4.20}$$

where we have defined the proper time $\tau = \sqrt{t^2 - z^2}$. We now define the space-time rapidity:

$$\eta = \frac{1}{2}\ln\left(\frac{1 + z/t}{1 - z/t}\right) \tag{4.21}$$

In the Bjorken scenario [110] is a central-plateau structure for the particle rapidity density in nucleus-nucleus collisions, i.e dN/dy independent of y in a given range. Also, in heavy ion collision at relativistic energies, the overlap region of the two nuclei can be pictured as a disk, with a very small width due to Lorentz contraction in the z-direction. It is reasonable to considered particle in the central rapidity region as having been emitted from this thin disk. This leads to following scaling behaviour:

$$v_z = z/t \tag{4.22}$$

With this, the space-time rapidity becomes equal to the rapidity:

$$\eta = \frac{1}{2}\ln\left(\frac{1 + z/t}{1 - z/t}\right) \rightarrow \frac{1}{2}\ln\left(\frac{1 + v_z}{1 - v_z}\right) = y\,. \tag{4.23}$$

This imply that dN/dy, and all thermodynamic quantities are also independent of η. Eq. 4.18 now simplifies to

$$\frac{ds}{d\tau} = -\frac{s}{\tau} \tag{4.24}$$

where $s = (\epsilon + P)/T$[1] is the entropy density, and the solution is

$$s\tau = C(r)\,. \tag{4.25}$$

[1] In this section, in order to be consistent with the literature, s will stand for the entropy density rather that the energy in the nucleus-nucleus center of mass.

C is a constant, which can depends on the radial position r if a transverse profile is included. The entropy density for a gas of quarks and gluons is [111]

$$s = \frac{2\pi^2}{45} g_Q T^3 \,. \tag{4.26}$$

We take the number of quark flavor as $N_f \sim 2.5$ to account for the mass of s quark. This gives a QGP degeneracy of $g_Q = 16 + 21/2\, N_f = 42.25$. Hence, Eq. 4.25 gives the well-known relation

$$T^3 \tau = T_i^3 \tau_i = C'(r) \tag{4.27}$$

We assume again the transverse profile 4.15 for the probability density, and the initial energy density will goes like $\epsilon(\mathbf{r}_\perp) \propto \mathcal{P}(\mathbf{r}_\perp)$:

$$\epsilon(\mathbf{r}_\perp, \tau_i) = C\mathcal{P}(\mathbf{r}_\perp) = \frac{g_Q \pi^2\, T^4(\mathbf{r}_\perp, \tau_i)}{30} \,. \tag{4.28}$$

The C constant is adjusted by [32, 112]

$$\epsilon_i = \frac{g_Q \pi^2\, T_i^4}{30} = \frac{1}{\pi R_\perp^2} \int d^2 r_\perp \epsilon(\mathbf{r}_\perp, \tau_i) = \frac{C}{\pi R_\perp^2} \,. \tag{4.29}$$

Then, the initial temperatures in the transverse direction is assigned according to

$$T(r, \tau_i) = \left(\frac{30\, C\, \mathcal{P}(\mathbf{r}_\perp)}{g_Q \pi^2} \right)^{1/4} = T_i \left[2 \left(1 - \frac{r^2}{R_\perp^2} \right) \right]^{1/4} \,. \tag{4.30}$$

Putting Eqs.(4.27) and (4.30) together, we get the temperature evolution of a QGP expanding in 1-D as

$$T(r, \tau) = T_i \left(\frac{\tau_i}{\tau} \right)^{1/3} \left[2 \left(1 - \frac{r^2}{R_\perp^2} \right) \right]^{1/4} \,. \tag{4.31}$$

The jet evolves in the QGP medium until it reaches the surface or until the temperature reaches the transition temperature T_c. In our calculation, we assume a first-order phase transition. The total entropy density during the mixed phase, which begins at τ_f and ends at τ_H, is

$$s = s_{mix} = s_{QGP} f_{QGP} + (1 - f_{QGP}) s_{HG} \tag{4.32}$$

where f_{QGP} is the fraction of the QGP phase in the mixed phase. The entropy density of the hadron gas phase, assuming only pions as degrees of freedom ($g_H = 3$), is

$$s_H = \frac{2\pi^2}{45} g_H T^3 \tag{4.33}$$

From Eq. 4.24, we find

$$f_{QGP} = \frac{1}{r_d - 1}\left(\frac{r_d \tau_f}{\tau} - 1\right) \tag{4.34}$$

Here $r_d = \frac{g_Q}{g_H}$ is the ratio of the degrees of freedom in the two phases. The gluons production rates are then scaled accordingly for $\tau > \tau_f$:

$$\frac{d\Gamma(p,k)}{dtdk} \rightarrow f_{QGP} \frac{d\Gamma(p,k)}{dtdk} \tag{4.35}$$

We take the critical temperature T_c to be 160 MeV. This is not a crucial value, since the bulk of energy loss will happen when the temperature will be high, and also because at the time the system will have reached the transition temperature, an important number of jets will already have left the medium. Finally, from entropy conservation, the initial time τ_i and the temperature are related by [113]

$$T_i^3 \tau_i = \frac{\pi^2}{\zeta(3) g_Q} \frac{1}{\pi R_\perp^2} \frac{dN}{dy} \,. \tag{4.36}$$

We can note from this equation that the effect of a reduced degeneracy, or an increased particle multiplicity, will be to increase the initial temperature, for a fixed initial time.

Is is now important to look at the validity of the Bjorken model, i.e. verify if it is correct to assume that dN/dy is constant. The approximation of a plateau is correct providing dN/dy is $\sim$ constant in the range Γ_y, with $\Gamma_y > \Delta y$, where Δy is the rapidity range covered by a thermal distribution. In other words, it means that the production of midrapidity photon, from matter having space-time rapidity $\eta > \Delta y/2$, is highly suppressed. From ref. [114], dN_{ch}/dy for charged particles in central Au-Au, turns out to be $\sim$ constant, within 5% changes, in the range $\Gamma_y = 2$, which is bigger than the thermal width at T=300 MeV, for particles with transverse momentum $p_T > 5$ GeV, which is $\Delta y < 1$.

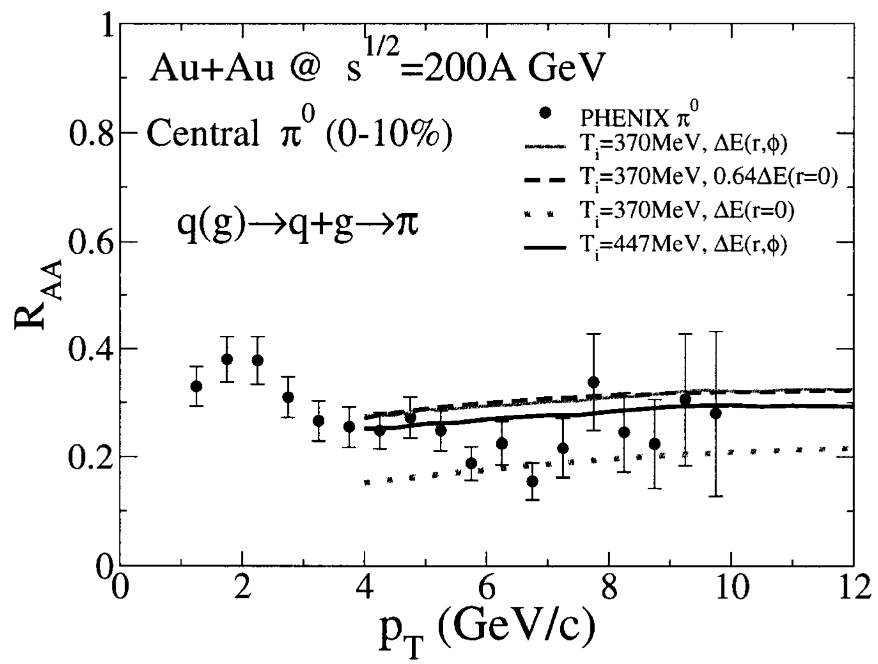

Figure 4.3: Nuclear modification factor for pions at RHIC. Data points are from PHENIX [12]. The solid lines show the full calculation of the spatial distribution of jets in the plane $z = 0$ for two initial temperatures. The dotted lines assume that all jets are created at the center and the dashed lines assume the same approximation but with a reduced energy loss.

4.1.2 R_{AA} for pions

The result of our calculation for RHIC energy is summarized in Fig. 4.3 together with the PHENIX data [12][1]. To cover the uncertainties in the initial conditions, we consider two different sets, one at a relatively high temperature of $T_i = 447\,\text{MeV}$ and a relatively short initial time of $\tau_i = 0.147\,\text{fm}/c$ taken from Refs. [32, 112], and one at a lower temperature $T_i = 370\,\text{MeV}$ and somewhat later time for the hydrodynamic evolution of $\tau_i = 0.26\,\text{fm}/c$ taken from our study of low-p_T photons, Chapter 2. Those two sets correspond to $dN/dy|_{y=0} \sim 1260$, estimated for central collisions in Ref. [112]. In deriving these results, we have used $\alpha_s = 0.3$. If the value is larger then energy loss will be greater, so R_{AA} will be smaller; if it is smaller, then R_{AA} increases. Besides this dependence on α_s, our results rely on no free parameters.

[1]See the presentation of Brian Cole at Quark Matter 2005, Budapest, for the preliminary version of the new data (http://qm2005.kfki.hu). They are however consistent with those presented here

The solid lines in the figure are full calculations with the initial spatial distribution $\mathcal{P}(\mathbf{r}_\perp)$ given in Eq. (4.15). For comparison, we also display two more sets of calculations. The dotted line is calculated with the jets originating only from the center of the disk ($\mathbf{r}_\perp = 0$). Comparing the dotted line with the solid line, it is apparent that the absolute magnitude of the R_{AA} depends very much on the density profile of the nucleus. The dashed line is calculated again with the jets from the center but with the energy loss rates reduced by a factor of 0.64. One may say that the average path of a jet has the length of about $0.64 \times R_A$.

In Fig. 4.3, one can see that both $T_i = 447\,\mathrm{MeV}$ and $T_i = 370\,\mathrm{MeV}$ describe the real data reasonably well. This is somewhat surprising. Since the density of thermal particle is proportional to T^3, the density at 447 MeV is about 1.8 times the density at 370 MeV. Yet the energy loss does not reflect such a big difference. The reason is because the energy loss depends mostly on the duration of evolution. Hence once dN/dy is fixed, the time evolution of the temperature follows a common curve regardless of the initial temperature (c.f. Eq. (4.31)). The only difference between the higher and the lower temperature cases is that the time evolution starts earlier for the higher temperature case. From the moment τ passes τ_i for the lower temperature, the evolution of the two systems is identical. Therefore, if energy loss at the beginning of the evolution is small compared to the later time energy loss, the amount of energy loss depends mostly on the duration of the QGP phase $\Delta\tau = \tau_f - \tau_i$. Since $\tau_f \gg \tau_i$, the duration of the QGP phase is approximately the same for high temperatures. We have verified that the energy loss between the times corresponding to $T_i = 1000\,\mathrm{MeV}$, $T_i = 447\,\mathrm{MeV}$ and $T_i = 370\,\mathrm{MeV}$ are at most about 10 %.

Since the suppression is mainly controlled by the duration of the evolution, the suppression should be sensitive to the particle rapidity density dN/dy, which fixes the lifetime of the QGP. We can see in Fig. 4.4 that it is indeed the case. For simplicity, we assume here that the jets are all created at the center of the system. We see that there is very little change in the suppression as the initial temperature varies from $T_i = 370$ MeV to $T_i = 1000$ MeV. However, the suppression shows a strong dependence on dN/dy; going from $dN/dy = 680$ to $dN/dy = 1260$ increases the suppression by a factor ~ 1.5.

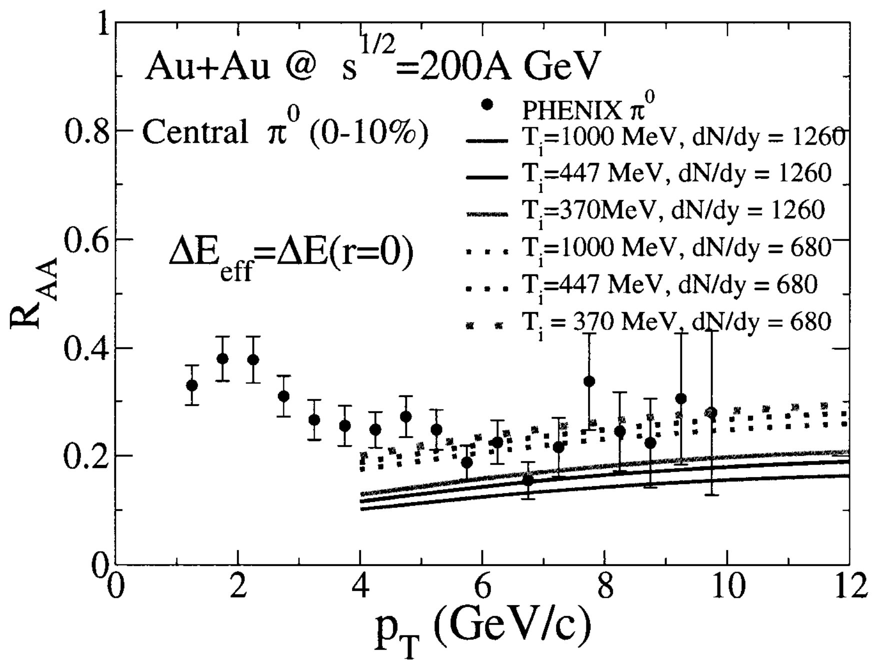

Figure 4.4: Nuclear modification factor for pions at RHIC, taking all jets to originate at the center of the nucleus. Data points are from PHENIX [12]. The solid lines are for initial conditions which lead to a particle multiplicity of $dN/dy = 1260$ while the dotted lines are for initial conditions leading to $dN/dy = 680$. For each set of lines, the initial temperature is, from bottom to top, 1000, 447 and 370 MeV.

For the LHC, we use the initial temperature from Chapter 2, T_i =845 MeV, giving $\tau_i = 0.088$ fm/c for $dN/dy \sim 5625$ [112, 140]. At this energy, jets could in principle be produced with energies as high as $\sqrt{s_{NN}}/2 = 2750$ GeV. However, the contribution from a jet having more than, let's say, 10 times the observed pion energy, should be sharply cut off by the steeply falling initial distribution function. As it can be seen in Fig. 4.5, the R_{AA} of pion with $p_T \lesssim 30\,\mathrm{GeV}$, for the LHC, doesn't receive any contribution from partons having more than 300 GeV. To be on the conservative side, we cut off the maximum jet energy at 400 GeV.

The calculated LHC nuclear modification factor is shown in Fig. 4.6 with the full fragmentation function from Eq. 4.16. We also show in the same figure the effect of not tracking the secondary partons (gluons emitted by quarks and quarks emitted by

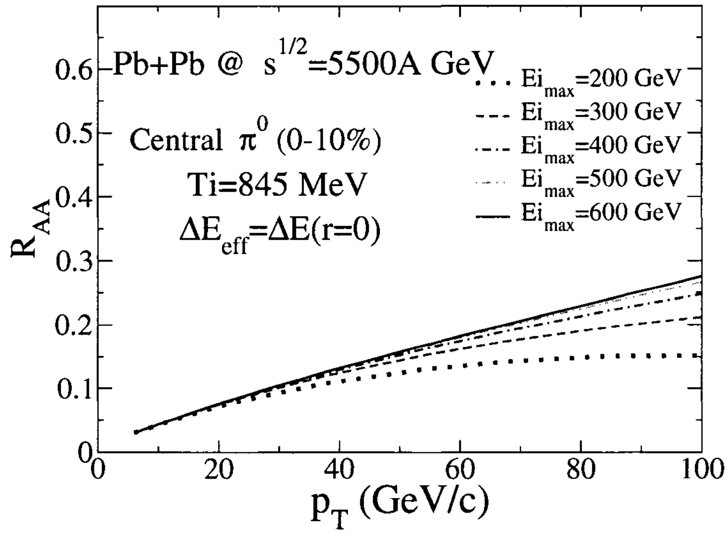

Figure 4.5: Nuclear modification factor for pions at LHC for different cuts on the energy of an incoming jet in the QGP. We assume here that all the jets are created at the center of the disk.

gluons). Comparison between the solid line and the dashed line shows that ignoring the secondaries can make an overall difference of 30%. This arises almost entirely from quark secondaries from gluon jets–that is, from hard gluons which split, due to plasma interactions, into $q\bar{q}$ pairs, which subsequently fragment. This is shown by the double dot-dashed line, which include only incoming gluons in the QGP. Those gluons can produce lower energy gluons or quark-antiquark pairs. This contribution is more important than the contribution from incoming quarks (dot-dashed line), because most hard jets at the LHC arise from gluons, whereas a larger fraction at RHIC are from quarks, as it can be seen in Fig. 4.7. The gluons emitted by quarks are mostly soft; they also lose energy quickly and fragment inefficiently. At RHIC energies the error from dropping secondaries is only 5%.

Comparing the RHIC and LHC results, we see that the suppression due to jet energy loss at RHIC is about a factor of 3 for a 10 GeV pion, while the suppression at the LHC for a pion at the same energy is about a factor of 6. This difference arises because the medium at the LHC remains hot for much longer than at RHIC. The cooling is governed by the product $T^3\tau \propto dN/dy$. Hence, smaller dN/dy implies faster cooling. We have also calculated the impact of assuming a first order phase transition.

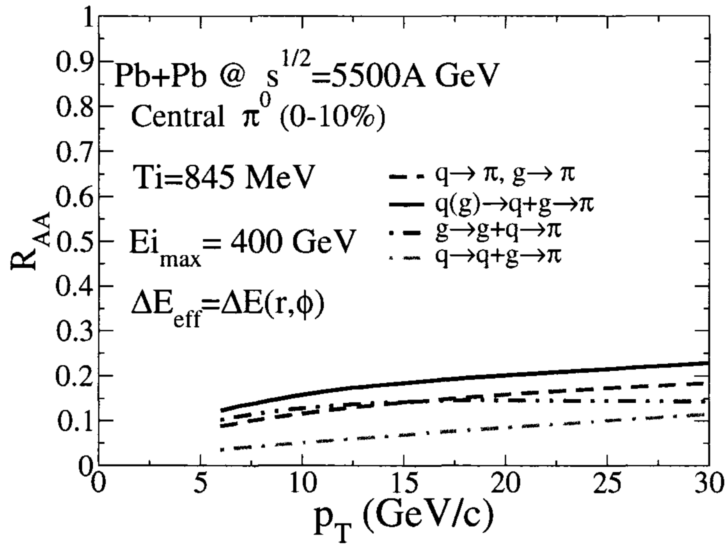

Figure 4.6: Nuclear modification factor of pions at the LHC. The solid line includes pions coming from bremsstrahlung secondaries emitted in the thermal medium; the dashed line does not. The dot-dashed line include only incoming quarks in the QGP, while the double dot-dashed line include only incoming gluons. For all lines, the full spatial distribution from Eq. (4.15) has been used.

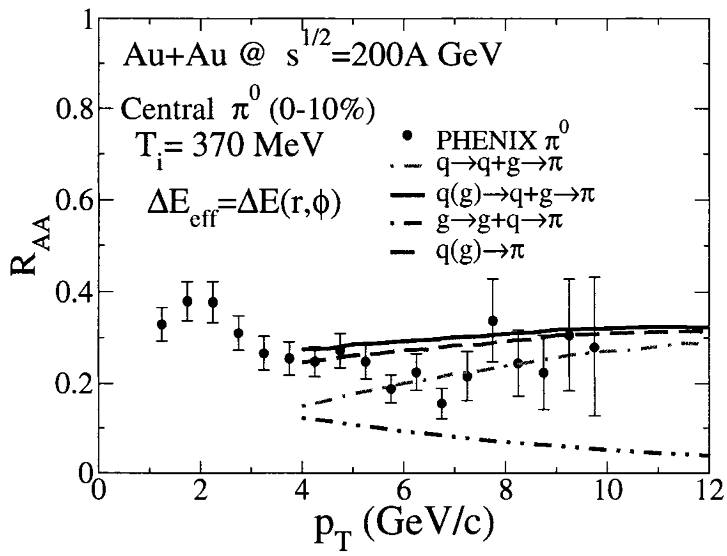

Figure 4.7: Nuclear modification factor of pions at RHIC. Same lines description than Fig. 4.6.

At RHIC, at the end of the QGP phase, a large number of jets has already left the medium, but those still inside will suffer additional suppression during the mixed phase, such that assuming a cross-over between the QGP and the hadron gas phase will increase R_{AA} by $\sim 20\%$. At the LHC, at the critical point, a much larger fraction of jets are out of the medium, such that R_{AA} is quite insensitive to assumptions related to the transition. Our initial conditions correspond to an initial time smaller than the common value of τ_i=0.6 fm/c used in hydrodynamic calculations [116]. We have verified that going from τ_i=.26 fm/c ($T_i = 370$ MeV) to 0.6 fm/c (T_i=280 MeV) increases R_{AA} by less than 20%.

In this section, the AMY formalism has been applied to successfully reproduce the π^0 spectra at RHIC. We will see in the following section, how the same formalism can be applied to determine the production of real photons.

4.2 Photon production

The hard photons produced in nucleon-nucleon collisions can be divided into three categories: primary hard direct photons, fragmentation photons, and background photons. Primary hard direct photons (N-N) are those produced by Compton scattering and annihilation of two incoming partons. Fragmentation photons (jet-frag) are those produced by bremsstrahlung emitted from final state partons. Background photons are those produced by the decay of hadrons subsequent to the collision, primarily from $\pi^0 \to \gamma\gamma$ decay. We define by 'prompt photons', the sum of the direct and the fragmentation contributions. The expression for prompt photon production is

$$\begin{aligned}\frac{d\sigma_{\gamma-prompt}}{dyd^2p_T} &= \sum_{a,b}\int dx_a dx_b g(x_a,Q)g(x_b,Q)\\ &\times\left[K_\gamma(p_T)\frac{d\sigma^{a+b\to\gamma+d}}{dt}\frac{2x_a x_b}{\pi(2x_a-2\frac{p_T}{\sqrt{s_{NN}}}e^y)}\delta\left(x_b-\frac{x_a p_T e^{-y}}{x_a\sqrt{s_{NN}}-p_T e^y}\right)\right.\\ &\left.+K_{brem}(p_T)\frac{d\sigma^{a+b\to c+d}}{dt}\frac{1}{\pi z}D_{\gamma/c}(z,Q)\right]. \qquad (4.37)\end{aligned}$$

K_γ and K_{brem} are correction factors to take into account NLO effects; we evaluate them using the approach of Aurenche *et al.* [117], obtaining K_γ(10 GeV)$\sim$ 1.5 for RHIC and LHC and K_{brem}(10 GeV)$\sim$ 1.8 at RHIC and 1.4 at LHC. All scales (renormalization, factorization and fragmentation) have been set equal to the photon transverse momentum p_T. The photon fragmentation function $D_{\gamma/c}$ is extracted without medium effects in $e^- + e^+$ collisions [118]. The validity of this expression for pp collisions at $\sqrt{s} = 200$A GeV is shown in the left panel of Fig.4.8 with data from PHENIX [119]. It appears clear that the baseline mechanism of high p_T photon production in nucleon-nucleon collisions is under quantitative control. The photon yield in d-Au collisions, where final state effects are not expected, is easily calculated from Eq. 4.64. The averaged number of nucleon-nucleon collision, $\langle N_{coll} \rangle$ is taken to be 8.5 [15]. From the right panel of Fig. 4.8, the photon yield data in d-Au collisions [120] also turn out to be well reproduced by the same mechanism described above, but with shadowing effect included. Note that, as it was for π, Cronin effect doesn't seem necessary for reproducing data at RHIC.

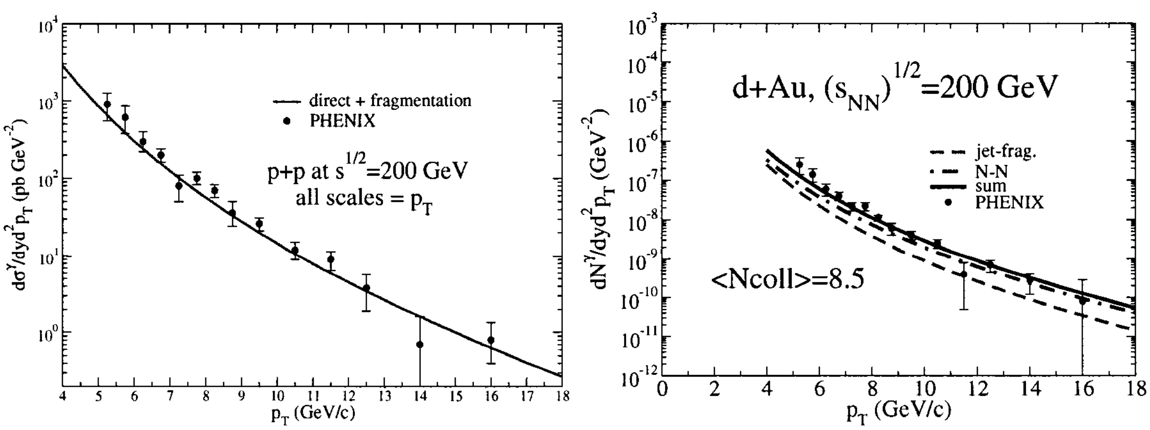

Figure 4.8: Left Panel: prompt photons produced in pp collision at RHIC. The solid line is calculated with Eq. (4.37). Right panel: Prompt photons produced in d-Au collision at RHIC. The dashed line include the fragmentation jets while the dot-dashed line include direct photons. The solid line is the sum of both. All lines include shadowing effects.

In AA collisions, there is an additional source of high p_T photons: the in-medium contribution. This contribution will include the direct conversion of a high energy parton to a high energy photon by annihilation with a thermal parton, in-medium bremsstrahlung from a jet, and thermal production of photons.

4.2.1 Jet-photon conversion

In Ref. [32], the conversion of a leading parton to a photon in the plasma was found to be an important process. This happens when a jet crossing the hot medium undergoes an annihilation ($q+\bar{q} \to g+\gamma$) or a Compton ($g+q \to q+\gamma$) process with a thermal parton. The related production rate of photons is given by Eq. 2.63. For incoming jet, we substitute the thermal phase-space distribution by that of the jet : $f_F \to f^q_{jet}/2 + f^{\bar{q}}_{jet}/2 \to f^{q\bar{q}}_{jet}/2$. We get

$$\frac{dR}{dyd^2p_T} = \sum_f \left(\frac{e_f}{e}\right)^2 \frac{T^2\alpha\alpha_s}{8\pi^2} f^{q\bar{q}}_{jet}(\overrightarrow{p_\gamma}) \left[2\ln\left(\frac{3E_\gamma}{\pi\alpha_s T}\right) - C_{\rm ann} - C_{\rm Com}\right], \tag{4.38}$$

where T is the temperature. The phase-space distribution function of the incoming particles is defined as

$$g_i \int \frac{d^3xd^3p}{(2\pi)^3} f(x,p) = N_i\,, \tag{4.39}$$

where N_i is the number of particles i and g_i is the spin-color degeneracy. The phase-space distribution function for an incoming jet, assuming a Bjorken $\eta - y$ correlation [121], is

$$\begin{aligned} f^{q\bar{q}}_{jet}(\overrightarrow{x}, \overrightarrow{p}, t_0) &= \frac{(2\pi)^3 \mathcal{P}(\mathbf{r}_\perp)}{g_q \tau p_T} \frac{dN^{q\bar{q}}_{jet}}{dyd^2p_T} \delta(\eta - y) \\ &= \frac{(2\pi)^3 \mathcal{P}(\mathbf{r}_\perp) t_0}{g_q\sqrt{t_0^2 - z_0^2}} \frac{p_T}{E^2} \frac{dN^{q\bar{q}}_{jet}}{dyd^2p_T} \delta(z_0 - v_z t_0)\,, \end{aligned} \tag{4.40}$$

where η is the space-time rapidity and t_0 is the formation time of the jets, and z_0 is its position in the QGP expansion direction. As before, the jets are taken to be massless and we suppose that energy loss of jets in the plasma does not change their direction. With this latter approximation, f_{jet} can be factorized into a position-space and a momentum-space part:

$$\begin{aligned} f^{q\bar{q}}_{jet}(\overrightarrow{x}, \overrightarrow{p}, t) &= \chi(\overrightarrow{x}, t) \frac{1}{E^2} \frac{dN^{q\bar{q}}_{jet}(E,t)}{dE} \\ &= \chi(\overrightarrow{x} - \hat{t}\frac{\overrightarrow{p}}{|\overrightarrow{p}|}, t_0) \frac{1}{E^2} \frac{dN^{q\bar{q}}_{jet}(E,t)}{dE}\,, \end{aligned} \tag{4.41}$$

where $\hat{t} = t - t_0$ is the propagation time of the jet. In the high energy limit, the cross-sections $\sigma_{q\bar{q}\to g\gamma}$ and $\sigma_{qg\to q\gamma}$ are dominated by direct exchange between the quark and the photons. Since we are interested in photons produced at mid-rapidity ($y = 0$), we only need to consider quark and anti-quark jets produced at mid-rapidity. This gives

$$f_{jet}^{q\bar{q}}(\vec{x}, \vec{p}, t)\big|_{y=0} = \frac{(2\pi)^3 \mathcal{P}(|\vec{w_r}|) t_0}{g_q\sqrt{t_0^2 - z_0^2}} \frac{1}{p_T} \frac{dN_{jet}^{q\bar{q}}}{dyd^2p_T}(p_T, t)\delta(z_0)\,, \tag{4.42}$$

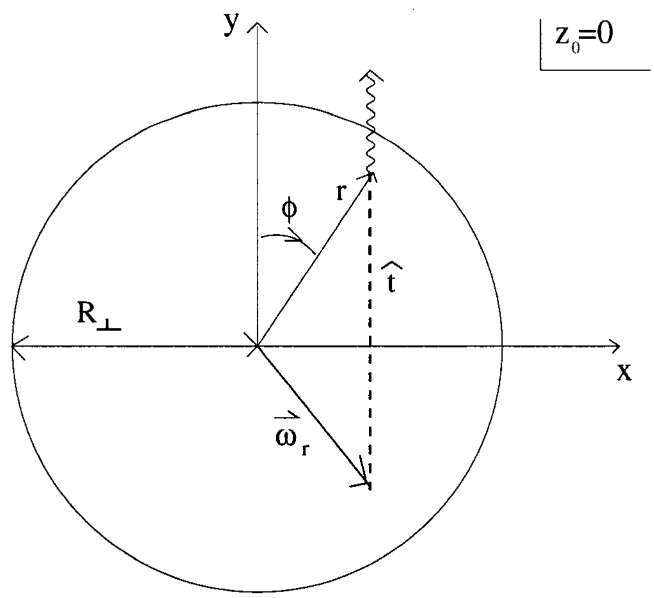

Figure 4.9: Jet propagation and photon production in the transverse plane.

$\vec{w_r}$ is, in the plane $z_0 = 0$, the initial radial position of the jet. From Fig. 4.9, the photon's creation coordinates are

$$\vec{X} = r(\sin\phi\,\hat{x} + \cos\phi\,\hat{y})\,, \tag{4.43}$$

and the propagation direction of the jet, during the time $\hat{t}$, is

$$\vec{d} = \hat{t}\,\hat{y}\,. \tag{4.44}$$

The jet's initial position is then given by:

$$|\vec{w_r}| = \left|\vec{X} - \vec{d}\right| = \left|r\sin\phi\,\hat{x} + (r\cos\phi - \hat{t})\hat{y}\right| = \sqrt{(r\cos\phi - \hat{t})^2 + r^2\sin^2\phi}\,, \tag{4.45}$$

where ϕ is the angle in the plane $z_0 = 0$ between the direction of the photon and the position where this photon has been produced. The AMY formalism is introduced here to calculate the evolution of $\frac{dN^{q\bar{q}}}{dyd^2p_T}(p_T, t)$. The output of Eq. (3.12) is $P_{q\bar{q}}(E, t)$, where

$$P_{q\bar{q}}(E,t) = \frac{dN^{q\bar{q}}}{dE}(E,t) = p_T \frac{dN^{q\bar{q}}}{dyd^2p_T}(p_T, t) \,. \tag{4.46}$$

In this equation, we got rid of an unimportant phase factor relating dN/dE (single differentiation) to dN/dyd^2pT (triple differentiation). The initial distributions $P_{q\bar{q}}(E, t_0)$ and $P_g(E, t_0)$ are fixed by the initial jet distribution at mid-rapidity:

$$\left.\frac{dN^{jet}}{dyd^2p_T}\right|_{\hat{t}=0} = \frac{\langle N_{coll}\rangle}{\sigma_{in}} \sum_{a,b} \int dx_a g(x_a, Q) g(x_b, Q) K_{jet}(p_T) \frac{d\sigma^{a+b\to jet+d}}{dt} \frac{x_a x_b}{\pi(x_a - \frac{p_T}{\sqrt{s_{NN}}} e^y)} \tag{4.47}$$

For simplicity, we use the parametrized forms from Ref. [32]:

$$\left.\frac{dN^{jet}}{dyd^2p_T}\right|_{\hat{t},y=0} = K_{jet} \frac{a}{(p_T + b)^c} \,, \tag{4.48}$$

where p_T is given in GeV. The parameters, averaged over u,d and s flavours, are given in Table 4.1, for RHIC and the LHC.

	a	b	c
RHIC q	2.041×10^4	1.6	7.872
RHIC $\bar{q}$	39341.45	1.947	8.919
LHC q	968.7	0.605	5.278
LHC $\bar{q}$	350	0.3183	5.246

Table 4.1: Parameters for the initial distributions of jets.

The total photon spectrum is given by a full space-time integration:

$$\begin{aligned} \frac{dN^\gamma}{dyd^2p_T} &= \int d\tau\tau \int rdr \int d\phi \int d\eta \frac{dR}{dyd^2p_T}(E_\gamma = p_T\cosh(y-\eta)) \\ &= \int dt \int rdr \int d\phi \int dz \frac{dR}{dyd^2p_T}(E_\gamma = p_T\cosh(y_0)) \,. \end{aligned} \tag{4.49}$$

The production rate is calculated in the local frame where the temperature is defined, and the photon rapidity becomes $y_0 = y - \eta$. The space-time rapidity is given by $\eta = \frac{1}{2}\ln\left((t+z)/(t-z)\right)$.

High-p_T photons are emitted preferentially early during the QGP phase, when the temperature is at its highest point. Indeed, explicit hydrodynamic calculations show that the nuclear space-time geometry smoothly evolve from 1-D to 3-D [122]. By the time the system reaches the temperature corresponding to the mixed phase in a first-order phase transition, the system is still very much 1-D [122]. For such a geometry, specific calculations [123] suggest that the flow effect on photons and dileptons from the QGP is not large at RHIC and LHC for $p_T > 2$ GeV. Assuming again a 1-D expansion, we get the production of photons from jet-medium interactions from Eqs. (4.38), (4.42) and (4.49),

$$\frac{dN^{\gamma}_{jet-th}}{dyd^2p_T}|_{y=0} = 2\int dt \int_0^{R_\perp} rdr \int_0^{\pi} d\phi \frac{(2\pi)^3\mathcal{P}(|\overrightarrow{w_r}|)}{g_q}\frac{1}{p_T}\frac{dN^{q\bar{q}}}{dyd^2p_T}(p_T,t)$$
$$\sum_f \left(\frac{e_f}{e}\right)^2 \frac{T^2\alpha\alpha_s}{8\pi^2}\left[2\ln\left(\frac{3p_t}{\pi\alpha_s T}\right) - C_{\rm ann} - C_{\rm Com}\right], \tag{4.50}$$

where the temperature T evolves according to Eq. (4.31). The ϕ integration can be done as follow:

$$\begin{aligned}\gamma(r,t) &= \int_0^{\pi} d\phi\mathcal{P}(|\overrightarrow{w_r}|) = \int_0^{\pi} d\phi\frac{2}{\pi R_\perp^2}\left(1-\frac{|\overrightarrow{w_r}|}{R_\perp^2}\right)\theta(R_\perp - |\overrightarrow{w_r}|)\\ &= \int_0^{\pi} d\phi\frac{2}{\pi R_\perp^2}\left(1-\frac{r^2+\hat{t}^2-2\hat{t}r\cos\phi}{R_\perp^2}\right)\theta(R_\perp^2 - r^2 - \hat{t}^2 + 2\hat{t}r\cos\phi)\end{aligned} \tag{4.51}$$

The θ-function leads to three possibles cases.

(1) $\underline{r^2+\hat{t}^2-2\hat{t}r > R_\perp^2}$:

Then we get simply $\gamma = 0$.

(2) $\underline{r^2+\hat{t}^2+2\hat{t}r < R_\perp^2}$:

$$\gamma = \int_0^{\pi} d\phi\frac{2}{\pi R_\perp^2}\left(1-\frac{r^2+\hat{t}^2-2\hat{t}r\cos\phi}{R_\perp^2}\right) = \frac{2}{R_\perp^2}\left(1-\frac{r^2+\hat{t}^2}{R_\perp^2}\right) \tag{4.52}$$

(3) $\underline{r^2+\hat{t}^2-2\hat{t}r \leq R_\perp^2 \leq r^2+\hat{t}^2+2\hat{t}r}$:

This imply the following condition on ϕ:

$$\cos\phi \geq \cos u_0 = \frac{r^2+\hat{t}^2-R_\perp^2}{2\hat{t}r} \tag{4.53}$$

which gives

$$\gamma = \int_0^{u_0} d\phi \frac{2}{\pi R_\perp^2}\left(1-\frac{r^2+\hat{t}^2-2\hat{t}r\cos\phi}{R_\perp^2}\right) = \frac{2u_0}{\pi R_\perp^2}\left(1-\frac{r^2+\hat{t}^2}{R_\perp^2}\right)+\frac{4\hat{t}r\sin u_0}{\pi R_\perp^4} \tag{4.54}$$

All thoses conditions are summarized in the following:

$$\int_0^{\pi} d\phi \mathcal{P}(|\overrightarrow{w_r}|) = \gamma(r,t) = \begin{cases} 0 \\ \frac{2}{R_\perp^2}\left(1-\frac{r^2+\hat{t}^2}{R_\perp^2}\right) \\ \frac{2u_0}{\pi R_\perp^2}\left(1-\frac{r^2+\hat{t}^2}{R_\perp^2}\right)+\frac{4\hat{t}r}{\pi R_\perp^4}\sin(u_0)\,, \end{cases} \tag{4.55}$$

for the cases that $r^2+\hat{t}^2-2\hat{t}r > R_\perp^2$, $r^2+\hat{t}^2+2\hat{t}r < R_\perp^2$ and all other cases, respectively. Then, the final expression for the jet-photon production becomes

$$\begin{aligned} \frac{dN^\gamma_{jet-th}}{dyd^2p_T}|_{y=0} = \quad & 2\int dt \int_0^{R_\perp} rdr \frac{(2\pi)^3}{g_q}\frac{1}{p_T}\frac{dN^{q\bar{q}}}{dyd^2p_T}(p_T,t)\gamma(r,t) \\ & \sum_f \left(\frac{e_f}{e}\right)^2 \frac{T^2\alpha\alpha_s}{8\pi^2}\left[2\ln\left(\frac{3p_t}{\pi\alpha_s T}\right)-C_{ann}-C_{Com}\right] \\ = & \int dt \frac{dN^\gamma_{jet-th}}{dtdyd^2p_T}|_{y=0} \end{aligned} \tag{4.56}$$

As before, we assume a first order phase transition beginning at the time τ_f and ending at $\tau_H = r_d\tau_f$ [110]. After τ_f we scale the production rate by f_{QGP} (Eq. (4.34)), such that

$$\frac{dN^\gamma_{jet-th}}{dyd^2p_T}|_{y=0} = \int_{\tau_i}^{\tau_f} dt \frac{dN^\gamma_{jet-th}}{dtdyd^2p_T}|_{y=0} + \int_{\tau_f}^{\tau_H} dt f_{QGP}(t)\frac{dN^\gamma_{jet-th}}{dtdyd^2p_T}|_{y=0} \tag{4.57}$$

The first term and second term correspond respectively to photons produced during the pure QGP and the mixed phase. Our results for RHIC and LHC, with and without energy loss are shown in Fig. 4.10. Here also, $\alpha_s = 0.3$. We see that higher energy photons are more sensitive to jet energy loss: photons at 4 GeV are suppressed by a factor 1.3 at RHIC, while 15 GeV photons are suppressed by a factor 1.6 due to jet energy-loss. We find approximately the same suppression for the LHC. This suppression is much smaller that the one observed from R_{AA} in the previous section. This is because the photons can be produced at any point in the hard parton's propagation through the medium, while the jet energy loss depends on the final parton energy. Hence, some of the photon rate arises from before, rather than after, the jet has lost much energy.

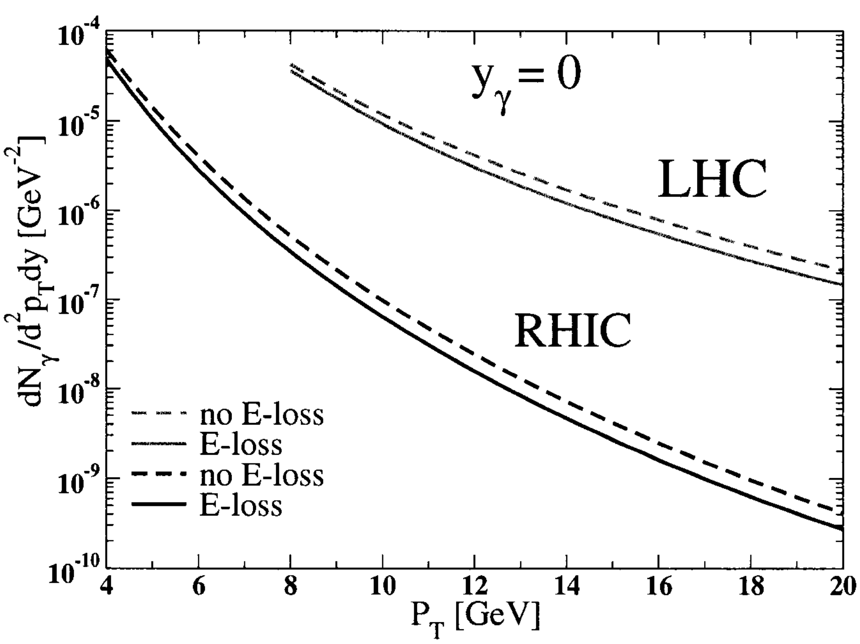

Figure 4.10: Direct production of photons by jets in the plasma for Au-Au at RHIC and Pb-Pb at the LHC. For the solid lines, jet energy loss is included; for the dashed lines it is neglected. The initial temperature is T_i = 370 MeV at RHIC and T_i=845 MeV at the LHC.

It's important to remember that in the jet-photon conversion, the emitted photon takes away all the momentum and follows the direction of the incoming jet, due to the approximation $\sigma \propto \delta^3(\vec{p}_{jet} - \vec{p}_\gamma)$ (see Sec. 2.4). We can verify this approximation, as we did for incoming thermal particles in Sec. 2.4. For simplicity, and only for this exercise, we assume a stationary QGP with constant temperature, and we neglect energy

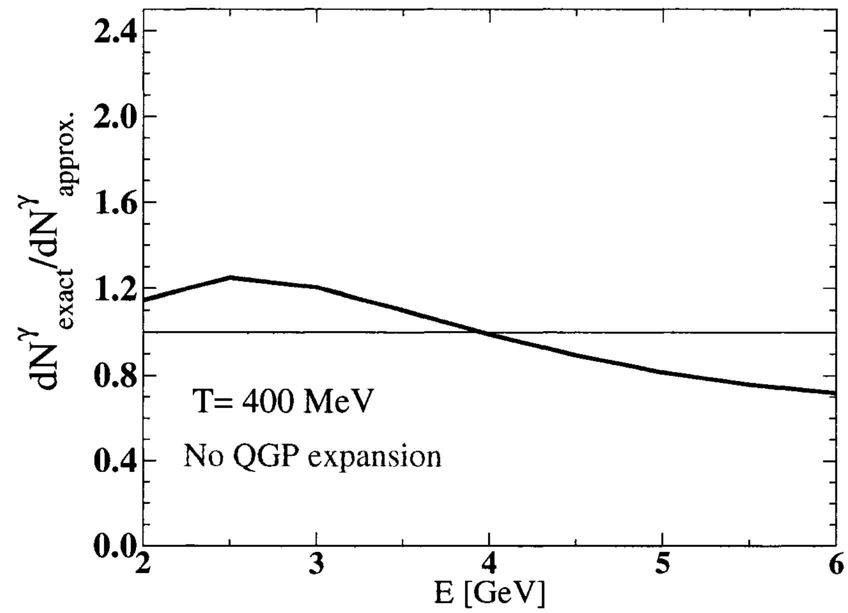

Figure 4.11: Ratio of exact to approximated yield, of direct photon production from interactions of jets with a stationary QGP, at constant temperature T=400 MeV.

loss. This allows us to kill many integrals, as $\int dtd^3xf^{q\bar{q}}_{jet} = \Delta t\,\frac{(2\pi)^3}{g_q}\frac{dN^{q\bar{q}}}{d^3p}$. The Fig. 4.11 shows the ratio $\left(dN^{jet-th}_{exact}/dy/d^2p_T\right)/\left(dN^{jet-th}_{approx.}/dy/d^2p_T\right)$, where $dN^{jet-th}_{exact}/dy/d^2p_T$ is obtained with the exact result definition, Eq. 2.66, and $dN^{jet-th}_{approx.}/dy/d^2p_T$ assumes the jet-photon conversion approximation. The effect of the approximate cross-section is to boost photon toward higher p_T values, as photon get 100% of the jet's energy, while for the exact calculation, photons are emitted with a smaller fraction of the jet's energy, giving a ratio greater that one in the intermediate p_T region. From Fig. 4.11, the error related to using the approximated cross-section, for RHIC conditions ($T \sim 400$ MeV), is found to be less than $\sim 25\%$ for $2 < p_T < 6$ GeV, but the error increases for higher values of p_T. Fortunately, as we will see in the results section, the jet-photon conversion contributes to the photon yield mainly at intermediate p_T, so that it is an appropriate approximation for our purpose here.

As it can be seen from Fig. 2.9, the error of using the approximate cross-section is weaker for incoming thermal partons. This is because the thermal distribution is steeper that the jet distribution, so that the shifting of the photons toward lower p_T

values is less important for incoming thermal partons. I have verified that for the LHC, ($T \sim 800$ MeV), the range of validity of the approximated cross-section, within 30%, is $7 < p_T < 13$ GeV.

4.2.2 *Bremsstrahlung photons*

Hard partons in the medium can also produce photons by bremsstrahlung when they scatter in the medium. The photon bremsstrahlung rate $d\Gamma^{q\to q\gamma}(p,k)/dkdt$ follows the same expression as $d\Gamma^{q\to qg}(p,k)/dkdt$ in Eq. (3.9), but with $C_s \to \frac{e_f^2}{e^2}$, $C_{\rm A} \to 0$, $m_\gamma = 0$ and $g_s^2 \to e^2$. The photon bremsstrahlung distribution is given by

$$\frac{dP_\gamma(p,t)}{dt} = \int dk\, P_{q\bar{q}}(p+k)\frac{d\Gamma^{q\to q\gamma}(p{+}k,p)}{dkdt}\,. \tag{4.58}$$

It is assumed here that the photon production rate is perturbative, so that the quark plus anti-quark distribution $P_{q\bar{q}}$ will be unchanged by the photon emission. The photon distribution is finally convolved with the initial spatial distribution of jets to get the final spectrum of bremsstrahlung photons,

$$\frac{dN_{jet-br}}{dyd^2p_T}\Big|_{y=0} = \frac{1}{p_T\Omega(y=0)}\frac{dN_{jet-br}}{dp_T} = \frac{1}{p_T}\int d^2r_\perp\, \mathcal{P}(\mathbf{r}_\perp)P_\gamma(p_T,d)\,, \tag{4.59}$$

where $r_\perp$ is the position where the jet has been created, and $d = d(r_\perp)$ is the distance crossed by the jet in the plasma. The factor $\Omega(y=0)$ corresponds to a $d\phi$ and a dy integration around the transverse plane $z_0 = 0$. This factor can be absorbed in the definition of the initial distribution $P_{q\bar{q}}(p_T, t=0)$.

Numerically, bremsstrahlung photons turn out to be subdominant to jet-photon conversion. While the rate at which such photons are produced is larger, these typically carry only a fraction of the jet's energy, while jet-photon conversion predominantly produces photons with the complete energy of the jet (hard parton). When folded against a steeply falling spectrum of jets, the process which produces the highest energy photons will dominate the final spectrum. The jet annihilation ($jet + th + th \to th + \gamma$), where th stands for a thermal parton, is also included in the calculations, but turns out to be negligible; this is why this section is called 'bremsstrahlung photons'. The annihilation process is however the dominant in-medium mechanism when the incoming particle is thermal [66]. This is because thermal particle distribution function is much steeper than for jets, implying that process involving parton phase-space distribution function at momentum lower than the momentum of the emitted photon, will be the dominant process. In other word, while the production of photon with energy E from bremsstrahlung involves the quark distribution function $f_q(E+\Delta E)$, the annihilation contribution involves $f_q(E-\Delta E)$. Since the thermal distribution is steep, i.e. $f_q(E+\Delta E) \ll f_q(E-\Delta E)$, the bremsstrahlung contribution will be suppressed.

Recently, Zakharov has also considered bremsstrahlung emission of photons from jets [124]. His work accounts for finite-size effects in the high energy limit; this is not considered here. However, the energy range of interest for this study, as discussed in Chapter 3, is below the factorization scale, so finite size effects are small at those energies.

4.2.3 Thermal photons

The thermal-thermal contribution comes from the photons produced by two scattering thermal particles. The Compton and annihilation rate have been calculated in the previous literature [49], and shown in Sec. 2.4. There are also bremsstrahlung and inelastic pair annihilation contributions [66], with LPM effects, discussed in Chapter 3. We use the parameterization for those rates presented there. The complete induced thermal radiation production rate takes the form

$$\frac{dR_{th-th}}{dy_0 d^2p_T} = \sum_f \left(\frac{e_f}{e}\right)^2 \frac{T^2 \alpha\alpha_s}{4\pi^2} f_F(p_T \cosh y_0) \Bigg[2\ln\left(\frac{3p_T \cosh y_0}{\pi\alpha_s T}\right) - C_{ann} - C_{Com} + 4B\left(\frac{p_T \cosh y_0}{T}\right)\Bigg] \tag{4.60}$$

with $B(x)$ given by Eq. 3.6.

As before, we obtain the photon yield by integrating the production rate over space and time:

$$\begin{aligned}\frac{dN_{th-th}}{dyd^2p_T} &= \int d\tau\,\tau \int d^2x_\perp \int d\eta \frac{dR_{th-th}}{dy_0d^2p_T}(y_0 = y-\eta) \\ &= 2\pi \int_{\tau_i}^{\tau_f} d\tau\,\tau \int_0^{R_\perp} dr\,r \int_{-\eta_{max}}^{\eta_{max}} d\eta \frac{dR_{th-th}}{dy_0d^2p_T}(y_0 = y-\eta)\,. \end{aligned} \tag{4.61}$$

The limit of integration η_{max} is given by

$$\eta_{max} = \frac{1}{2}\ln\left(\frac{1+v_z^{max}}{1-v_z^{max}}\right) \tag{4.62}$$

where the maximum speed in the longitudinal direction is

$$v_z^{max} = v_{projectile} = \frac{p_N}{E_N} = \sqrt{1-\frac{4m_N^2}{s_{NN}}}. \tag{4.63}$$

E_N, p_N and m_N are respectively the energy, momentum and mass of an incoming nucleon in the nucleus-nucleus center of mass. For RHIC, $\sqrt{s} = 200$A GeV, this gives $\eta_{max} = 5.36$, while for LHC, $\sqrt{s} = 5.5$A TeV, this gives $\eta_{max} = 8.6$.

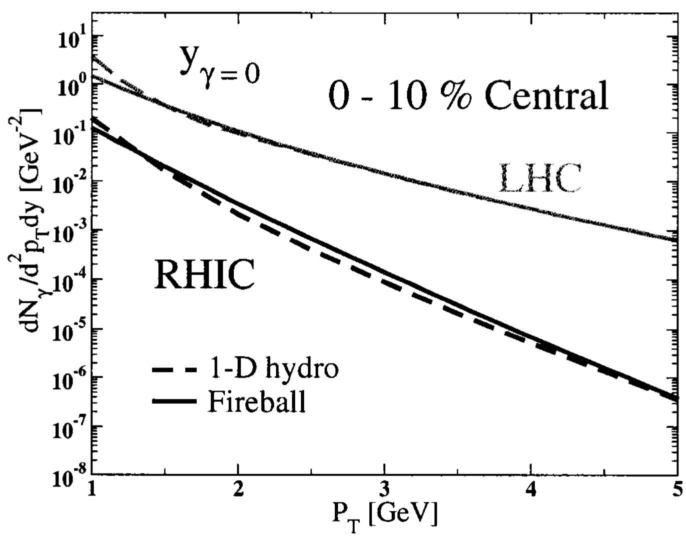

Figure 4.12: QGP radiation for RHIC and LHC. The solid lines are obtained from the fireball model shown in Chapter 2, while the dashed lines assumed a 1-D Bjorken expansion. The initial temperature is T_i=370 MeV at RHIC and T_i=845 MeV at the LHC.

The Fig. 4.12 shows the induced QGP radiation for RHIC and the LHC. The fireball model [69] used for low-p_T photons in Chapter 2 is compared to the 1-D Bjorken expansion used in this chapter, for the same initials conditions (T_i, τ_i). It is remarkable that the two models give almost the same results, reinforcing the supposition of a weak transverse expansion in the QGP phase.

4.2.4 Non-thermal contributions

The expression for prompt photons produced in AA collisions is

$$\frac{dN_{\gamma-prompt}}{dyd^2p_T} = \frac{d\sigma_{\gamma-prompt}}{dyd^2p_T}\frac{\langle N_{\rm coll}\rangle}{\sigma_{in}}\,, \tag{4.64}$$

where we take the values $\langle N_{\rm coll}\rangle = 975$, $\sigma_{in} = 40$ mb for RHIC [29] and $\langle N_{\rm coll}\rangle = 1670$, $\sigma_{in} = 72$ mb for the LHC [125]. $\frac{d\sigma_{\gamma-prompt}}{dyd^2p_T}$ is taken from Eq. (4.37) but with the photon fragmentation function accounting for the jet energy loss.

We will assume, as we did for pion production, that photon production via fragmentation of a jets occurs after the jet parton leaves the QGP. Therefore, the photon fragmentation function including the full spatial distribution and the secondary jets, is given by Eq. (4.16), with the substitution $\pi^0 \to \gamma$.

The preequilibrium contribution of photons, corresponding to photons emitted after the transit time of the two nuclei but before thermalization time, is not explicitly included in this work. However, a rough estimate might be had by choosing a smaller formation time. The modeling of those contributions is accessible to the parton cascade model [81]. Finally, in order to have a complete photon description, we have also calculated the background production, which mainly comes from the decay $\pi^0 \to \gamma\gamma$. This is given by [126]

$$\frac{dN^{\pi\to\gamma\gamma}_{\gamma-BG}}{dyd^2p_T} = \int dy^\pi d^2p^\pi_T \frac{dN^\pi}{dy^\pi d^2p^\pi_T}\frac{dP(\mathbf{p}_\pi \to \mathbf{p}_\gamma)}{dyd^2p_T}\,. \tag{4.65}$$

All the previous procedures for jet energy loss, initial spatial distribution and the effect of secondary jets are included in the calculation of the pion spectrum $\frac{dN^\pi}{dy^\pi d^2p^\pi_T}$:

$$\frac{dN^\pi}{dy^\pi d^2p^\pi_T} = \frac{\langle N_{coll}\rangle}{\sigma_{in}}\frac{d\sigma^{AA}_{NN}}{dyd^2p_T} \tag{4.66}$$

where the AA cross-section is given by Eq. 4.17. In the pion center of mass frame, the photon distribution is given by

$$\frac{dP(\mathbf{p}_\pi \to \mathbf{p}_\gamma)}{dyd^2p_T} = \frac{\delta(E^\gamma_{cm} - \frac{m_\pi}{2})}{2\pi E^\gamma_{cm}}\,, \tag{4.67}$$

normalized to

$$\int dyd^2p_T \frac{dP(\mathbf{p}_\pi \to \mathbf{p}_\gamma)}{dyd^2p_T} = 2\,. \tag{4.68}$$

We can express the photon energy in the pion center-of-mass frame, E^γ_{cm}, in terms of θ,E_π and p_T, which are respectively the angle between $\vec{p}_\pi$ and $\vec{p}_\gamma$ in the laboratory frame, and the pion and photon's energies in that frame. We get $\vec{p}^{\,\gamma}_{cm}$ from a boost $\beta = |\vec{p}_\pi|/E_\pi$ in the pion direction $\hat{\pi}_{||}$:

$$\vec{p}^{\,\gamma}_{cm} = p_T\mathrm{sin}\theta\,\hat{\pi}_\perp + p_T\frac{(\mathrm{cos}\theta - \beta)}{\sqrt{1-\beta^2}}\,\hat{\pi}_{||} \tag{4.69}$$

giving

$$\begin{aligned} E^\gamma_{cm} = |\vec{p}^{\,\gamma}_{cm}| &= p_T\sqrt{\sin^2\theta + \frac{(E_\pi\cos\theta - p_\pi)^2}{m_\pi^2}} \\ &= \frac{p_T}{m_\pi}(E_\pi - p_\pi\mathrm{cos}\theta)\,. \end{aligned} \tag{4.70}$$

Using the relation

$$dy^\pi d^2p^\pi_T = \frac{d^3p_\pi}{E_\pi} = \frac{p_\pi^2 dp_\pi d\mathrm{cos}\theta\, d\psi}{E_\pi} \tag{4.71}$$

we can express the photon yield by

$$\begin{aligned} \frac{dN^{\pi\to\gamma\gamma}_{\gamma-BG}}{dyd^2p_T} &= \int dp_\pi \frac{p_\pi^2}{E_\pi}\int_0^{2\pi} d\psi \int_{\mathrm{cos}_{min}}^1 d\mathrm{cos}\theta \frac{dN^\pi}{dy^\pi d^2p^\pi_T}\frac{\delta(E^\gamma_{cm} - \frac{m_\pi}{2})}{2\pi E^\gamma_{cm}} \\ &= \int_0^{2\pi} d\psi \int_{\mathrm{cos}_{min}}^1 d\mathrm{cos}\theta \frac{p_\pi^2}{E_\pi}\frac{dN^\pi}{dy^\pi d^2p^\pi_T}(p_\pi, y^\pi)\frac{\mathcal{J}^{-1}}{\pi m_\pi} \end{aligned} \tag{4.72}$$

where the Jacobian is

$$\mathcal{J} = \frac{p_T}{m_\pi}\left|\frac{\partial(E_\pi - p_\pi\mathrm{cos}\theta)}{\partial p_\pi}\right| = \frac{p_T}{E_\pi m_\pi}\left|p_\pi - E_\pi\mathrm{cos}\theta\right|\,. \tag{4.73}$$

The pion momentum p_π is solution of

$$E_\pi = \sqrt{p_\pi^2 + m_\pi^2} = p_T + \sqrt{(p_T - p_\pi \cos\theta)^2 + p_\pi^2 \sin^2\theta} \tag{4.74}$$

which gives:

$$p_\pi = \begin{cases} (4p_T^2 m_\pi^2 - m_\pi^4)/(4p_T m_\pi^2) & \cos^2\theta = 1 \\ \left(m_\pi^2 \cos\theta - m_\pi^2\sqrt{1 - 4p_T^2 \sin^2\theta / m_\pi^2}\right) / \left(2p_T \sin^2\theta\right) & \cos^2\theta \neq 1 \end{cases} \tag{4.75}$$

The lower bound of the cosine integration is given by

$$1 - 4p_T^2(1 - \cos^2\big|_{min})/m_\pi^2 = 0 \rightarrow \cos|_{min} = \sqrt{1 - \frac{m_\pi^2}{4p_T^2}}. \tag{4.76}$$

The ψ dependence in Eq. 4.72 is included in the pion rapidity y^π. However, for high-p_T photons, $\cos|_{min} \sim 1$, such that $y^\pi = y = 0$, and the ψ integration gives a factor 2π. Thus, we obtain

$$\frac{dN^{\pi\rightarrow\gamma\gamma}_{\gamma-BG}}{dyd^2p_T} = 2\int_{\cos|_{min}}^{1} d\cos\theta \frac{dN^\pi}{dy^\pi d^2p_T^\pi}(p_\pi, y)\frac{p_\pi^2}{p_T\,|p_\pi - E_\pi \cos\theta|} \tag{4.77}$$

To have a more complete picture of the photon background, we can also include the η contribution : $\eta \rightarrow \gamma + \gamma$. With the η branching ratio $\Gamma^{\eta\rightarrow\gamma\gamma}/\Gamma^\eta \sim 40\%$ [127] and its relative yield $N^\eta/N^{\pi^0} \sim 0.5$ [128], the total photon-background contribution becomes

$$\begin{aligned}\frac{dN_{\gamma-BG}}{dyd^2p_T} &= \frac{dN^{\pi^0\rightarrow\gamma\gamma}_{\gamma-BG}}{dyd^2p_T} + \frac{dN^{\eta\rightarrow\gamma\gamma}_{\gamma-BG}}{dyd^2p_T} = \frac{dN^{\pi^0\rightarrow\gamma\gamma}_{\gamma-BG}}{dyd^2p_T}\left(1 + \frac{N^\eta}{N^{\pi^0}}\frac{\Gamma^{\eta\rightarrow\gamma\gamma}}{\Gamma^\eta}\right) \\ &\sim 1.2\frac{dN^{\pi^0\rightarrow\gamma\gamma}_{\gamma-BG}}{dyd^2p_T}\end{aligned} \tag{4.78}$$

4.2.5 Results

The contributions to high p_T photon production, but the background coming from neutral meson decay, are illustrated in Fig. 4.13 for clarity, and their corresponding yield are shown in Fig. 4.14 for central collisions at RHIC and the LHC. The energy loss is included in all processes involving jets. Prompt photons have been split into a primary hard direct component (N-N) and a fragmentation component (jet-frag.). All those processes, except the contribution from jet-medium bremsstrahlung, have been presented in Ref. [32], in the case of no energy-loss. For RHIC, as in Ref. [32], the high p_T region is dominated by primary hard direct photons. However, in Ref. [32], the jet-photon conversion was dominant below 6 GeV, while in our study, direct photons dominate the high p_T spectrum down to $\sim$ 4 GeV. A few reasons explain this difference. The jet energy loss is included here; the constants $C_{\rm ann}$ and $C_{\rm Com}$ appearing in Eq. (4.38) have been set equal to 1.916 in Ref. [32]; the K_{jet} factor in the original publication is larger than ours: $K_{jet} = 2.5$ is used for both RHIC and the LHC while we use $K_{jet} = 1.7$ for RHIC and 1.6 for LHC. Finally, no K_γ factor has been used for the primary hard direct contribution in Ref. [32]. It is however satisfying that the inclusion of jet energy loss does not spoil the original premise: jet-photon conversion is an important source of electromagnetic radiation.

At the LHC, our result is dominated by direct photons for p_T above 20 GeV, but there is a window, below 14 GeV, where the jet-photon conversion in the plasma is the dominant mechanism of photon production. In Ref. [32], however, the jet fragmentation (called bremsstrahlung in their study) was the most important process at the LHC, but jet suppression was not included. Photon production via jet bremsstrahlung in the plasma (dotted lines) turns out to be weak, but non-negligible. It is approximately a factor 3 below the jet-photon conversion contribution. Finally, the thermal induced photons (short dashed lines) are far below all other contributions in intensity.

Fig. 4.15 shows the QGP photons for three different initial conditions: (T_i = 447 MeV, τ_i=0.147 fm/c),(T_i = 370 MeV, τ_i=0.26 fm/c) and (T_i = 280 MeV, τ_i=0.6 fm/c). As the high-p_T photons are produced early in the collision, they may be affected by the choice of initial conditions. However, the high-p_T region is dominated by jet-therm processes, which are weakly sensitive to (T_i, τ_i), since the jet distribution function f_{jet} has a weak temperature dependence. We see that going from τ_i=0.6

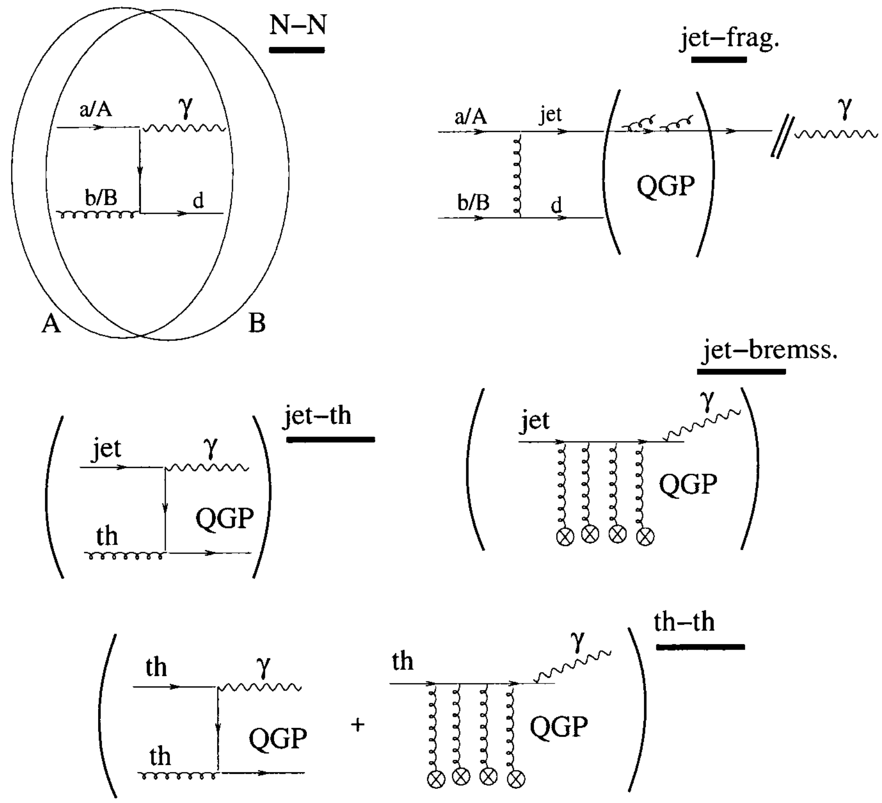

Figure 4.13: Picture showing all contributions of direct photons. a and b represent parton coming respectively from the nuclei A and B, and Th stands for a thermal particle from the QGP

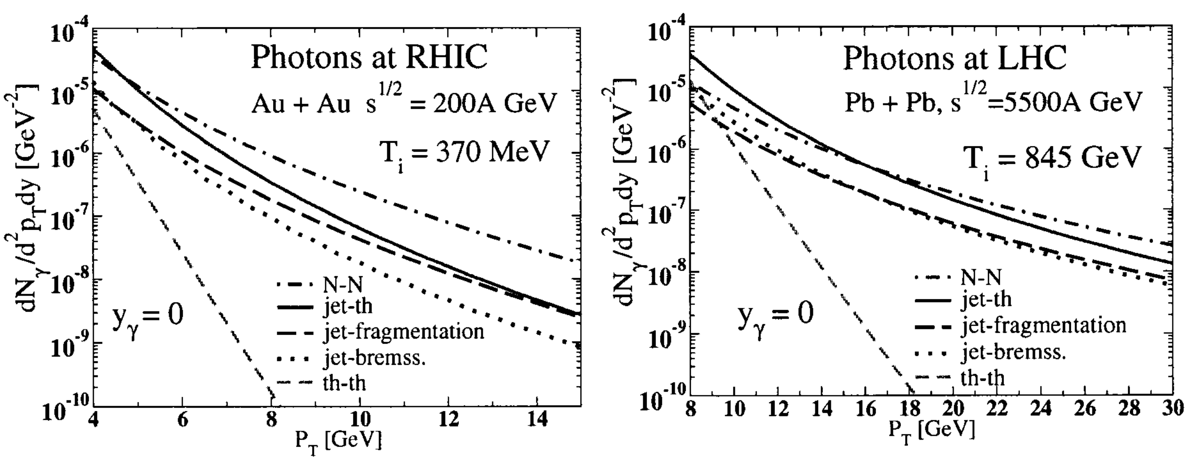

Figure 4.14: Contributing sources of high-p_T photons at mid-rapidity in central Au-Au collisions at RHIC (left panel) and Pb-Pb collisions at the LHC (right panel). Solid line: jet-photon conversion in the plasma; dotted line: bremsstrahlung from jets in the plasma; short dashed line: thermal induced production of photons; long dashed line: fragmentation of jets outside the plasma; and dot-dashed line: direct contribution from the primordial hard scattering.

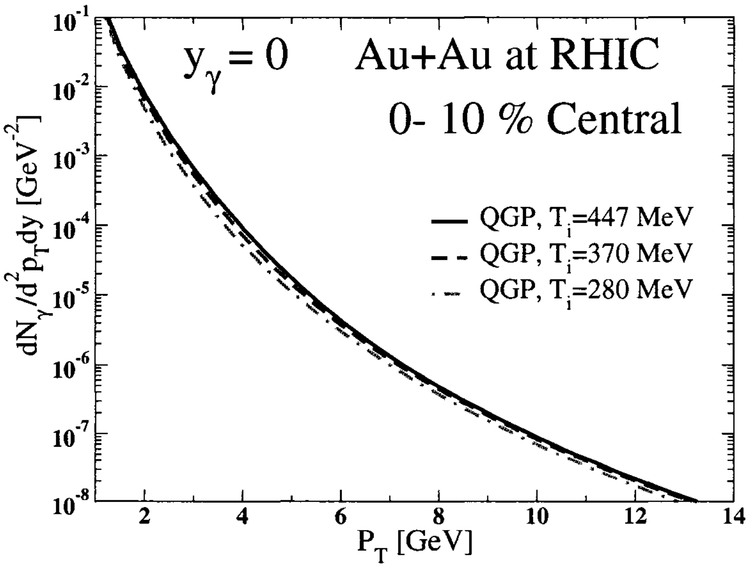

Figure 4.15: Production of photons during the QGP phase for three QGP initial conditions: solid line, (T_i = 447 MeV,τ_i=0.147 fm/c); dashed line, (T_i = 370 MeV,τ_i=0.26 fm/c); and dot-dashed line, (T_i = 280 MeV,τ_i=0.6 fm/c).

fm/c to τ_i=0.26 fm/c increases the photon production in the QGP phase by less that a factor 2; this additional contribution could be interpreted in some sense as a preequilibrium contribution.

Results for total photon production, after background subtraction, are available [129]. Our calculations are compared to experimental data on Fig. 4.16. In the top panel, the solid line includes the prompt photon contribution, the QGP (jet-th, th-th and jet-bremss.) and hadron gas contribution, calculated in Chapter 2. The initial condition for the thermal phase corresponds to T_i = 370 MeV and τ_i=0.26 fm/c. For a better comparison with data, we have extended our calculation down to p_T=1 GeV. No cutoff has been applied on either jet-th or prompt process. NLO calculations are not very reliable is this region, but thermal induced reactions and hadron gas contributions turn out to dominate there and NLO results play a minor role. When the jet-photon conversion is not included (dot-dashed line), the total photon production is reduced by up to 45 %, around p_T = 3 GeV. The result expected from pp collisions scaled to Au-Au is also shown (dashed line). The plasma contribution,

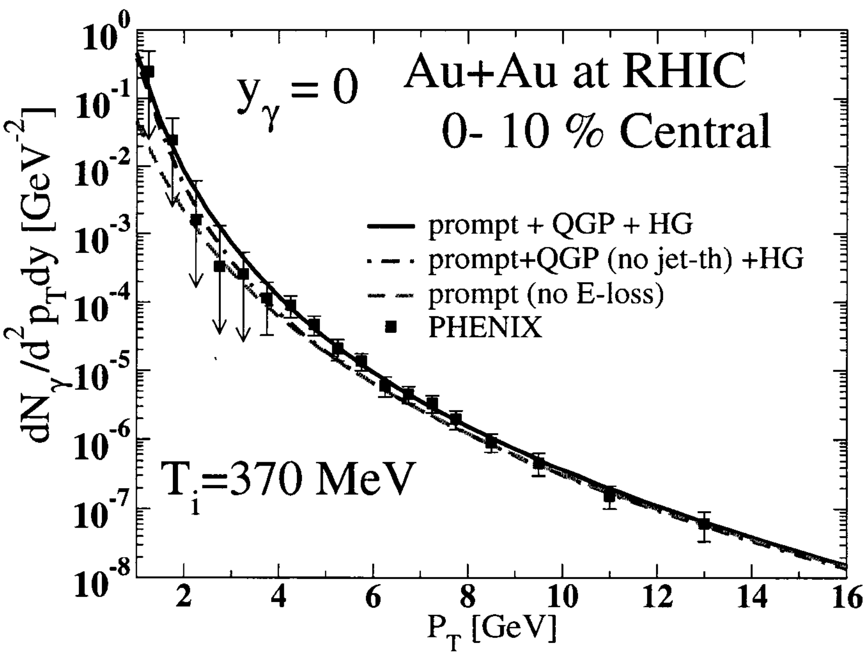

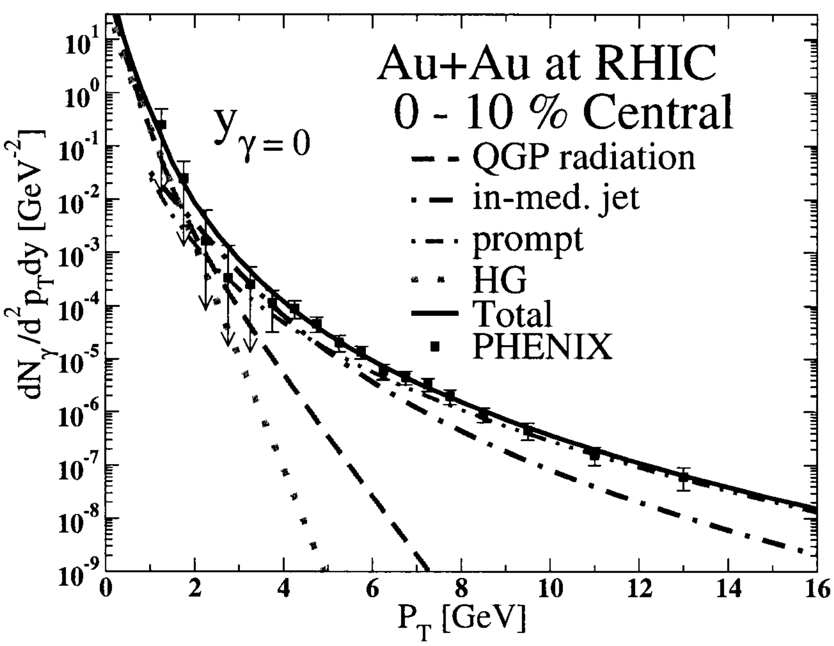

Figure 4.16: Total production of photons, after background subtraction, in central Au-Au collisions. Top panel : the solid line includes all processes from Fig. 4.14 and the hadron gas contribution, while the dot-dashed line doesn't include the jet-thermal contribution. pp collisions scaled to Au-Au are shown by the dashed line. Data are from PHENIX [129]. Bottom panel : dot-dashed line, jet-photon conversion and in-medium jet-bremsstrahlung; dashed line, thermal induced processes in the QGP; double dot-dashed line, prompt contribution; dotted line, hadron gas contribution; and the solid line, sum of all contributions.

specially the jet-thermal process, is very important for $p_T < 6$ GeV. However, those data contain large error bars which prevent a strong claim about the presence of a QGP. The different sources contributing to the top panel's solid line are shown in the bottom panel. As we have seen in Fig. 4.14, prompt photons (N-N added to jet-frag.) dominate the spectrum above p_T =6 GeV. The range $2 < p_T < 4$ GeV appears to be dominated by processes induced by the propagation of jets in the QGP, especially the jet-photon conversion. It is important here to say that in this range, the approximated cross-section for the jet-photon conversion process produces an error smaller than 25% (see Fig. 4.11). Finally, below $p_T = 1.5$ GeV, the hadron gas and the QGP radiation dominate the spectrum equally.

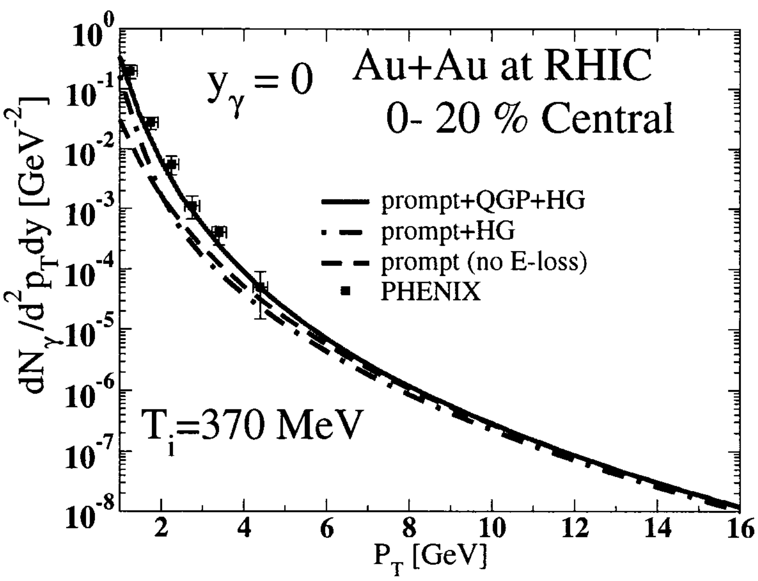

Figure 4.17: Production of photons at RHIC from differents contributions, compared to recent results from PHENIX [130] at intermediate p_T, for the centrality class 0-20%.

Very recent intermediate p_T photons data have been presented by PHENIX, in the centrality class $0-20\%$ [130]. They are shown in Fig. 4.17. With the enhanced quality of the data, relatively to those presented in Fig. 4.16, we can claim that, according to our calculations, a contribution from the QGP is necessary to reproduce the experimental measurements, since only the line including QGP photons (solid line) agrees with the data. When we remove the QGP components, calculations underpredict the data by a factor $\sim$ 3 around p_T=3 GeV (dot-dashed line).

Our prediction for the LHC is shown in Fig. 4.18. The signature of the QGP phase is much stronger than at RHIC, increasing the photon yield, relatively to pp scaled to Pb-Pb collision, by one order of magnitude around p_T = 3 GeV, where the hadron gas contribution turns out to be negligible.

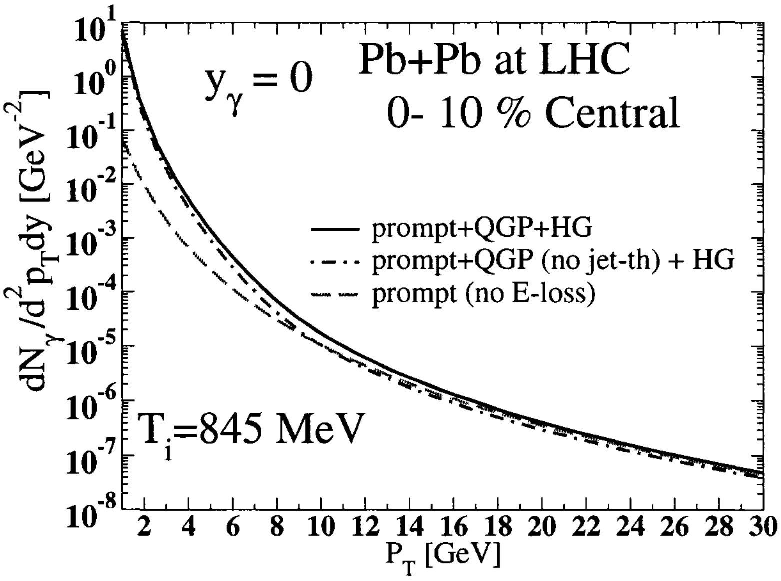

Figure 4.18: Production of photons at the LHC. Same line description that for the top panel of Fig. 4.16.

An interesting way to visualize the in-medium effect is to plot the nuclear modification factor R_{AA} for photons, as we did for pions (see Eq. 4.9). In the absence of medium effects, we expect to have R_{AA} $\sim$1. We can see however from Fig. 4.19 that R_{AA} is much greater than 1, especially when the jet-photon conversion is included, reaching a factor 4 for RHIC around p_T =2 GeV, and more that a factor 10 at the LHC.

Finally, we have calculated the ratio of the total number of photons and the background photons

$$\gamma_{\text{Total}}/\gamma_{\text{BG}} = \frac{\frac{dN_{\gamma-\text{BG}}}{d^2p_Tdy} + \sum \text{all other sources}}{\frac{dN_{\gamma-\text{BG}}}{d^2p_Tdy}}$$

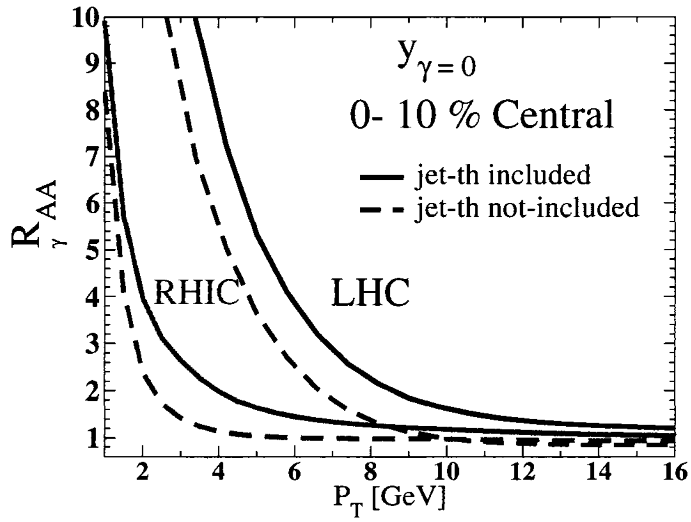

Figure 4.19: Nuclear modification factor of photons at RHIC and the LHC. The solid lines include the jet-photon conversion process but the dashed lines don't.

$$= 1 + \frac{\frac{dN_{jet-th}}{d^2p_Tdy} + \frac{dN_{jet-br}}{d^2p_Tdy} + \frac{dN_{th-th}}{d^2p_Tdy} + \frac{dN_{\gamma-prompt}}{d^2p_Tdy}}{\frac{dN_{\gamma-\mathrm{BG}}}{d^2p_Tdy}} \tag{4.79}$$

and compared in Fig. 4.20, with the result from PHENIX [129], with and without the QGP contribution. The calculation including the QGP contribution is in agreement with the data from RHIC, except for a few data points in the range $7 < p_T < 9$ GeV. Without the thermal contributions, the resulting line (dot-dashed) does not overlap at all with the experimental data. That could constitute an another signature of the importance of the jet-photon conversion inside the QGP, since this is the most important thermal process as we have seen in Fig. 4.14. We also show the weak effect of the initial temperature. The ratio $\gamma_{\mathrm{Total}}/\gamma_{\mathrm{BG}}$ at $T_i = 447$ MeV is only enhanced by $\sim 5\%$ relatively to the result at T_i=370 MeV. Finally at the LHC (right panel), the thermal contribution is also visible: including the photons from the thermal phase enhances the calculation by $\sim 15\%$.

4.3 Summary and Conclusions

We have used a complete leading-order treatment of jet energy loss in the QCD plasma to calculate the pion and photon spectra for both RHIC and the LHC. The

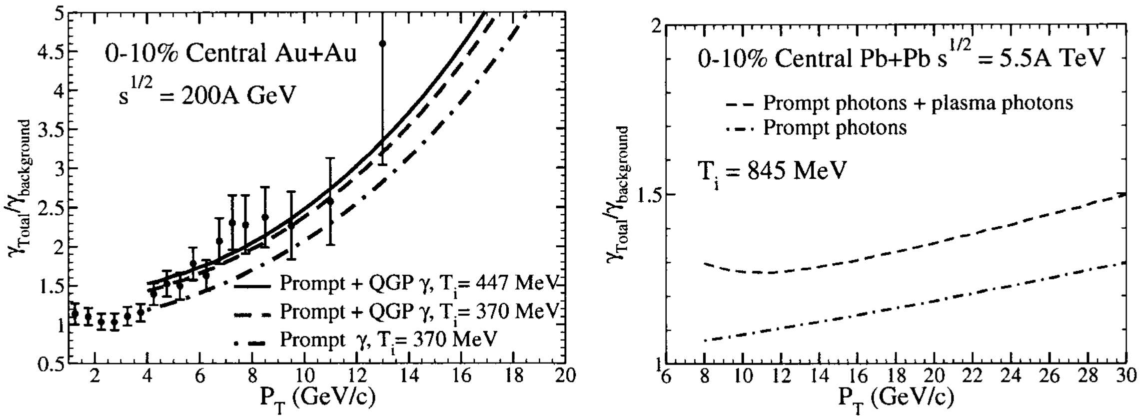

Figure 4.20: (Color online) Ratio of all photons over all decay photons as a function of p_T, in Au-Au collisions at RHIC (left panel) and Pb-Pb at the LHC (right panel), with and without the thermal contribution. In the left panel, the effect of the initial temperature is also shown. The data are from the PHENIX [129] collaboration.

calculations have been confronted with available data from RHIC and turn out to be in good agreement. These results reinforce the idea that high p_T suppression is a final state effect caused by jet energy loss through bremsstrahlung in the hot medium.

The neutral pion nuclear modification factor at RHIC as been reproduced with an initial temperature T_i =370 MeV and a formation time τ_i=0.26 fm/c, corresponding to dN/dy=1260. Those parameters are consistent with the analysis in Chapter 2. R_{AA} has shown a large dN/dy dependence, but a weak dependence on the initial temperature T_i (provided the starting time τ_i is changed to keep dN/dy constant). The calculation included the nuclear geometry; assuming that all jets are produced at the center overestimates the suppression by $\sim$ 50%.

We have also computed the production of high p_T photons from the initial collision, from the medium, and from jet-medium interactions. The jet-medium photons improve the agreement between experiment and theory at RHIC, and they are expected to dominate the signal at the LHC below about 14 GeV. Thermally-induced photons are not very important to either experiment, in the kinematical range on which we have concentrated. In light of these results, the in-medium production of dileptons should also be reconsidered. This will be the topic of Chapter 6

5

Non-central relativistic heavy ion collisions

In this chapter, we calculate photon and pion spectrum in non-central heavy ions collisions. Nuclear collisions at finite impact parameter $b > 0$ start out in an initial state which is not azimuthally symmetric around the beam axis. Instead, the initial overlap zone of the two nuclei has an "almond" shape. Therefore particle spectra measured in the final state are not necessarily isotropic around the beam axis. We show that a sizeable azimuthal asymmetry, characterized by a coefficient v_2, is to be expected for direct photons produced in those high energy nuclear collisions. This signal is generated by photons radiated by jets interacting with the surrounding hot plasma. The anisotropy is out of phase by an angle $\pi/2$ with respect to that associated with the elliptic anisotropy of hadrons, leading to negative values of v_2. The observation of such an asymmetry would be a signature for the presence of a quark gluon plasma and would establish the importance of jet-plasma interactions as a source of electromagnetic radiation.

5.1 Framework for non-central collisions

5.1.1 Non-thermal processes

The thickness function of a nucleus with nucleon number A, is defined by [65]

$$T_A(\vec{r}^{\,a}_{\perp}) = \int dz_a \, \rho_A(\vec{r}^{\,a}_{\perp}, z_a) \tag{5.1}$$

where ρ_A is the nucleon density. The thickness function is normalized to

$$\int d\vec{r}^{\,a}_{\perp} T_A(\vec{r}^{\,a}_{\perp}) = \int d^3x \, \rho_A(\vec{x}) = A \tag{5.2}$$

For a collision $A-B$ at an impact parameter b, the overlap function of the nuclei is

$$T_{AB}(b)=\int d\overrightarrow{r}^{a}_{\perp}\, T_A(\overrightarrow{r}^{a}_{\perp})\, T_B(\overrightarrow{r}^{a}_{\perp}+\overrightarrow{b})\,. \tag{5.3}$$

This is a purely geometrical function. It gives the number of nucleon pairs, per unit of area, which come to the vicinity of each other, during a collision at impact parameter b. The number of inelastic nucleon-nucleon collisions at b is simply given by

$$n(b)=T_{AB}(b)\sigma_{in} \tag{5.4}$$

The probability to have at least one inelastic nucleon-nucleon collision is

$$P(b)=\frac{d\sigma_{AB}}{d^2b}(b)=\sum_n (n|AB)\left(\frac{T_{AB}(b)}{AB}\sigma_{in}\right)^n\left(1-\frac{T_{AB}(b)}{AB}\sigma_{in}\right)^{AB-n} \tag{5.5}$$

where n is the number of collisions suffered by one nucleon, and $(n|AB)$ represents the number of combinations of having one nucleon scattering n-times. $\left(\frac{T_{AB}(b)}{AB}\sigma_{in}\right)^n$ gives the probability for the nucleon to scatter n-times, where σ_{in} is the inelastic nucleon-nucleon cross-section, and $\left(1-\frac{T_{AB}(b)}{AB}\sigma_{in}\right)^{AB-n}$ represents the probability, for all other possible pairs of nucleons, of having no interaction. The probability of having no interaction at all, $n=0$, is

$$t(b)=\left(1-\frac{T_{AB}(b)}{AB}\sigma_{in}\right)^{AB}\,. \tag{5.6}$$

Since, we must have $P(b)+t(b)=1$, we can write the differential cross-section as

$$\frac{d\sigma_{AB}}{d^2b}(b)=P(b)=1-t(b)=1-\left(1-\frac{T_{AB}(b)}{AB}\sigma_{in}\right)^{AB}\,. \tag{5.7}$$

A centrality class is defined experimentally by a relative number of collisions. For example, if 100 collisions are detected, the centrality class $0-10\%$ will include ten of those collisions : those having the lowest impact parameter b. Theoretically, all collisions with an impact parameter b, with $b_x<b<b_y$, are included in a $x-y\%$ centrality class, where b_x and b_y are solutions of :

$$x(y)\%=\frac{\int_0^{b_{x(y)}} d^2b\,\frac{d\sigma_{AB}}{d^2b}}{\int_0^{\infty} d^2b\,\frac{d\sigma_{AB}}{d^2b}}\,. \tag{5.8}$$

Assuming that an inelastic nucleon-nucleon collision happens, the probability to emit a prompt photon is given by the ratio $\sigma_{\gamma-prompt}/\sigma_{in}$, where the prompt photon cross-section is given by

$$\sigma_{\gamma-prompt} = \int dy\, d^2p_T\, \frac{d\sigma_{\gamma-prompt}}{dyd^2p_T} \tag{5.9}$$

and $d\sigma_{\gamma-prompt}/dyd^2p_T$ is given in Eq. 4.37. When particles are produced at midrapidity with a large p_T, we can assume that a nucleus-nucleus collision represents an addition of nucleon-nucleon collisions, and neglect interference effects among them, because the exchanged momentums are big, which imply very small timescales. Then the number of prompt photons emitted in a AB collision at impact parameter b is just the number of inelastic NN collisions times the probability to emit a prompt photon :

$$N_{\gamma-prompt}(b) = n(b)\frac{\sigma_{\gamma-prompt}}{\sigma_{in}} = T_{AB}(b)\,\sigma_{\gamma-prompt} \tag{5.10}$$

It follows that

$$\frac{dN_{\gamma-prompt}}{dyd^2p_T}(b) = T_{AB}(b)\frac{d\sigma_{\gamma-prompt}}{dyd^2p_T}(b)\,. \tag{5.11}$$

Note than $d\sigma_{\gamma-prompt}/dyd^2p_T$ gets an impact parameter dependence when final state effects are present. The averaged number of photons emitted in a centrality class $x-y\%$ is given by

$$\frac{dN_{\gamma-prompt}}{dyd^2p_T} = \frac{\sum_{b=b_x}^{b_y}\frac{dN_{\gamma-prompt}}{dyd^2p_T}(b)}{\sum_{b=b_x}^{b_y}P(b)} = \frac{\int d^2b\,\xi(b)\frac{dN_{\gamma-prompt}}{dyd^2p_T}(b)}{\int d^2b\,\xi(b)\frac{d\sigma_{AB}}{d^2b}(b)} \tag{5.12}$$

where ξ is the number of impact parameter, per unit area, in a small surface around $\overrightarrow{b}$. For an uniform distribution of impact parameter, ξ is constant. This gives

$$\frac{dN_{\gamma-prompt}}{dyd^2p_T} = \frac{\int_{b_x}^{b_y}db\,b\,\frac{dN_{\gamma-prompt}}{dyd^2p_T}(b)}{\int_{b_x}^{b_y}db\,b\,\frac{d\sigma_{AB}}{d^2b}(b)} = \frac{\int_{b_x}^{b_y}db\,b\,T_{AB}(b)\frac{d\sigma_{\gamma-prompt}}{dyd^2p_T}(b)}{\int_{b_x}^{b_y}db\,b\,\frac{d\sigma_{AB}}{d^2b}(b)} \tag{5.13}$$

When the centrality class is narrow enough, the cross-section can be evaluated at some averaged impact parameter between b_x and b_y and factorized from the integral:

$$\begin{aligned}\frac{dN_{\gamma-prompt}}{dyd^2p_T} &= \frac{\frac{d\sigma_{\gamma-prompt}}{dyd^2p_T}(\bar{b})\int_{b_x}^{b_y}db\,b\,T_{AB}(b)}{\int_{b_x}^{b_y}db\,b\,\frac{d\sigma_{AB}}{d^2b}(b)} \\ &= \frac{\langle N_{coll}\rangle}{\sigma_{in}}\frac{d\sigma_{\gamma-prompt}}{dyd^2p_T}(\bar{b}) \end{aligned}\tag{5.14}$$

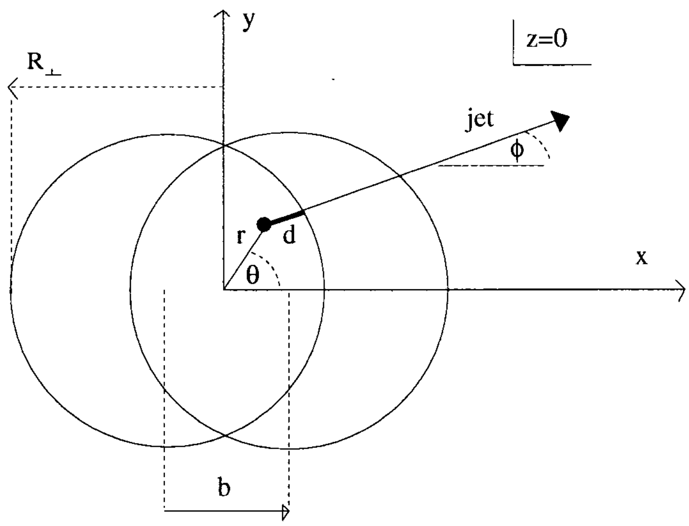

Figure 5.1: Picture of an nucleus-nucleus collision in the transverse plane, for an impact parameter b.

where the averaged number of collisions is

$$\langle N_{coll}\rangle = \frac{\int_{b_x}^{b_y} db\, b\, T_{AB}(b)\sigma_{in}}{\int_{b_x}^{b_y} db\, b\, \frac{d\sigma_{AB}}{d^2b}(b)} = \frac{\int_{b_x}^{b_y} db\, b\, n(b)}{\int_{b_x}^{b_y} db\, b\, \frac{d\sigma_{AB}}{d^2b}(b)}\,. \tag{5.15}$$

Now, as we did in Chapter 4, we have to include the energy suppression of the jets, as they propagate in the QGP. However, it is a little more complicated here as the medium is not-symmetric. The Fig. 5.1 shows the profile of a AB collision in the transverse plane, at an impact parameter b. The interacting zone is shown be the overlap of the two nuclei. In this picture, a jet is created at the coordinates (r,θ), and propagates thereafter in the hot matter in the direction ϕ, relatively to the x-axis. The jet will suffer the suppression induced by the medium, during an amount of time t_x, given by the smallest value between the duration of the QGP phase, and the propagation distance d in the interacting zone, shown by the thick line. Those features are included in the in-medium fragmentation function, discussed in Chapter 4:

$$\tilde{D}_{h/c}(z,Q) = \int_0^{2\pi} d\theta \int_0^{r_{max}} dr\, r\mathcal{P}(\mathbf{r}_\perp) \int dp_f \frac{z'}{z} \left(P_{q\bar{q}/c}(p_f;p_i|t_x) D_{h/q}(z',Q) + P_{g/c}(p_f;p_i|t_x) D_{h/g}(z',Q)\right)\,. \tag{5.16}$$

The maximum radial distance from the center, r_{max}, depends on the angle θ:

$$r_{max} = \frac{-b|\cos\theta|}{2} + \frac{\sqrt{4R_\perp^2 - b^2\sin^2\theta}}{2} \tag{5.17}$$

We also need to evaluate the initial radial distribution of jets $\mathcal{P}(\mathbf{r}_\perp)$. Assuming a uniform distribution of nucleons ρ_0 in the nucleus, the number of nucleons, per unit area, at a transverse distance r from the center of the nucleus is

$$X_A(r) = \int_0^{2\pi} d\theta \int_{-\sqrt{R_\perp^2-r^2}}^{\sqrt{R_\perp^2-r^2}} dz\, \rho_0 = 4\pi\, \rho_0 \sqrt{R_\perp^2 - r^2}\,. \tag{5.18}$$

The radial jet distribution at an impact parameter b is thus given by

$$\begin{aligned}\mathcal{P}(\mathbf{r}_\perp, b) &= C\, X_A\left(\left|\vec{r} + \frac{\vec{b}}{2}\right|\right) X_B\left(\left|\vec{r} - \frac{\vec{b}}{2}\right|\right) \\ &= C\sqrt{\left(R_\perp^2 - r^2 - \frac{b^2}{4}\right)^2 - b^2 r^2 \cos^2\theta}\end{aligned} \tag{5.19}$$

where the normalization factor C is fixed by

$$\int_0^{2\pi} d\theta \int_0^{r_{max}} dr\, r\mathcal{P}(\mathbf{r}_\perp, b) = 1\,. \tag{5.20}$$

In the limit $b = 0$, it reproduces the radial distribution from Eq. 4.15. Finally, to do the calculations, we need to evaluate $T_{AB}(b)$. We could start with a nucleon density ρ_A and evaluate the thickness function T_A with Eq. 5.1, and finally the overlap function with the help of Eq. 5.3. For our work, we rather take a parametrization of T_{AB}, given by Wong in Ref. [65]:

$$T_{AB}(b) = \frac{AB}{2\pi\beta^2} e^{-b^2/(2\beta^2)} \tag{5.21}$$

with

$$\beta^2 = 0.68^2 + \frac{r_0^2 A^{2/3}}{3} + \frac{r_0^2 B^{2/3}}{3} \tag{5.22}$$

and r_0 ~0.97 fm. This gives a good reproduction of the $\langle N_{coll}\rangle$ values calculated in Ref. [125].

5.1.2 Thermal processes

Using the same argument as in central collisions, we assume again a 1-D hydro expansion for the QGP phase during peripheral collisions. This argument was based on the weakness of the transverse flow during the QGP phase. For peripheral collisions, there is, in addition to transverse flow, an elliptic flow [122]. But again, this elliptic flow will take some time to develop, so that its effect on the early QGP phase should be negligible. However, this argument could be faulty at the LHC, as the expected duration of the QGP is larger.

In the absence of transverse expansion, the temperature evolves again according to

$$T(\mathbf{r}_\perp, b) = T_i(\mathbf{r}_\perp, b) \left(\frac{\tau_i}{\tau}\right)^{1/3} \tag{5.23}$$

The initial energy density is given by

$$\epsilon(\mathbf{r}_\perp, \tau_i, b) \propto \mathcal{P}(\mathbf{r}_\perp, b) \tag{5.24}$$

with

$$\int d^2r\, \epsilon(\mathbf{r}_\perp, \tau_i, b) \sim \epsilon_0(\tau_i, b)\, A_\perp(b)\,, \tag{5.25}$$

where $A_\perp$ is the surface area of the interacting zone, in the transverse plane (see Fig. 5.1):

$$A_\perp(b) = \pi R_\perp^2 - b\sqrt{R_\perp^2 - \frac{b^2}{4}} - 2R_\perp^2 \sin^{-1}(\frac{b}{2R_\perp}) \tag{5.26}$$

At thermalization, the averaged energy density is [111]

$$\epsilon_0(\tau_i, b) = \frac{g_Q \pi^2}{30} T_i(b)^4\,. \tag{5.27}$$

It follows that

$$T_i(\mathbf{r}_\perp, b) = T_i(b)\, [A_\perp(b)\mathcal{P}(\mathbf{r}_\perp, b)]^{1/4}\,. \tag{5.28}$$

The initial conditions are fixed by Eq. 4.36, extrapolated to non-central collisions:

$$T_i(b)^3\tau_i = \frac{\pi^2}{\zeta(3)g_Q}\frac{1}{A_\perp(b)}\frac{dN}{dy}(b) \tag{5.29}$$

where the particle radidity densities dN/dy are obtained from Ref. [92] for different classes of centrality. The thermal photons yield are finally given by the usual space-time integration:

$$\frac{dN_{\gamma-thermal}}{dyd^2p_T}(b) = \int_{\tau_i} d\tau\,\tau \int_0^{2\pi} d\theta \int_0^{r_{max}(b)} dr\,r \int_{-\eta_{max}}^{\eta_{max}} d\eta\,\frac{dR}{dyd^2p_T}(E = p_T\cosh(y-\eta))\,. \tag{5.30}$$

The average over impact parameters is done as before:

$$\frac{dN_{\gamma-thermal}}{dyd^2p_T} = \frac{\int_{b_x}^{b_y} db\,b\,\frac{dN_{thermal}}{dyd^2p_T}(b)}{\int_{b_x}^{b_y} db\,b\,\frac{d\sigma_{AB}}{d^2b}(b)} \tag{5.31}$$

For the jet-conversion and jet-bremsstrahlung processes, it is important to also scale the initials jet distributions, Eq. 4.48, to non-central collisions:

$$\left.\frac{dN^{jet}}{dyd^2p_T}(b)\right|_{y,\hat{t}=0} = \frac{T_{AB}(b)}{T_{AB}(b=0)}\left.\frac{dN^{jet}}{dyd^2p_T}(b=0)\right|_{y,\hat{t}=0}\,. \tag{5.32}$$

5.2 *Pion and photon yields*

The nuclear modification factor of pions at RHIC, as been evaluated in Fig. 5.2, for peripheral collisions. R_{AA}, for centrality class $x-y\%$, is calculated by

$$R_{AA} = \frac{\sigma_{in}\int_0^{2\pi} d\phi\,dN_\pi^{AA}/dyd^2p_T}{\langle N_{coll}\rangle\int_0^{2\pi} d\phi\,d\sigma_\pi^{NN}/dy/d^2p_T} = \frac{\int_{b_x}^{b_y} db\,b\int_0^{2\pi} d\phi\,T_{AB}(b)d\sigma_{NN}^{AA}/dyd^2p_T}{2\pi d\sigma_\pi^{NN}/dy/d^2p_T\int_{b_x}^{b_y} db\,b\,T_{AA}(b)}\,. \tag{5.33}$$

We have calculated the nuclear modification factor for the following centrality classes: $10-20\%$, $20-30\%$, $30-40\%$, and $40-50\%$. For simplicity, we assume the same formation time for all centralities, $\tau_i = 0.26$ fm/c, corresponding to the value taken for central collisions at RHIC in Chapter 4. The initials temperatures are fixed by Eq. 5.29. The corresponding initials temperatures are respectively T_i =380, 360, 340 and 310 MeV.

It turns out, from Fig. 5.2, that the AMY formalism, together with the Bjorken expansion, extrapolated to non-central collisions is quite consistent with the PHENIX data [12] even though the errors bars are large. It is important to notice that the free parameter of the AMY formalism is α_s. In this thesis, we take $\alpha_s = 0.3$, but the sensibility of AMY to α_s is shown in Fig. 5.2. As the gluon bremsstrahlung rate goes like α_s^2, the jet suppression and R_{AA}^{-1} follow approximately this scaling. We have verified however, that the total photon yield, after background subtraction, is only weakly sensitive to this parameter. Indeed, the very high-p_T region is dominated by the primary hard direct contribution coming from initial NN scatterings. Since, this is a non-thermal process, α_s is rather determined by

$$\alpha_s = \frac{12\pi}{(33 - 2\,N_f)\ln(Q^2/\Lambda^2)} \tag{5.34}$$

where the momentum scale Q has been set to p_T, N_f=3 and the QCD scale $\Lambda \sim 200$ MeV. Also, the region $2 < p_T < 4$ GeV is dominated at RHIC, by the jet-photon conversion. Increase α_s increases the jet-photon production rate, but also enhances the suppression of the jets distribution function $f^{q+\bar{q}}$ prior they produce photons, so that those two opposite effects almost cancel. Finally, the thermally-induced radiation from the QGP depends of course on α_s, but they are subdominant in the high-p_T range.

Our photon yield calculations, for non-central Au-Au collisions, are shown in Fig. 5.3 along with PHENIX data [129]. Each contributions are averaged over impact parameter according to Eqs. 5.13 and 5.31. The solid lines, include all processes discussed in Chapter 4, after background subtraction, while the dashed lines represent the NN calculations scaled to Au-Au collisions, so without final state effects. Any discrepancies between the two calculations can be explained in terms of final state effects (jet suppression) and QGP contributions. For $p_T < 4$ GeV, the solid lines stand above the dashed lines, implying a non-negligible QGP contribution, according to our calculations. For more central collisions, including the QGP enhances the result by a factor $\sim$3 around p_T =2 GeV, while this factor reduced to $\sim$ 2 for more peripheral

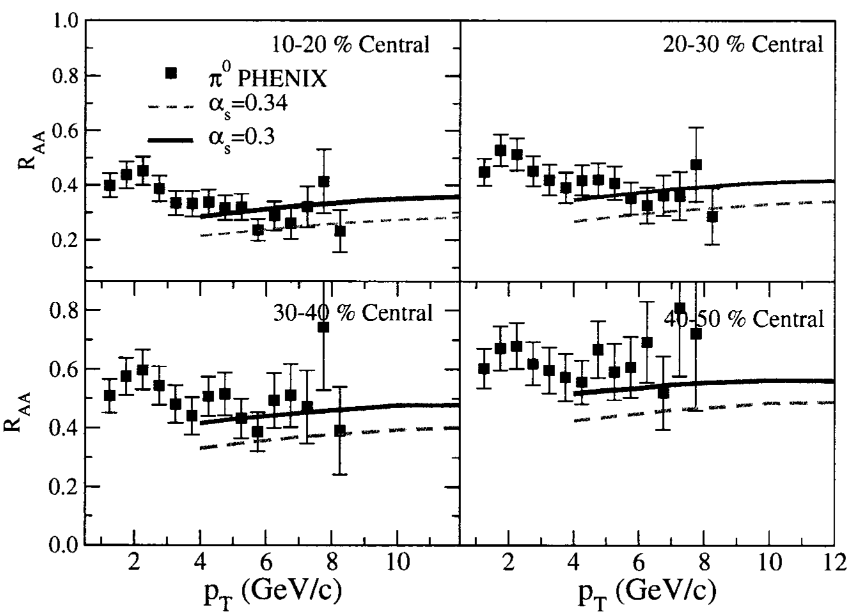

Figure 5.2: Nuclear modification factor of pions for Au+Au at RHIC, for different classes of centrality. Solid lines, α_s=0.3; dashed lines, α_s=0.34.

collisions. Since the initial temperature decreases with increasing impact parameter, the cooling is faster and the expected lifetime of the QGP phase is smaller, for more peripheral collisions, so that the QGP contribution and the p_T suppression become smaller. Finally, the ratios of all photons over all decay photons have also been calculated. This is shown in Fig. 5.4 for different centrality class at RHIC, with (solid lines) and without (dashed lines) QGP contributions. Again, the QGP contributions are more considerable for central collisions, where they are important for reproducing data.

In this section, we have compared with success our photon and pion calculations to PHENIX measurements in non-central collisions. It tells us that the 1-D Bjorken expansion, extrapolated to non-central collisions, can correctly describe high p_T data in Au-Au collisions at RHIC. In the next section, this model will be used, to calculate for the first time, the elliptic distribution of direct photons.

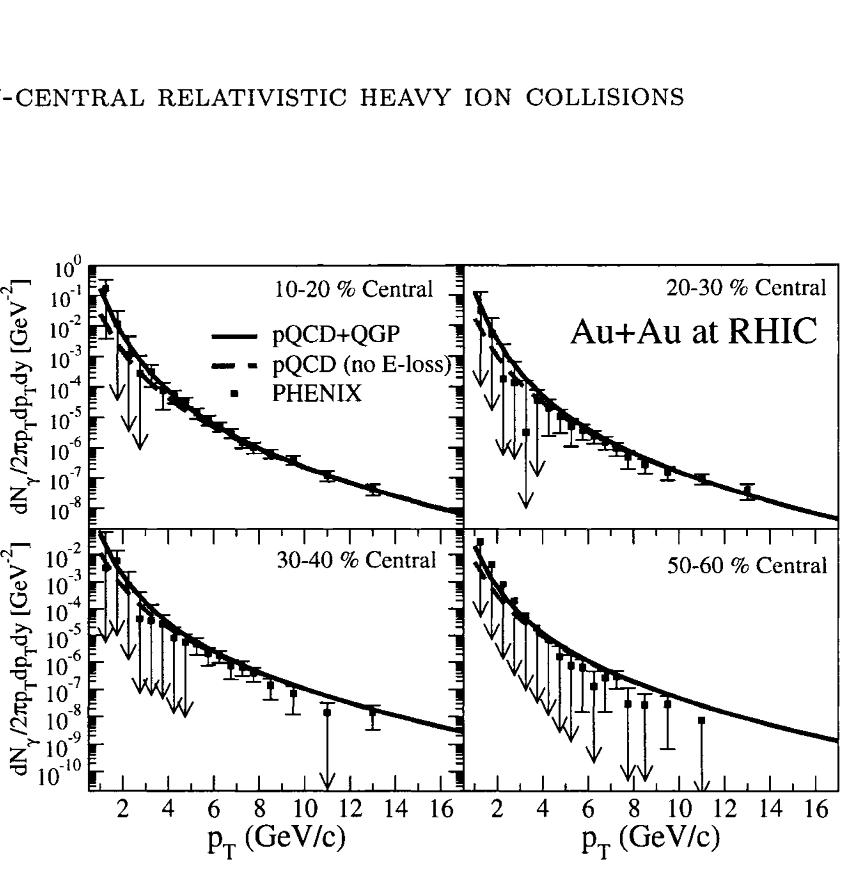

Figure 5.3: Photon production in Au-Au at RHIC for different class of centrality. The solid lines include all photon sources after background subtraction, while the dashed lines represent NN collisions scaled to Au-Au, without energy loss.

5.3 *Azimuthal asymmetry*

5.3.1 *Definition*

It has been argued that the translation of the original space-time asymmetry into a momentum space anisotropy can reveal important information about the system [131]. Two different mechanisms are important here: hydrodynamic pressure from the bulk of the matter, at low- to intermediate-p_T, and a simple optical-depth argument for intermediate- to high-p_T particles.

Let us define the event plane as the plane spanned by the beam axis and the impact parameter of the colliding nuclei. For the bulk of the matter, the initial space-time asymmetry leads to an anisotropic pressure gradient which is larger where the material is thinner, i.e. *in* the reaction plane, in a direction parallel to the impact parameter (in the x-direction, see Fig. 5.1). This in turn translates into a larger flow

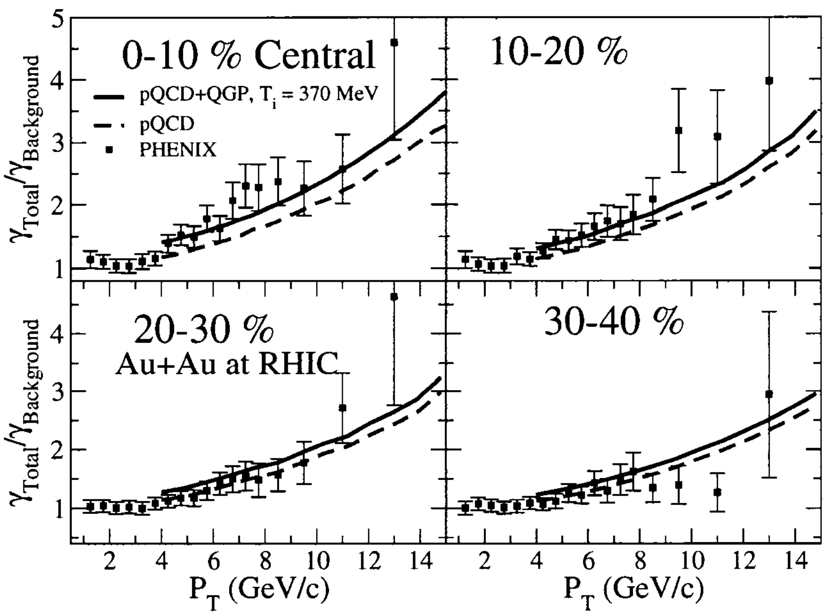

Figure 5.4: Ratio of all photons over all decay photons, in Au-Au collisions at RHIC, for different centrality class. The solid lines include QGP contributions, while the dashed lines don't.

of matter in this direction. The anisotropy is usually analyzed in terms of Fourier coefficients v_k defined from the particle yield $dN/p_T dp_T d\phi$, a function of period 2π, as

$$\frac{dN}{p_T dp_T dy d\phi} = \frac{dN}{2\pi p_T dp_T dy}\left[1 + \sum_k 2v_k(p_T, y)\cos(k\phi)\right] \tag{5.35}$$

with the coefficients v_k given by

$$v_k(p_T, y) = \frac{\int_0^{2\pi} d\phi \cos k\phi \, dN/dyd^2p_T}{\int_0^{2\pi} d\phi \, dN/dyd^2p_T}\,. \tag{5.36}$$

The angle ϕ is defined with respect to the reaction plane (see Fig. 5.1). At midrapidity all odd coefficients vanish for symmetry reasons, leaving the coefficient v_2 to be the most important one. We average over the impact parameter belonging to the $x-y\%$ centrality class, in the following way [133]

$$v_2(p_T, y)|_{x-y} = \frac{\int_{b_x}^{b_y} db\, b \int_0^{2\pi} d\phi \cos 2\phi \, dN/dy/d^2p_T(b)}{\int_{b_x}^{b_y} db\, b \int_0^{2\pi} d\phi \, dN/dyd^2p_T(b)} \tag{5.37}$$

The size of v_2 determines the ellipsoidal shape of the anisotropy. From what was said above it is clear that the elliptic anisotropy coefficient v_2 is always positive for hadrons at low and intermediate p_T due to the hydrodynamic flow. On the other hand, jets loose more energy when they are born into a direction where the medium is thicker, i.e. out of the reaction plane (in the y-direction, see Fig. 5.1). The stronger jet quenching leads to fewer hadrons at intermediate and high p_T emitted into this direction. This implies that the "optical v_2" for hadrons is also positive. RHIC measurements [134] of pion and kaon v_2, for the centrality class $0-20\%$, $20-40\%$ and $40-60\%$ are shown in Fig. 5.5. The data cover however only the low to intermediate p_T region, which can be explained by recombination models [132]. Our calculations, however, include only jet-fragmentation, so that our results are only reliable above p_T = 4-5 GeV. There is no overlap between data and our calculations, but a naive extrapolation of the data toward high-p_T values would suggest some agreement with our results. Fig. 5.5 shows also the effect of α_s on v_2. It appears that v_2 follows also a α_s^2 scaling: increasing α_s to $\alpha_s^{'}$ will increase the suppression, and v_2, by $\sim (\alpha_s^{'}/\alpha_s)^2$.

5.3.2 *Photon v_2*

In this section, we discuss the elliptic anisotropy of direct photons. We concentrate on intermediate and high p_T and argue that some of the processes mentioned previously are effective in converting the initial azimuthal asymmetry into elliptic anisotropy. Here we define a mechanism that works by having particles or jets going through the medium, thus being sensitive to the thickness of the medium. This defines an 'optical' process. It turns out that in some cases an inverse-optical mechanism is in place for photons: there are more particles emitted into the direction where the nuclear overlap zone is thicker, thus leading to a situation where the anisotropy is shifted by a phase $\pi/2$. Correspondingly, v_2 is negative in this case.

Let us now discuss the different contributions to the photon spectrum and their expected v_2 contribution. All photon sources that we will discuss here have been presented in Chapter 4. Direct photons from primary hard Compton and annihilation

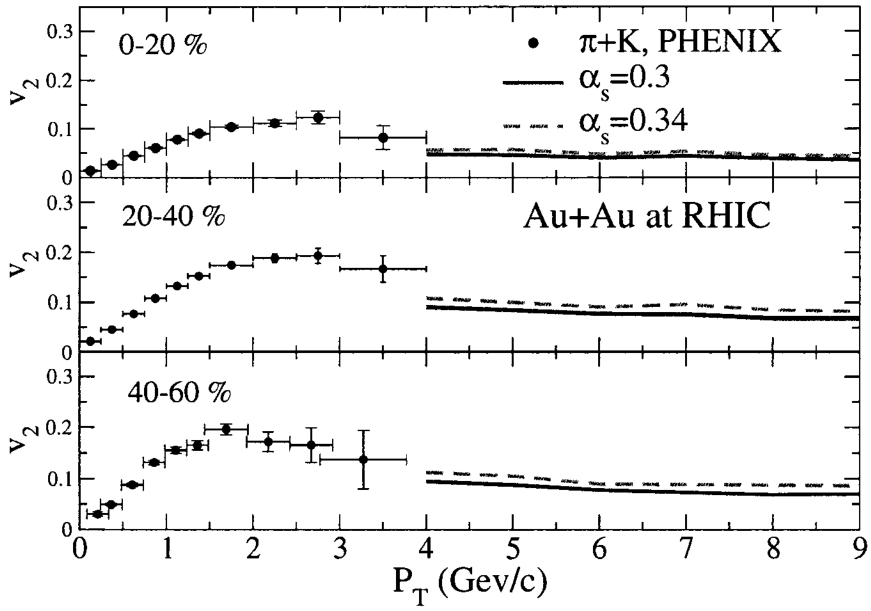

Figure 5.5: Elliptic anisotropy of π and K mesons in Au-Au collisions at RHIC, for different centrality class. Solid lines, α_s=0.3; dashed lines, α_s=0.34.

processes $a + b \to \gamma + c$, see Eq. 4.37, are produced symmetrically with

$$\frac{dN^{N-N}}{p_T dp_T dy d\phi} = T_{AB} f_{a/A} \otimes \sigma_{a+b\to\gamma+c} \otimes f_{b/B}. \tag{5.38}$$

Here $\sigma_{a+b\to\gamma+c}$ is the cross section between partons and $f_{a/A}$ is the parton distribution function of parton a in nucleus A. With final state interactions absent, primary hard photons do not exhibit any elliptic anisotropy.

Jets are also produced symmetrically, however they are quenched once they start to propagate through the plasma. This is the optical mechanism that leads to positive v_2 for hadrons fragmenting from jets. We expect photons fragmenting from jets to exhibit the same anisotropy. Their yield at midrapidity, see Eqs. 4.37 and 4.64, is given by

$$\frac{dN^{jet-frag}}{p_T dp_T d\phi} = \sum_f \left.\frac{dN^f(\phi)}{dE}\right|_{E=p_T/z} \otimes D_{f\to\gamma}(z, p_T) \tag{5.39}$$

where $dN^f(\phi)/dE$ is the distribution of jet partons of kind f with energy E leaving the fireball in the direction given by the angle ϕ.

The thermal photon emission from the plasma is not prone to any optical effects, but the emitting matter might experience an anisotropic hydrodynamic push. However, we neglect this here for two reasons. First, we are only interested in intermediate and large $p_T > 3$ GeV/c, where the yield of thermal photons is sub-dominant. Second, emission of thermal photons is peaked at early times; indeed we have verified that more than 90% of thermal photons with $p_T > 3$ GeV/c are emitted within the first 1 fm/c, where the expansion is purely longitudinal [122, 123] and where the time is not sufficient to effectively convert the spatial asymmetry into a flow anisotropy [135].

The interaction of jets with the medium can produce photons in different ways. In the jet-photon conversion, discussed in Chapter 4, the entire momentum of the jet is transfered to the photon, $\mathbf{p}_\gamma \approx \mathbf{p}_{\rm jet}$. It is clear that an anisotropy in ϕ is introduced by the different path lengths for jets traveling parallel and perpendicular to the reaction plane, leading to an increased probability for a jet-photon conversion in the direction where the medium is thicker. Such an inverse optical effect has not been considered before. It is also obvious that medium-induced bremsstrahlung $(jet + q(g) \rightarrow jet + q(g) + \gamma)$ increases with the path length of the jet. Hence these photons are preferentially emitted into the direction where the medium is thicker.

Let us summarize what we have so far. We identified two processes, induced bremsstrahlung from jets and jet-photon conversion, that we expect to exhibit an inverse optical anisotropy. Photon fragmentation from jets shows the known regular optical anisotropy while thermal and primary hard photons do not contribute to elliptic asymmetry.

To quantify our arguments, we carry out a numerical calculation for Au+Au collisions at RHIC ($\sqrt{s} = 200A$ GeV). Photon spectra at midrapidity with their dependence on the azimuthal angle ϕ are calculated as described above for three different centrality classes. Our initial temperatures, fixed with initial time $\tau_i = 0.26$ fm/c, are T_i=370, 360 and 310 MeV for centrality classes $0-20\%, 20-40\%$ and $40-60\%$ respectively. The parameters for central collisions are the same as those used in Chapter 4.

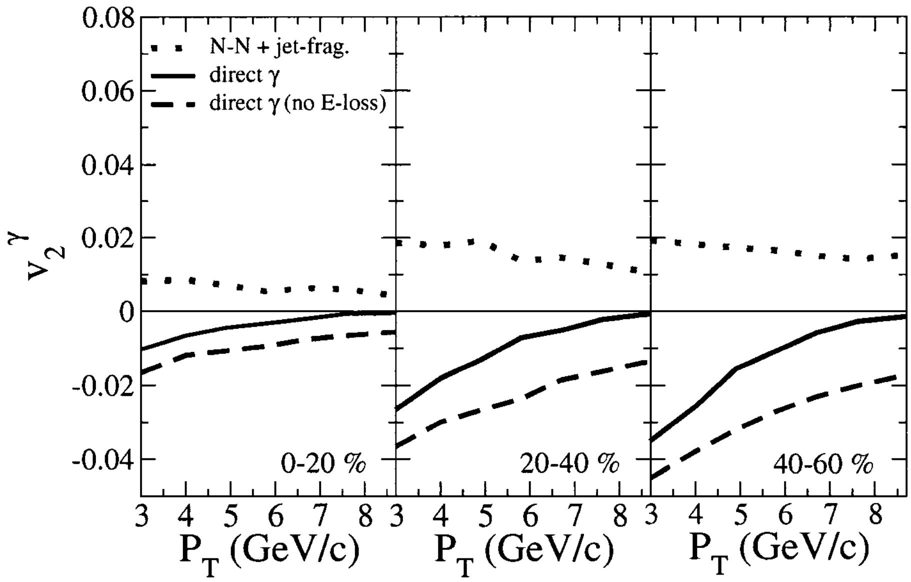

Figure 5.6: v_2 as a function of p_T for Au+Au collisions at RHIC. Three different centrality bins are shown. The dotted lines shows v_2 for primary hard photons and jet fragmentation only, and the solid line includes all direct photons. Energy loss is included in both calculations. The dashed line is the same as the solid line but without energy loss of jets taken into account.

Fig. 5.6 shows v_2 of midrapidity photons, as a function of p_T for Au+Au collisions at RHIC and for the centrality classes 0-20%, 20-40% and 40-60%. The dotted lines give the results for primary hard photons and photon fragmentation. As expected photon fragmentation leads to a positive v_2 which is diluted by adding primary hard photons which only contribute to the denominator of Eq. 5.37. The solid lines are our results also including bremsstrahlung and jet-photon conversion as well as thermal photons. They resemble our expectations for the elliptic anisotropy of direct photons including all source discussed above. The v_2 for induced bremsstrahlung and jet-photon conversion is indeed negative. Together they are able to overcome the positive v_2 from fragmentation, leading to an overall negative elliptic anisotropy for direct photons at not too large p_T. Only above 8 GeV/c the v_2 of direct photons would become positive again, because the yield of photons from fragmentation is dominating over induced bremsstrahlung and jet-photon conversion, see Fig. 4.14. The dashed lines in Fig. 5.6 show the v_2 for direct photons with no jet energy loss included. In this case, fragmentation photons do not exhibit an anisotropy and v_2 is only due to jet-photon conversion. v_2 measurements with sufficient accuracy could therefore constrain models for jet energy loss. We also verified the dependence of v_2 on the temperature of the medium, by varying the initial temperature T_i with $\tau_i T_i^3$ kept constant. The resulting changes are small : a change in T_i of 40% generates a shift in v_2 of less than 20%.

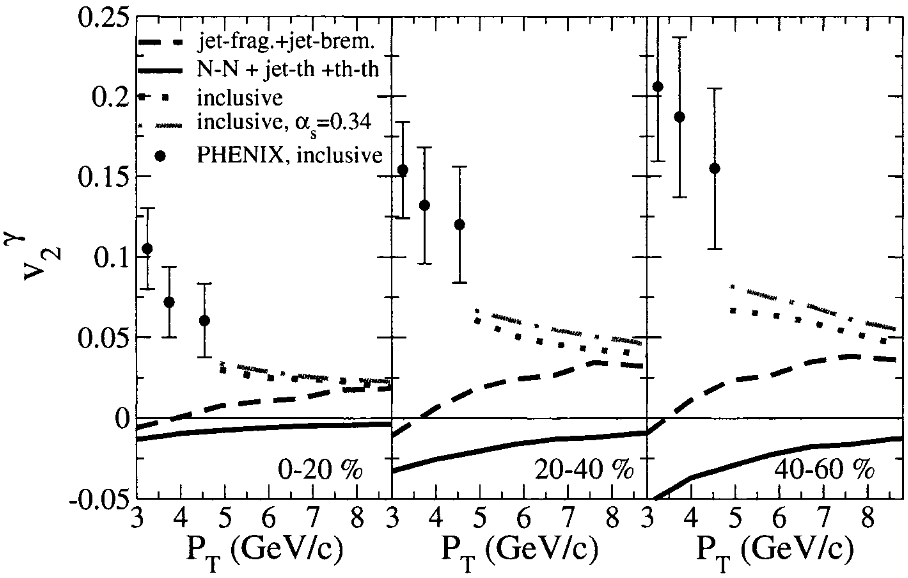

Figure 5.7: v_2 as a function of p_T for Au+Au collisions at RHIC. Three different centrality bins are shown. The dashed line includes jet-fragmentation and induced bremsstrahlung only while the solid line includes jet-photon conversion, primary hard and thermal photons. The dotted line add the background from neutral mesons decays to the sum of all other sources of photons discussed here, while the dot-dashed line do the same, but for α_s=0.34 rather that α_s=0.3. Data for inclusive photons are from PHENIX [137].

The absolute size of v_2 is not large. It is about 2-3% for the 20-40% centrality bin around $p_T = 4$ GeV/c and up to 5% for the more peripheral bin. Dilution of the signal by the isotropic primary and thermal processes and partial cancellations between the optical and reverse optical mechanisms are reasons for this. In Fig. 5.7 we show some v_2 signals that might be detectable at RHIC in the near future. We show the elliptic anisotropy for photons before background subtraction (dotted lines). In this case the v_2 signal is dominated by contributions from decaying π^0 and η hadrons. The resulting v_2 is positive and larger in magnitude. Only fragmentation of hadrons has again been included, so that the contribution at low to intermediate p_T is not shown, where production of hadrons through recombination is likely to dominate, or to have a non-negligible contribution, and will lead to larger values of hadronic v_2 [132] (see Ref. [136] for calculations of inclusive photon v_2, including decay of recombined pions as well). The effect of α_s is also studied in Fig. 5.7, for the inclusive photon v_2: higher values of α_s produce higher anisotropy, as it was for pions in Fig. 5.5. Preliminary data on the elliptic anisotropy of photons without background subtraction have been made available by the PHENIX collaboration [137]. Their experimental data for p_T >3 GeV are shown in Fig. 5.7. There is no overlap in p_T between data, stopping at $p_T \sim 4.5$ GeV, and our calculations, but at least, a naive extrapolation of the data toward higher p_T doesn't seems to rule out our calculations.

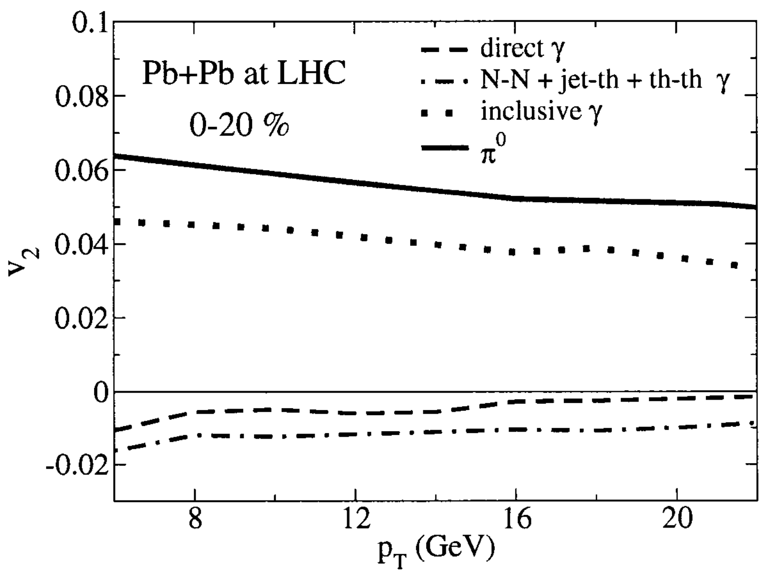

Figure 5.8: Elliptic anisotropy of neutral pions (solid line), inclusive photons (dotted line), all photons after background subtraction (dashed line), and jet-photon conversion, thermal and primary hard photons (dot-dashed line) at the LHC, for the centrality class 0-20%.

A more interesting option for the future is the possibility to experimentally distinguish between direct photons associated with jets and isolated direct photons.

Photons from jet fragmentation and induced bremsstrahlung are in the former category, while the latter includes thermal, primary hard and photons from jet-photon conversion. We mean by direct photon associated with jet, an event which produces in a small solid angle around ϕ, jet and photon with high p_T. So, photons entering into the former category should be present when tagging a jet in a given direction. The dashed line in Fig. 5.7 shows the result for the fragmentation and bremsstrahlung processes only. They contribute with different signs and one notes a characteristic change of sign from negative values at low p_T to larger positive values, up to 5%, at large p_T, where fragmentation dominates. The dash-dotted line shows the v_2 of all isolated direct photon processes, including primary, thermal and jet-photon conversion. Only jet-photon conversion gives a (reverse) optical anisotropy, so that the resulting v_2 is relatively large and negative.

As we have discussed already, the Bjorken 1-D expansion might be not-reliable at the LHC for non-central collisions, as the QGP lifetime is bigger than at RHIC. Bigger lifetime would imply that the anisotropic pressure generated by the fluid, could have time to develop and to become important in the QGP phase. Nevertheless, in order to have baseline predictions for the LHC, we plot in Fig. 5.8, the coefficient v_2 for pions and photons. Compared to the left panel of Figs. 5.6 and 5.7, the magnitude of the elliptic anisotropy at the LHC appears to be bigger than at RHIC. Indeed, for the centrality class $0-20\%$, v_2 of inclusive photons reaches almost 5% (dotted line), while v_2 for photons not associated with jets (dot-dashed line), is $\sim$ -1.8% around p_T =6 GeV.

5.4 *Conclusion*

To summarize, we present the first calculation of the lowest order azimuthal asymmetry coefficient v_2 for direct photons in high energy nuclear collisions. Jets interacting with a deconfined quark gluon plasma provide photons exhibiting an inverse optical anisotropy with characteristic negative values of v_2. An experimental confirmation would emphasize the existence of a quark gluon plasma and confirm jet-medium interactions as important sources of photons at intermediate p_T. The v_2 signal is generally of order 3-5% and should be experimentally accessible for direct photons at RHIC. Even more promising would be a separation of photons emitted in a jet from isolated photons. Both sources carry their own characteristic p_T dependence for v_2. The arguments presented here for direct photons immediately apply to the production of lepton pairs as well. Dileptons from annihilation of jets in the medium and from medium-induced virtual photon bremsstrahlung should also exhibit negative v_2.

6

HIGH-p_T DILEPTON PRODUCTION

We calculate the emission of high momentum lepton pairs in central Au+Au collisions at RHIC ($\sqrt{s_{NN}}$ =200 GeV) and Pb+Pb collisions at the LHC ($\sqrt{s_{NN}}$ =5500 GeV). Dileptons produced through interactions of jets with thermal partons have been evaluated, with next to leading order corrections through the hard thermal loop (HTL) resummation, and compared to thermal dilepton emission and the Drell-Yan process. A complete leading order treatment of jet energy loss has been included. While the jet-plasma interaction dominates thermal emission for all values of the invariant mass M, the Drell-Yan process is the dominant source of high momentum lepton pairs for $M > 3$ GeV at RHIC, after the background from heavy quark decays is subtracted. At LHC, the range $M < 8$ GeV is dominated by jet-plasma interactions. Effects from jet energy loss on jet-plasma interactions turn out to be weak, but non-negligible, reducing the yield of low-mass dileptons by a factor ~ 1.3.

6.1 Introduction

Finding experimental evidence for the existence of a Quark-Gluon Plasma (QGP) is one of the main reasons for conducting relativistic heavy ion collisions. In Chapters 2, 4 and 5, we have evaluated the importance of real photon radiation, as a good signature of the QGP. Here, we evaluate the role played by virtual photons.

Several sources for lepton pairs compete and have to be considered: dileptons from the Drell-Yan process [138], thermal dileptons [139] both from the QGP [140, 141] and from the subsequent hadronic phase [142, 62], dileptons from the absorption of jets by the plasma [112] and dileptons from bremsstrahlung of jets. Besides the thermal emission, dileptons from the latter two sources carry information about the medium. Comparing with the baseline $p+p$ process, we note that absorption of jets exclusively happens in nucleus-nucleus collisions in the presence of a medium. There is a also a significant change in bremsstrahlung emission expected in a medium (in A+A) compared to the case of vacuum (in $p+p$).

The main background for dileptons is correlated charm decays ($D\bar{D} \to e^+e^-X$) at intermediate mass [143], while one has to cope with Dalitz decays of light mesons ($\pi^0 \to \gamma e^+e^-, \omega \to \pi^0 e^+e^-$) at low mass $M \leq 1$ GeV. In principle, there is an another source of dileptons corresponding to preequilibrium emission. It is difficult to assess both theoretically and experimentally, nevertheless, such calculations have been attempted in Ref. [144].

In Ref. [112] the dilepton yield from the passage of jets through a plasma has been evaluated as a function of invariant mass at leading order. The results show that this process dominates over thermally induced reactions at high invariant mass M. However, energy loss of jets in the medium has not been included in this calculation. Large energy loss of jets was discovered as one of the most exciting results from the Relativistic Heavy Ion Collider (RHIC) and has been observed in the suppression of single hadron spectra [12, 13] and through the disappearance of back-to-back correlations of high p_T hadrons [14].

In this chapter we revisit the leading order dilepton production from jets [149] and we explore the effect of energy loss. The dominant mechanism for jet energy loss is induced gluon bremsstrahlung [19, 20]. We will use again the AMY formalism presented in Chapter 3. Jets will be defined by all partons produced initially with transverse momentum $p_T^{\text{jet}} \gg 1$ GeV. The total dilepton production could be influenced by the choice of the cutoff p_T^{jet}. As we will discuss below, in order to avoid such sensitivity, we limit our study to high momentum dileptons.

In perturbation theory at high temperature, it is important to distinguish between hard momenta, on the order of the temperature T, and soft momenta, on the order of g_sT, where g_s is the QCD coupling constant. When a line entering in a vertex is soft, there are an infinite number of diagrams with loop corrections contributing to the same order in the coupling constant as the tree amplitude. These corrections can be treated with the hard thermal loop (HTL) resummation technique developed in Ref. [145]. This technique has been used thereafter in Refs. [146, 147, 148] to show that the production rate of low mass dilepton ($M < T$) could differ from the Born-term quark-antiquark annihilation by orders of magnitude. In this work, we apply this technique to go beyond the leading order jet-medium interaction.

The dilepton production rate in finite-temperature field theory is discussed in Sec. 6.2 and the physical processes underlying each contribution are discussed in Sec. 6.3 in the framework of relativistic kinetic theory. In Sec. 6.4, we include these dilepton production rates into a 1-D expanding QGP, and in Sec. 6.4.3, we turn to the Drell-Yan process and correlated leptons from heavy quark decays. The results are presented in Sec. 6.5 and finally, Sec. 6.6 contains a summary and conclusion.

6.2 Dilepton production rate from finite-temperature field theory

6.2.1 Derivation of the production rate expression

The probability for a transition from an initial state I to a final state F, plus a lepton pair e^+e^-, with $p_I = p_F + p_+ + p_-$, is [33]

$$S_{IF} = \left|\left\langle Fe^+e^-|I\right\rangle\right|^2 \tag{6.1}$$

In quantum field theory, it can be written as a time ordered product [8]:

$$S_{IF} = \left|\left\langle (Fe^+e^-)_0 \middle| T\left\{\exp[-i\int dtH_I]\right\}\middle| (I)_0\right\rangle\right|^2 \tag{6.2}$$

where $(Fe^+e^-)_0$ and I_0 are assympotic states, eigenstates of the unperturbed Lagrangian. The interaction Hamiltonian is given by

$$H_I = \int d^3x J_\mu^{lep} A^\mu + \int d^3x J_\mu^{had} A^\mu \,. \tag{6.3}$$

J^{lep} and J^{had} are the leptonic and hadronic current densities, while A^μ is the electromagnetic field. We get

$$\begin{aligned} S_{IF} &= \left| \left\langle (Fe^+e^-)_0 \left| \int d^4x d^4y J^{lep}_\mu(x) J^{had}_\nu(y) T[A^\mu(x)A^\nu(y)] \right| (I)_0 \right\rangle \right|^2 \\ &= \left| \int d^4x d^4y \, \langle 0| T[A^\mu(x)A^\nu(y)] |0\rangle \left\langle (e^+e^-)_0 \left| J^{lep}_\mu(x) \right| 0 \right\rangle \left\langle F_0 \left| J^{had}_\nu(y) \right| I_0 \right\rangle \right|^2 \end{aligned} \tag{6.4}$$

where the photon propagator is given by

$$\langle 0| T[A^\mu(x)A^\nu(y)] |0\rangle = -i \int \frac{d^4p}{(2\pi)^4} e^{-ip(x-y)} \frac{g^{\mu\nu}}{p^2} \tag{6.5}$$

and the vacuum-dilepton pair transition is [8]

$$\left\langle (e^+e^-)_0 \left| J^{lep}_\mu(x) \right| 0 \right\rangle = e \, \bar{u}_s(p_-)\gamma_\mu v_{s'}(p_+) e^{ix(p_+ + p_-)} \, . \tag{6.6}$$

The $x-$ integration produces a delta function,

$$\int d^4x \, e^{-ip\,x} e^{ix(p_+ + p_-)} = (2\pi)^4 \delta^4(p_+ + p_- - p) \, , \tag{6.7}$$

such that

$$\begin{aligned} S_{IF} &= e^2 \left| \int d^4y \frac{g^{\mu\nu}}{(p_+ + p_-)^2} \bar{u}_s(p_-)\gamma_\mu v_{s'}(p_+) \left\langle F_0 \left| J^{had}_\nu(y) \right| I_0 \right\rangle e^{iy(p_+ + p_-)} \right|^2 \\ &= e^2 \int d^4z d^4y \left\langle F_0 \left| J^{had}_\mu(y) \right| I_0 \right\rangle \left\langle I_0 \left| J^{had}_\nu(z) \right| F_0 \right\rangle \\ &\quad \times e^{i(p_+ + p_-)(y-z)} \frac{1}{(p_+ + p_-)^4} \\ &\quad \times \sum_{s,s'} \bar{v}_{s'}(p_+)\gamma^\nu u_s(p_-) \bar{u}_s(p_-)\gamma^\mu v_{s'}(p_+) \, . \end{aligned} \tag{6.8}$$

The summation can be handled easily:

$$\begin{aligned} \sum_{s,s'} \bar{v}_{s'}(p_+)\gamma^\nu u_s(p_-) \bar{u}_s(p_-)\gamma^\mu v_{s'}(p_+) &= \mathrm{Tr}\,[\not{p}_+ \gamma^\nu \not{p}_- \gamma^\mu] \\ &= 4 \left(p_+^\mu p_-^\nu + p_+^\nu p_-^\mu - g^{\mu\nu} p_+ \cdot p_- \right) \, . \end{aligned} \tag{6.9}$$

Now, from translation invariance, we have

$$\left\langle I_0 \left| J^{had}_\nu(z) \right| F_0 \right\rangle = e^{ip_I z} \left\langle I_0 \left| J^{had}_\nu(0) \right| F_0 \right\rangle e^{-ip_F z} = e^{i(p_+ + p_-)z} \left\langle I_0 \left| J^{had}_\nu(0) \right| F_0 \right\rangle \, . \tag{6.10}$$

Putting this back into the transition probability expression ,we find

$$S_{IF} = e^2 Vt \int d^4y \left\langle F_0 \left| J_\mu^{had}(y) \right| I_0 \right\rangle \left\langle I_0 \left| J_\nu^{had}(0) \right| F_0 \right\rangle \\ \times e^{i(p_+ + p_-)y} \frac{4}{(p_+ + p_-)^4} \left(p_+^\mu p_-^\nu + p_+^\nu p_-^\mu - g^{\mu\nu} p_+ \cdot p_- \right) \tag{6.11}$$

where V is the volume, and t the time. To obtain the production rate, we average over initial state, with the Boltzmann factor $e^{-\beta p_I}/Z$, $Z = \sum_l e^{-\beta p_l}$, $\beta = 1/T$, sum over final state and integrate over lepton momentum. Also, as the production rate is by definition the number of particles per unit of time and volume, we divide by Vt, such that:

$$\begin{aligned} R^{e^+e^-} &= \int \frac{d^3p_+}{2(2\pi)^3 E_+} \frac{d^3p_-}{2(2\pi)^3 E_-} \sum_{I,F} \frac{S_{IF}}{Vt} \frac{e^{-\beta p_I}}{Z} \\ &= e^2 \int \frac{d^3p_+ d^3p_-}{(2\pi)^6 E_+ E_-} \frac{1}{(p_+ + p_-)^4} e^{-\beta(E_+ + E_-)} \\ &\quad \times \left(p_+^\mu p_-^\nu + p_+^\nu p_-^\mu - g^{\mu\nu} p_+ \cdot p_- \right) \\ &\quad \times \int d^4y \, e^{i(p_+ + p_-)y} \sum_F \left\langle F_0 \left| J_\mu^{had}(y) J_\nu^{had}(0) \right| F_0 \right\rangle \frac{e^{-\beta p_F}}{Z} \end{aligned} \tag{6.12}$$

The expression in the last line corresponds to the current-current correlation function [150]:

$$\begin{aligned} W_{\mu\nu}^{>}(p) &= \int d^4y \, e^{i(p_+ + p_-)y} \sum_F \left\langle F_0 \left| J_\mu^{had}(y) J_\nu^{had}(0) \right| F_0 \right\rangle \frac{e^{-\beta p_F}}{Z} \\ &= \int d^4y \, e^{i(p_+ + p_-)y} \, \mathrm{Tr} \left[e^{-\beta H} J_\mu^{had}(y) J_\nu^{had}(0) \right] \\ &= \frac{f_{\mu\nu}(p)}{e^{-\beta(E_+ + E_-)} - 1} \end{aligned} \tag{6.13}$$

where we have define $p = p_+ + p_-$. The spectral function $f_{\mu\nu}$ can be written in term of the improper photon self-energy $P_{\mu\nu}$ [33]:

$$f_{\mu\nu}(p) = -2 \mathrm{Im} P_{\mu\nu}(p) \, . \tag{6.14}$$

In lowest order in e, the improper photon self-energy $P_{\mu\nu}$ corresponds to the retarded photon self-energy $\Pi_{\mu\nu}^R$. We finally get

$$R^{e^+e^-} = e^2 \int \frac{d^3p_+ d^3p_-}{(2\pi)^6 E_+ E_-} \frac{1}{(p_+ + p_-)^4} e^{-\beta(E_+ + E_-)}$$

$$\times\left(p_+^\mu p_-^\nu + p_+^\nu p_-^\mu - g^{\mu\nu} p_+ \cdot p_-\right)$$
$$\times\frac{-2\mathrm{Im}\Pi^R_{\mu\nu}(p)}{e^{-\beta(E_+ + E_-)} - 1}\,. \tag{6.15}$$

Converting the total rate into a differential one, we find

$$E_+E_-\frac{dR^{e^+e^-}}{d^3p_+d^3p_-} = \frac{2e^2}{(2\pi)^6(p_+ + p_-)^4}(p_+^\mu p_-^\nu + p_-^\mu p_+^\nu - g^{\mu\nu}p_+\cdot p_-)\frac{\mathrm{Im}\Pi^R_{\mu\nu}}{e^{(E_+ + E_-)/T} - 1} \tag{6.16}$$

It will be more convenient to write the production rate in terms of the dilepton momentum p:

$$\frac{dR^{e^+e^-}}{d^4p} = \int \frac{d^3p_+}{E_+}\frac{d^3p_-}{E_-}\delta^4(p - p_+ - p_-)E_+E_-\frac{dR^{e^+e^-}}{d^3p_+d^3p_-} \tag{6.17}$$

After integration over leptons momentum, using current conservation ($p^\mu\Pi^R_{\mu\nu} = 0$), we get

$$\frac{dR^{e^+e^-}}{d^4p} = \frac{\alpha}{12\pi^4M^2}\frac{\mathrm{Im}\Pi^{R\,\mu}_{\mu}}{1 - e^{E/T}} = 2E\frac{dR^{e^+e^-}}{dM^2d^3p} \tag{6.18}$$

where $\vec{p} = \vec{p_+} + \vec{p_-}$, E and M are respectively the dilepton momentum, energy and invariant mass.

The real photon production rate follows almost the same development than for virtual photons. The transition probability is

$$S_{IF} = \left|\int d^4x \,\langle(\gamma)_0\,|A^\mu(x)|\,0\rangle \left\langle F_0\left|J^{had}_\mu(x)\right| I_0\right\rangle\right|^2 \tag{6.19}$$

while the production rate become

$$E\frac{dR^\gamma}{d^3p} = \frac{1}{(2\pi)^3}\frac{\mathrm{Im}\Pi^{R\,\mu}_{\mu}}{1 - e^{E/T}}\,. \tag{6.20}$$

Comparing Eqs. 6.18 and 6.20, we can express the dilepton production rate as

$$\frac{dR^{e^+e^-}}{d^4p} = \frac{2\alpha}{3\pi M^2}E\frac{dR^{\gamma^*}}{d^3p} \tag{6.21}$$

where

$$\lim_{M\to 0} E\frac{dR^{\gamma^*}}{d^3p} = E\frac{dR^\gamma}{d^3p}\,. \tag{6.22}$$

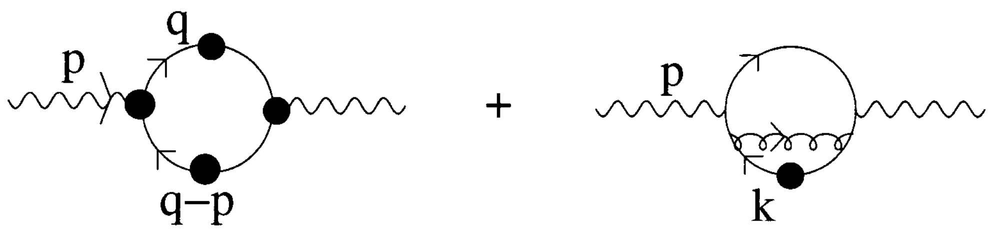

Figure 6.1: Resummed photon self-energy diagrams.

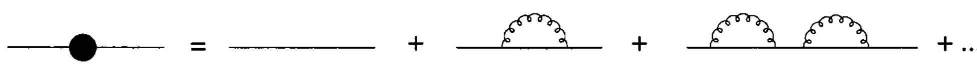

Figure 6.2: Resummed quark propagator.

6.2.2 *Dilepton production with HTL effects*

In the HTL formalism, the leading order resummed photon self-energy diagrams is shown in the left hand side of Fig. 6.1. The heavy dots indicate a resummed propagator or vertex. The second diagram in Fig. 6.1, coming from the effective two-photon-two quark vertex is added in order to fulfill the Ward Identity

$$p^{\mu}\Pi^{R}_{\mu\nu}(p) = 0\,. \tag{6.23}$$

Using power counting [145, 150], the HTL resummation gives corrections of order $g_s^2T^2/|\overrightarrow{p}|^2$ to each bare vertex of the first diagram of Fig. 6.1, while the bare propagators receive $g_s^2T^2/|\overrightarrow{q} - \overrightarrow{p}|^2$ and $g_s^2T^2/|\overrightarrow{q}|^2$ corrections. A resummed propagator consist of an infinite number of gluon correction, as shown in Fig. 6.2. In this work, we study the high momentum dilepton limit ($|\overrightarrow{p}| \gg T$), so that vertex corrections

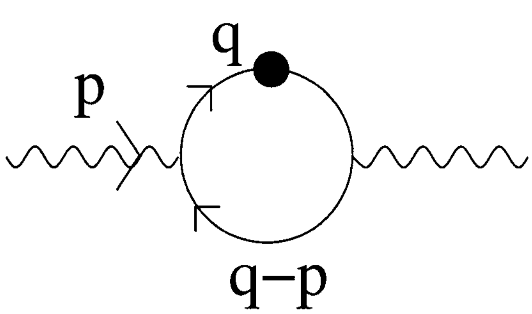

Figure 6.3: Effective photon self-energy diagram for hard external momentum p

can be neglected, and at least one propagator is guaranteed to be hard. We assume that it is the propagator associated with momentum $q - p$. Then the propagator associated with q can be soft or hard, implying that is has to be resummed. Also, for the high $|\vec{p}|$ limit, the second diagram of Fig. 6.1 gives only $g_s^2 T^2/|\vec{p}|^2$ corrections to the first diagram. The resulting diagram that we need to evaluate (see Fig. 6.3) has the following expression [49]:

$$\Pi^{\mu}_{\mu}(p) = 3e^2 \sum_f \left(\frac{e_f}{e}\right)^2 T \sum_n \int \frac{d^3q}{(2\pi)^3} \mathrm{Tr}\left[\gamma^{\mu} S_D(q) \gamma^{\nu} S(q-p)\right] \delta_{\mu\nu} \tag{6.24}$$

The diagram in Fig. 6.3 includes the leading order effect, and some next-to leading order corrections in g_s. In order to have a complete next-to leading order production rate in the region $|\vec{p}| \gg T$, contributions like bremsstrahlung need to be included. This will be discussed in the last section.

The second summation in Eq. 6.24 runs over the Matsubara frequencies. This particular feature appears in thermal field theory, due to the constraint of periodicity in the trace from Eq. 6.13, which reads, $F_0(\mathbf{x}, t = 0) = F_0(\mathbf{x}, t = i\beta)$. This trace can be evaluated in the imaginary time formalism [150], where we switch to an imaginary time variable, which imply a discretization of the energy variable: $-iq_0 = \pi(2n+1)T$, n being an integer number. At the end of the calculation, in order to get a production rate, the discrete photon energy will have to be analytically continued to a real value, such that $ip_0 \to E + i\epsilon$.

The dressed fermion propagator, in Euclidian space ($\not{q} = -iq_0\gamma^0 + \vec{q} \cdot \hat{\gamma}$), is given by [150]

$$S_D(q) = \frac{1}{\not{q} + \Sigma} = \frac{\gamma^0 - \hat{\gamma} \cdot \hat{\mathbf{q}}}{2D_+(q)} + \frac{\gamma^0 + \hat{\gamma} \cdot \hat{\mathbf{q}}}{2D_-(q)} \tag{6.25}$$

where

$$D_{\pm}(q) = -iq_0 \pm |\vec{q}| + A \pm B \tag{6.26}$$

The terms A and B describe the quark self-energy

$$\Sigma = A\gamma^0 + B\hat{\gamma} \cdot \hat{\mathbf{q}}\,. \tag{6.27}$$

In the HTL approximation, one obtains [150]

$$A = \frac{m_F^2}{|\vec{q}|} Q_0 \left(\frac{iq_0}{|\vec{q}|} \right), \quad B = -\frac{m_F^2}{|\vec{q}|} Q_1 \left(\frac{iq_0}{|\vec{q}|} \right) \tag{6.28}$$

where $m_F = g_s T/\sqrt{6}$ is the effective quark mass induced by the thermal medium and Q_n are Legendre functions of the second kind. The bare propagator $S(q)$ follows the same expression than $S_D(q)$, with $D_\pm$ replaced by

$$d_\pm(q) = -iq_0 \pm |\vec{q}| \,. \tag{6.29}$$

Using those expressions for the quark propagators and carrying out the trace, Eq. 6.24 leads to

$$\begin{aligned}\Pi_\mu^\mu(p) = 6e^2 \sum_f \left(\frac{e_f}{e} \right)^2 T \sum_n \int \frac{d^3q}{(2\pi)^3} \Bigg[&\frac{1}{D_+(q)} \left(\frac{1 - \hat{\mathbf{q}} \cdot \hat{\mathbf{k}}}{d_+(k)} + \frac{1 + \hat{\mathbf{q}} \cdot \hat{\mathbf{k}}}{d_-(k)} \right) \\ &+ \frac{1}{D_-(q)} \left(\frac{1 + \hat{\mathbf{q}} \cdot \hat{\mathbf{k}}}{d_+(k)} + \frac{1 - \hat{\mathbf{q}} \cdot \hat{\mathbf{k}}}{d_-(k)} \right) \Bigg]\end{aligned} \tag{6.30}$$

where we have defined $k = q - p$.

At this point, it is convenient to introduce the spectral representation of the effective quark propagator defined by

$$\begin{aligned}\rho_\pm(\omega, |\vec{q}|) &= -2\,\mathrm{Im} \frac{1}{D_\pm(iq_0, |\vec{q}|)}, \\ \frac{1}{D_\pm(iq_0, |\vec{q}|)} &= \int_{-\infty}^{\infty} \frac{d\omega}{2\pi} \frac{\rho_\pm(\omega, |\vec{q}|)}{iq_0 - \omega + i\epsilon} \,.\end{aligned} \tag{6.31}$$

This imply

$$\begin{aligned}\rho_\pm(\omega, |\vec{q}|) = &- 2\pi \frac{\omega^2 - |\vec{q}|^2}{2m_F^2} \left[\delta\left(\omega - \omega_\pm(|\vec{q}|)\right) + \delta\left(\omega + \omega_\mp(|\vec{q}|)\right) \right] \\ &- 2\pi \beta_\pm\left(\omega, |\vec{q}|\right) \Theta\left(|\vec{q}|^2 - \omega^2 \right)\end{aligned} \tag{6.32}$$

with

$$\beta_\pm(\omega, |\vec{q}|) = \frac{\frac{m_F^2}{2|\vec{q}|}\left(1 \mp \omega/|\vec{q}|\right)}{\left[-\omega \pm |\vec{q}| + \frac{m_F^2}{|\vec{q}|} \left(\pm 1 + \frac{1}{2} \ln \left| \frac{\omega + |\vec{q}|}{\omega - |\vec{q}|} \right| \right) (1 \mp \frac{\omega}{|\vec{q}|}) \right]^2 + \left(\frac{\pi m_F^2}{2|\vec{q}|} (1 \mp \frac{\omega}{|\vec{q}|}) \right)^2} \,. \tag{6.33}$$

Here, $\omega_\pm = \omega_\pm(|\vec{q}|)$ correspond to the poles of the effective quark propagator. They are solution of $D_\pm(\omega, |\vec{q}|) = 0$. The solution $\omega = \omega_+$ represents an ordinary quark with an effective thermal mass $\sqrt{2}m_F$ and a positive helicity over chirality ratio, $\chi = 1$ [150]. The solution $\omega = \omega_-$ represents a particle having negative helicity over chirality ratio, $\chi = -1$. This collective mode, called plasminos, has no analog at zero temperature. Following the notation of Ref. [146], we denote the ordinary modes by q_+ and the plasminos by q_-. The spectral density of the bare propagator is simply

$$r_\pm(\omega', |\vec{k}|) = -2\,\mathrm{Im}\frac{1}{d_\pm(ik_0, |\vec{k}|)} = -2\pi\delta(\omega' \mp |\vec{k}|) \tag{6.34}$$

Using the spectral density representation has the advantage that one can carry out the sum over Matsubara frequencies with help of the elegant identity [150],

$$\begin{aligned}\mathrm{Im}\, T\sum_n F_1(iq_0)F_2(iq_0 - ip_0) = \pi\left(1 - e^{E/T}\right)\int_{-\infty}^{\infty}\frac{d\omega}{2\pi}\int_{-\infty}^{\infty}\frac{d\omega'}{2\pi} \\ \times\rho_1(\omega)\rho_2(-\omega')\delta(E - \omega - \omega')f_{FD}(\omega)f_{FD}(\omega')\end{aligned} \tag{6.35}$$

where f_{FD} is the Fermi-Dirac phase-space distribution function and ρ_i is the spectral density associated with F_i. We use the analytical continuation $ip_0 \to E + i\epsilon$ with the dilepton energy E. Putting all information together, we obtain

$$\begin{aligned}\mathrm{Im}\Pi_\mu^{R\mu} = &-6e^2\sum_f\left(\frac{e_f}{e}\right)^2\pi\left(1 - e^{E/T}\right)\int\frac{d^3q}{(2\pi)^3}\int_{-\infty}^{\infty}\frac{d\omega}{2\pi}f_{FD}(\omega) \\ &\times\Big[\rho_+(\omega, |\vec{p}|)\Big\{\delta(E - \omega + E_1)(1 - \hat{\mathbf{q}}\cdot\hat{\mathbf{k}})f_{FD}(-E_1) \\ &+\delta(E - \omega - E_1)(1 + \hat{\mathbf{q}}\cdot\hat{\mathbf{k}})f_{FD}(E_1)\Big\} \\ &+\rho_-(\omega, |\vec{p}|)\Big\{\delta(E - \omega + E_1)(1 + \hat{\mathbf{q}}\cdot\hat{\mathbf{k}})f_{FD}(-E_1) \\ &+\delta(E - \omega - E_1)(1 - \hat{\mathbf{q}}\cdot\hat{\mathbf{k}})f_{FD}(E_1)\Big\}\Big]\end{aligned} \tag{6.36}$$

with $E_1 = |\vec{q} - \vec{p}|$. Since both $E \gg T$ and $E_1 \gg T$, the terms proportional to $\delta(E - \omega + E_1)$ are exponentially suppressed by the factor $f_{FD}(\omega)$ for $\omega \gg T$. Also, because E_1 corresponds to a massless parton, energy and momentum conservation does not permit the terms containing $\delta(E + |\omega| - E_1)$ for $\omega^2 > |\vec{q}|^2$, i.e. there is no phase space available for the process $1 \to 2+3$ if parton 1 is on-shell. These arguments lead to further simplifications and we have

$$\begin{aligned}
\mathrm{Im}\Pi^{R\mu}_{\mu} &= 6e^2 \sum_f \left(\frac{e_f}{e}\right)^2 \pi \left(1-e^{E/T}\right) \int \frac{d^3q}{(2\pi)^3} \\
&\times \left[f_{FD}(\omega_+) f_{FD}(E_1) \frac{\omega_+^2 - |\vec{q}|^2}{2m_F^2} \delta(E-\omega_+-E_1)(1+\hat{\mathbf{q}}\cdot\hat{\mathbf{k}}) \right. \\
&+ f_{FD}(\omega_-) f_{FD}(E_1) \frac{\omega_-^2 - |\vec{q}|^2}{2m_F^2} \delta(E-\omega_--E_1)(1-\hat{\mathbf{q}}\cdot\hat{\mathbf{k}}) \\
&+ \int_{-\infty}^{\infty} d\omega f_{FD}(\omega) f_{FD}(E_1) \left\{\beta_+(\omega,|\vec{q}|)(1+\hat{\mathbf{q}}\cdot\hat{\mathbf{k}}) \right. \\
&\left.\left. + \beta_-(\omega,|\vec{q}|)(1-\hat{\mathbf{q}}\cdot\hat{\mathbf{k}})\right\} \delta(E-\omega-E_1) \right] \qquad (6.37)
\end{aligned}$$

Now we analyze the integral over $d^3q = |\vec{q}|^2\, d|\vec{q}|\, d\Omega$. When $|\vec{q}|$ becomes as large as E_1, the propagator associated with q does not have to be resummed. If $|\vec{q}|$ gets much bigger, implying $E_1 \sim g_s T$, then this is the propagator associated with E_1 which should be resummed. We have a symmetry relatively to the point $|\vec{q}| = E_1$, such that $\int_0^\infty d|\vec{q}| \to \int_0^\infty d|\vec{q}|\, 2\Theta(E_1 - |\vec{q}|)$. We finally obtain the dilepton production rate, with HTL effects, by putting Eq. 6.37 into Eq. 6.18, which gives

$$\begin{aligned}
\frac{dR^{e^+e^-}}{d^4p} &= \frac{2\alpha^2}{\pi^2 M^2} \sum_f \left(\frac{e_f}{e}\right)^2 \int_0^\infty 2\,|\vec{q}|^2\, d|\vec{q}| \int \frac{d\Omega}{(2\pi)^3} \\
&\left[f_{FD}(\omega_+) f_{FD}(E_1) \frac{\omega_+^2 - |\vec{q}|^2}{2m_F^2} \delta(E-\omega_+-E_1)(1-\hat{\mathbf{q}}\cdot\hat{\mathbf{p}}_1)\Theta(E_1-|\vec{q}|) \right. \\
&+ f_{FD}(\omega_-) f_{FD}(E_1) \frac{\omega_-^2 - |\vec{q}|^2}{2m_F^2} \delta(E-\omega_--E_1)(1+\hat{\mathbf{q}}\cdot\hat{\mathbf{p}}_1)\Theta(E_1-|\vec{q}|) \\
&+ \int_{-\infty}^{\infty} d\omega f_{FD}(\omega) f_{FD}(E_1) \delta(E-\omega-E_1)\Theta(E_1-|\vec{q}|) \\
&\left. \left\{ \beta_+(\omega,|\vec{q}|)(1-\hat{\mathbf{q}}\cdot\hat{\mathbf{p}}_1) + \beta_-(\omega,|\vec{q}|)(1+\hat{\mathbf{q}}\cdot\hat{\mathbf{p}}_1) \right\} \right], \qquad (6.38)
\end{aligned}$$

where $\hat{\mathbf{p}}_1 = \vec{p_1}/|\vec{p_1}| = -\hat{\mathbf{k}}$. In the next section we will analyze the physical processes behind the production rate derived above. This is done so that $f_{\rm FD}(E_1)$ can be interpreted as the phase-space distribution function of an incoming parton of energy E_1. Once this is established one can apply the usual technique and obtain the production rate involving jets by substituting the thermal distribution $f_{\rm FD}(E_1)$ by the time-dependent jet distribution $f_{\rm jet}(E_1, t)$.

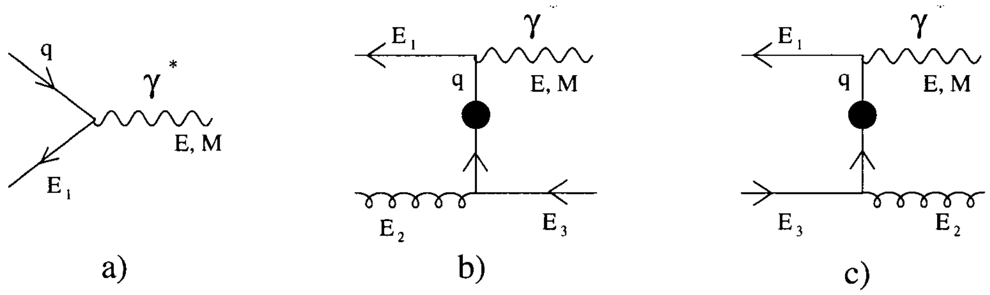

Figure 6.4: Processes extracted from photon self-energy in Fig. 6.3. In the picture, the particle with energy E_1 is an anti-quark, but the quark contribution is also included in the calculation.

6.3 *Dilepton production rate from relativistic kinetic theory*

We will show in this section that the production rate in Eq. (6.38) can also be interpreted in relativistic kinetic theory. Indeed, after cutting the diagram in Fig. 6.3, we get the Feynman amplitudes shown in Fig. 6.4. The process in Fig. 6.4(a) corresponds to the annihilation of the hard antiquark of energy E_1 with a soft quasiparticle q_+ or q_-. This is the pole-pole contribution, as it involves the propagation of the poles of the propagator in the diagram shown in Fig. 6.3. Fig. 6.4(b) corresponds to Compton scattering of an antiquark with energy E_1 with a hard gluon from the medium, with the exchange of a soft quasiparticle and Fig. 6.4(c) represents the annihilation of an antiquark E_1 with a hard quark from the medium with the exchange of a soft quasiparticle. They correspond to a cut through the self-energy of the dressed propagator in Fig. 6.3: this is thus called the cut-pole contribution. There is no s-channel process because hard thermal loops have imaginary parts for $q^2 < 0$ only [150]. The dots mean that the quasiparticle propagator is resummed. That modification of the propagator in the space-like region at non-zero temperature is known as Landau damping.

As we have shown in Appendix B, the production rate, as computed from relativistic kinetic theory (kt), for reactions $1 + 2 \to \gamma^* + 3 + ...$ is

$$E\frac{dR^{\gamma^*}_{\rm kt}}{d^3p} = \int \frac{d^3p_1}{2(2\pi)^3E_1}\frac{d^3p_2}{2(2\pi)^3E_2}\frac{d^3p_3}{2(2\pi)^3E_3}...(2\pi)^4\delta^4(p_1+p_2-p-p_3-...)\,|\mathcal{M}|^2$$

$$\times \frac{f(E_1)f(E_2)(1 \pm f(E_3))...}{2(2\pi)^3} \tag{6.39}$$

where $\mathcal{M}$ is the invariant scattering matrix element.

6.3.1 Pole-Pole contributions ($1 + q_\pm \to \gamma^*$)

The production rate for the processes of Fig. 6.4(a) is

$$\begin{aligned} E\frac{dR^{\gamma^*}_{\mathrm{kt}a}}{d^3p} &= \int \frac{d^3p_1}{2(2\pi)^3E_1}\frac{d^3q}{2(2\pi)^3q_0}(2\pi)^4\delta^4(p_1+q-p)\left|\mathcal{M}_{\mathrm{kt}a}\right|^2\frac{f^{q+\bar{q}}(E_1)f_{FD}(q_0)}{2(2\pi)^3} \\ &= \int \frac{d^3q}{8(2\pi)^5q_0E_1}\delta(E_1+q0-E)\left|\mathcal{M}_{\mathrm{kt}a}\right|^2 f^{q+\bar{q}}(E_1)f_{FD}(q_0) \end{aligned} \tag{6.40}$$

where $f^{q+\bar{q}}(E_1)$ is the phase-space distribution of quarks and antiquarks with energy E_1. The square of the matrix element, after summation over spin and color is

$$\begin{aligned} \left|\mathcal{M}_{\mathrm{kt}a}\right|^2 &= \left|\mathcal{M}_{1+q_+\to\gamma^*}\right|^2 + \left|\mathcal{M}_{1+q_-\to\gamma^*}\right|^2 \\ &= 6e^2\sum_f\left(\frac{e_f}{e}\right)^2 \mathrm{Tr}\left[\not{p}_1\left(\sum_s u_s^{q+}(q)\bar{u}_s^{q+}(q) + \sum_s u_s^{q-}(q)\bar{u}_s^{q-}(q)\right)\right] \end{aligned} \tag{6.41}$$

To go further, we need to find the completeness relations $\sum_s u_s^{q\pm}(q)\bar{u}_s^{q\pm}(q)$. The dressed propagator in Minkowski space is

$$-iS_D(q) = \frac{1}{\not{q} - \Sigma} = -\frac{\gamma^0 - \hat{\gamma}\cdot\hat{\mathbf{q}}}{2D_+(q)} - \frac{\gamma^0 + \hat{\gamma}\cdot\hat{\mathbf{q}}}{2D_-(q)} \tag{6.42}$$

and by definition, a propagator is given by [8]

$$-iS_D(q) = \frac{\sum_s u_s^{q+}(q)\bar{u}_s^{q+}(q)}{q^2 - m_{q+}^2} + \frac{\sum_s u_s^{q-}(q)\bar{u}_s^{q-}(q)}{q^2 - m_{q-}^2} + ... \tag{6.43}$$

where m_+ and m_- are the physical mass of the quasiparticles. The omitted terms in Eq. 6.43 correspond to the branch cut. For HTL, this branch cut, corresponding to the imaginary part of the quark self-energy, contributes for space-like quarks only.

We expand $D_\pm$ around the pole located at $q_0 = \omega_\pm$:

$$\begin{aligned} D_\pm(q) &\approx (q_0 - \omega_\pm)\frac{\partial D_\pm}{\partial q_0}\Bigg|_{q_0=\omega_\pm} = (q_0-\omega_\pm)\left(-1 + \frac{\partial}{\partial q_0}(A \pm B)\right)\Bigg|_{q_0=\omega_\pm} \\ &= -\frac{m_F^2(q^2 - m_\pm^2)}{(\omega_\pm^2 - |\vec{q}|^2)\omega_\pm} \end{aligned} \tag{6.44}$$

From Eqs. 6.42, 6.43 and 6.44, we finally obtain the relation

$$\sum_s u_s^{q\pm}(q)\bar{u}_s^{q\pm}(q) = \frac{\omega_\pm(\omega_\pm^2 - |\vec{q}|^2)}{2m_F^2}(\gamma^0 \mp \hat{\gamma}\cdot\hat{\mathbf{q}})\,. \tag{6.45}$$

Substituting this into Eq. 6.41 gives

$$\left|\mathcal{M}_{\mathrm{kt}a}\right|^2 = 12e^2\sum_f\left(\frac{e_f}{e}\right)^2\frac{E_1}{m_F^2}\left[\omega_+(\omega_+^2 - |\vec{q}|^2)(1-\hat{\mathbf{q}}\cdot\hat{\mathbf{p}}_1) + \omega_-(\omega_-^2 - |\vec{q}|^2)(1+\hat{\mathbf{q}}\cdot\hat{\mathbf{p}}_1)\right] \tag{6.46}$$

and the virtual photon production rate for this process becomes

$$\begin{aligned} E\frac{dR^{\gamma^*}_{\mathrm{kt}a}}{d^3p} = {} & \frac{12}{m_f^2}e^2\sum_f\left(\frac{e_f}{e}\right)^2\int\frac{d^3q}{8(2\pi)^5} \\ & \Big\{f_{FD}(\omega_+)f^{q+\bar{q}}(E_1)(\omega_+^2 - |\vec{q}|^2)(1-\hat{\mathbf{q}}\cdot\hat{\mathbf{p}}_1)\delta(E_1+\omega_+-E)\Theta(E_1-|\vec{q}|) \\ & +f_{FD}(\omega_-)f^{q+\bar{q}}(E_1)(\omega_-^2 - |\vec{q}|^2)(1+\hat{\mathbf{q}}\cdot\hat{\mathbf{p}}_1)\delta(E_1+\omega_--E)\Theta(E_1-|\vec{q}|)\Big\} \end{aligned} \tag{6.47}$$

We have introduced here the same cut $\Theta(E_1 - |\vec{q}|)$ as in the previous section. Finally the dilepton production rate from the processes in Fig. 6.4(a) is

$$\begin{aligned} \frac{dR^{e^+e^-}_{\mathrm{kt}a}}{d^4p} &= \frac{2\alpha}{3\pi M^2}E\frac{dR^{\gamma^*}_{\mathrm{kt}a}}{d^3p} \\ &= \frac{2\alpha^2}{\pi^2 M^2}\sum_f\left(\frac{e_f}{e}\right)^2\int_0^\infty\frac{|\vec{q}|^2\,d\,|\vec{q}|}{(2\pi)^3}\int d\Omega \\ & \left\{f_{FD}(\omega_+)f^{q+\bar{q}}(E_1)\frac{(\omega_+^2 - |\vec{q}|^2)}{2m_F^2}(1-\hat{\mathbf{q}}\cdot\hat{\mathbf{p}}_1)\delta(E_1+\omega_+-E)\Theta(E_1-|\vec{q}|)\right. \\ & \left.+f_{FD}(\omega_-)f^{q+\bar{q}}(E_1)\frac{(\omega_-^2 - |\vec{q}|^2)}{2m_F^2}(1+\hat{\mathbf{q}}\cdot\hat{\mathbf{p}}_1)\delta(E_1+\omega_--E)\Theta(E_1-|\vec{q}|)\right\}\,. \end{aligned} \tag{6.48}$$

6.3.2 *Cut-pole contributions* ($1 + 2 \to 3 + \gamma^*$)

The expressions for the annihilation and Compton scattering processes from Figs. 6.4b and 6.4c are

$$E\frac{dR^{\gamma^*}_{\mathrm{kt}bc}}{d^3p} = \int\frac{d^3p_1}{2(2\pi)^3E_1}\frac{d^3p_2}{2(2\pi)^3E_2}\frac{d^3p_3}{2(2\pi)^3E_3}(2\pi)^4\delta^4(p_1+p_2-p-p_3)\left|\mathcal{M}_{\mathrm{kt}b}\right|^2$$

$$
\begin{aligned}
&\times \frac{f^{q+\bar{q}}(E_1) f_{BE}(E_2)(1-f_{FD}(E_3))}{2(2\pi)^3} \\
&+ \int \frac{d^3p_1}{2(2\pi)^3 E_1} \frac{d^3p_3}{2(2\pi)^3 E_3} \frac{d^3p_2}{2(2\pi)^3 E_2} (2\pi)^4 \delta^4(p_1+p_3-p-p_2) \left|\mathcal{M}_{\mathrm{kt}c}\right|^2 \\
&\times \frac{f^{q+\bar{q}}(E_1) f_{FD}(E_3)(1+f_{BE}(E_2))}{2(2\pi)^3} ,
\end{aligned}
\tag{6.49}
$$

where f_{BE} is the Bose-Einstein distribution function. The square of the diagrams in Fig. 6.4b and Fig. 6.4 c are given by

$$
\left|\mathcal{M}_{\mathrm{kt}b}\right|^2 = \left|\mathcal{M}_{\mathrm{kt}c}\right|^2 = 3C_F g_s^2 e^2 \sum_f \left(\frac{e_f}{e}\right)^2 \mathrm{Tr}\left[4\, \not{p}_1 S_D^*(p-p_1)\, \not{p}_3 S_D(p-p_1)\right] ,
\tag{6.50}
$$

where $C_F = 4/3$ is the quark Casimir. It is important to point out that only the t-channel exchange is considered in the Compton scattering process. For the annihilation process shown in Fig. 6.4c, the particle with energy E_1 is an antiquark and the one with energy E_3 is a quark. There is also a contribution with E_1 and E_3 being associated with a quark and an antiquark respectively. Those two contributions are added incoherently, since coherence effect are suppressed by higher powers of g_s. After inserting $1 = \int_{-\infty}^{\infty} d\omega\, \delta(\omega - E + E_1)$ and using $p_1 = p - q$ we obtain

$$
\begin{aligned}
E\frac{dR^{\gamma^*}_{\mathrm{kt}bc}}{d^3p} &= \int_{-\infty}^{\infty} d\omega \int \frac{d^3q}{16(2\pi)^5 E_1} \frac{d^3p_2}{(2\pi)^3 E_2 E_3} \delta(\omega - E + E_1) \\
&\quad \left[\ \delta(\omega - E_2 + E_3) \left|\mathcal{M}_{\mathrm{kt}b}\right|^2 f^{q+\bar{q}}(E_1) f_{BE}(E_2)(1-f_{FD}(E_3)) \right. \\
&\quad \left. + \delta(\omega - E_3 + E_2) \left|\mathcal{M}_{\mathrm{kt}c}\right|^2 f^{q+\bar{q}}(E_1) f_{FD}(E_3)(1+f_{BE}(E_2))\right]
\end{aligned}
\tag{6.51}
$$

To compare this result with the one obtained in the last section, we take advantage of the quark self-energy Σ, shown in Fig. 6.5. The expression for the discontinuity of Σ, in the space-like region is [34]

$$
\begin{aligned}
\mathrm{Disc}\Sigma(\omega, |\vec{q}|) = -i\pi C_F g_s^2 \int \frac{d^3p_2}{(2\pi)^3 E_2 E_3}\, \not{p}_3 \Big\{ & \delta(\omega - E_3 + E_2) f_{FD}(E_3)(1+f_{BE}(E_2)) \\
& + \delta(\omega + E_3 - E_2) f_{BE}(E_2)(1-f_{FD}(E_3)) \Big\} f_{FD}^{-1}(\omega)
\end{aligned}
\tag{6.52}
$$

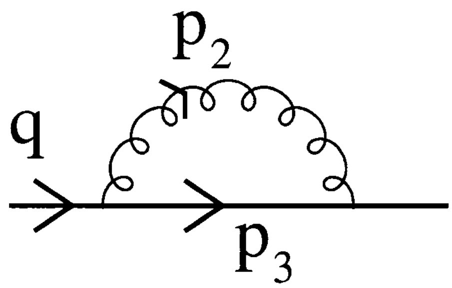

Figure 6.5: Quark self-energy with gluon propagator in the loop.

Eqs. 6.50, 6.51 and 6.52 lead to

$$E\frac{dR^{\gamma^*}_{\text{kt}bc}}{d^3p} = 3ie^2\sum_f \left(\frac{e_f}{e}\right)^2 \int_{-\infty}^{\infty} d\omega \int \frac{d^3q}{8(2\pi)^6 E_1}\delta(\omega - E + E_1) f^{q+\bar{q}}(E_1) f_{FD}(\omega)$$
$$\times \operatorname{Tr}\left[4\, \not{p}_1 S^*_D(q)\, \text{Disc}\Sigma(\omega, |\vec{q}|)\, S_D(q)\right] . \tag{6.53}$$

We can use the relation (see Appendix D)

$$S^*_D(q)\, \text{Disc}\Sigma(\omega, |\vec{q}|)\, S_D(q) = \text{Disc}\left(-iS_D(q)\right) \tag{6.54}$$

which hold providing $D_\pm(q) = D^*_\pm(q^*)$. This is indeed the case as can be inferred from the definition of $D_\pm$, Eqs. 6.26 and 6.28. For $\omega^2 - |\vec{q}|^2 < 0$, we use Eqs. 6.31, 6.32 and 6.42 to express the right hand side as

$$\begin{aligned}
\text{Disc}\left(-iS_D(q)\right) &= -\frac{(\gamma^0 - \hat{\gamma}\cdot\hat{\mathbf{q}})}{2}\text{Disc}\frac{1}{D_+(q)} - \frac{(\gamma^0 + \hat{\gamma}\cdot\hat{\mathbf{q}})}{2}\text{Disc}\frac{1}{D_-(q)} \\
&= -i(\gamma^0 - \hat{\gamma}\cdot\hat{\mathbf{q}})\text{Im}\frac{1}{D_+(q)} - i(\gamma^0 + \hat{\gamma}\cdot\hat{\mathbf{q}})\text{Im}\frac{1}{D_-(q)} \\
&= -i\pi(\gamma^0 - \hat{\gamma}\cdot\hat{\mathbf{q}})\beta_+(\omega, |\vec{q}|) - i\pi(\gamma^0 + \hat{\gamma}\cdot\hat{\mathbf{q}})\beta_-(\omega, |\vec{q}|) \, .
\end{aligned} \tag{6.55}$$

Using the latter result in Eq. 6.53 and carrying out the trace, we find

$$E\frac{dR^{\gamma^*}_{\text{kt}bc}}{d^3p} = 3e^2\sum_f \left(\frac{e_f}{e}\right)^2 \int_{-\infty}^{\infty} d\omega \int_0^{\infty} \frac{|\vec{q}|^2\, d\,|\vec{q}|}{(2\pi)^5} \int d\Omega\, \delta(\omega - E + E_1) f^{q+\bar{q}}(E_1) f_{FD}(\omega)$$
$$\times \left[\beta_+(\omega, |\vec{q}|)(1 - \hat{\mathbf{q}}\cdot\hat{\mathbf{p_1}}) + \beta_-(\omega, |\vec{q}|)(1 + \hat{\mathbf{q}}\cdot\hat{\mathbf{p_1}})\right] \Theta(E_1 - |\vec{q}|) \tag{6.56}$$

As before, we have introduced the term $\Theta(E_1 - |\vec{q}|)$, since we consider only the region where HTL may be important. The dilepton pair production rate for the processes shown in Figs. 6.4b-c is

$$\begin{aligned}\frac{dR^{e^+e^-}_{\mathrm{ktbc}}}{d^4p} &= \frac{2\alpha}{3\pi M^2} E \frac{dR^{\gamma^*}_{\mathrm{ktbc}}}{d^3p} \\ &= \frac{2\alpha^2}{\pi^2 M^2} \sum_f \left(\frac{e_f}{e}\right)^2 \int_{-\infty}^{\infty} d\omega \int_0^{\infty} \frac{|\vec{q}|^2\, d\,|\vec{q}|}{(2\pi)^3} \int d\Omega\, \delta(\omega - E + E_1) f^{q+\bar{q}}(E_1) f_{FD}(\omega) \\ &\times \Big[\beta_+(\omega, |\vec{q}\,|)(1 - \hat{\mathbf{q}}\cdot\hat{\mathbf{p}}_1) + \beta_-(\omega, |\vec{q}\,|)(1 + \hat{\mathbf{q}}\cdot\hat{\mathbf{p}}_1)\Big]\, \Theta(E_1 - |\vec{q}|)\end{aligned} \tag{6.57}$$

Once adding Eqs. 6.48 and 6.57, we find

$$\begin{aligned}\frac{dR^{e^+e^-}_{Kin.-Th.}}{d^4p} &= \frac{2\alpha^2}{\pi^2 M^2} \sum_f \left(\frac{e_f}{e}\right)^2 \int_0^{\infty} \frac{|\vec{q}|^2\, d\,|\vec{q}|}{(2\pi)^3} \int d\Omega \\ &\Bigg[\Bigg\{ f_{FD}(\omega_+) f^{q+\bar{q}}(E_1) \frac{(\omega_+^2 - |\vec{q}|^2)}{2m_F^2} (1 - \hat{\mathbf{q}}\cdot\hat{\mathbf{p}}_1)\delta(E_1 + \omega_+ - E)\Theta(E_1 - |\vec{q}|) \\ &+ f_{FD}(\omega_-) f^{q+\bar{q}}(E_1) \frac{(\omega_-^2 - |\vec{q}|^2)}{2m_F^2} (1 + \hat{\mathbf{q}}\cdot\hat{\mathbf{p}}_1)\delta(E_1 + \omega_- - E)\Theta(E_1 - |\vec{q}|)\Bigg\}\,. \\ &+ \int_{-\infty}^{\infty} d\omega\, \delta(\omega - E + E_1) f^{q+\bar{q}}(E_1) f_{FD}(\omega) \\ &\times \Big[\beta_+(\omega, |\vec{q}\,|)(1 - \hat{\mathbf{q}}\cdot\hat{\mathbf{p}}_1) + \beta_-(\omega, |\vec{q}\,|)(1 + \hat{\mathbf{q}}\cdot\hat{\mathbf{p}}_1)\Big]\, \Theta(E_1 - |\vec{q}|)\Bigg]\,.\end{aligned} \tag{6.58}$$

This reproduces exactly the result from Eq. 6.38, when the particle associated to E_1 is thermal, i.e $f^{q+\bar{q}}(E_1) \to 2f_{FD}(E_1)$, showing that both methods, finite-temperature field theory and the relativistic kinetic formalism, lead to the same result.

We now briefly compare our approach with the method used by Thoma and Traxler in Ref. [148]. They have calculated the photon self-energy shown in Fig. 6.3 with an imposed cutoff $k_s \ll T$ on the momentum $|\vec{q}|$ in the loop-integral, such that $0 \leq |\vec{q}| \leq k_s$. They then added the Compton scattering and annihilation processes coming from cutting the two-loop photon self-energy without HTL propagators or HTL vertices. Those two latter process have an infrared divergence, which is regulated by imposing a low value cutoff k_s for the exchange momentum. When adding all those processes, the final production rate is infrared safe and independent of k_s. They have also calculated the $\alpha^2\alpha_s$ contribution coming from the pole of the effective quark propagator in Fig. 6.3. However in their approach, the information about the parton phase space distribution is lost, i.e. it is not possible at the end to make the substitution $f^{q+\bar{q}} \to f_{\text{jet}}^{q+\bar{q}}$. Here, we only consider the one-loop diagram from Fig. 6.3, but we use the dressed propagator $S^*(q)$ up to the scale $|\vec{q}| = k_c$, where k_c corresponds to E_1 due to the $\theta(E_1 - |\vec{q}|)$ function. With this method we do not have to specify the shape of $f^{q+\bar{q}}$ until the end of the calculation. We have verified that our numerical result depends only weakly on the scale k_c. For example, taking $k_c = 0.6 \times E_1$ reduces the production rate by ~ 20 %.

Fig 6.6 shows, for $f^{q+\bar{q}}(E_1) \to 2f_{\text{FD}}(E_1)$, the different sources of dileptons at a temperature $T = 300$ MeV. In all cases, the particle with energy E_1 corresponds to a pole with positive χ. The pole-pole contributions are shown by the dot-dashed and the short-dashed lines. They correspond to the diagram in Fig. 6.4a. The annihilation of two partons with positive helicity over chirality ratio, $\chi = 1$, (dotted-dashed line) dominates at high invariant mass. For $M > 1$ GeV it converges toward the Born term (dotted line) obtained from a one-loop photon self-energy calculation with two bare propagators. The cut-pole contribution (long-dashed line) is dominant for $M < 1$ GeV. The corresponding physical processes are the annihilation and Compton processes in Fig. 6.4b and c. The sum of our HTL contributions is shown by the solid line. It agrees very well (within 30 %) with the sum of the Born term and the $\alpha^2\alpha_s$ result from Ref. [148], given by the double dot-dashed line.

6.4 Dilepton yield in relativistic heavy-ions collisions

6.4.1 Thermal dileptons

High-p_T real and virtual photons are preferentially emitted early during the QGP phase, when the temperature is largest, and the transverse flow small. Assuming again a 1-D expansion [110], as in Chapters 4 and 5, that is cut off at a maximal

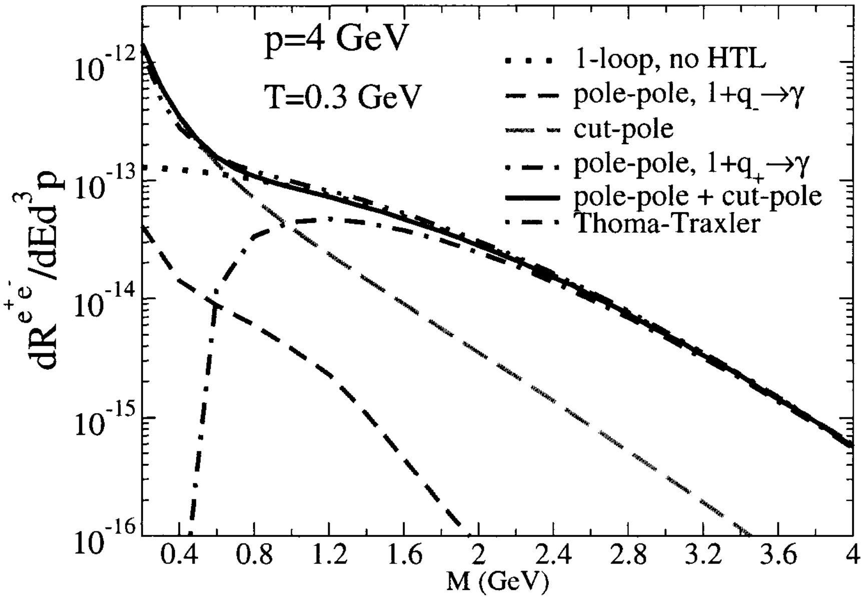

Figure 6.6: (Color online) Production rate of dilepton with momentum p = 4 GeV, from thermal induced reactions, at a temperature T = 300 MeV. Dotted line: Born term; short-dashed line: pole-pole contribution with different ratio χ; dot-dashed: pole-pole contribution with identical helicity over chirality ratio χ; long-dashed: cut-pole contribution; solid line: sum of our HTL processes; and double dot-dashed line: born term plus $\alpha^2\alpha_s$ contributions from Ref. [148].

space-time rapidity $\eta_{\max}$, the yield as a function of invariant mass M and dilepton rapidity y_d is given by the rate $R^{e^+e^-} = R^{e^+e^-}(\tau, \eta, \mathbf{r}_\perp)$ as

$$\frac{dN^{e^+e^-}}{dM^2dy_d} = \int d^4x \frac{dR^{e^+e^-}}{dM^2dy_d} = \int \tau d\tau d^2r_\perp \int_{-\eta_{max}}^{\eta_{max}} d\eta \frac{dR^{e^+e^-}}{dM^2dy_d}. \tag{6.59}$$

Since $dR^{e^+e^-}/dM^2dy_d$ is invariant under a boost in the z direction, we can do the previous integral in any frame. Let's define two important frames: the fireball frame (FB) which is the nucleus-nucleus collision system, and the local thermal frame (LT), the system where the temperature is defined. The LT, as seen from the FB, moves with rapidity $y = \eta$. Then, the rapidity y_{FB} of a particle in the fireball frame is

$$y_{FB} = \eta + y_{LT} \tag{6.60}$$

where y_{LT} is the rapidity of the particle in LT. The η integration of $dR^{e^+e^-}/dM^2dy_d$ is also a Lorentz invariant:

$$\int_{-\eta_{max}}^{\eta_{max}} d\eta \frac{dR^{e^+e^-}}{dM^2dy_d} = \int_{-\eta_{max}}^{\eta_{max}} d\eta \frac{dR^{e^+e^-}(\eta_{FB}=\eta, y_{FB}=y_d)}{dM^2dy_{FB}}$$
$$= \int_{-\eta_{max}}^{\eta_{max}} d\eta \frac{dR^{e^+e^-}(\eta_{LT}=0, y_{LT}=y_d-\eta)}{dM^2dy_{LT}} \qquad (6.61)$$

where η_{FB} and η_{LT} are respectively the (space-time)rapidity of the slice of matter into which the dilepton is produced, as seen from the FB and the LT frame. In FB, $\eta_{FB} = \eta$ while in LT, the medium is at rest, so $\eta_{LT} = 0$. In LT, with the transformation $\eta \to -\eta + 2y_d$, we get for $\eta_{max} \gg |y_d|$:

$$\int_{-\eta_{max}}^{\eta_{max}} d\eta \frac{dR^{e^+e^-}(\eta_{LT}=0, y_{LT}=y_d-\eta)}{dM^2dy_{LT}} = \int_{-\eta_{max}}^{\eta_{max}} d\eta \frac{dR^{e^+e^-}(\eta_{LT}=0, y_{LT}=\eta-y_d)}{dM^2dy_{LT}}$$
$$= \int_{-\eta_{max}}^{\eta_{max}} d\eta \frac{dR^{e^+e^-}(\eta_{FB}=y_d, y_{FB}=\eta)}{dM^2dy_{FB}}$$
$$= \left.\frac{dR^{e^+e^-}(\eta_{FB}=y_d)}{dM^2}\right|_{FB} \qquad (6.62)$$

So, $\frac{dR^{e^+e^-}(\bar{\eta}=y_d)}{dM^2}|_{FB}$ is the production rate calculated in a slice of matter moving with rapidity y_d, as seen from the fireball frame. Hence the rate of lepton pairs with a fixed rapidity y_d integrated over the entire longitudinal extent of the fireball is the same as the rate of all lepton pairs integrated over rapidity from the slice of the fireball at $\eta = y_d$. The yield of dilepton at midrapidity becomes

$$\frac{dN^{e^+e^-}}{dM^2dy_d} = \int \tau d\tau d^2r_\perp \left.\frac{dR^{e^+e^-}(\eta_{FB}=0)}{dM^2}\right|_{FB} = \int \tau d\tau d^2r_\perp \left.\frac{dR^{e^+e^-}}{dM^2}\right|_{LT}$$
$$= \int \tau d\tau d^2r_\perp \int dp_T p_T \int dp_z \frac{2\pi}{E_0}\frac{1}{2}\frac{dR^{e^+e^-}}{d^4p}\,. \qquad (6.63)$$

Eq. 6.18 has been used for the second line of the above expression. Here $\vec{p}_0$ is the three-momentum of the lepton pair with p_T and p_z being its transverse and longitudinal momentum respectively. Then we have $|\vec{p}_0| = \sqrt{p_T^2 + p_z^2}$, and $E_0 = \sqrt{M^2 + p_T^2 + p_z^2}$ is the energy of the pair. The dilepton energy as seen from the lab frame is $E = \sqrt{M^2 + p_T^2}$.

At this point, we add two constraints in order to facilitate the comparison with experimental data. First, we introduce a lower cutoff $p_{T\mathrm{cut}}$ for the transverse momentum of the lepton pair; second, a cut on the individual lepton rapidities which reflects the finite geometrical acceptance of any detector, is included, such that $|y_{e^\pm}| \leq y_{\mathrm{cut}}$. We introduce a multiplicative factor $P_{\mathrm{cut}} = P(|y_{e^\pm}| \leq y_{cut}, p_T)$ to include the latter condition. In the center of mass frame of the lepton pair, the distribution of positive leptons, normalized to unity, is given by

$$\frac{E^+_{cm} dP_{\gamma^* \to e^+e^-}}{d^3 p^+_{cm}} = \frac{\delta(E^+_{cm} - \frac{M}{2})}{4\pi E^+_{cm}}. \tag{6.64}$$

Then the probability for a virtual photon with momentum p_T at midrapidity to emit two leptons with rapidities $|y_{e^\pm}| \leq y_{\mathrm{cut}}$ can be obtained by a boost back to the lab frame as

$$\begin{aligned} P(|y_{e^\pm}| \leq y_{cut}, p_T) &= \int \frac{d^3 p^+_{cm}}{E^+_{cm}} \frac{E^+_{cm} dP_{\gamma \to e^+e^-}}{d^3 p^+_{cm}} \Theta(|y_{e^\pm}| \leq y_{\mathrm{cut}}) \\ &= \int \frac{d\cos\theta d\phi}{\pi} \left(\frac{E^+}{M}\right)^2 \Theta(|y_{e^\pm}| \leq y_{\mathrm{cut}}). \end{aligned} \tag{6.65}$$

Note that in this frame

$$y_{e^\pm} = \frac{1}{2} \ln \frac{E^\pm + p_z^\pm}{E^\pm - p_z^\pm}, \tag{6.66}$$

$$E^+ = \frac{M^2}{2(\sqrt{M^2 + p_T^2} - p_T \cos\theta)}, \tag{6.67}$$

$$p_z^\pm = \pm E^+ \sin\theta \, \sin\phi \tag{6.68}$$

and $E^- = E - E^+$.

The dilepton yield through a 1-D QGP expansion is finally given by

$$\frac{dN}{dM^2 dy_d} = \int d\tau\, \tau \int_0^{R_\perp} dr\, r \int_0^{2\pi} d\phi \int_{p_{T_{cut}}}^{\infty} dp_T\, p_T \int_{-\infty}^{\infty} dp_z \frac{2\pi}{E_0} \frac{1}{2} \frac{dR^{e^+e^-}}{d^4p} P(|y_{e^\pm}| \leq y_{cut}, p_T) \tag{6.69}$$

The thermal-thermal yield at midrapidity is thus obtained by putting Eq. 6.38 into Eq. 6.69.

6.4.2 Jet-thermal dileptons

In this subsection, we calculate the emission rate of dileptons from interaction of jets with the medium. The initial phase-space distribution function for partons from jets produced in heavy ion collisions has been shown in Chapter 4

$$f_{q\bar{q}}^{\rm jet}(\vec{x},\vec{p},t_0) = \frac{(2\pi)^3\mathcal{P}(\mathbf{r}_\perp)}{g_q \tau p_T}\frac{dN_{q\bar{q}}^{\rm jet}}{dyd^2p_T}\delta(\eta - y) \tag{6.70}$$

in a boost invariant Bjorken scenario. $\mathcal{P}(\mathbf{r}_\perp)$ represents the probability to create a jet at position $\mathbf{r}_\perp$ in the transverse plane :

$$\mathcal{P}(\mathbf{r}_\perp) = \frac{2}{\pi R_\perp^2}\left(1 - \frac{r_\perp^2}{R_\perp^2}\right)\theta(R_\perp - r_\perp)\,, \tag{6.71}$$

where $R_\perp = A^{1/3}1.2$ fm is the radius of the nucleus in the transverse plane. The time evolution of the jet distribution is given, within the AMY formalism, by Eq. 4.46.

The dileptons produced from the passage of jets through the QGP is finally obtained from Eq. 6.69 and by the substitution $f^{q+\bar{q}}(E_1) \to f_{q\bar{q}}^{\rm jet}(E_1)$ into Eq. 6.58. Note that $\eta = 0$, together with the boost invariance of the jet distribution, imply that the longitudinal momentum of the jet parton vanishes, and that $p_z = q_z$. After some algebra, we get

$$\begin{aligned}
\frac{dN_{jet-th}}{dM^2dy_d} &= \frac{8\alpha^2\sum_f\left(\frac{e_f}{e}\right)^2}{\pi M^2 g_q}\int dt\int_0^{R_\perp} rdr\,\gamma\int_{p_{T_{cut}}}^\infty dp_T P(|y_{e^\pm}| \le y_{cut}, p_T) \\
&\times \int_0^\infty dq_T \int_{-\infty}^\infty dq_z \frac{1}{E_0}\sum_{j=\pm} \\
&\times \left[\frac{f_{FD}(\omega_j(|\vec{q}|))}{2m_F^2}\frac{(\omega_j(|\vec{q}|)^2 - |\vec{q}|^2)}{\sqrt{1-\cos^2\theta_j}}(1 + j\frac{|\vec{q}|}{E_1^j} - j\frac{\mathbf{q}\cdot\mathbf{p}}{|\vec{q}|\,E_1^j})E_1^j\left.\frac{dN_{q\bar{q}}^{jet}(t)}{dy_1d^2p_{T_1}}\right|_{y_1=0}\right. \\
&\left. + \int_{-\infty}^\infty d\omega f_{FD}(\omega)\beta_j(\omega,|\vec{q}|)\left(1 + j\frac{|\vec{q}|}{E_1} - j\frac{\mathbf{q}\cdot\mathbf{p}}{|\vec{q}|\,E_1}\right)\frac{E_1}{\sqrt{1-\cos^2\theta}}\left.\frac{dN_{q\bar{q}}^{jet}(t)}{dy_1d^2p_{T_1}}\right|_{y_1=0}\right]
\end{aligned} \tag{6.72}$$

with $|\vec{q}| = \sqrt{q_T^2 + q_z^2}$. γ represent the ϕ integration over the initial transverse distribution (see Sec. 4.2.1)

$$\gamma = \begin{cases} 0 \\ \frac{2}{R_\perp^2}\left(1 - \frac{r^2+t^2}{R_\perp^2}\right) \\ \frac{2u_0}{\pi R_\perp^2}\left(1 - \frac{r^2+t^2}{R_\perp^2}\right) + \frac{4tr}{\pi R_\perp^4}\sin u_0\,, \end{cases} \tag{6.73}$$

for the cases that $r^2+t^2-2tr > R_\perp^2$, $r^2+t^2+2tr \leq R_\perp^2$ and all other cases, respectively. Here we have defined

$$u_0 = \arccos\frac{r^2+t^2-R_\perp^2}{2t\,r}\,. \tag{6.74}$$

The other quantities to be specified are

$$\begin{aligned} \mathbf{q}\cdot\mathbf{p} &= p_T\, q_T \cos\theta_\pm + q_z^2\,; \\ \theta_\pm &= \cos^{-1}\left(\frac{p_T^2+q_T^2-(E_0-\omega_\pm)^2}{2p_T q_T}\right)\,; \\ E_1^\pm &= E_0 - \omega_\pm\,. \end{aligned} \tag{6.75}$$

We get the jet-thermal result without HTL effects, i.e the Born term, by keeping only the pole-pole(q_+) term in Eq. 6.72. In this case, we have to substitute:

$$\begin{aligned} \beta_\pm &\to 0\,; \\ \frac{(\omega_-^2-|\vec{q}|^2)}{2m_F^2} &\to 0\,; \\ \frac{(\omega_+^2-|\vec{q}|^2)}{2m_F^2} &\to 1\,; \\ (1+\frac{|\vec{q}|}{E_1^+} - \frac{\mathbf{q}\cdot\mathbf{p}}{|\vec{q}|E_1^+}) &\to \frac{M^2}{2E_1E_q}\,; \\ \omega_+ &\to E_q = |\vec{q}|\,. \end{aligned} \tag{6.76}$$

This leads to the final expression for the jet-thermal dilepton yield without HTL effects:

$$\begin{aligned} \frac{dN^{no-HTL}_{jet-th}}{dM^2dy_d} &= \frac{4\alpha^2\sum_f\left(\frac{e_f}{e}\right)^2}{\pi g_q}\int dt\int_0^{R_\perp} rdr\,\gamma\int_{p_{T_{cut}}}^\infty dp_T\int_0^\infty dq_T\int_{-\infty}^\infty dq_z\frac{dN^{q\bar{q}}(t)}{dy_1d^2p_{T_1}}\Big|_{y_1=0} \\ &\times\frac{1}{E_0E_q\sqrt{1-\cos^2\theta_+}}\,f^{th}(E_q)P(|y_{e^\pm}|\leq y_{cut},p_T)\,. \end{aligned} \tag{6.77}$$

The Bjorken model has been presented in Chapter 4. We assign again the initial temperatures in the transverse direction according to the local density so that [32, 112]

$$T(r_\perp, \tau_i) = T_i \left[2\left(1 - \frac{r_\perp^2}{R_\perp^2}\right)\right]^{1/4} . \tag{6.78}$$

We assume a first-order phase transition and use Eq. 4.34 as the fraction of the QGP present during the mixed phase [110]. The t integration is carried out from τ_i to τ_H and in addition it is scaled between τ_f and τ_H to account for the fact that only a fraction of the system is still a QGP, such that

$$\int dt = \int_{\tau_i}^{\tau_f} dt + \int_{\tau_f}^{\tau_H} dt f_{\mathrm{QGP}}(t) . \tag{6.79}$$

τ_f is fixed to be the time when the temperature reaches the critical temperature of 160 MeV, while τ_H is determined by the condition $f_{\mathrm{QGP}} = 0$. However, since signals associated with jets are sensitive to early times, the order of the phase transition is not crucial.

6.4.3 Drell-Yan and heavy flavour decay

We calculate the Drell-Yan process to order $\mathcal{O}(\alpha_s)$ in the strong coupling, which is the leading order result with non-vanishing p_T of the lepton pair. We also have to take into account virtual photon bremsstrahlung from jets. The total Drell-Yan yield is the sum of the direct and Bremsstrahlung contributions, $\sigma_{\mathrm{DY}} = \sigma_{\mathrm{direct}} + \sigma_{\mathrm{frag}}$ [151, 152]. The direct contribution in collisions of two nuclei A and B is given by [153]

$$\begin{aligned} \frac{d\sigma_{\mathrm{direct}}}{dM^2 dy_d\, dp_T^2} = & \frac{\alpha^2 \alpha_s}{3M^2 s_{NN}} \sum_{a,b} \\ & \times \int \frac{dx_a}{x_a x_b} f_{a/A}(x_a, Q) f_{b/B}(x_b, Q) \\ & \times \frac{\left|\bar{M}_{a+b\to c+\gamma^*}\right|^2}{s_{NN} x_a - \sqrt{s_{NN} M^2 + s_{NN}\, p_T^2 e^{y_d}}} . \end{aligned} \tag{6.80}$$

The squared scattering amplitudes $\left|\bar{M}_{a+b\to c+\gamma^*}\right|^2$ for the Compton and annihilation processes of two incoming partons can be found in [153]. When p_T and M are both large and of the same order, the direct contribution is the dominant mechanism. However, when $\Lambda_{\rm QCD} \ll M \ll p_T$, logarithmic corrections with powers of $\ln(p_T^2/M^2)$ are large. They can be effectively resummed into a virtual-photon fragmentation function $D_{\gamma^*/c}(z, Q_F)$, giving rise to the fragmentation contribution

$$\frac{d\sigma_{\rm frag}}{dM^2 dy_d\, dp_T^2} = \frac{\alpha}{3\pi M^2} \int \frac{dz}{z^2} \frac{d\sigma^{A+B\to c+d}}{dy_d\, dp_{cT}^2}\Big|_{p_{cT}=p_T/z} \times D_{\gamma^*/c}(z, Q_F)\,. \tag{6.81}$$

The cross sections for the production of a massless partons c in $A+B$ collisions, $d\sigma^{A+B\to c+d}/dy_d\, dp_{cT}^2$, can be found in [99]. The factorization scale Q and the fragmentation scale Q_F are both set to $\sqrt{M^2+p_T^2}$. The typical fragmentation time of a jet into a virtual photon of mass M should be proportional to $1/M$. Thus low-M dileptons should fragment outside the medium with their yield affected by the full energy loss suffered by the jet, while dileptons with larger M could be created in the medium, with only small corrections due to energy loss of their parent jet. Since the interesting region for the fragmentation process is at low-M values, where it is expected to be as important as the direct Drell-Yan process, we assume that virtual photons fragment outside the medium after the parent jet has obtained its final energy. We define a medium-inclusive effective fragmentation function (see Chapter 4)

$$D_{\gamma^*/c}(z, Q_F) = \int d^2 r_\perp \mathcal{P}(\mathbf{r}_\perp) \int dE_f \frac{z'}{z} P_{q\bar{q}/c}(E_f; E_i|d) D^0_{\gamma^*/q}(z', Q_F) \tag{6.82}$$

where $z = p_T/E_i$ and $z' = p_T/E_f$. $P_{q\bar{q}/c}(E_f; E_i|d)$ represents the solution to Eq. (3.12), which is the probability to get a given quark or an antiquark with final energy E_f after a propagation length d, when the initial condition is a particle of type c and energy E_i. The propagation length d depends in turn of the transverse position $\mathbf{r}_\perp$ where the jet has been created, and its direction. $D^0_{\gamma^*/q}$ is the leading order vacuum fragmentation function, taken from Refs. [152, 151].

We implement our cuts for the Drell-Yan process as well, so that the final yield is given by

$$\frac{dN_{\rm DY}}{dM^2 dy_d} = \frac{2\langle N_{\rm coll}\rangle}{\sigma_{in}} \int_{p_{T\rm cut}}^{\infty} dp_T\, p_T \left[\frac{d\sigma_{\rm direct}}{dM^2 dy_d\, dp_T^2} + \frac{d\sigma_{\rm frag}}{dM^2 dy_d\, dp_T^2}\right]$$

$$\times P(|y_{e^\pm}| \leq y_{cut}, p_T)\,. \tag{6.83}$$

Here we assume $\langle N_{\rm coll}\rangle = 975$, $\sigma_{in} = 40$ mb for RHIC [29] and $\langle N_{\rm coll}\rangle = 1670$, $\sigma_{in} = 72$ mb for the LHC [125]. In our calculations we use CTEQ5 parton distribution functions [101] with EKS98 shadowing corrections [106].

The main background at RHIC energies for the dilepton production processes considered so far is expected to be decay of open charm and bottom mesons [154]. During the initial hard scattering, $c\,\bar{c}$ ($b\bar{b}$) pairs are produced and can thereafter fragment into $D(B)$ and $\bar{D}(\bar{B})$ mesons. We consider here only correlated decay, which happens when a positron coming from the semileptonic decay of a $D(B)$ is measured together with the electron from the semileptonic decay of a $\bar{D}(\bar{B})$. The results for heavy quark decay have been obtained with the techniques of Ref. [155]. For complementary informations, we show here the expression describing the cross-section calculated by this program:

$$\begin{aligned}\frac{E_H E_{\bar{H}} d\sigma_{H\bar{H}}}{d^3p_H d^3p_{\bar{H}}} &= \int dx_a dx_b f_{a/A}(x_a) f_{b/B}(x_b) dz_H dz_{\bar{H}} \frac{E_H E_{\bar{H}}}{E_Q E_{\bar{Q}} z_H^3 z_{\bar{H}}^3} \\ &\quad \times D_{H/Q}(z_H) D_{\bar{H}/\bar{Q}}(z_{\bar{H}}) \frac{E_Q E_{\bar{Q}} d\sigma^{a+b\to Q+\bar{Q}+c}}{d^3p_Q d^3p_{\bar{Q}}}\end{aligned} \tag{6.84}$$

which represent the production of correlated heavy quarks-antiquarks Q and $\bar{Q}$, and their fragmentation into heavy hadrons H and $\bar{H}$. The leptons production yield is given by

$$\frac{E^{e^+}E^{e^-}dN_{Heavy-q}}{d^3p_{e^+}d^3p_{e^-}} = \frac{\langle N_{\rm coll}\rangle}{\sigma_{in}} \int \frac{d^3p_H}{E_H}\frac{d^3p_{\bar{H}}}{E_{\bar{H}}} \frac{E_H E_{\bar{H}} d\sigma_{H\bar{H}}}{d^3p_H d^3p_{\bar{H}}} \frac{E^{e^+}P_{H\to e^+}}{d^3p_{e^+}} \frac{E^{e^-}P_{\bar{H}\to e^-}}{d^3p_{e^-}} \tag{6.85}$$

where $P_{H\to e^+}$ represent the probability to get a lepton e^+ from the H decay. The dilepton is finally expressed as

$$\begin{aligned}\frac{dN_{Heavy-q}}{dM^2dy_d} &= \int \frac{d^3p_{e^+}}{E^{e^+}}\frac{d^3p_{e^-}}{E^{e^-}} \frac{E^{e^+}E^{e^-}dN_{Heavy-q}}{d^3p_{e^+}d^3p_{e^-}} \frac{\delta(E - E^{e^+} - E^{e^-})}{2E} \\ &\quad \times\delta\left(y_d - \frac{1}{2}\ln\left(\frac{E + p_z^{e^+} + p_z^{e^-}}{E - p_z^{e^+} - p_z^{e^-}}\right)\right)\end{aligned} \tag{6.86}$$

Collisional energy loss, which is expected to be the dominant energy loss mechanism for non-ultra-relativistic heavy quarks propagating in a hot medium [156], has not been included. Since this constitutes a background to our process, we adopt this conservative point of view.

6.5 Results

We choose the same parametrization of the plasma phase that was previously used successfully in the studies of high (Chap. 4) and low to intermediate p_T photons (Chap. 2). For central Au+Au collisions at RHIC we have T_i=370 MeV, τ_i=0.26 fm/c corresponding to dN/dy=1260. For LHC the values are T_i=845 MeV, τ_i=0.088 fm/c corresponding to dN/dy=5625 [112, 140]. For the processes involving the QGP, we assume three light flavors and we fix $\alpha_s = 0.3$. As the jets are defined to be particles having a transverse momentum greater than a scale p_Q, with $p_Q \gg 1$GeV, we have set the dilepton momentum cutoff $p_{T_{\rm cut}}$ high enough to avoid any sensitivity to the choice of p_Q. We take $p_{T_{\rm cut}} = 4(8)$ GeV for RHIC (LHC). The cuts on leptons rapidities emulate the PHENIX experiment at RHIC, $y_{\rm cut}$=0.35, while we use y_{cut} =0.5 at LHC.

The dileptons produced at RHIC by the interaction of jets with the medium are shown in Fig. 6.7. Dileptons from jet-pole interactions, i.e. from annihilation of a jet parton with a (q_-)-mode, are negligible, while the jet-pole interactions involving (q_+)-modes tends toward the Born term at high invariant mass, as it was the case for thermal-thermal reactions in Fig. 6.6. On the other hand dileptons from jet-cut interactions do not behave like the cut-pole process in Fig. 6.6. They become the dominant contribution at high-M. The expressions for the cut-pole process, shown in Fig. 6.4b+c, involve the functions $\beta_\pm(|\vec{q}|)$ with $\beta_\pm(|\vec{q}|) \to 0$ for $|\vec{q}| \gg T$. When M is large, in order to keep the value of q modest, the energy E_1 of the incoming parton has to be large: $E_1 \geq M^2/4\,|\vec{q}|$. As the thermal phase space distribution function f_{FD} decreases exponentially for large E_1, the cut-pole contribution turns out to be negligible for large M. However, when the incoming particle is a jet with a power-law distribution, high values of E_1 are not suppressed and the cut-pole contribution

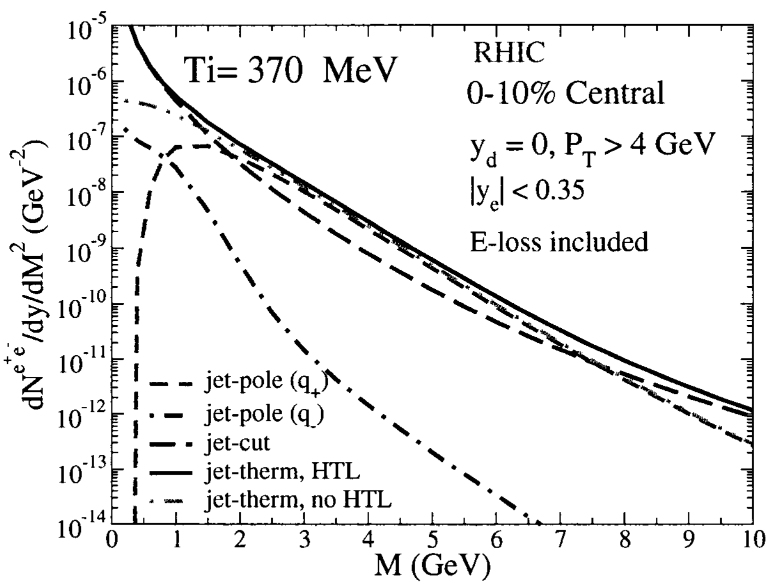

Figure 6.7: High-momentum dileptons produced from the interaction of jets with QGP in Au+Au collisions at 200 GeV (RHIC). The initial temperature is T_i=370 MeV. Short-dashed line: interaction of jets with poles with positive χ; dot-dashed line: interaction of jets with poles with negative χ; long-dashed line: interaction of jets with cuts; solid line: sum of the latter processes; and double dot-dashed line: interaction of jet with QGP without HTL effects (Born term).

is important. Therefore the sum of all the jet-thermal processes with HTL effects included (solid line), is more important than the jet-thermal contribution without HTL effects (double dot-dashed line) by more than a factor 2 for M above 8 GeV. For M below 1 GeV HTL corrections increase the Born term by one order of magnitude, because of the $1/M^2$ behavior in Eq. (6.72).

In Fig. 6.8 we show the mass spectrum of dileptons in central Au+Au collisions at RHIC ($\sqrt{s_{NN}}$ = 200 GeV) and central Pb+Pb at LHC ($\sqrt{s_{NN}}$ = 5.5 TeV). All contributing sources are shown separately. For both collider energies, the jet-thermal contribution exceeds the thermal dilepton production by an order of magnitude, which was also the case for high-p_T photon production. However, at RHIC the dominant contributions for $M > 3$ GeV come from heavy quark decay and the direct Drell-Yan process. At intermediate masses, between 1 GeV and 3 GeV, the jet-thermal contribution becomes as important as these two processes. Below 1 GeV, the fragmentation of jets into virtual photons turns out to be comparable to the direct Drell-Yan produc-

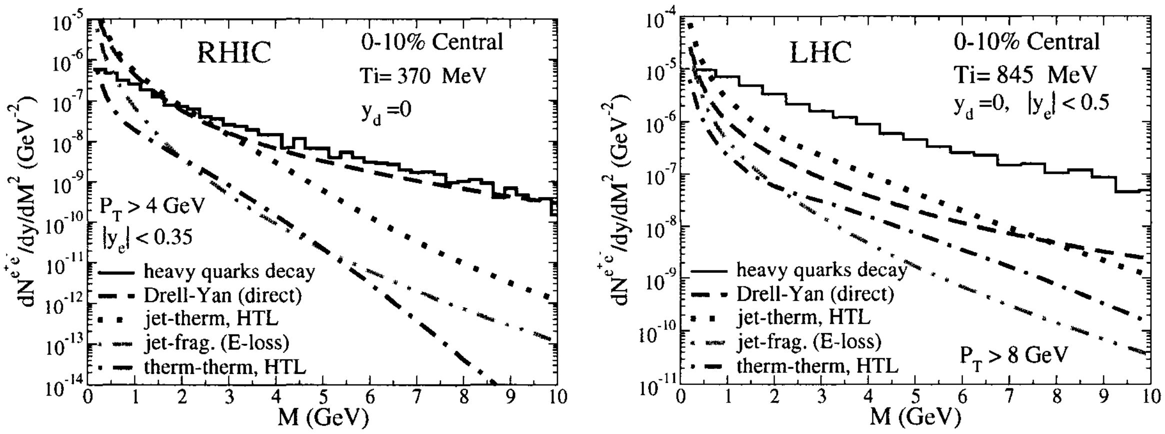

Figure 6.8: Sources of high-p_T dileptons in central Au+Au collisions at RHIC (left) and Pb+Pb at the LHC (right). Solid lines, semileptonic decay of heavy quarks; dashed lines, direct Drell-Yan contribution; dotted lines, jet-thermal interaction with HTL effects; double dot-dashed lines, jet-fragmentation process; and dot-dashed lines, thermal induced dilepton production with HTL effects.

tion and the jet-thermal contribution. At LHC, the whole range of invariant mass is dominated by charm decay, but on the other hand the jet-thermal lepton pairs exceed the direct Drell-Yan yield below 7 GeV. We want to stress the point that energy loss of heavy partons has not been included here, so that the heavy quark contribution is an upper limit of what is to be expected. Lepton pairs from jet-plasma interactions are an important source at RHIC and even more at LHC. If the background from heavy quark decays could be subtracted experimentally, they would be a very valuable plasma probe.

The effect of the cut on single lepton rapidity is shown in Fig. 6.9 at RHIC energy for Drell-Yan and thermal-thermal processes without HTL corrections. For both cases, the cut reduces the yield by a factor $\sim$ 3 and is almost independent of M, except in the low mass region. When M is small, the lepton rapidities tend to be very close to the pair rapidity $y_d = 0$, making the cut less important.

The effect of jet energy loss on the jet-thermal lepton pair production is explored in Fig. 6.10 for RHIC. We observe that for the case without HTL effects (Born term), low mass dileptons are reduced by a factor $\sim$ 1.3, while the suppression is weaker (about 15%) above M = 4 GeV. For a given invariant mass M and jet energy E_1,

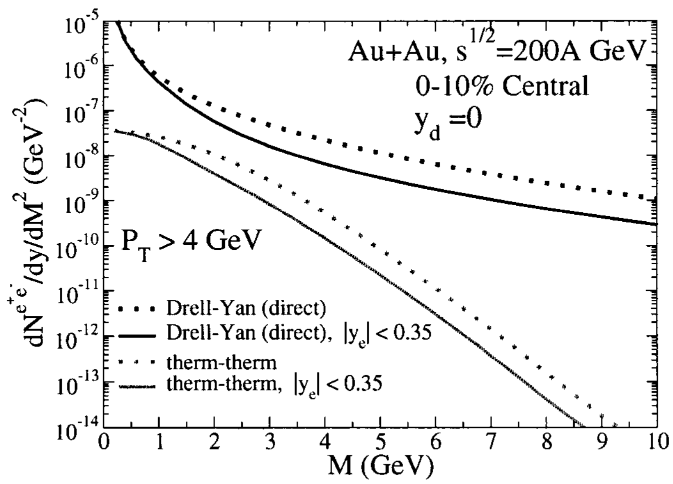

Figure 6.9: Effect of the cut on leptons rapidities for direct Drell-Yan (top) and thermal induced reactions (bottom) without HTL effects at RHIC. The dotted lines include all leptons while the solid lines include only leptons having absolute value of rapidity smaller than 0.35.

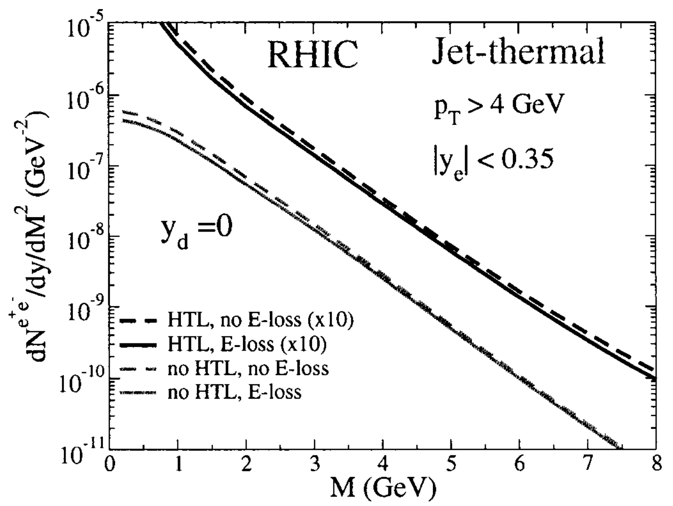

Figure 6.10: Effect of jet energy loss in jet-thermal production of dileptons at RHIC, with HTL effects (top) and without (bottom). The solid lines include the effect of energy loss, while the dashed lines don't. The results for jet-plasma interactions with HTL have been rescaled by a factor 10 for clarity.

the minimum energy for the thermal parton is $E_{2_{min}} = M^2/4E_1$. This minimal value is then favored by the steep thermal spectrum, leading to a dependence of the yield as $\exp(-M^2/4E_1T)$. This implies that dileptons with large mass M are more likely to be emitted at times where the temperatures T is still high which favors small jet propagation time and small energy loss. Low mass dileptons are less sensitive to high temperatures and the suppression is then comparable to the one found for direct photons from jets in Chapter 4. The scenario with HTL effects included leads also to a suppression factor $\sim$ 1.3 for the range dominated by the cut-pole contribution, $M < 2$ GeV and $M > 7$ GeV. The region $2 < M < 7$ GeV, dominated by the pole-pole contribution, shows a weaker suppression, equivalent in magnitude to that of the Born term in the corresponding invariant mass range.

It is also interesting to discuss the dilepton yield as a function of the dilepton transverse momentum p_T in certain windows of the mass M. This is done by substituting the integral over p_T in Eqs. (6.69) and (6.83), by $\int dM^2/(2\pi p_T)$. The results for RHIC and the LHC are displayed in Fig. 6.11, for the mass integrated in the range $0.5 < M <1$ GeV. The ordering of the contributing sources here is very similar to the one seen for real photons distribution in Chapter 4 (see Fig. 4.14). The direct component of the Drell-Yan process dominates for high-p_T dileptons at RHIC while the jet-thermal contribution, with HTL, dominates for p_T <5 GeV, increasing by more than a factor 4 the jet-thermal contribution without HTL. At the LHC, jet-thermal dileptons (HTL effects included) are the most important source in the entire p_T range, $8 < p_T < 17$ GeV. The jet-thermal interaction appears to be as important for dileptons as it was for real photon production.

The total direct dilepton spectrum for RHIC is shown in the left panel of Fig. 6.12. The solid line includes Drell-Yan and QGP contribution (jet-thermal and thermal-thermal) with HTL effects. Leaving out the HTL resummation for jet-thermal dileptons (dashed line) reduces the yield by about 50% around p_T=5 GeV. The absence of any jet-thermal interactions at all (dot-dashed line) would reduce the total yield by a factor $\sim$ 2 at p_T=5 GeV. This emphasizes the importance of this process in the

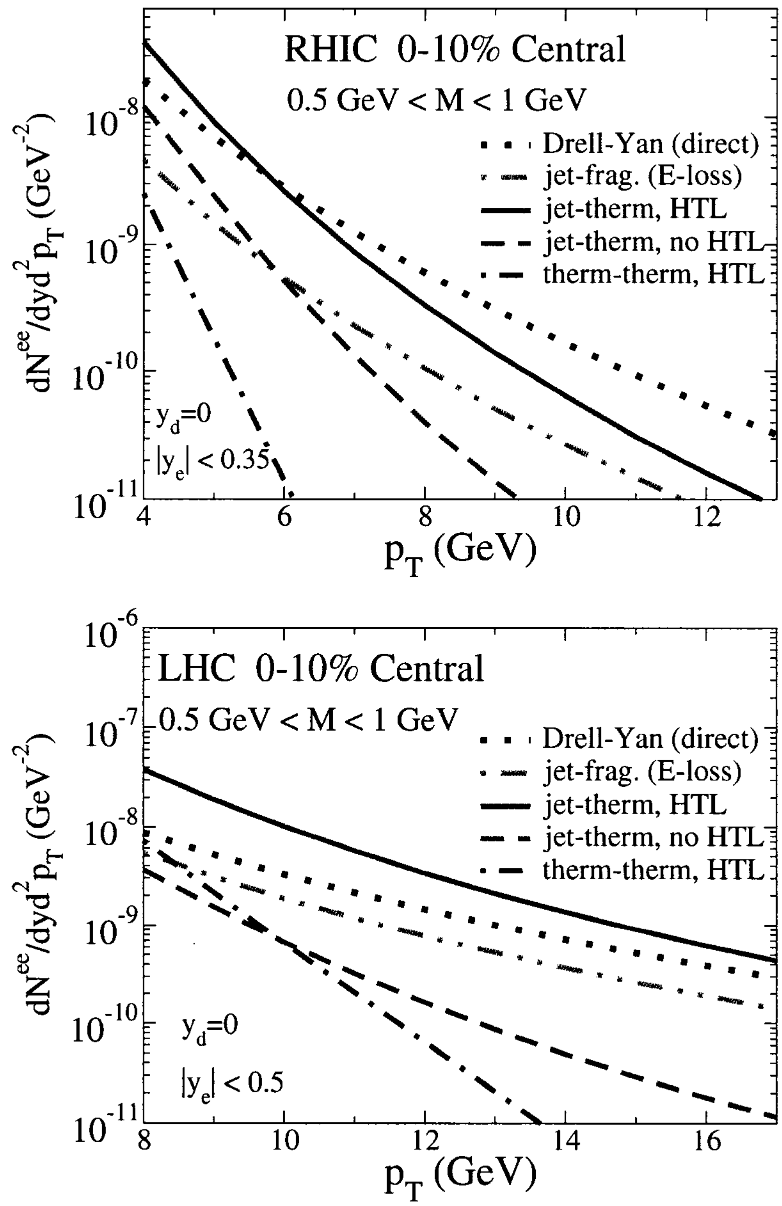

Figure 6.11: p_T distribution of dileptons, integrated in the range $0.5 < M < 1$ GeV, for RHIC (top) and the LHC (bottom). Dotted lines: direct Drell-Yan process; double dot-dashed lines: jet-fragmentation process; solid lines: jet-thermal process with HTL effects; dashed lines: jet-thermal process without HTL effects; and dot-dashed lines: thermal induced reactions with HTL effects.

presence of a QGP.

The only potentially important contribution that is not included in our work is in-medium bremsstrahlung ($q\,i \to q\,i\gamma^*$) and annihilation ($q\bar{q}i \to \gamma^* i$) of an incoming

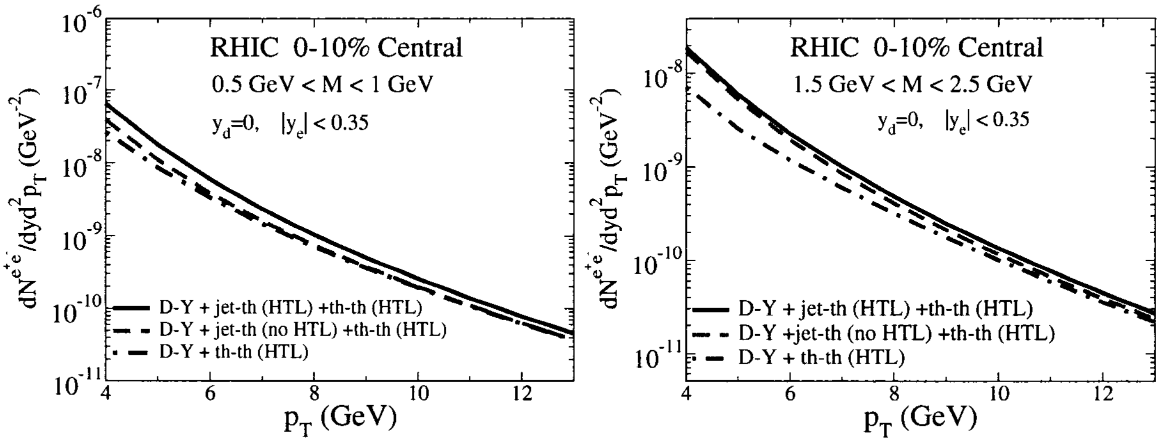

Figure 6.12: p_T distribution of dileptons, integrated in the range $0.5 < M < 1$ GeV (left panel) and $1.5 < M < 2.5$ GeV (right panel), for central Au+Au at RHIC. Solid line: sum of Drell-Yan process, jet-thermal and thermal-thermal process with HTL effects; dashed line: sum of Drell-Yan process, jet-thermal without HTL and thermal-thermal with HTL effects; and dot-dashed line: sum of Drell-Yan process and thermal-thermal reactions with HTL effects.

thermal parton or jet, where i denotes a quark, antiquark or gluon. This goes beyond the current formulation of AMY. However, they have been calculated in Ref. [157] for the case of incoming *thermal* partons, showing that for low mass dileptons, the bremsstrahlung and annihilation more than double the contribution obtained from $2 \to 2$ processes ($q + g \to q + \gamma^*, q + \bar{q} \to g + \gamma^*$). It thus turns out that thermally induced bremsstrahlung and annihilation are as important relatively to $2 \to 2$ processes, no matter if the photons are virtual or real [66]. On the other hand, for the case of real photons and incoming jets, it has been shown in Sec. 4 that those bremsstrahlung and annihilation processes are reduced by a factor 3-4, relatively to the in-medium jet-photon conversion process. This is because the momentum distribution of jets is less steep than the thermal one, making the jet-photon conversion the most important in-medium process. Therefore, if one assumes that the in-medium jet-bremsstrahlung contributes in the same way to virtual and to real photons, it would enhance the solid line by less than 15%.

Finally, the right panel of Fig. 6.12 shows the dilepton spectrum for an another invariant mass window. It is located at higher values $1.5 < M < 2.5$ GeV between the ϕ and the J/ψ masses. As we could have expected from Fig. 6.7, the effect of the

HTL resummation is not very important for this mass window. However interactions of jets with the plasma are still a very important source of dileptons, and this should be detectable.

6.6 Summary and Conclusions

In this chapter we presented a complete calculation of the different sources of lepton pairs in high energy nuclear collisions. We take into account Drell-Yan, fragmentation from jets, thermal emission from the QGP and heavy quark decay. Hard thermal loop resummation has been included in the calculation of the leading order photon self-energy. We explicitly checked that the imaginary part of this self-energy, evaluated within finite-temperature field theory, and a different approach starting from relativistic kinetic theory and using the corresponding Feynman amplitudes, lead to the same results. We obtain the jet-plasma interaction by substituting the phase-space distribution of one incoming thermal parton, by the distribution of jets. While the HTL corrections are important for thermal-thermal processes at low-invariant mass, they are important for both low and high invariant mass when the incoming parton is a jet.

Dilepton emissions due to jet-plasma interactions are found to be much larger than thermal dilepton emission. At low to intermediate dilepton mass, productions from jet-plasma interactions are comparable in size to the Drell-Yan contribution and constitute a good signature for the presence of a quark gluon plasma provided the dominant background of heavy quark decay could be subtracted. The AMY formalism has been used to account for energy loss of jets in the QCD plasma; this energy degradation reduces the effect of jet-thermal processes by $\sim 30\%$. Further study involving heavy quark energy loss will be needed to obtain a better estimate of this channel, together with an explicit calculation of dileptons from medium-induced bremsstrahlung.

7

CONCLUSION

We have discussed in Chapter 1 that one of the ultimate goal in relativistic heavy ions collisions is to find if whether or not, the formation of a quark-gluon plasma is possible. Since the electromagnetic coupling constant is parametrically small, the photons produced during the nucleus-nucleus collision escape the interacting zone without rescattering, in good approximation. This make the photons very useful for two important reasons. First, their production rate can be calculated in perturbation theory, and second, they probe the feature of the medium at the time they have been produced. However, it is not possible experimentally to discriminate a contribution from the QGP, only the total photon spectrum is measured. The goal of this thesis was therefore to calculate the photons yield from each contributing sources, compare with available experimental data, and find if a contribution from the QGP was essential to reproduce them.

In Chapter 2, we have evaluated the photon production at low to intermediate p_T. In this respect, earlier calculations of photon radiation from interacting mesons was reexamined with new constraints. In particular, the coupling constants have been adjusted with the D to S wave ratio of the decay $a_1 \to \pi + \rho$, and finite size effects have been taken into account by the inclusion of form-factors. Also, the pertinence of new channels has been evaluated. Indeed, we have found that the t-channel exchange of ω meson is the dominant source of photons with energy greater than ~ 1.5 GeV, in the hadronic sector. Our new mesonic production rate, together with baryonic and QGP contributions, have finally been included into a fireball model, emulating the space-time expansion of the thermal medium, and compared to data from SPS. We found that with a moderate value for the initial temperature (T_i=205 MeV), our photon yield reproduced SPS result once added to prompt photons including Cronin effect, suggesting that either the QGP is not present at SPS, or either it is too weak to be detected.

For RHIC and LHC collider energies, the high-p_T suppression has to be taken into account. The Arnold-Moore-Yaffe (AMY) formalism has been presented in Chapter 3. In this model, the jets propagate in the QGP and loose energy by induced gluon bremsstrahlung. The destructive interference due to the LPM effect is included in this model through the solution of a linear integral equation.

In Chapter 4, the AMY formalism has first been used to calculate R_{AA} for neutral pions, in the jet-fragmentation scenario, and compared with success to RHIC data, with an initial temperature T_i =370 MeV, a formation time τ_i =0.26 fm/c and a 1D expanding QGP model. The nuclear geometry was included, and we found that the usual assumption that the jets are produced at the center overestimates the suppression by a factor $\sim$2. Thereafter, the high-p_T photon production in Au-Au collisions at RHIC and Pb-Pb at the LHC, have been evaluated. For the same initial conditions and expansion model than for pions production, we found a good agreement between experiment and our calculations at RHIC, provided the jet-photon conversion in the QGP was included. Indeed, this contribution turns out to dominate the direct photon spectrum in the range $2 < p_T < 4$ GeV, even when the p_T suppression suffered by the jets is included.

In the Chapter 5, we have extended our calculations to non-central collisions. We have verified the validity of our hydronamical model by reproducing photons and pions spectra at RHIC, for different classes of centrality. We have been the first, to our knowledge, to calculate the elliptic anisotropy of direct photons. We found that the jet-photon conversion, acting as an inverse optical mechanism, produced a negative v_2. Though the absolute value of v_2 is small when all sources of direct photons are included, it is increased when one select only photons not associated with high-p_T

hadrons, and reaches -5%. We think that it would constitutes a good signature of the QGP.

Finally, in Chapter 6, we have evaluated the production of high-p_T dileptons at RHIC and at the LHC. We have calculated for the first time, the dilepton yield induced by jets, with HTL resummation effect. We found a perfect analogy between the p_T distribution of dileptons and real photons. Indeed, the jet-QGP direct interaction, with Drell-Yan process, turn out to be the dominant mechanisms, at RHIC, orders of magnitude above thermal-induced dileptons. The HTL resummation increases the dilepton yield at low invariant mass M for incoming thermal partons, while it increases the yield at both low and high M for incoming jets.

In conclusion, from our work, we gain more indications that the high-p_T suppression should be due to energy loss of jet propagating in the QGP, and that the intermediate p_T photons at RHIC might come from QGP contribution. While it is too soon to claim the existence of the QGP, those results constitute a definite step in that direction. A natural extension of this work would be to verify our approximation of a purely longitudinal expansion, in particular at the LHC. Such comparison has been done in Chapter 4 for purely thermal photons, but it would be nice to see if we get the same results by convolving the photon production rate induced by jets with a 3-D hydrodynamical model. Also, for all processes involving the QGP, it is always assumed that α_s is parametrically small. We know however from Lattice QCD calculations that this is not quite true. It would then be very important, in the near future, to look at higher topologies and extract electromagnetic emissions from lattice calculations.

A

PHOTON EQUILIBRATION TIME

The evolution of the photon phase-space distribution f toward equilibrium is given by the Boltzmann Equation:

$$\frac{\partial f}{\partial t} = -f\Gamma_d + (1+f)\,\Gamma_i \tag{A.1}$$

where Γ_d and Γ_i are the photon absorption and production rates. From detailed balance [34], they are related to each other by the photon energy p_0 and the temperature T:

$$\Gamma_d = \Gamma_i\, e^{p_0/T}\,. \tag{A.2}$$

The production is also related to the photon self-energy:

$$\Gamma_i = \frac{\mathrm{Im}\Pi^R}{p_0\,(1-e^{p_0/T})} \tag{A.3}$$

This gives

$$\begin{aligned}\frac{\partial f}{\partial t} &= \Gamma_i\left(1+\left[1-e^{p_0/T}\right]f\right)\\ &= -f\frac{\Gamma_i}{n_{eq}} + \Gamma_i\end{aligned} \tag{A.4}$$

where the photon equilibrium function is defined by

$$n_{eq} = \frac{1}{e^{p_0/T}-1}\,. \tag{A.5}$$

The solution of A.4 is easy to find. It is

$$f = n_{eq} + C\,e^{-\Gamma_i\,t/n_{eq}}\,. \tag{A.6}$$

At the beginning of the reaction, there is no photons. From this condition, we can fix the constant C:

$$f(t=0) = 0 \rightarrow C = -n_{eq} \tag{A.7}$$

Finally,

$$f(t) = n_{eq}\left(1 - e^{-t/\tau_{eq}}\right) \tag{A.8}$$

where the equibration time is given by

$$\begin{aligned} \tau_{eq} &= \frac{n_{eq}}{\Gamma_i} = \frac{n_{eq}\, p_0 \left(1 - e^{p_0/T}\right)}{\mathrm{Im}\Pi^R} \\ &= \frac{n_{eq}\, p_0}{(2\pi)^3 p_0 dR/d^3p} \end{aligned} \tag{A.9}$$

Eq. 2.1 has been used in the second line above. From the photon production rate expression in the QGP, Eq. 4.60, we find for p_0=1 and 3 GeV, the following equilibration times: 87 and 133 fm/c, at T= 200 MeV, and 50 and 76 fm/c at T =300 MeV. For the hadron gas, using the parametrizations for the mesonic contribution, Eq. 2.53, at T = 140 MeV, we find τ_{eq} =967 fm/c for p_0=1 GeV. So, the photon equilibration times turn out to be much greater than the transverse size of the hot medium and than the life-time of the fireball ($t_f \sim 13$ fm/c at SPS, and $t_f \sim 15-20$ fm/c at RHIC). As the photon's equilibration time gives also its mean free path, it means that the photons, once produced, will unlikely suffer rescattering during their path to leave the medium.

B

HADRONIC PRODUCTION RATE DERIVATION

In the present appendix, we show the derivation of Eq. 2.4. The cross-section for a process $1 + 2 \to 3 + \gamma$ is given by [8]

$$\sigma = \int \frac{1}{4E_1 E_2 v_{1-2}} \frac{d^3 p_3}{2E_3 (2\pi)^3} \frac{d^3 p}{2p_0} (2\pi) \left|\mathcal{M}\right|^2 \delta^4(p_1 + p_2 - p_3 - p) \tag{B.1}$$

where v_{1-2} is the relative velocity between particles 1 and 2, p is the photon momentum, and p_0 its energy. By definition, a production rate is

$$R = \sum_{E_1, E_2} I \times n \times \sigma \tag{B.2}$$

where I is the intensity of the incoming projectile and n is the target density. Their expressions are:

$$I = v_{1-2} \frac{dE_1 g(E_1) f(E_1)}{V}, \quad n = \frac{dE_2 g(E_2) f(E_2)}{V}. \tag{B.3}$$

$g(E_i)$ is the energy density of particle i inside a volume V, and $f(E_i)$ its occupation number. Putted together, this gives

$$\begin{aligned} R = \sum_{E_1} dE_1 \frac{g(E_1) f(E_1)}{V} \sum_{E_2} dE_2 \frac{g(E_2) f(E_2)}{V} \int \frac{1}{4E_1 E_2} \frac{d^3 p_3}{2E_3 (2\pi)^3} \frac{d^3 p}{2p_0} (2\pi) \\ \left|\mathcal{M}\right|^2 \delta^4(p_1 + p_2 - p_3 - p)(1 \mp f(E_3)) \end{aligned} \tag{B.4}$$

where the suppression (enhancement) factor has been introduced for the particle in the final state. In the thermodynamical limit ($V \to \infty$), we have

$$\sum_{E_{1(2)}} dE_{1(2)} g(E_{1(2)}) \to \int d^3 x \frac{d^3 p_{1(2)}}{(2\pi)^3} = V \int \frac{d^3 p_{1(2)}}{(2\pi)^3} \tag{B.5}$$

Finally, converting the total rate into a differential one, we get

$$p_0 \frac{dR}{d^3p} = \int \frac{d^3p_1}{2E_1(2\pi)^3} \frac{d^3p_2}{2E_2(2\pi)^3} \frac{d^3p_3}{2E_3(2\pi)^3} \frac{2\pi}{2} |\mathcal{M}|^2$$
$$\delta^4(p_1 + p_2 - p_3 - p) f(E_1) f(E_2)(1 \mp f(E_3)) \tag{B.6}$$

With the identity

$$\frac{d^3p_3}{2E_3} = d^4p_3\, \delta(p_3^2 - m_3^2)\,, \tag{B.7}$$

and the substitutions

$$1 = \int ds\, \delta(s - (p_1 + p_2)^2)\,, \quad 1 = \int dt\, \delta(t - (p_2 - p)^2)\,, \tag{B.8}$$

we get

$$p_0 \frac{dR}{d^3p} = \int ds \int dt \int \frac{d^3p_1}{8E_1(2\pi)^8} \frac{d^3p_2}{E_2} \delta((p_1 + p_2 - p)^2 - m_3^2)\, |\mathcal{M}|^2$$
$$f(E_1) f(E_2)(1 \mp f(E_1 + E_2 - p_0))\delta(s - (p_1 + p_2)^2)\delta(t - (p_2 - p)^2) \tag{B.9}$$

where s, t, u are the Mandelstam variables. The elements of integration are $d^3p_{1,2}/E_{1,2} = |\overrightarrow{p_{1,2}}| dE_{1,2} d\phi_{1,2} d\cos\theta_{1,2}$. The angles are defined relatively to the photon direction, such that $\theta_{1,2}$ is the angle between $\vec{p}_{1,2}$ and $\vec{p}$, and $\phi_{1,2}$ is the azumuthal angle following a rotation of $\vec{p}_{1,2}$ around $\vec{p}$. With this definition, we have

$$\vec{p}_1 \cdot \vec{p}_2 = |\vec{p}_1||\vec{p}_2|\cos\theta \tag{B.10}$$

with

$$\cos\theta = \cos\theta_1 \cos\theta_2 + \sin\theta_1 \sin\theta_2 \cos(\phi_2 - \phi_2)\,. \tag{B.11}$$

This leads to the following relations

$$(p_1 + p_2)^2 = m_1^2 + m_2^2 + 2E_1E_2 - 2|\vec{p}_1||\vec{p}_2|\cos\theta$$
$$(p_2 - p)^2 = m_2^2 - 2E_2p_0 + 2p_0|\vec{p}_2|\cos\theta_2\,. \tag{B.12}$$

Killing the integration over $\cos\theta_2$ with $\delta(t-(p_2-p)^2)$, and the integration over $\cos\theta_1$ with $\delta((p_1+p_2-p)^2-m_3^2)$, we get

$$p_0\frac{dR}{d^3p} = \frac{1}{2^5(2\pi)^8 p_0^2}\int ds\int dt\int dE_1\int dE_2\int_0^{2\pi}d\phi_1\int_0^{2\pi}d\phi_2\,|\mathcal{M}|^2$$
$$\delta(s-m_1^2-m_2^2-2E_1E_2+2|\vec{p}_1||\vec{p}_2|\cos\theta)f(E_1)f(E_2)(1\mp f(E_1+E_2-p_0)) \tag{B.13}$$

with

$$\cos\theta_1 = \frac{-t-s+m_2^2+m_3^2+2p_0E_1}{2p_0|\vec{p}_1|}, \quad \cos\theta_2 = \frac{t-m_2^2+2p_0E_2}{2p_0|\vec{p}_2|}. \tag{B.14}$$

The roots of the remaining delta function are

$$\bar{\phi}_\pm = \phi_1 \pm \cos^{-1}\left(\frac{-s+m_1^2+m_2^2+2E_1E_2-2|\vec{p}_1||\vec{p}_2|\cos\theta_1\cos\theta_2}{2|\vec{p}_1||\vec{p}_2|\sin\theta_1\sin\theta_2}\right). \tag{B.15}$$

Using Jacobian, we can use the delta function to do the ϕ_2 integration:

$$\begin{aligned}
&\int d\phi_2\delta(s-m_1^2-m_2^2-2E_1E_2+2|\vec{p}_1||\vec{p}_2|\cos\theta) \\
&\qquad = \int d\phi_2\sum_{j=\pm}\frac{\delta(\phi_2-\bar{\phi}_j)}{2\left||\vec{p}_1||\vec{p}_2|\sin\theta_1\sin\theta_2\sin(\bar{\phi}_j-\phi_1)\right|} \\
&\qquad = \frac{1}{2|\vec{p}_1||\vec{p}_2|\sin\theta_1\sin\theta_2}\frac{2}{\sqrt{1-\cos^2(\bar{\phi}_+-\phi_1)}} \\
&\qquad = \frac{1}{|\vec{p}_1||\vec{p}_2|\sin\theta_1\sin\theta_2}\frac{4p_0^2\sin\theta_1\sin\theta_2|\vec{p}_1||\vec{p}_2|}{2p_0\sqrt{aE_2^2+2bE_2+c}} \\
&\qquad = \frac{2p_0}{\sqrt{aE_2^2+2bE_2+c}}
\end{aligned} \tag{B.16}$$

The coefficients in the denominator are given by

$$\begin{aligned}
a &= -(s+t-m_2^2-m_3^2)^2, \\
b &= p_0\left[(s+t-m_2^2-m_3^2)(s-m_1^2-m_2^2)-2m_1^2(m_2^2-t)\right] \\
&\quad +E_1(m_2^2-t)(s+t-m_2^2-m_3^2), \\
c &= -(t-m_2^2)^2E_1^2
\end{aligned}$$

$$-2p_0\left(2m_2^2(s+t-m_2^2-m_3^2)-(m_2^2-t)(s-m_1^2-m_2^2)\right)E_1$$
$$+4p_0^2m_1^2m_2^2+m_2^2(s+t-m_2^2-m_3^2)^2+m_1^2(m_2^2-t)^2$$
$$-p_0^2(s-m_1^2-m_2^2)^2+(s-m_1^2-m_2^2)(t-m_2^2)(s+t-m_2^2-m_3^2)\,. \quad \text{(B.17)}$$

The integration over ϕ_1 gives 2π, and the production rate finally become

$$p_0\frac{dR}{d^3p}=\frac{1}{16(2\pi)^7p_0}\int_{s^{min}}^{\infty}ds\int_{t^{min}}^{t^{max}}dt\int_{E_1^{min}}^{\infty}dE_1\int_{E_2^{min}}^{E_2^{max}}dE_2\ |\mathcal{M}|^2$$
$$f(E_1)f(E_2)(1\mp f(E_1+E_2-p_0))\frac{1}{\sqrt{aE_2^2+2bE_2+c}} \quad \text{(B.18)}$$

The lower bound for s has to satisfy :

$$s^{min}\geq(m_1+m_2)^2 \quad \text{and} \quad s^{min}\geq m_3^2\,. \quad \text{(B.19)}$$

Since t is a Lorentz invariant, we can find its boundary conditions in any frame. We take here the center of mass frame of the reaction $1+2\to 3+\gamma$. We have

$$\begin{aligned}t^{min(max)} &= (p2-p)^2=(p_1-p_3)^2\\ &= m_1^2+m_3^2-2E_1^{CM}E_3^{CM}-(+)2|\overrightarrow{p}_1^{CM}||\overrightarrow{p}_3^{CM}|\\ &= m_1^2+m_3^2-2\left(\frac{s+m_1^2-m_2^2}{2\sqrt{s}}\right)\left(\frac{s+m_3^2}{2\sqrt{s}}\right)\\ &\quad -(+)2\frac{\sqrt{(s+m_1^2-m_2^2)^2-4sm_1^2}}{2\sqrt{s}}\frac{(s-m_3^2)}{2\sqrt{s}}\end{aligned} \quad \text{(B.20)}$$

For fixed values of p_0, s and t, we can find the lower bound for E_1 from

$$\begin{aligned}u &= -s-t+m_1^2+m_2^2+m_3^2=(p_1-p)^2\\ &= m_1^2-2p_0E_1+2|\overrightarrow{p}_1|p_0\cos\theta_1\\ &\to 2E_1p_0\geq m_1^2-u-2p_0|\overrightarrow{p}_1|\end{aligned} \quad \text{(B.21)}$$

which gives

$$E_1^{min}=\frac{p_0m_1^2}{m_1^2-u}+\frac{m_1^2-u}{4p_0}\,. \quad \text{(B.22)}$$

We can derive a similar relation for E_2 from the definition of t:

$$\begin{aligned}t &= (p_2-p)^2=m_2^2-2E_2p_0+2p_0|\overrightarrow{p}_2|\cos\theta_2\\ &\to E_2\geq\frac{p_0m_2^2}{m_2^2-t}+\frac{m_2^2-t}{4p_0}\end{aligned} \quad \text{(B.23)}$$

Furthermore, the function under the square root in Eq. B.18 has to be positive ($aE_2^2 + 2bE_2 + c > 0$), giving

$$\frac{-b + \sqrt{b^2 - ac}}{a} < E_2 < \frac{-b - \sqrt{b^2 - ac}}{a} \tag{B.24}$$

for $a < 0$.

C

SCATTERING MATRIX ELEMENTS

In this Appendix we present our scattering amplitudes expressions for each mesonic process included in the photon production rate calculation (Eq. 2.4).

C.1 $\pi + \rho \to \pi + \gamma$

C.1.1 $\mathcal{M}_{\pi^+ + \rho^0 \to (a_1, \pi, \rho) \to \pi^+ + \gamma} = \mathcal{M}_{\pi^- + \rho^0 \to (a_1, \pi, \rho) \to \pi^- + \gamma}$

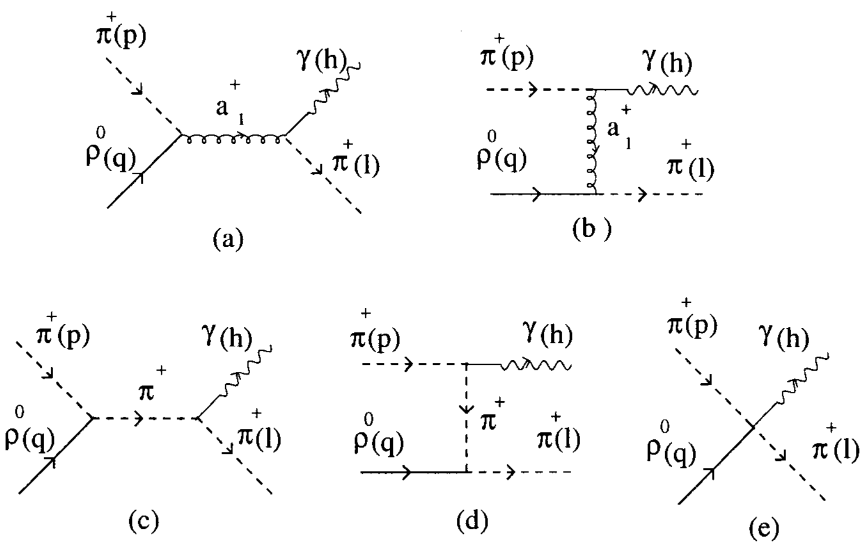

Figure C.1: Diagrams for $\pi^+ + \rho^0 \to (a_1, \pi, \rho) \to \pi^+ + \gamma$.

$$
\begin{aligned}
\mathcal{M}_a^{C.1.1} &= \frac{-C\hat{g}^2}{2(s-m_{a_1}^2+im_{a_1}\Gamma_{a_1})}\epsilon_\mu(q)\epsilon_\nu^*(h)[(\eta_1-\eta_2)^2\{-g^{\mu\nu}p\cdot q\, l\cdot h+p\cdot q\, h^\mu l^\nu \\
&\quad -p^\mu l^\nu q\cdot h+p^\mu q^\nu l\cdot h\}+\eta_2(\eta_1-\eta_2)m_\rho^2(l\cdot h g^{\mu\nu}-h^\mu l^\nu)\}] \\
\mathcal{M}_b^{C.1.1} &= \frac{-C\hat{g}^2}{2(t-m_{a_1}^2)}\epsilon_\mu(q)\epsilon_\nu^*(h)[(\eta_1-\eta_2)^2\{-g^{\mu\nu}p\cdot h\, l\cdot q+p\cdot h\, l^\mu q^\nu \\
&\quad +h^\mu p^\nu q\cdot l-l^\mu p^\nu q\cdot h\}+\eta_2(\eta_1-\eta_2)m_\rho^2(-p\cdot h g^{\mu\nu}+h^\mu p^\nu)\}] \\
\mathcal{M}_c^{C.1.1} &= -2C\hat{g}^2(1-\frac{\delta}{2})\frac{l^\nu p^\mu}{(s-m_\pi^2)}\epsilon_\mu(q)\epsilon_\nu^*(h) \\
\mathcal{M}_d^{C.1.1} &= -2C\hat{g}^2(1-\frac{\delta}{2})\frac{p^\nu l^\mu}{(t-m_\pi^2)}\epsilon_\mu(q)\epsilon_\nu^*(h) \\
\mathcal{M}_e^{C.1.1} &= C\left[g^{\mu\nu}\hat{g}^2(1-\frac{\delta}{2})+\left(\frac{\hat{g}^2\delta}{m_\rho^2}-4C_4\hat{g}^2\right)(g^{\mu\nu}q\cdot h-h^\mu q^\nu)\right]\epsilon_\mu(q)\epsilon_\nu^*(h) \qquad \text{(C.1)}
\end{aligned}
$$

where $s=(p+q)^2$,$t=(p-h)^2$ and $u=(q-h)^2$.

Ward identity:

$$
\begin{aligned}
h_\nu\mathcal{M}_a^{C.1.1\,\mu\nu} &= 0 \\
h_\nu\mathcal{M}_b^{C.1.1\,\mu\nu} &= 0 \\
h_\nu\mathcal{M}_c^{C.1.1\,\mu\nu} &= -2C\hat{g}^2(1-\frac{\delta}{2})\frac{l\cdot h p^\mu}{(s-m_\pi^2)} \\
h_\nu\mathcal{M}_d^{C.1.1\,\mu\nu} &= -2C\hat{g}^2(1-\frac{\delta}{2})\frac{p\cdot h l^\mu}{(t-m_\pi^2)} \\
h_\nu\mathcal{M}_e^{C.1.1\,\mu\nu} &= C\hat{g}^2(1-\frac{\delta}{2})h^\mu \qquad \text{(C.2)}
\end{aligned}
$$

such that

$$
\begin{aligned}
h_\nu\mathcal{M}^{C.1.1\,\mu\nu} &= h_\nu\mathcal{M}_a^{C.1.1\,\mu\nu}+h_\nu\mathcal{M}_b^{C.1.1\,\mu\nu}+h_\nu\mathcal{M}_c^{C.1.1\,\mu\nu}+h_\nu\mathcal{M}_d^{C.1.1\,\mu\nu}+h_\nu\mathcal{M}_e^{C.1.1\,\mu\nu} \\
&= -2C\hat{g}^2(1-\frac{\delta}{2})(\frac{p^\mu}{2}-\frac{l^\mu}{2}-\frac{h^\mu}{2}) = C\hat{g}^2(1-\frac{\delta}{2})q^\mu \qquad \text{(C.3)}
\end{aligned}
$$

Finally,

$$
h_\nu\mathcal{M}^{C.1.1\,\nu} = \epsilon_\mu(q)h_\nu\mathcal{M}^{C.1.1\,\mu\nu} = C\hat{g}^2(1-\frac{\delta}{2})q\cdot\epsilon(q) = 0 \qquad \text{(C.4)}
$$

C.1.2 $\mathcal{M}_{\pi^0+\rho^+\to(a_1,\pi,\rho)\to\pi^++\gamma} = \mathcal{M}_{\pi^0+\rho^-\to(a_1,\pi,\rho)\to\pi^-+\gamma}$

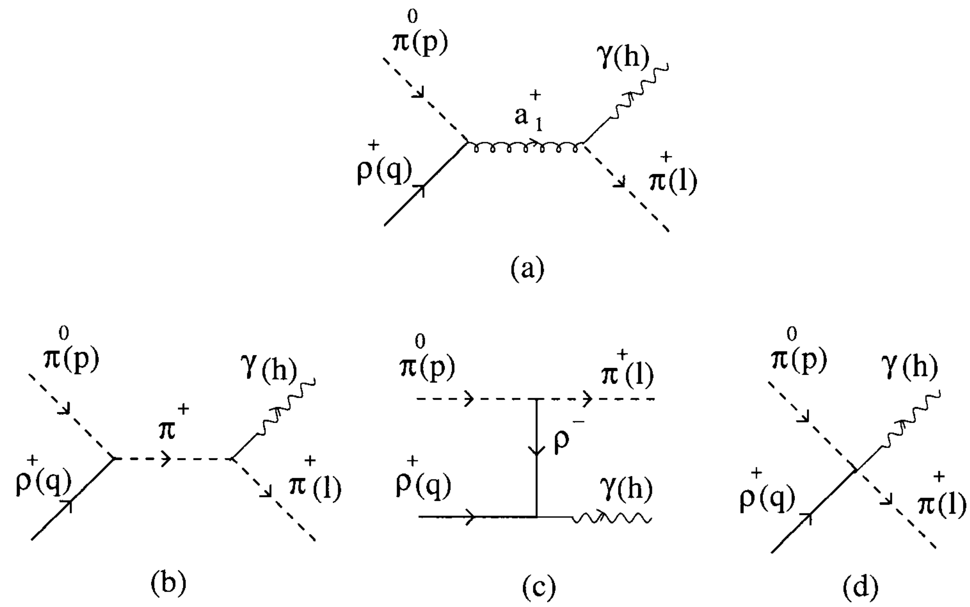

Figure C.2: Diagrams for $\pi^0 + \rho^+ \to (a_1, \pi, \rho) \to \pi^+ + \gamma$.

$$
\begin{aligned}
\mathcal{M}_a^{C.1.2} &= \frac{C\hat{g}^2}{2(s - m_{a_1}^2 + i m_{a_1}\Gamma_{a_1})}\epsilon_\mu(q)\epsilon_\nu^*(h)[(\eta_1-\eta_2)^2\{-g^{\mu\nu}p\cdot q\, l\cdot h + p\cdot q\, h^\mu l^\nu \\
&\quad -p^\mu l^\nu q\cdot h + p^\mu q^\nu l\cdot h\} + \eta_2(\eta_1-\eta_2)m_\rho^2(l\cdot h g^{\mu\nu} - h^\mu l^\nu)\}] \\
\mathcal{M}_b^{C.1.2} &= 2C\hat{g}^2(1-\frac{\delta}{2})\frac{l^\nu p^\mu}{(s-m_\pi^2)}\epsilon_\mu(q)\epsilon_\nu^*(h) \\
\mathcal{M}_c^{C.1.2} &= -C\frac{\hat{g}^2}{2(u-m_\rho^2)}\left(1-\frac{\delta}{2}-\frac{\delta(u-m_\rho^2)}{2m_\rho^2}\right)((l+p)\cdot(q+h)g^{\mu\nu} \\
&\quad -2h^\mu(l+p)^\nu - 2q^\nu(l+p)^\mu)\epsilon_\mu(q)\epsilon_\nu^*(h) \\
\mathcal{M}_d^{C.1.2} &= C[-g^{\mu\nu}\frac{\hat{g}^2}{2}(1-\frac{\delta}{2}) + \frac{\hat{g}^2\delta}{2m_\rho^2}(-2h\cdot l\, g^{\mu\nu} + 2h^\mu l^\nu + q^\nu(p^\mu + l^\mu)) \\
&\quad +2C_4\hat{g}^2(g^{\mu\nu}q\cdot h - h^\mu q^\nu)]\epsilon_\mu(q)\epsilon_\nu^*(h)
\end{aligned}
\tag{C.5}
$$

C.1.3 $\mathcal{M}_{\pi^+ + \rho^- \to (a_1, \pi, \rho) \to \pi^0 + \gamma} = \mathcal{M}_{\pi^- + \rho^+ \to (a_1, \pi, \rho) \to \pi^0 + \gamma}$

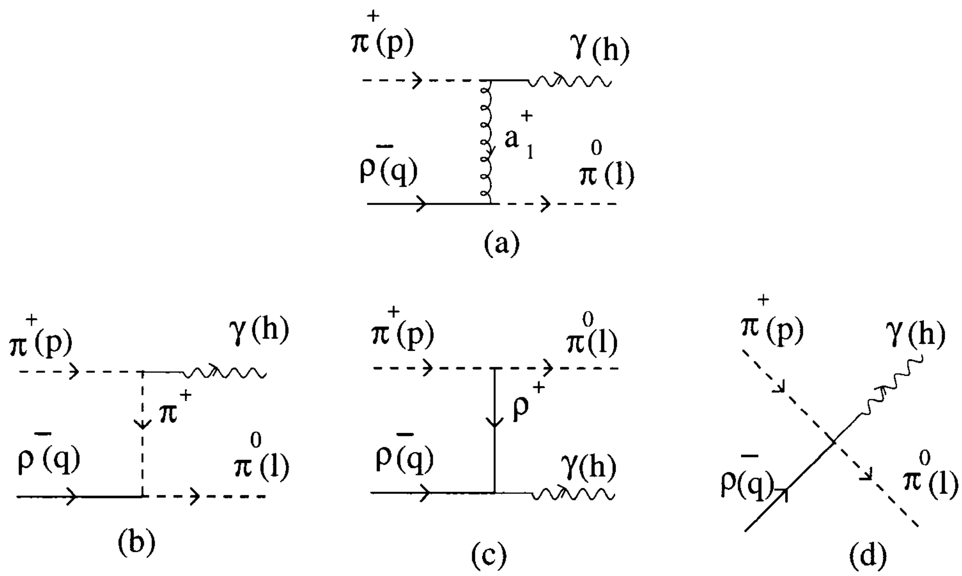

Figure C.3: Diagrams for $\pi^+ + \rho^- \to (a_1, \pi, \rho) \to \pi^0 + \gamma$.

$$
\begin{aligned}
\mathcal{M}_a^{C.1.3} &= \frac{C\hat{g}^2}{2(t - m_{a_1}^2)} \epsilon_\mu(q) \epsilon_\nu^*(h) [(\eta_1 - \eta_2)^2 \{ -g^{\mu\nu} p \cdot h \, l \cdot q + p \cdot h \, l^\mu q^\nu \\
&\quad + h^\mu p^\nu q \cdot l - l^\mu p^\nu q \cdot h \} + \eta_2(\eta_1 - \eta_2) m_\rho^2 (-p \cdot h g^{\mu\nu} + h^\mu p^\nu)\}] \\
\mathcal{M}_b^{C.1.3} &= 2C\hat{g}^2 (1 - \frac{\delta}{2}) \frac{p^\nu l^\mu}{(t - m_\pi^2)} \epsilon_\mu(q) \epsilon_\nu^*(h) \\
\mathcal{M}_c^{C.1.3} &= C \frac{\hat{g}^2}{2(u - m_\rho^2)} \left(1 - \frac{\delta}{2} - \frac{\delta(u - m_\rho^2)}{2m_\rho^2} \right) ((l + p) \cdot (q + h) g^{\mu\nu} \\
&\quad - 2h^\mu (l + p)^\nu - 2q^\nu (l + p)^\mu) \epsilon_\mu(q) \epsilon_\nu^*(h) \\
\mathcal{M}_d^{C.1.3} &= C[- g^{\mu\nu} \frac{\hat{g}^2}{2} (1 - \frac{\delta}{2}) + \frac{\hat{g}^2 \delta}{2m_\rho^2} (2h \cdot p \, g^{\mu\nu} - 2h^\mu p^\nu - q^\nu (p^\mu + l^\mu)) \\
&\quad + 2C_4 \hat{g}^2 (g^{\mu\nu} q \cdot h - h^\mu q^\nu)] \epsilon_\mu(q) \epsilon_\nu^*(h)
\end{aligned} \tag{C.6}
$$

C.1.4 $\mathcal{M}_{\pi^0+\rho^0\to(\omega)\to\pi^0+\gamma}$

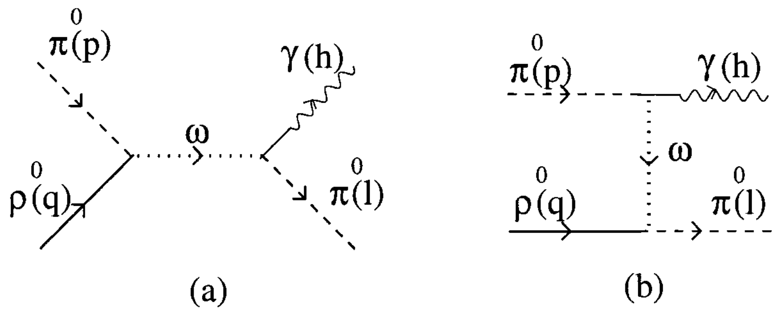

Figure C.4: Diagrams for $\pi^0 + \rho^0 \to (\omega) \to \pi^0 + \gamma$.

$$
\begin{aligned}
\mathcal{M}_a^{C.1.4} &= -C g_{\omega\rho\pi}(p+q)_\alpha (p+q)_y h_\mu q_x \left(\frac{-g_{\beta\gamma} + \frac{(p+q)_\beta (p+q)_\gamma}{m_\omega^2}}{s - m_\omega^2}\right) \epsilon^{\mu\nu\alpha\beta} \epsilon^{x\sigma y\gamma} \epsilon_\nu^*(h) \epsilon_\sigma(q) \\
\mathcal{M}_b^{C.1.4} &= -C g_{\omega\rho\pi}(p-h)_\alpha (p-h)_y h_\mu q_x \left(\frac{-g_{\beta\gamma} + \frac{(p-h)_\beta (p-h)_\gamma}{m_\omega^2}}{t - m_\omega^2}\right) \epsilon^{\mu\nu\alpha\beta} \epsilon^{x\sigma y\gamma} \epsilon_\nu^*(h) \epsilon_\sigma(q)
\end{aligned}
\tag{C.7}
$$

Ward Identity:

$$
\begin{aligned}
h_\nu \mathcal{M}_a^{C.1.4\,\mu\nu} &= 0 \\
h_\nu \mathcal{M}_b^{C.1.4\,\mu\nu} &= 0
\end{aligned}
\tag{C.8}
$$

C.1.5 $\mathcal{M}_{\pi^+ + \rho^- \to (\omega) \to \pi^0 + \gamma} = \mathcal{M}_{\pi^- + \rho^+ \to (\omega) \to \pi^0 + \gamma}$

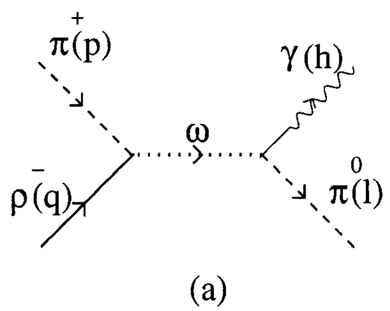

Figure C.5: Diagrams for $\pi^+ + \rho^- \to (\omega) \to \pi^0 + \gamma$.

$$\mathcal{M}_a^{C.1.5} = -C g_{\omega\rho\pi} (p+q)_\alpha (p+q)_y h_\mu q_x \left(\frac{-g_{\beta\gamma} + \frac{(p+q)_\beta (p+q)_\gamma}{m_\omega^2}}{s - m_\omega^2} \right) \epsilon^{\mu\nu\alpha\beta} \epsilon^{x\sigma y\gamma} \epsilon_\nu^*(h) \epsilon_\sigma(q) \tag{C.9}$$

C.1.6 $\mathcal{M}_{\pi^0 + \rho^+ \to (\omega) \to \pi^+ + \gamma} = \mathcal{M}_{\pi^0 + \rho^- \to (\omega) \to \pi^- + \gamma}$

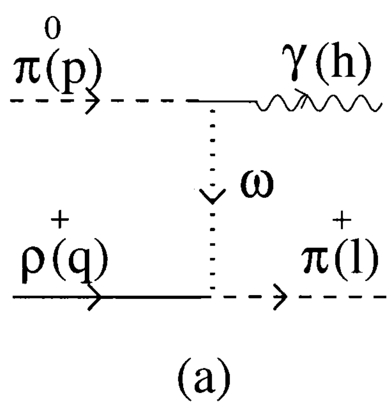

Figure C.6: Diagrams for $\pi^0 + \rho^+ \to (\omega) \to \pi^+ + \gamma$.

$$\mathcal{M}_a^{C.1.6} = -C g_{\omega\rho\pi} (p-h)_\alpha (p-h)_y h_\mu q_x \left(\frac{-g_{\beta\gamma} + \frac{(p-h)_\beta (p-h)_\gamma}{m_\omega^2}}{t - m_\omega^2} \right) \epsilon^{\mu\nu\alpha\beta} \epsilon^{x\sigma y\gamma} \epsilon_\nu^*(h) \epsilon_\sigma(q) \tag{C.10}$$

C.2 $\pi + \pi \to \rho + \gamma$

C.2.1 $\mathcal{M}_{\pi^+ + \pi^- \to (a_1, \pi, \rho) \to \rho^0 + \gamma}$

From crossing symmetry,

$$\begin{aligned}&\mathcal{M}^{C.2.1}\Big(\pi^+(p) + \pi^-(q) \to (a_1, \pi, \rho) \to \rho^0(l) + \gamma(h)\Big)\\&= \mathcal{M}^{C.1.1}\left(\pi^+(p) + \rho^0(-l) \to (a_1, \pi, \rho) \to \pi^+(-q) + \gamma(h)\right)\end{aligned} \tag{C.11}$$

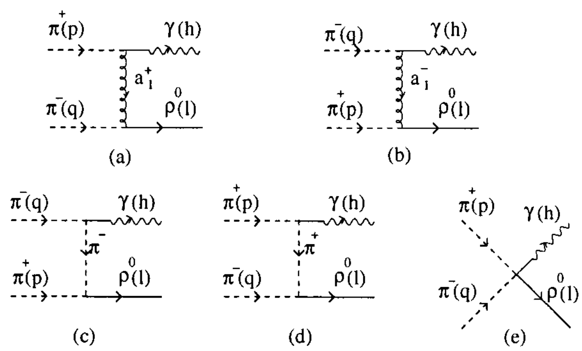

Figure C.7: Diagrams for $\pi^+ + \pi^- \to (a_1, \pi, \rho) \to \rho^0 + \gamma$.

C.2.2 $\mathcal{M}_{\pi^+ + \pi^0 \to (a_1, \pi, \rho) \to \rho^+ + \gamma} = \mathcal{M}_{\pi^- + \pi^0 \to (a_1, \pi, \rho) \to \rho^- + \gamma}$

$$\begin{aligned}&\mathcal{M}^{C.2.2}\Big(\pi^+(p) + \pi^0(q) \to (a_1, \pi, \rho) \to \rho^+(l) + \gamma(h)\Big)\\&= \mathcal{M}^{C.1.3}\left(\pi^+(p) + \rho^-(-l) \to (a_1, \pi, \rho) \to \pi^0(-q) + \gamma(h)\right)\end{aligned} \tag{C.12}$$

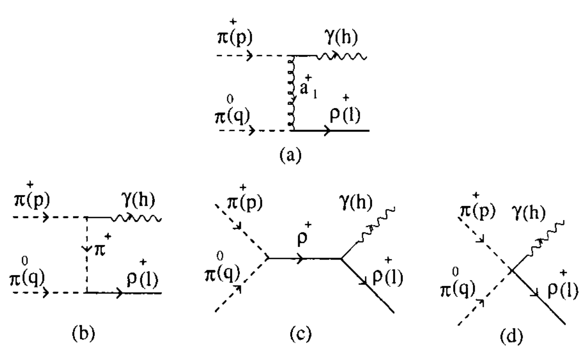

Figure C.8: Diagrams for $\pi^+ + \pi^0 \to (a_1, \pi, \rho) \to \rho^+ + \gamma$.

C.3 $\rho \rightarrow \pi + \pi + \gamma$

C.3.1 $\mathcal{M}_{\rho^0 \rightarrow (a_1, \pi, \rho) \rightarrow \pi^+ + \pi^- + \gamma}$

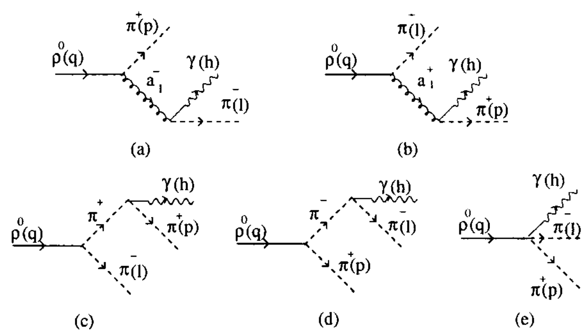

Figure C.9: Diagrams for $\rho^0 \rightarrow (a_1, \pi, \rho) \rightarrow \pi^+ + \pi^- + \gamma$.

$$
\begin{aligned}
&\mathcal{M}^{C.3.1}\Big(\rho^0(q) \rightarrow (a_1, \pi, \rho) \rightarrow \pi^+(p) + \pi^-(l) + \gamma(h)\Big) \\
&\quad = \mathcal{M}^{C.1.1}\Big(\pi^+(-p) + \rho^0(q) \rightarrow (a_1, \pi, \rho) \rightarrow \pi^+(l) + \gamma(h)\Big) \qquad \text{(C.13)}
\end{aligned}
$$

C.3.2 $\mathcal{M}_{\rho^+ \rightarrow (a_1, \pi, \rho) \rightarrow \pi^+ + \pi^0 + \gamma} = \mathcal{M}_{\rho^- \rightarrow (a_1, \pi, \rho) \rightarrow \pi^- + \pi^0 + \gamma}$

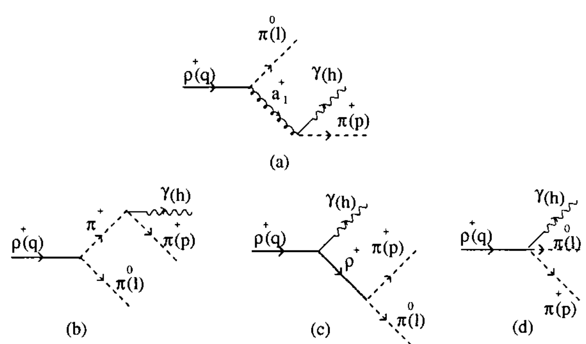

Figure C.10: Diagrams for $\rho^+ \rightarrow (a_1, \pi, \rho) \rightarrow \pi^+ + \pi^0 + \gamma$.

$$
\begin{aligned}
&\mathcal{M}^{C.3.2}\Big(\rho^+(q) \rightarrow (a_1, \pi, \rho) \rightarrow \pi^+(p) + \pi^0(l) + \gamma(h)\Big) \\
&\quad = \mathcal{M}^{C.1.3}\Big(\pi^+(-p) + \rho^-(q) \rightarrow (a_1, \pi, \rho) \rightarrow \pi^0(l) + \gamma(h)\Big) \qquad \text{(C.14)}
\end{aligned}
$$

C.4 $\pi + K^* \to K + \gamma$

C.4.1 $\mathcal{M}_{\pi^+ + K^{*0} \to K^+ + \gamma} = \mathcal{M}_{\pi^- + \bar{K}^{*0} \to K^- + \gamma}$ $= \mathcal{M}_{\pi^+ + K^{*-} \to \bar{K}^0 + \gamma} = \mathcal{M}_{\pi^- + K^{*+} \to K^0 + \gamma}$

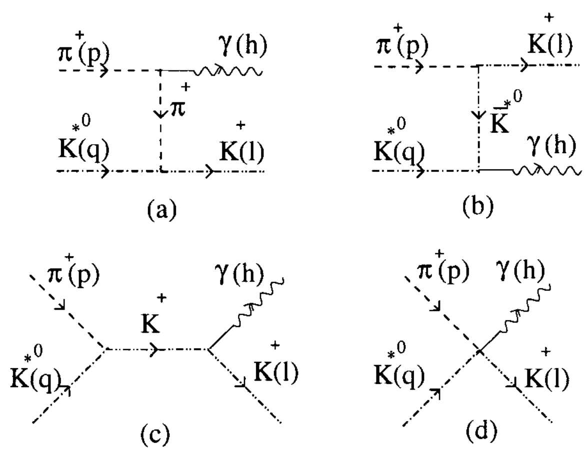

Figure C.11: Diagrams for $\pi^+ + K^{*0} \to K^+ + \gamma$.

$$
\begin{aligned}
\mathcal{M}_a^{C.4.1} &= 2C\frac{g_k^2}{\sqrt{2}}\frac{p^\nu l^\mu}{t - m_\pi^2}\epsilon_\mu(q)\epsilon_\nu^*(h) \\
\mathcal{M}_b^{C.4.1} &= -C\frac{g_k^2}{4\sqrt{2}(u - m_{K^*}^2)}\big[-g^{\mu\nu}(q+h)\cdot(l+p) + 2h^\mu(l+p)^\nu + 2q^\nu(l+p)^\mu \\
&\quad + g^{\mu\nu}(m_K^2 - m_\pi^2)\big]\epsilon_\mu(q)\epsilon_\nu^*(h) \\
\mathcal{M}_c^{C.4.1} &= C\frac{g_k^2}{\sqrt{2}}\frac{l^\nu p^\mu}{s - m_K^2}\epsilon_\mu(q)\epsilon_\nu^*(h) \\
\mathcal{M}_d^{C.4.1} &= -C\frac{3g_k^2}{4\sqrt{2}}g^{\mu\nu}\epsilon_\mu(q)\epsilon_\nu^*(h) \qquad \text{(C.15)}
\end{aligned}
$$

Ward Identity:

$$
\begin{aligned}
h_\nu \mathcal{M}_a^{C.4.1\,\mu\nu} &= -C\frac{g_k^2}{\sqrt{2}}l^\mu, \quad h_\nu \mathcal{M}_b^{C.4.1\,\mu\nu} = \frac{Cg_k^2}{4\sqrt{2}}(l+p)^\mu \\
h_\nu \mathcal{M}_c^{C.4.1\,\mu\nu} &= C\frac{g_k^2}{2\sqrt{2}}p^\mu, \quad h_\nu \mathcal{M}_d^{C.4.1\,\mu\nu} = -C\frac{3g_k^2}{4\sqrt{2}}h^\mu \qquad \text{(C.16)}
\end{aligned}
$$

$$
h_\nu \mathcal{M}^{C.4.1\,\nu} = \epsilon_\mu(q)h_\nu[\mathcal{M}_a^{C.4.1\,\mu\nu} + \mathcal{M}_b^{C.4.1\,\mu\nu} + \mathcal{M}_c^{C.4.1\,\mu\nu} + \mathcal{M}_d^{C.4.1\,\mu\nu}] = 0 \qquad \text{(C.17)}
$$

C.4.2 $\mathcal{M}_{\pi^0+K^{*\pm}\to K^{\pm}+\gamma} = \mathcal{M}_{\pi^0+K^{*0}\to K^0+\gamma} = \mathcal{M}_{\pi^0+\bar{K}^{*0}\to \bar{K}^0+\gamma}$

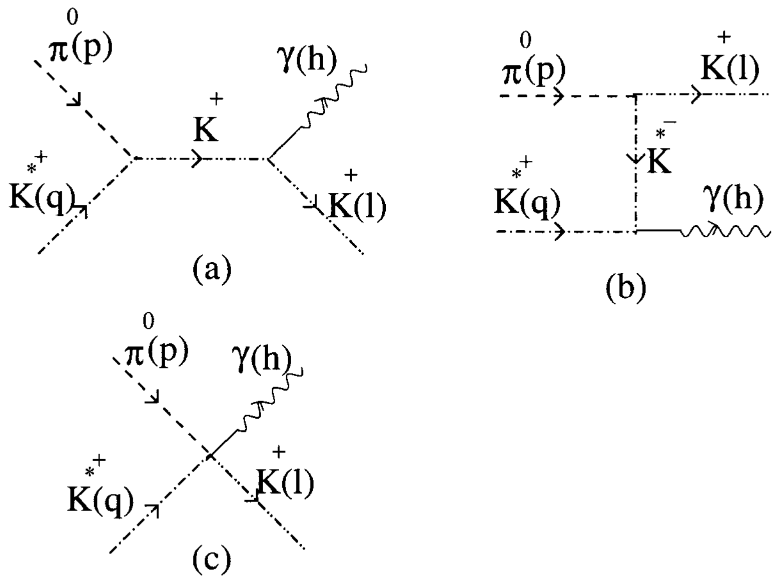

Figure C.12: Diagrams for $\pi^0 + K^{*+} \to K^+ + \gamma$.

$$
\begin{aligned}
\mathcal{M}_a^{C.4.2} &= C\frac{g_k^2}{2}\frac{l^\nu p^\mu}{s-m_K^2}\epsilon_\mu(q)\epsilon_\nu^*(h) \\
\mathcal{M}_b^{C.4.2} &= C\frac{g_k^2}{8(u-m_{K^*}^2)}[-g^{\mu\nu}(q+h)\cdot(l+p)+2h^\mu(l+p)^\nu+2q^\nu(l+p)^\mu \\
&\quad +g^{\mu\nu}(m_K^2-m_\pi^2)]\epsilon_\mu(q)\epsilon_\nu^*(h) \\
\mathcal{M}_c^{C.4.2} &= -C\frac{g_k^2}{8}g^{\mu\nu}\epsilon_\mu(q)\epsilon_\nu^*(h) \qquad (C.18)
\end{aligned}
$$

C.5 $\pi + K \to \bar{K}^* + \gamma$

C.5.1 $\mathcal{M}_{\pi^+ + K^- \to \bar{K}^{*0} + \gamma} = \mathcal{M}_{\pi^- + K^+ \to K^{*0} + \gamma}$ $= \mathcal{M}_{\pi^+ + K^0 \to K^{*+} + \gamma} = \mathcal{M}_{\pi^- + \bar{K}^0 \to K^{*-} + \gamma}$

$$\begin{aligned}\mathcal{M}^{C.5.1}&\Big(\pi^+(p) + K^-(q) \to \bar{K}^{*0}(l) + \gamma(h)\Big)\\ &= \mathcal{M}^{C.4.1}\Big(\pi^+(p) + K^{*0}(-l) \to K^+(-q) + \gamma(h)\Big)\end{aligned} \tag{C.19}$$

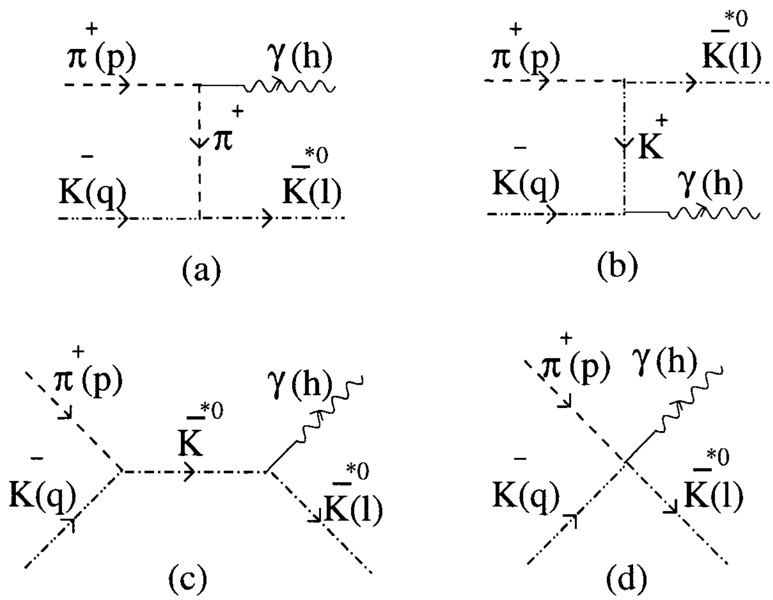

Figure C.13: Diagrams for $\pi^+ + K^- \to \bar{K}^{*0} + \gamma$.

C.5.2 $\mathcal{M}_{\pi^0+\bar{K}^0\to\bar{K}^{*0}+\gamma} = \mathcal{M}_{\pi^0+K^0\to K^{*0}+\gamma} = \mathcal{M}_{\pi^0+K^\pm\to K^{*\pm}+\gamma}$

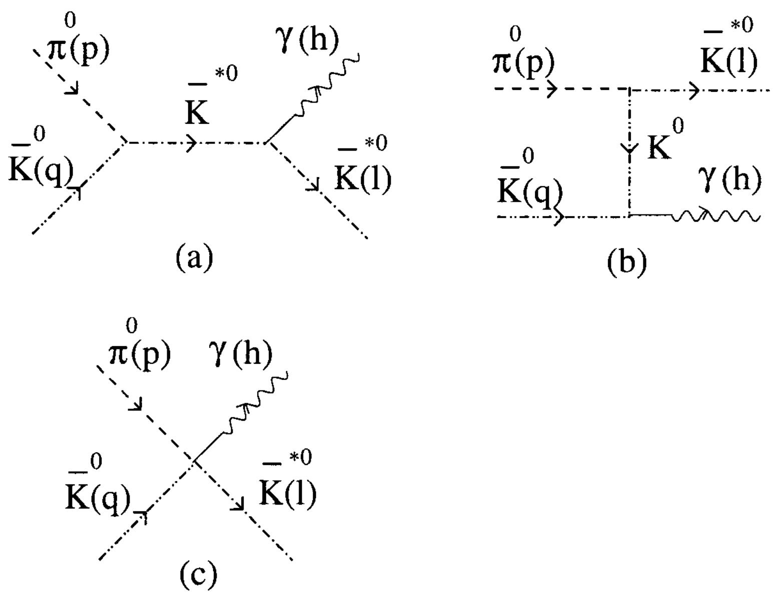

Figure C.14: Diagrams for $\pi^0 + \bar{K}^0 \to \bar{K}^{*0} + \gamma$.

$$\begin{aligned}
&\mathcal{M}^{C.5.2}\Big(\pi^0(p) + \bar{K}^0(q) \to \bar{K}^{*0}(l) + \gamma(h)\Big) \\
&\qquad = \mathcal{M}^{C.4.2}\Big(\pi^0(p) + K^{*0}(-l) \to K^0(-q) + \gamma(h)\Big) \qquad \text{(C.20)}
\end{aligned}$$

C.6 $\rho + K \to \bar{K} + \gamma$

C.6.1 $\mathcal{M}_{\rho^+ + K^- \to \bar{K}^0 + \gamma} = \mathcal{M}_{\rho^- + K^+ \to K^0 + \gamma}$ $= \mathcal{M}_{\rho^+ + K^0 \to K^+ + \gamma} = \mathcal{M}_{\rho^- + \bar{K}^0 \to K^- + \gamma}$

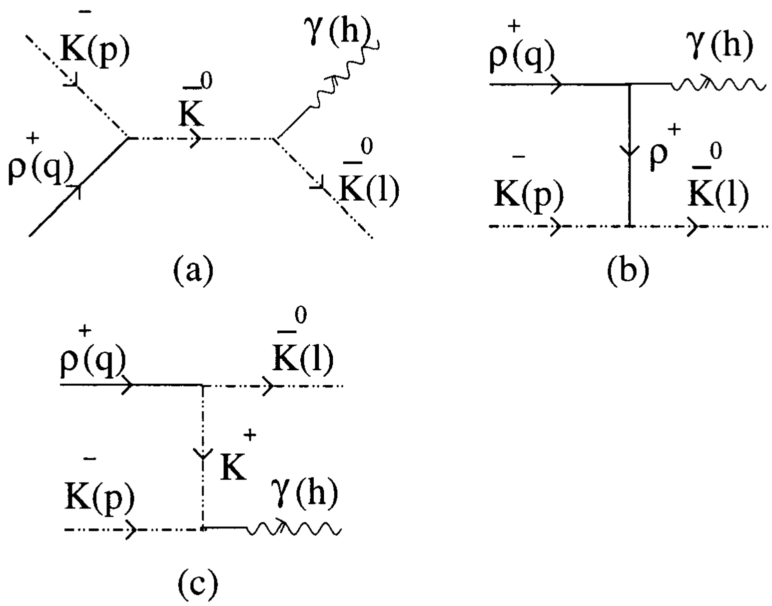

Figure C.15: Diagrams for $\rho^+ + K^- \to \bar{K}^0 + \gamma$.

$$
\begin{aligned}
\mathcal{M}_a^{C.6.1} &= C\frac{g_k^2}{\sqrt{2}}\frac{l^\nu p^\mu}{s - m_k^2}\epsilon_\mu(q)\epsilon_\nu^*(h) \\
\mathcal{M}_b^{C.6.1} &= C\frac{g_k^2}{2\sqrt{2}(u - m_\rho^2)}[-g^{\mu\nu}(q+h)\cdot(l+p) + 2h^\mu(l+p)^\nu + 2q^\nu(l+p)^\mu \\
&\quad + g^{\mu\nu}(m_K^2 - m_\pi^2)]\epsilon_\mu(q)\epsilon_\nu^*(h) \\
\mathcal{M}_c^{C.6.1} &= -C\frac{g_k^2}{\sqrt{2}}\frac{p^\nu l^\mu}{t - m_k^2}\epsilon_\mu(q)\epsilon_\nu^*(h)
\end{aligned}
\tag{C.21}
$$

C.6.2 $\mathcal{M}_{\rho^0+K^\pm\to K^\pm+\gamma} = \mathcal{M}_{\rho^0+K^0\to K^0+\gamma} = \mathcal{M}_{\rho^0+\bar{K}^0\to\bar{K}^0+\gamma}$

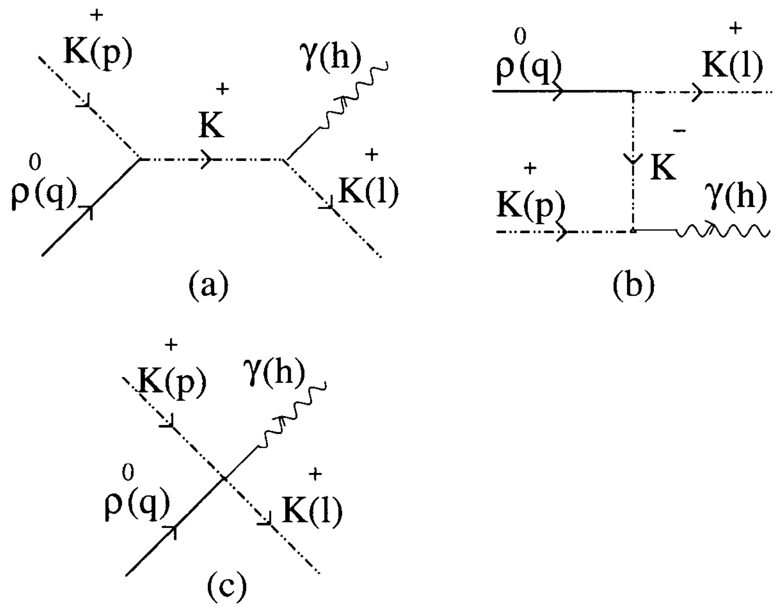

Figure C.16: Diagrams for $\rho^0 + K^+ \to K^+ + \gamma$.

$$\mathcal{M}_a^{C.6.2} = -C\frac{g_k^2}{2}\frac{l^\nu p^\mu}{s - m_k^2}\epsilon_\mu(q)\epsilon_\nu^*(h)$$
$$\mathcal{M}_b^{C.6.2} = -C\frac{g_k^2}{2}\frac{p^\nu l^\mu}{t - m_k^2}\epsilon_\mu(q)\epsilon_\nu^*(h)$$
$$\mathcal{M}_c^{C.6.2} = Cg^{\mu\nu}\frac{g_k^2}{4}\epsilon_\mu(q)\epsilon_\nu^*(h) \tag{C.22}$$

C.7 $K + K^* \to \pi + \gamma$

C.7.1 $\mathcal{M}_{K^-+K^{*0}\to\pi^-+\gamma} = \mathcal{M}_{K^++\bar{K}^{*0}\to\pi^++\gamma}$ $= \mathcal{M}_{K^0+K^{*-}\to\pi^-+\gamma} = \mathcal{M}_{\bar{K}^0+K^{*+}\to\pi^++\gamma}$

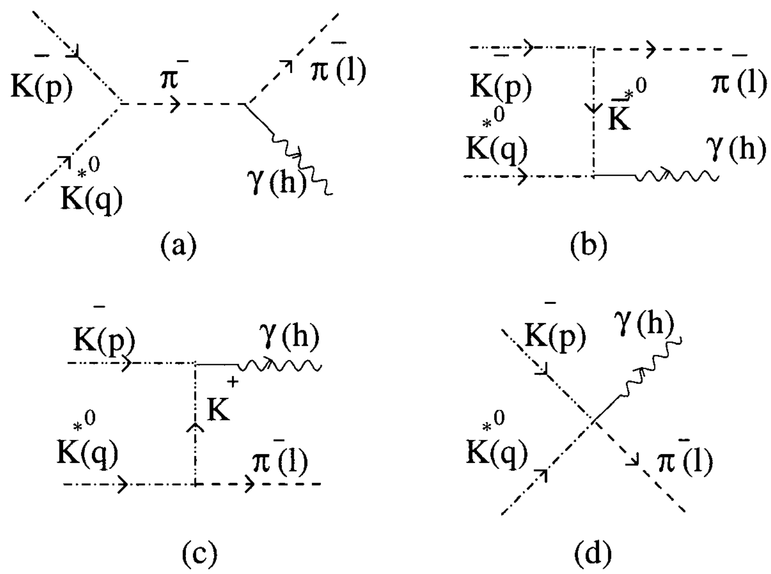

Figure C.17: Diagrams for $K^- + K^{*0} \to \pi^- + \gamma$.

$$\begin{aligned}\mathcal{M}^{C.7.1}&\Big(K^-(p) + K^{*0}(q) \to \pi^-(l) + \gamma(h)\Big)\\ &= \mathcal{M}^{C.4.1}\Big(\pi^+(-l) + K^{*0}(q) \to K^+(-p) + \gamma(h)\Big)\end{aligned} \tag{C.23}$$

C.7.2 $\mathcal{M}_{K^{\mp}+K^{*\pm}\to\pi^0+\gamma} = \mathcal{M}_{K^0+\bar{K}^{*0}\to\pi^0+\gamma} = \mathcal{M}_{\bar{K}^0+K^{*0}\to\pi^0+\gamma}$

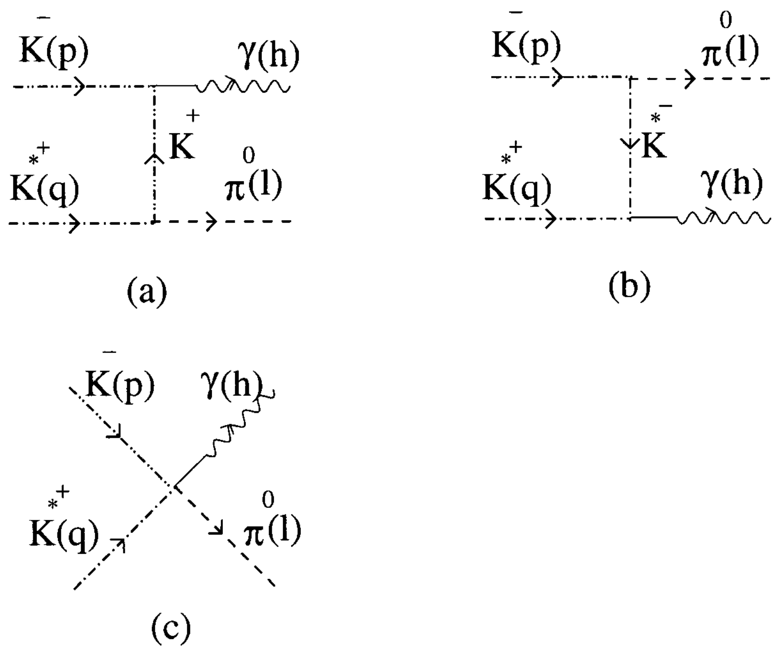

Figure C.18: Diagrams for $K^- + K^{*+} \to \pi^0 + \gamma$.

$$
\begin{aligned}
&\mathcal{M}^{C.7.2}\Big(K^-(p) + K^{*+}(q) \to \pi^0(l) + \gamma(h)\Big) \\
&\qquad = \mathcal{M}^{C.4.2}\left(\pi^0(-l) + K^{*+}(q) \to K^+(-p) + \gamma(h)\right)
\end{aligned} \tag{C.24}
$$

D

Σ-S_D DISCONTINUITY RELATION

First, the quark self-energy is given by

$$\Sigma = A\gamma^0 + B\hat{\gamma}\cdot\hat{\mathbf{q}}\,, \tag{D.1}$$

the quark propagator is

$$-iS_D(q) = -\frac{\gamma^0 - \hat{\gamma}\cdot\hat{\mathbf{q}}}{2D_+(q)} - \frac{\gamma^0 + \hat{\gamma}\cdot\hat{\mathbf{q}}}{2D_-(q)}\,, \tag{D.2}$$

while the complexe conjugate of the propagator is

$$iS_D^*(q) = -\frac{\gamma^0 - \hat{\gamma}\cdot\hat{\mathbf{q}}}{2D_+^*(q)} - \frac{\gamma^0 + \hat{\gamma}\cdot\hat{\mathbf{q}}}{2D_-^*(q)}\,. \tag{D.3}$$

The left hand side of Eq. 6.54 is now given by

$$\begin{aligned} S_D^*(q)\,\mathrm{Disc}\Sigma(\omega,|\vec{q}|)\,S_D(q) = {} & \left(\frac{\gamma^0 - \hat{\gamma}\cdot\hat{\mathbf{q}}}{2D_+^*(q)} + \frac{\gamma^0 + \hat{\gamma}\cdot\hat{\mathbf{q}}}{2D_-^*(q)}\right)\left(\gamma^0\mathrm{Disc}A + \hat{\gamma}\cdot\hat{\mathbf{q}}\mathrm{Disc}B\right) \\ & \times\left(\frac{\gamma^0 - \hat{\gamma}\cdot\hat{\mathbf{q}}}{2D_+(q)} + \frac{\gamma^0 + \hat{\gamma}\cdot\hat{\mathbf{q}}}{2D_-(q)}\right)\,. \end{aligned} \tag{D.4}$$

With $\gamma^0\gamma^0 = 1$, $\hat{\gamma}\cdot\hat{\mathbf{q}}\hat{\gamma}\cdot\hat{\mathbf{q}} = -1$ and $\gamma^0\hat{\gamma}\cdot\hat{\mathbf{q}}\gamma^0 = -\hat{\gamma}\cdot\hat{\mathbf{q}}$, the expression simplifies to

$$\begin{aligned} S_D^*(q)\,\mathrm{Disc}\Sigma(\omega,|\vec{q}|)\,S_D(q) = {} & \frac{1}{2D_+^*(q)D_+(q)}\left(\gamma^0 - \hat{\gamma}\cdot\hat{\mathbf{q}}\right)(\mathrm{Disc}A + \mathrm{Disc}B) \\ & + \frac{1}{2D_-^*(q)D_-(q)}\left(\gamma^0 + \hat{\gamma}\cdot\hat{\mathbf{q}}\right)(\mathrm{Disc}A - \mathrm{Disc}B)\,. \end{aligned} \tag{D.5}$$

On the other hand, the right hand side of Eq. 6.54 is

$$\begin{aligned} \mathrm{Disc}\left(-iS_D(q)\right) &= -\left(\gamma^0 - \hat{\gamma}\cdot\hat{\mathbf{q}}\right)\mathrm{Disc}\frac{1}{2D_+(q)} - \left(\gamma^0 + \hat{\gamma}\cdot\hat{\mathbf{q}}\right)\mathrm{Disc}\frac{1}{2D_-(q)} \\ &= -\frac{(\gamma^0 - \hat{\gamma}\cdot\hat{\mathbf{q}})}{2D_+^*(q)D_+(q)}\mathrm{Disc}D_+^*(q) - \frac{(\gamma^0 + \hat{\gamma}\cdot\hat{\mathbf{q}})}{2D_-^*(q)D_-(q)}\mathrm{Disc}D_-^*(q)\,. \end{aligned} \tag{D.6}$$

When $D_\pm(q) = D^*_\pm(q^*)$, it follows that

$$\begin{aligned} \mathrm{Disc} D^*_\pm(q) &= D^*_\pm(q_0 + i\epsilon) - D^*_\pm(q_0 - i\epsilon) \\ &= D_\pm(q_0 - i\epsilon) - D_\pm(q_0 + i\epsilon) \\ &= -\mathrm{Disc} D_\pm(q)\,. \end{aligned} \tag{D.7}$$

With $D_\pm(q) = -q_0 \pm |\vec{q}| + A \pm B$, we get

$$\begin{aligned} \mathrm{Disc}\,(-iS_D(q)) = &\frac{(\gamma^0 - \hat{\gamma}\cdot\hat{\mathbf{q}})}{2D^*_+(q)D_+(q)}\,(\mathrm{Disc}A + \mathrm{Disc}B) \\ &+\frac{(\gamma^0 + \hat{\gamma}\cdot\hat{\mathbf{q}})}{2D^*_-(q)D_-(q)}\,(\mathrm{Disc}A - \mathrm{Disc}B)\ . \end{aligned} \tag{D.8}$$

Finally, from Eqs. D.5 and D.8, we obtain the relation

$$S^*_D(q)\,\mathrm{Disc}\Sigma(\omega, |\vec{q}|)\,S_D(q) = \mathrm{Disc}\,(-iS_D(q))\ . \tag{D.9}$$

BIBLIOGRAPHY

[1] V. E. Viola, Nucl. Phys. A **734**, 487 (2004).

[2] S. Turbide *et al.*, Phys. Rev. C **70**, 014608 (2004).

[3] P. Danielewicz and G.F. Bertsch, Nucl. Phys. A **533**, 712 (1991).

[4] L. Beaulieu *et al.* Phys. Rev. C **64**, 064604 (2001).

[5] U. W. Heinz, arXiv:hep-ph/0407360.

[6] K. Rajagopal, Acta Phys. Polon. B **31**, 3021 (2000) [Comments Nucl. Part. Phys. A **2**, 120 (2002 APCPC,549,95-119.2002)] [arXiv:hep-ph/0009058].

[7] R. Ouyed, R. Rapp and C. Vogt, arXiv:astro-ph/0503357.

[8] M.E. Peskin and D.V. Schroeder, *An Introduction to Quantum Field Theory*, Ed. Perseus Books, 1995, 842 p.

[9] F. Karsch, Nucl. Phys. A **698**, 199 (2002).

[10] K. Adcox *et al.* [PHENIX Collaboration], Nucl. Phys. A **757**, 184 (2005).

[11] J. I. Kapusta and S. M. H. Wong, Phys. Rev. C **62**, 027901 (2000).

[12] S.S. Adler *et al.*, Phys. Rev. Lett. **91**, 072301 (2003).

[13] J.Adams *et al.*, Phys. Rev. Lett. **91**, 172302 (2003).

[14] C.Adler *et al.*, Phys. Rev. Lett. **90**, 082302 (2003).

[15] S.S. Adler *et al.*, Phys. Rev. Lett. **91**, 072303 (2003).

[16] J. P. Blaizot and F. Gelis, "Searching evidence for the color glass condensate at RHIC," arXiv:hep-ph/0405305.

[17] X.N. Wang, Phys. Rev. C **63**, 054902 (2001).

[18] M. Gyulassy, I. Vitev and X.N. Wang, Phys. Rev. Lett. **86**, 2537 (2001).

[19] M. Gyulassy and M. Plümer, Phys. Lett. B **243**, 432 (1990).

[20] X.N. Wang, M. Gyulassy and M. Plümer, Phys. Rev. D **51**, 3436 (1995).

[21] A.B. Migdal, Phys. Rev. **103**, 1811 (1956).

[22] R. Baier, Y.L. Dokshitzer, A.H. Mueller, S. Peigné and D.Schiff, Nucl. Phys. b **484**, 291 (1997).

[23] R.Baier, Y.L. Dokshitzer, A.H. Mueller and D.Schiff, JHEP **0109**, 033 (2001).

[24] M. Gyulassy, P. Levai and I. Vitev, Phys. Rev. Lett. **85**, 5535 (2000); Nucl. Phys. B **594**, 371 (2001).

[25] A. Kovner and U. A. Wiedemann, "Gluon radiation and parton energy loss", in Quark Gluon Plasma, R.C Hwa (Ed), World Scientific, Singapore, 192 (2003).

[26] B.G. Zakharov, JETP Lett. **63**, 952 (1996); JETP Lett. **70**, 176 (1999); JETP Lett. **65**, 615 (1997); Phys.Atom.Nucl. **61**, 838 (1998).

[27] X. N. Wang and M. Gyulassy, Phys. Rev. Lett. **68**, 1480 (1992).

[28] X. N. Wang, Z. Huang and I. Sarcevic, Phys. Rev. Lett. **77**, 231 (1996) [arXiv:hep-ph/9605213].

[29] S. Jeon, J.J. Marian and I. Sarcevic, Phys. Lett. B **562**, 45 (2003).

[30] M. Gyulassy, I. Vitev, X. N. Wang and B. W. Zhang, arXiv:nucl-th/0302077.

[31] P. Arnold, G.D. Moore and L. Yaffe, JHEP **0111**, 057 (2001); JHEP **0206**, 030 (2002).

[32] R.J. Fries, B. Müller and D.K. Srivastava, Phys. Rev. Lett **90**, 132301 (2003).

[33] C. Gale and J.I. Kapusta, Nucl. Phys. **B357**, 65 (1991).

[34] H.A. Weldon, Phys. Rev. D **28**, 2007 (1983).

[35] K.L. Haglin, J.Phys. G **30**:L27 (2004).

[36] V. Koch, nucl-th/9706075.

[37] H. Gomm, Ö. Kaymakcalan, and J. Schechter, Phys. Rev. **D30**, 2345 (1984).

[38] C. Song, Phys. Rev. **C47**, 2861 (1993).

[39] J. Schechter, Phys. Rev. D **34**, 868 (1986).

[40] Q. Ho-Kim and P.X. Yem, *Elementary Particles and their Interactions: Concept and Phenomena*, Springer, (1998).

[41] J. Sakurai, *Current and Mesons*, University of Chicago Press,(1969).

[42] U.G. Meissner, Phys. Rep. **161**, 213 (1988).

[43] I. Zahed and G.E. Brown, Phys. Rep. **142**, 1 (1986).

[44] T.D. Lee, *Particle Physics and Introduction to Field Theory*, Science Press, 865 pages (1988).

[45] S. Gao and C. Gale, Phys. Rev. **C57**, 254 (1998).

[46] Particle Data Group, Phys. Rev. **D66**, 010001 (2002).

[47] R. Rapp, G. Chanfray and J. Wambach, Nucl. Phys. **A617**, 472 (1997).

[48] R. Rapp and C. Gale, Phys. Rev. **C60**, 024903 (1999).

[49] J. Kapusta, P. Lichard and D. Seibert, Phys. Rev. **D44**, 2774 (1991) [erratum-*ibid.* **D47**, 4171 (1991)].

[50] K. Haglin, Phys. Rev. C **50**, 1688 (1994).

[51] C. Song and G. Fai, Phys. Rev. **C58**, 1689 (1998).

[52] Reaction (iii) in part 1 and reaction (ii) in part 2 of the Appendix A in [38] contain a Ward identity-violating component.

[53] J.E. Alam, P. Roy and S. Sarkar, Phys. Rev. C **71**, 059802 (2005).

[54] R. Rapp and J. Wambach, Adv. Nucl. Phys. **25** (2000) 1.

[55] R. Rapp, Proc. of 4. ICPAQGP (Jaipur, India, Nov. 26-30, 2001), Pramana **60**, 675 (2003) [arXiv:hep-ph/0201101].

[56] CERES/NA45 Collaboration (G. Agakichiev *et al.*), Phys. Rev. Lett. **75**, 1272 (1995);
Phys. Lett. **B422**, 405 (1998); Nucl. Phys. **A661**, 23 (1999).

[57] CERES/NA45 Collaboration (D. Adamova *et al.*), Phys. Rev. Lett. **91**, 042301 (2003) [arXiv:nucl-ex/0209024].

[58] J.V. Steele, H. Yamagishi and I. Zahed, Phys. Rev. **D56**, 5605 (1997).

[59] G.Q. Li and G.E. Brown, Nucl. Phys. **A632**, 153 (1998).

[60] J. Alam, P. Roy and S. Sarkar, arXiv:nucl-th/0304056.

[61] R. Rapp, M. Urban, M. Buballa and J. Wambach, Phys. Lett. **B417**, 1 (1998).

[62] R. Rapp and J. Wambach, Eur. Phys. J. **A6**, 415 (1999).

[63] M. Urban, M. Buballa, R. Rapp and J. Wambach, Nucl. Phys. **A673**, 357 (2000).

[64] S. Jeon and P.S. Ellis, Phys. Rev. D **58**, 045013 (1998).

[65] C.Y. Wong, *Introduction to High-Energy Heavy Ion Collisions*, (World Scientific, Singapore, 1994).

[66] P. Arnold, G.D. Moore and L. Yaffe, JHEP **0112** 9 (2001).

[67] P. Huovinen, P.V. Ruuskanen and S.S. Räsänen, Phys. Lett. **B535**, 109 (2002).

[68] R. Rapp and E.V. Shurayk, Phys. Lett. **B473**, 13 (2000).

[69] R. Rapp, Phys. Rev. C **63**, 054907 (2001).

[70] P. Braun-Munzinger, I. Heppe and J. Stachel, Phys. Lett. **B465**, 15 (1999); P. Braun-Munzinger, D. Magestro, J. Stachel and K. Redlich, Phys. Lett. **B518**, 41 (2001).

[71] A. Dumitru *et al.*, Phys. Rev. **C51**, 2166 (1995).

[72] D.K. Srivastava and B. Sinha, Phys. Rev. **C64**, 034902 (2001).

[73] R. Rapp, talk at the 3. plenary meeting of the CERN workshop on *Hard Probes in Heavy-Ion Collisions at the LHC*, CERN (Geneva), Oct. 7-11, 2002; http://wwwth.cern.ch/lhcworkshop/plenary_oct02.html

[74] R. Rapp, Phys. Rev. **C66**, 017901 (2002).

[75] P. Aurenche *et al.*, Eur. Phys. J. **C9**, 107 (1999).

[76] D.K. Srivastava, Eur. Phys. J. **C22**, 129 (2001).

[77] T. Peitzmann and M. Thoma, Phys. Rep. **364**, 175 (2002); C. Gale and K.L. Haglin, arXiv:hep-ph/0306098.

[78] WA98 Collaboration (M.M. Aggarwal *et al.*), Phys. Rev. Lett. **85**, 3593 (2000).

[79] M. McLaughlin *et al.* (E629 Collaboration), Phys. Rev. Lett. **31**, 971 (1983).

[80] J. Badier *et al.* (NA3 Collaboration), Z. Phys. **C31**, 341 (1986).

[81] S.A. Bass, B. Müller, and D.K. Srivastava, Phys. Rev. Lett. **90**, 082301 (2003).

[82] NA50 Collaboration (M.C. Abreu *et al.*), Eur. Phys. J. **C14**, 443 (2000); NA50 Collaboration (L. Capelli *et al.*), Nucl. Phys. **A698**, 539 (2002).

[83] I. Kvasnikova, C. Gale, and D.K. Srivastava, Phys. Rev. **C65**, 064903 (2002).

[84] R. Rapp and J. Wambach, Proc. of the 2. KEK-Tanashi International Symposium on *Hadron and Nuclear Physics with Electromagnetic Probes*, (Tanashi, Tokyo, 25.-27.10.99), edited by K. Maruyama and H. Okuno, ELSEVIER (Amsterdam, 2000) p. 21, [arXiv:nucl-th/0001014].

[85] WA80 Collaboration (R. Albrecht *et al.*), Phys. Rev. Lett. **76**, 3506 (1996).

[86] F. Karsch, E. Laermann and A. Peikert, Phys. Lett. **B478**, 447 (2000).

[87] T. Renk, Phys. Rev. C **67**, 064901 (2003) [arXiv:hep-ph/0301133].

[88] A. Dumitru, L. Frankfurt, L. Gerland, H. Stöcker, and M. Strickman, Phys. Rev. **C64**, 054909 (2001).

[89] G. Papp, P. Lévai, and G. Fai, Phys. Rev. **C61**, 021902(R) (1999).

[90] WA98 Collaboration (M.M. Aggarwal *et al.*), Eur. Phys. J. **C23**, 225 (2002).

[91] BRAHMS Collaboration (I.G. Bearden *et al.*), Phys. Rev. Lett. **88**, 202301 (2002).

[92] PHOBOS Collaboration (B.B. Back *et al.*), Phys. Rev. **C65**, 061901 (2002).

[93] I. Tserruya, Proc. of 4. ICPAQGP (Jaipur, India, Nov. 26-30, 2001), Pramana **60**, 577 (2003) [arXiv:nucl-ex/0204012].

[94] P.F. Kolb and U. Heinz, arXiv:nucl-th/0305084.

[95] P. Aurenche, F.Gelis and H.Zaraket, JHEP **0205**, 043 (2002).

[96] G.D. Moore, hep-ph/0403169.

[97] R. Baier, D. Schiff and B. G. Zakharov, Ann. Rev. Nucl. Part. Sci. **50**, 37 (2000) [arXiv:hep-ph/0002198].

[98] E. Wang and X.N. Wang, Phys. Rev. Lett. **87**, 142301 (2001).

[99] J.F. Owens, Rev. Mod. Phys. **59**, 465 (1987).

[100] G. Barnaföldi, G. Fai, P. Lévai, G. Papp and Y. Zhang, J.Phys. G: Nucl. Part. Phys. **27**, 1767 (2001).

[101] H.L. Lai, J. Huston, S. Kuhlmann, J. Morfin, F. Olness, J.F. Owens, J. Pumplin and W.K. Tung, Eur. Phys. J. C **12**, 375 (2000).

[102] J. Binnewies, B.A. Kniehl and G. Kramer, Phys. Rev. D **52**, 4947 (1995).

[103] S.S Adler *et al.*, Phys. Rev. Lett. **91**, 241803 (2003).

[104] R.J. Fries, B. Müller, C. Nonaka and S.A. Bass, Phys. Rev. C **68**, 044902, (2003).

[105] K.J. Eskola, V.J. Kolhinen and P.V. Ruuskanen, Nucl. Phys. B **535**, 351 (1998).

[106] K.J. Eskola, V.J. Kolhinen and C.A. Salgado, Eur. Phys. J. C **9**, 61 (1999).

[107] X.N. Wang, Phys. Lett. B **579**, 299 (2004).

[108] H.Niemi, S.S. Räsänen and P.V. Ruuskunen, CERN Yellow Report, hep-ph/0311131.

[109] M. Gyulassy, I. Vitev, X.N. Wang, and P. Huovinen, Phys. Lett. B **526**, 301 (2002).

[110] J.D. Bjorken, Phys. Rev. D **27**, 140 (1983).

[111] W. Greiner, L. Neise and H. Stoöcker, *Thermodynamics and Statistical Mechanics*, Springer, (1995).

[112] D.K. Srivastava, C. Gale and R.J. Fries, Phys. Rev. C **67**, 034903 (2003).

[113] R.C. Hwa and K. Kajantie, Phys. Rev. D **32**, 1109 (1985).

[114] I.G. Bearden, Phys. Rev. Lett. **94**, 162301 (2005).

[115] J. Kapusta, L.D. McLerran and D.K. Srivastava, Phys. Lett. B **283**, 145 (1992).

[116] T. Hirano and Y. Nara, Phys. Rev. C **69**. 034908 (2004).

[117] P. Aurenche, R. Baier, A. Douiri, M. Fontannaz and D. Schiff, Nucl. Phys. B **286**, 553 (1987); Nucl. Phys. **297**, 661 (1988).

[118] M. Gluck, E. Reya and A. Vogt, Phys. Rev. D **48**, 116 (1993); Erratum: *ibid.* D **51**, 1427 (1995); L. Bourhis, M. Fontannaz and J.Ph. Guillet, Eur. Phys. J. C **2**, 529 (1998).

[119] K. Reygers, talk at the Intern. Conf. on Hard Probes of High Energy Nuclear Collisions, Lisbon, Portugal, 2004.

[120] T.C. Awes, talk at DIS2005, Madison, U.S.A., 2005.

[121] Z. Lin and M. Gyulassy, Phys. Rev. C **51**, 2177 (1995).

[122] P.F. Kolb and U. Heinz, nucl-th/0305084.

[123] D.K. Srivastava, M.G. Mustafa and B. Müller, Phys. Rev. C **56**, 1064 (1997).

[124] B.G. Zakharov, JETP Lett. **80**, 1 (2004).

[125] F. Arleo *et al.*, hep-ph/0311131

[126] R.N. Cahn, Phys. Rev. D **7**, 247 (1973).

[127] S. Eidelman *et al.* (Particle Data Group), Phys. Lett. B **592**, 1 (2004).

[128] R. Albrecht *et al.*, Phys. Lett. B **361**, 14 (1995).

[129] S.S. Adler *et al.*, Phys. Rev. Lett. **94**, 232301 (2005).

[130] S. Bathe, talk given at Quark Matter 2005, Budapest, Hongary (2005).

[131] J. Y. Ollitrault, Phys. Rev. D **46**, 229 (1992); S. Voloshin and Y. Zhang, Z. Phys. C **70**, 665 (1996).

[132] R. J. Fries, B. Müller, C. Nonaka and S. A. Bass, Phys. Rev. Lett. **90**, 202303 (2003); Phys. Rev. C **68**, 044902 (2003); R. J. Fries, J. Phys. G **30**, S853 (2004).

[133] D. Molnar and M. Gyulassy, Nucl. Phys. A**697**, 495 (2002).

[134] S.S. Adler *et al.*, Phys. Rev. Lett. **91**, 182301 (2003).

[135] P. F. Kolb, J. Sollfrank and U. W. Heinz, Phys. Rev. C **62**, 054909 (2000).

[136] S. Turbide, C. Gale and R.J. Fries, Phys. Rev. Lett. **96**, 032303 (2006).

[137] S. S. Adler *et al.* [PHENIX Collaboration], Phys. Rev. Lett. **96**, 032302 (2006).

[138] S. D. Drell and T. M. Yan, Phys. Rev. Lett. **25**, 316 (1970).

[139] K. Kajantie, J. I. Kapusta, L. McLerran and A. Mekjian, Phys. Rev. D **34**, 2746 (1986).

[140] J. Kapusta, L. D. McLerran and D. K. Srivastava, Phys. Lett. B **283**, 145 (1992).

[141] T. Altherr and P.V. Ruuskanen, Nucl. Phys. B **380**, 377 (1992).

[142] C. Gale and P. Lichard, Phys. Rev. D **49**, 3338 (1994).

[143] A. Shor, Phys. Lett. B **233**, 231 (1989) [Erratum-ibid. B **252**, 722 (1990)].

[144] K. Geiger and J. I. Kapusta, Phys. Rev. Lett. **70**, 1920 (1993).

[145] E. Braaten and R.D. Pisarski, Nucl. Phys. B **337**, 569 (1990).

[146] E. Braaten, R.D. Pisarski and T.C. Yuan, Phys. Rev. Lett. **64**, 2242 (1990).

[147] S. M. H. Wong, Z. Phys. C **53**, 465 (1992).

[148] M.H. Thoma and C.T. Traxler, Phys. Rev. D **56**, 198 (1997).

[149] A numerical error as been found in the program used to calculate the graphs in Ref. [112].

[150] M. Le Bellac, *Thermal Field Theory*,(Cambridge University Press, 1996).

[151] J. Qiu and X. Zhang, Phys. Rev. D **64**, 074007 (2001).

[152] E. L. Berger, J. Qiu, and X. Zhang, Phys. Rev. D **65**, 034006 (2002).

[153] X. Guo, Phys. Rev. D **58**, 036001 (1998).

[154] R. Rapp, J. Phys. G**31**, s217 (2005).

[155] M. L. Mangano, P. Nason, and G. Ridolfi, Nucl. Phys. B **373**, 295 (1992).

[156] G. D. Moore and D. Teaney, Phys. Rev. C **71**, 064904, 2005.

[157] P. Aurenche, F. Gelis, G. D. Moore and H. Zaraket, JHEP **0212**, 006 (2002).